ABSTRACT

Title of dissertation: CMOS SINGLE-PHOTON AVALANCHE DIODES AND MICROMACHINED OPTICAL FILTERS FOR INTEGRATED FLUORESCENCE SENSING

Marc Péralte Dandin,
Doctor of Philosophy, 2012

Dissertation directed by: Professors Pamela Abshire & Elisabeth Smela
Fischell Department of Bioengineering

This dissertation presents a body of work that addresses the two most pressing challenges in the field of integrated fluorescence sensing, namely, the design of integrated optical sensors and the fabrication of high-rejection micro-scale optical filters. Two novel enabling technologies were introduced. They are: the perimeter-gated single-photon avalanche diode (PGSPAD), for on-chip photon counting, and the benzotriazole (BTA)-doped thin-film polymer filter, for on-chip ultraviolet light rejection.

Experimental results revealed that the PGSPAD front-end, fabricated in a 0.5 μm standard mixed-signal CMOS process, had the capability of counting photons in the MHz regime. In addition, it was found that a perimeter gate, a structural feature used to suppress edge breakdown in the diode, also maximized the signal-to-noise-ratio in the high-count rate regime whereas it maximized sensitivity at low count rates.

On the other hand, BTA-doped filters were demonstrated utilizing three commonly used polymers as hosts. The filters were patternable, utilizing the same procedures traditionally used to pattern the undoped polymer hosts, a key advantage for integration into microsystems. Filter performance was analyzed using a set of metrics developed for optoelectronic characterization of integrated fluorescence sensors; high rejection levels (nearing -40 dB) of UV light were observed in films of only 5 μm in thickness. Ultimately, BTA-doped filters were integrated into a portable sensor, and their use was demonstrated in two types of bioassays.

CMOS SINGLE-PHOTON AVALANCHE DIODES AND MICROMACHINED OPTICAL FILTERS FOR INTEGRATED FLUORESCENCE SENSING

by

Marc Péralte Dandin

Dissertation submitted to the Faculty of the Graduate School of the
University of Maryland, College Park in partial fulfillment
of the requirements for the degree of
Doctor of Philosophy
2012

Advisory Committee:
Professor Pamela Abshire, Chair/Advisor
Professor Elisabeth Smela
Professor Ian White
Professor Yu Chen
Professor Peter Sandborn

Dedication

I dedicate this dissertation to the founders of the Haitian nation: Jean-Jacques Dessalines le Grand, François-Dominique Toussaint l' Ouverture, Alexandre Pétion, Jean-Pierre Boyer, Henri Christophe, François Capois-la-Mort, Marie-Jeanne Lamartinière, Catherine Flon, Boukman Dutty, and Cécile Fatiman. Over two hundred years ago they stood erect and unafraid, and against all odds, they lit the flame of the Haitian Dream. On November 18^{th}, 1803 that flame flickered through the night threatened by many foes. And again, against all odds, it emerged from the hallowed battlefields of Vertières undimmed and brighter than ever.

On January 12^{th}, 2010, as the earth shook and Port-au-Prince collapsed, that same flame laid beneath piles of concrete and severed iron bars. But its gleams escaped through the cracks in the rubble and reached me from afar, soothing my grief and despair, giving me the strength to move forward.

It is my hope that we, sons and daughters of Vertières, recapture the unswerving will and unyielding courage of our illustrious forebears. Only then can we realize the Haitian Dream of a free, sovereign, democratic, prosperous, and proud nation, in which justice and righteousness prevail.

Non nobis Domine, non nobis, sed vexillum nostrum da gloriam.

Marc Péralte Dandin,
Washington DC, États-Unis d'Amérique,
le 23 Mai, en l'an 208 de l' Indépendance.

Acknowledgments

First and foremost, I am thankful to my advisors: Dr. Pamela Abshire and Dr. Elisabeth Smela. The work that follows would not have come to fruition without their valuable contributions.

When I met them over 8 years ago, it was their vision and enthusiasm for this project that convinced me to stay at UMD after my undergraduate studies. I thank them for having given me a chance to partake in this research, and for renewing their commitment to my education time and time again, especially at times when I failed. More importantly, however, I want to thank them for having taught me the principles of scientific research, and for having set the bar high and for helping me reach it.

My thanks also go to Dr. Robert Fischell and the leadership of the Fischell Department of Bioengineering. I thank them for establishing the Fischell Fellowship Fund, and thus making it possible for me to stay at UMD to complete the doctoral program. I also acknowledge the staff and faculty of the Electrical and Computer Engineering Department and that of the Mechanical Engineering Department for providing support for my Ph. D research. Furthermore, I thank Dr. David Barbe at the Maryland Technology Institute for introducing me to the field of Entrepreneurship; his course helped me a great deal in evaluating the commercial potential of my research.

In that same spirit, I also want to thank the following individuals for having supported and/or participated in several entrepreneurial ventures undertaken

during my time here at Maryland. They are: Mrs. Lin and the Jimmy H. C. Lin Endowment for Entrepreneurship and the Ibis Microtech team, namely Dr. David Sander, Dr. Roland Probst, Dr. Marc Cohen, and Dr. Pamela Abshire.

My thanks also go to numerous colleagues who helped me with technical aspects of the work. I only name a few: Dr. Honghao Ji, Mr. Babak Nouri, Mr. Samuel Moseley, Dr. Somashekar Bangalore Prakash, Dr. Mario Urdaneta, Dr. Kuangwen Hsieh, Dr. Nicole McFarlane, Dr. David Sander, Ms. Anshu Sarje, and Mr. Jay Renner. I also thank Mr. Tom Loughran, Mr. Jon Hummel, and Mr. John Abrahams for their help in the Fab Lab. In addition, I thank Dr. Yu Chen, Dr. Ian White, and Dr. Sandborn for their feedback on this work and for serving on my examination committee.

I am also indebted to the professorial corps of the Nouveau Collège Bird. These individuals shaped my thinking from a very early age. I am particularly thankful to Mr. Denis Regis for teaching me History; Ms. Maguy Durcé, for having taught me how to "master the dew" through perseverance and renewal, and finally, Mr. Hugues Jean-Baptiste, for inspiring me and for instilling in me a love for mathematics.

This section would not be complete if I did not acknowledge those who have had a direct and personal impact on my journey. I thank my parents Yanick Guiteau and Jean Marvel Dandin for their love and for having worked tirelessly to grant me access to a high quality education. Many thanks also to my dear sister Sanite for her love and for having supported me throughout the final stages of this endeavor.

I am equally grateful to my surrogate family, Frantz and Dominique Verella, for their love and support. I thank Frantz for bringing me to the University of

Maryland, College Park 12 years ago and for convincing me to say and join the A. James Clark School of Engineering. I am also grateful to Dr. Larry Pierre for his friendship and for his moral support throughout my studies. I would not be here were it not for him.

I also want to acknowledge the following individuals for their continuing love and support: my aunts Roseline and Marie-France, my uncles Rony and Yves, my dear friends Siah, Ena, Mona, her sister Jeannette, and her husband Antoine, Jean-Max, Tipan, Sameena, Tenoch and his family, and my grand-mother, Carmélite, and many others I have not listed here!

Lastly, I would like to acknowledge the People of the United States of America, that shining light from the North. I salute its spirit and unstoppable drive for excellence. I also salute its commitment to its founding principles, and I stand in admiration at its undeviating will to perfect this Union, it too, created against all odds over 200 years ago. The relationships that I developed during the many years I have lived here bind me strongly to this land.

Preface

Integrated circuit (IC) technology has permeated every aspect of modern life. It is difficult to imagine that Bell Labs scientists Drs. J. Bardeen and W. Brattain anticipated in 1947 that their invention, the germanium point-contact transistor [1, 2], and a year later, Dr. W. Shockley 's junction version of the same device, namely the bipolar junction transistor (BJT) [3,4], would both bring forth an era of such unparalleled technological innovation. Within three decades of the first BJT, the advent of state-of-the-art material processing and high-volume semiconductor manufacturing technologies made possible the integration of hundreds of thousands of transistors onto millimeter-sized semiconductor dice. The modern microchip was born.

In 2012, it is now possible to fabricate *hundreds of millions* of metal-oxide-semiconductor field-effect transistors[1] (MOSFETs) in a 1 cm^2-large and 500 μm-thick silicon chip. The Pentium 4 microprocessor (Intel Corporation), which by today's standards has reached obsolescence, comprises 42 million transistors in a single substrate [7].

The IC industry is fast-paced, and it is driven following the so-called Moore's Law which shows that for the past 30 years, the number of transistors per chip has nearly doubled every 18 to 24 months [7]. Following this trend means ever-shrinking device sizes.

[1] The field-effect transistor pre-dates the BJT by almost two decades [5, 6]. Although BJTs made up the core of early ICs, they have now been largely replaced by their field-effect counterparts. Complementary-metal-oxide semiconductor (CMOS) processes which use two-types of MOSFETS (n and p) within the same substrate are nowadays the technology of choice for fabricating very-large scale integrated circuits.

One direct off-shoot of the technological advancements described above has been the field of micro-electro-mechanical systems (MEMS). Capitalizing on the lessons learned from the heyday of semiconductor technology and on novel materials and processing technologies, MEMS research brought forth a new class of devices referred to as *micromachines*.

In a landmark 1995 article titled "Micromachines on the March", Bryzek et al. defined a micro-electro-mechanical system as "a miniature device or an array of devices combining electrical and mechanical components fabricated with IC batch-processing techniques" [8]. In addition, the authors surveyed microfabrication techniques used in the MEMS industry, and they provided a comprehensive account of the then commercially available MEMS devices as well as future research directions. It is interesting to point out that the article barely mentioned Microfluidics, an important subset of MEMS.

This was by no means an oversight. Microfluidic chips have made significant inroads in the life sciences only recently; they are used to route and mix fluids in micrometer-sized channels and reservoirs for the purpose of conducting biochemical analyses utilizing limited amounts of reagents. The potential for microfluidics as an enabling technology for miniature analytical devices was discussed in a visionary paper by Manz et al. in 1990 [9].

Since then, the *bio-analytical microchip* made possible by microfludics has become a pervasive concept, and there are many commercially viable products that make use of the *lab-on-a-chip* (LOC) paradigm, also commonly known as the micro-(Total Analysis System) (μTAS) paradigm.

Despite steadfast progress in the field, significant challenges remain. For instance, a quick survey the literature reveals that despite the complexities of state-of-the-art LOCs (see for example the device reported in ref. [10]), they must still be tethered to bench-top hardware. That is, the majority of LOCs require conventional laboratory measurement equipment in order to provide a quantitative interpretation of the analyses they perform. Although this may be sufficient for some applications, in order to benefit from the inherent miniaturization of LOCs and render them portable for in-field or point-of-care use, or for use as implantable devices, measurement capability must be integrated within the microfluidic chips.

The research presented herein seeks to bridge that gap. It focuses on two enabling technologies, a novel optical sensor and a novel micro-scale optical filter, both designed specifically for integrated fluorescence sensing, *i.e.* the operation of performing a fluorescence-mediated bio-assay in an LOC without interfacing it with typical laboratory peripherals. The principles guiding the design of these components are taken from both IC and MEMS technologies.

The optical sensor is an integrated circuit based on the 0.5 μm, 3-metal, 2-poly mixed-signal CMOS process from ON Semiconductors Inc., and prototypes were fabricated through the MOSIS service. On the other hand, the optical filter consists of a polymer composite custom-designed for absorbing ultraviolet (UV) radiation. Fabrication and testing of the filters was undertaken using the Maryland Nanocenter FabLab, and at facilities located in the Mechanical Engineering Department's Laboratory for Microtechnologies.

The dissertation features a number of multi-authored journal articles. They

are marked with a dagger (†) in the Table Contents. My contributions to each of these articles, and that of my co-authors, are highlighted in Chapter 1.

Table of Contents

List of Tables

List of Figures

List of Abbreviations

APD	Avalanche Photo-Diode
APS	Active Pixel Sensor
BAOSM	Bovine Aortic Smooth Muscle (cells)
BSA	Bovine Serum Albumen
BTA	*(2–(2'–hydroxy-5'-methylphenyl)* BenzoTriAzole
CCD	Charge-Coupled Device
CDS	Correlated Double Sampling
CMOS	Complementary Metal-Oxide Semiconductor
DAQ	Data AcQuisition (card)
DIP40	Dual Inline Package (40-pin)
DUT	Device Under Test
FWHM	Full-Width Half-Max
GMAPD	Geiger Mode APD
HBSS	Hank's Balanced Salt Solution
IFS	Integrated Fluoresence Sensing
LCD	Liquid Crystal Display
LED	Light Emitting Diode
LOC	Lab-on-a-Chip
μTAS	Micro-(Total Analysis System)
MEMS	Micro-Electro-Mechanical Systems
NIST	National Institute of Standards and Technology
NEP	Noise Equivalent Power
PAMAM	Poly-(amidoamine) (dendrimers)
PCB	Printed Circuit Board
PD	Photodiode
PDMS	Poly-Dimethyl Siloxane
PGSPAD	Perimeter-Gated Single-Photon Avalanche Diodes
RMS	Root Mean-Square
S–H	Sample-and-Hold
SPAD	Single-Photon Avalanche Diodes
SMU	Source-Measure Units
UV	UltraViolet
VLSI	Very Large Scale Integration

Chapter 1

Preamble

1.1 Why Fluorescence?

There exist several analytical methods for monitoring molecular interactions mediated by ligand-binding events. These methods utilize several transduction modalities for representing these interactions by measurable signals. The modalities that have been demonstrated to date are either mechanical, electrical, magnetic, electrochemical, or optical [11]. Figure 1.1 illustrates how they compare with one another on the basis of complexity in sample preparation, portability, and most importantly, detection limit. Of these, fluorescence spectroscopy, an optical transduction method, stands out in terms of performance because it has detection limits that are orders of magnitude lower than what can be achieved with electrochemical methods, surface plasmon resonance sensors (SPR), and mechanical transduction techniques such as micro-cantilever mass sensors [11].

This ability to register biological activity at femtomolar concentrations makes fluorescence sensing one of the most widely used analytical techniques in biochemistry. In addition to unparalleled sensitivity, fluorescence-based assays offer high specificity due to the inherent selective affinity between target and probe molecules. Moreover, fluorescent moieties can be coupled with native biological receptors that lack transduction functions to engineer novel classes of molecular reporters [12].

Lastly, fluorescent probes exhibit high spatio-temporal resolution, and thus, they allow real-time and spatial monitoring of sub-cellular protein complexes [12].

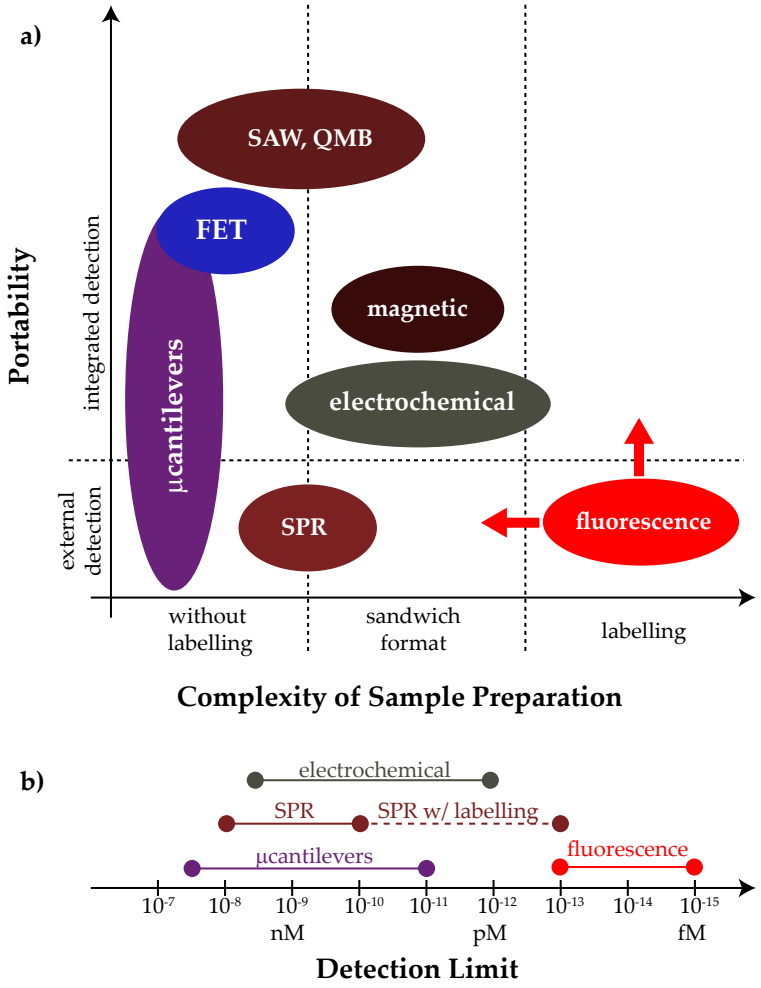

Figure 1.1: a) State-of-the-art biosensing methods. The arrows indicate current trends in on-chip fluoresence sensing research. b) Performance evaluation of several methods. Fluorescence sensing extends to the fM regime. Figure adapted from ref. [11].

In recent years, there have been significant efforts deployed towards integrating fluorescence spectroscopy in lab-on-a-chip (LOC) devices. *Integrated* fluorescence spectroscopy (IFS) is expected to broaden the scope of analyses that LOCs can

undertake.

Ideally, LOCs equipped with such integrated sensing capability will be able to replicate *on-chip* all the steps required to conduct a fluorescence-based assay, i.e. sample cleaning, incubation, detection, and quantification. Unlike other LOCs that require interfacing with peripheral equipment, IFS-enabled LOCs may be used in situations where access to a laboratory is limited or non-existent, such as, for example, point-of-care diagnostics or bio-agent threat assessment in environmental monitoring and homeland security applications, or in implantable devices.

1.2 Challenges in Integrated Fluorescence Sensing

As depicted in Figure 1.1, there are currently two thrust areas in integrated fluorescence sensing research. The first is the development of technologies for reducing the complexity of on-chip sample preparation, and the second, the development of on-chip measurement techniques for the purpose of making portable devices.

Advances in the field of microfluidics have shown that automated on-chip sample preparation can be performed in LOCs (see for example refs. [13–15]). However, the integration of photodetector arrays and optical filters, which is needed for achieving portability, has lagged. There have been efforts towards miniaturizing these components [16] but their assembly into configurations suitable for high-throughput multiplexed experiments, i.e. their *integration* in a such a fashion that truly exploits the benefits of LOC technology, has not yet matured.

This lack of progress stems from several technological hurdles. For instance, it

is difficult to achieve high performance optical sensing utilizing photodetectors that are fabricated in complementary metal-oxide semiconductors (CMOS)[1]. Moreover, integrated optical filters are inherently thin, and as a result, they cannot achieve high rejection of the excitation light. In addition, there is a lack of integrative fabrication methods for assembling all these components into a compact format as is required for a portable LOC.

This dissertation focuses on establishing a design paradigm that will mitigate the above-mentioned issues. The following section covers the research approach taken and on how it contrasts with the state-of-the-art.

1.3 Focus of this Dissertation

The block diagram of an IFS pixel[2] is shown in Figure 1.2. The photonic input to pixel P_j consists of the fluorescent light (the signal of interest), the excitation light, cross-talk from neighboring pixels, background light from other fluorescencing molecules as well as auto-fluorescence from the components that make up the optics, filter, and microfluidic subsystems[3]. This research seeks to understand the trade-offs that exist between integration and performance for two key system components of Figure 1.2 (gray-shaded blocks), namely, the optical detector and the optical filter.

[1] CMOS processes offer the possibility of fabricating microchips that can readily be integrated within microfluidics. Therefore, an optical transducer platform fabricated in a CMOS technology is a natural design choice for integrated fluorescence sensing.

[2] Here, the term pixel is used to refer to a single IFS in an array of identical elements.

[3] The materials comprised in these integrated components are often polymers, and thus they may have intrinsic fluorescence properties. This will be discussed in greater detail in Chapter 6.

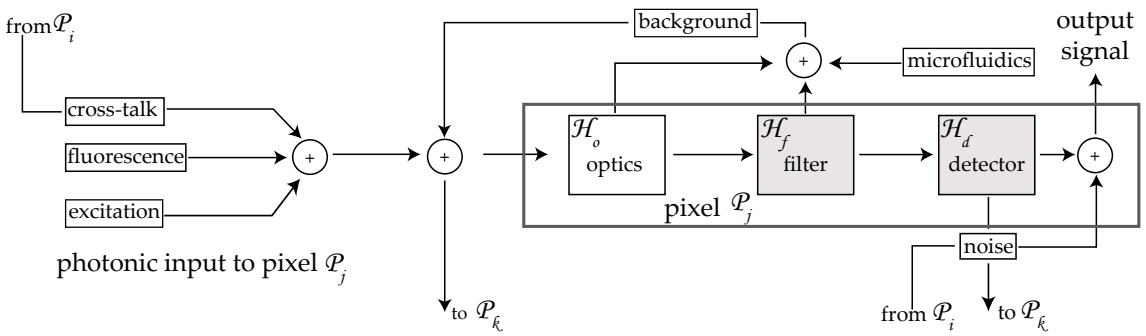

Figure 1.2: Block diagram of an integrated fluorescence sensor pixel. H_o, H_f, and H_d are the efficiency measures of the optics, the filter, and that of the detector at pixel P_j, respectively.

The optical detector developed in this research is a perimeter-gated single-photon avalanche diode (PGSPAD) fabricated in a 3-metal, 2-poly, mixed signal CMOS process. It has a novel architecture that allows photon counting with high sensitivity and high timing resolution, two features required for integrated fluorescence sensing.

Several research groups have demonstrated the fabrication of single-photon avalanche diodes (SPADs) in CMOS processes [17–20]. In order to achieve high performance photon counting, these devices relied on fabrication procedures[4] available only to the specific CMOS technologies in which they were fabricated. The PGSPAD presented herein is unique in that, unlike the SPADs referenced above, it can be ported to *any* process since it uses a fabrication technique that is generic to all CMOS technologies.

This is an important advantage for integrating high-performance photon counting sensors in LOCs at a lower cost because the detectors can be fabricated in the

[4] For example, they used: shallow trench isolation (STI), retrograde well doping, perimeter guard ring implant, etc... These techniques will be discussed in greater detail in Chapter 4.

simplest and thus least expensive CMOS processes. Furthermore, as shall be explained in Chapter 4, the PGSPAD detector can achieve similar performance to that of state-of-the-art CMOS SPADs despite having a larger active area. This indicates that further reduction in area could lead to additional improvements in performance.

The second integrated component discussed in this dissertation is the optical filter. The integrated filter technology reported consists of novel polymer composites that can be microfabricated and deposited directly on top of the CMOS detectors. These polymeric filters have the benefit of rejecting the excitation light with a high attenuation factor while transmitting the fluorescence with nearly zero loss. This means that very thin films (micrometers in thickness) of these polymers can be employed as a material for achieving, in an integrated device, performance that is comparable to that of filters used in bench-top spectrometers (in which the filters have millimeter to centimeter thicknesses).

Compared with other integrated filters [21–30], the polymer composites presented herein are amongst the few material systems developed for UV-excited fluorescence sensing. Moreover, the polymeric filters are easy to pattern, which confers them the ability to be easily integrated into LOCs.

1.4 Organization

The work is presented in two parts. The first part covers the optical sensor's design and its experimental evaluation, and the second discusses the optical filter's fabrication and its optical characterization. A summary of the chapters is given

below; the dissertation is written so that each chapter may be read independently.

Chapter 2 provides theoretical background information on phototransduction utilizing solid-state sensors. Furthermore, the chapter covers the metrics that were used to assess the SPAD sensor's optoelectronic performance.

Chapter 3 describes the perimeter-gated single-photon avalanche photodiode (PGSPAD)[5], a novel sensor front-end designed specifically for time-resolved integrated fluorescence sensing. It identifies the challenges of implementing such a detector in a standard CMOS fabrication technology. The chapter features an article published in the IEEE Sensors Journal, authored by myself, Dr. Akin Akturk, Mr. Babak Nouri, Dr. Neil Goldsman, and Dr. Pamela Abshire.

Dr. Akturk performed self-consistent simulations in order to formulate a theoretical basis for perimeter edge breakdown, an issue, as we shall see, that impedes the proper functioning of CMOS avalanche-based detectors. Mr. Nouri performed experimental work that studied the performance of these device under varying temperature conditions. Dr. Goldsman and Dr. Abshire served as editors of the final manuscript in addition to providing guidance for the experimental and theoretical investigations. I designed all the experiments featured in the paper.

Chapter 4 features published experimental results from the PGSPAD front-end equipped with an active readout circuit. This work appears in the latest issue of the IEEE Electron Device Letters Journal. Dr. Abshire, my sole co-author on this publication, served as editor. The design and experimental investigation were

[5] The initial concept for the PGSPAD was from Dr. Honghao Ji who designed the first lot of chips that I tested.

my own work.

Chapter 5 is the first to discuss the challenges in optical filtering at the micro-scale. This is done through a comprehensive critical review article that was published in the Lab-on-a-Chip Journal. That paper was co-authored by Dr. Abshire and Dr. Smela, who shared with me the responsibility of parsing through the literature in order to identify the long-standing issues in the field and foster new research directions. The set of performance metrics used to characterized the filters described in Chapter 6 was developed as a result of that effort.

Chapter 6 describes the polymer optical filter technology developed specifically for UV fluorescence sensing. This material is comprised in a manuscript that has been submitted for publication in the Journal of Micromechanics and Micro-engineering.

The chapter also features excerpts from an article that shows the use of the aforementioned filters in a hand-held micro-fluorometer.

The article, which appeared in the IEEE Transactions on Biomedical Circuits and Systems, was authored by Dr. Nicole McFarlane, with Dr. David Sander, myself, Ms. Anshu Sarje, Dr. Somashekar Prakash, and Dr. Pamela Abshire as co-authors. My contributions to this work were the optical filter design, fabrication, and integration, as well as an instrumentation test-bed along with software protocols for evaluating the fluorometer's performance. I also took part in conducting the two bioassay experiments reported in this dissertation.

Chapter 7 concludes the dissertation and offers future directions for this research. The key scientific and engineering contributions of the work are also

summarized there.

Appendix A describes experimental and analytical methods for estimating the spectral responsivity, a key detector performance metric, for active pixel sensors (APS). (The APS front-end was comprised in the IFS described in Chapter 6.)

Appendix B discusses of a photo-polymerization model developed for cross-linking benzotriazole-doped polymer filters that are based on UV photosensitive matrices.

Appendix C describes the optoelectronic characterization of a 4H-SiC avalanche photodiode. The methods developed in this work were the same as that developed for characterizing the spectral responsivity of the PGSPAD although the two detectors were designed for different bands of the electromagnetic spectrum.

Appendix D features an invited paper which appered in the 2009 IEEE Conference on Sensors. It describes efforts towards developing a microfabrication-based post-CMOS package that allows the integration of microfluidics with the filters and the detectors. This work was a joint effort between the many authors listed in the appendix.

Appendix E provides a derivation of the Poisson statistics that govern photoelectron emission processes, and from that result, a derivation of the shot noise equation used in discussing the signal-to-noise ratio (SNR) metric of various transducers in Chapter 2.

Chapter 2

Fundamentals of Phototransduction

2.1 Introduction

The study of the interaction of light with semiconductors is extensive; in this chapter we provide only the fundamental notions that are necessary to understand the operation of the photosensor[1]. Our discussion begins with the physical mechanism underlying the conversion of photons to free carriers in a semiconductor material. This process, which is referred to as photogeneration or photoelectric emission, is at the core of imaging science, and a thorough understanding of its nature is required when designing the front-end and the readout chain.

We then center our discussion on the concept of *phototransduction* and on a set of system-level performance metrics, namely the SNR, the noise equivalent power (NEP), and the spectral responsivity (S(λ)). Taken together, these figures-of-merit provide important insights into device performance by allowing the identification, at the design stage, of the trade-offs that exist between various circuit parameters. To illustrate this fact, and also to understand the operation of the PGSPAD detector featured in this dissertation, we focus on three distinct photosensor configurations.

[1] Here, the term photosensor is used to designate the front-end (i.e. the detector) and the readout circuit (ROC).

2.2 Photoelectron Emission in Semiconductors

2.2.1 Absorption Coefficient

The transmission of light through a semiconductor is governed by the Beer-Lambert law (Equation 2.1) [31]. It states that within the material, an incident light beam (of intensity I_{IN}) is attenuated by an exponential factor that depends on the material's thickness (d) and on a wavelength-dependent parameter α, the absorption coefficient. Thus, the exiting light beam (of intensity I_{OUT}) has a smaller intensity than the incident beam. Figure 2.1 shows the absorption coefficient data for commonly used semiconductors.

$$I_{OUT} = I_{IN} e^{-\alpha d}. \tag{2.1}$$

If the incident photons have enough energy, they will cause the valence electrons to migrate to the conduction band. These band-to-band transitions occur only when the incoming photons have energies that exceed the band gap energy of the semiconductor [31]; otherwise the photons pass through the material.

2.2.2 Quantum Efficiency

Once photons are absorbed, they generate charge with an efficiency factor denoted η. This quantum efficiency is an important metric in detector design. It is the ratio of the number of photoelectrons generated to the number of photons incident

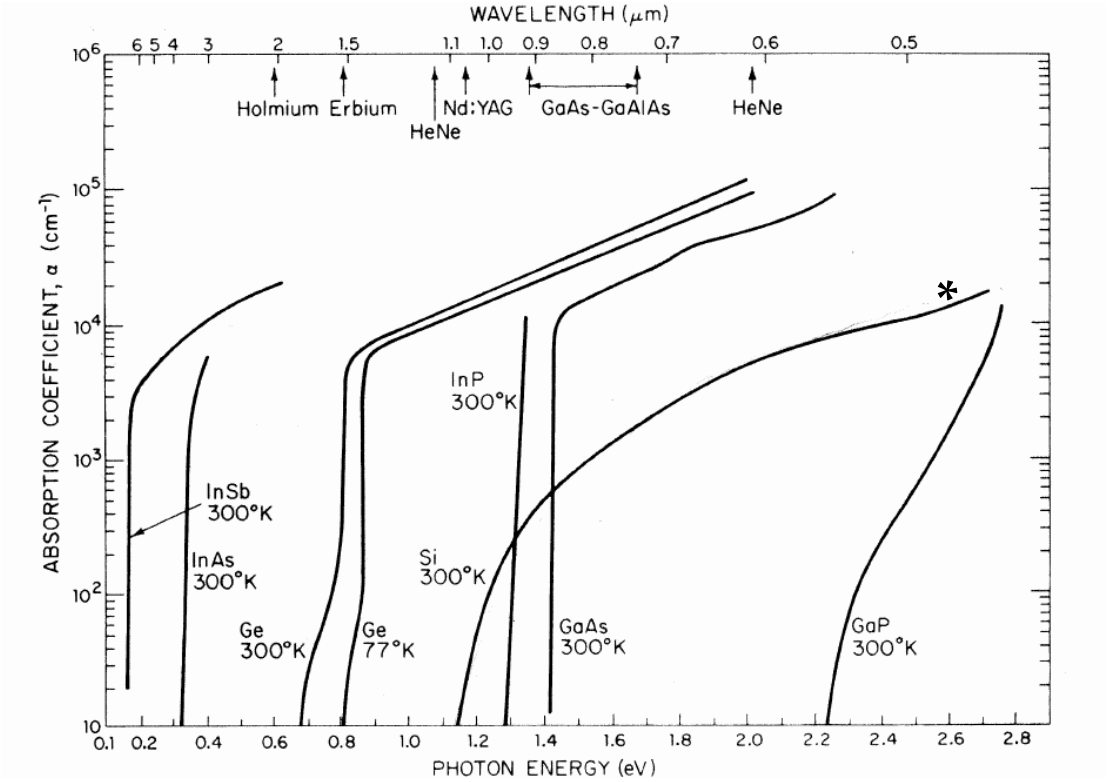

Figure 2.1: Absorption coefficient of different semiconductor materials as a function of photon energy and wavelength. Figure adapted from ref. [32]. The asterisk indicates the data for silicon, the material with which the detectors featured in this dissertation were fabricated.

on the material. Since photon absorption is wavelength-dependent as shown above, so is η[2]. Moreover, it also depends on the reflection coefficient (R) of the interface formed by the medium in which the incident light originates and the semiconductor's surface [33].

[2] If the incoming light is modulated, the quantum efficiency also depends on the modulation frequency. This dependence is not fundamental, rather it is related to circuit and device parameters (see ref. [32]). Thus, for completeness, the quantum efficiency is denoted $\eta(\lambda, w)$, where λ is the photon's wavelength and w the modulation frequency.

2.2.3 Thermal and Shot-Noise

The emission of electrons from the valence to the conduction band is not without noise. In other words, an ensemble measurement of the number of photo-generated carriers will show a spread around a mean value. This uncertainty is the aggregate result of several phenomena. The two most important ones being: the inherent randomness in the absorption of light quanta, i.e. the shot noise, and the random motion of charges due to thermal energy imparted by the surroundings to the semiconductor [33].

While the latter effect can be mitigated by cooling the detector and actively regulating the ambient temperature, the former cannot be suppressed. Shot noise is the fundamental noise limit of photodetection and it sets a lower bound to the noise figure of optical sensing circuits [32,33]. It is characterized by Poisson statistics as is shown in Appendix E. (Although a vacuum diode was used as a model for arriving to that result, it extends to all photosensor front-ends.)

2.3 Phototransduction and System-Level Metrics

Phototransduction, although subtly related to photoelectron emission, is functionally different. It is the process through which photo-generated carriers are converted into an electrical signal (i.e. a current or a voltage) that can be processed to infer, using a calibration curve, radiometric (e.g. light intensity) or photo-electric (e. g. photon flux) characteristics of the incident light beam. It is thus a system-level process unlike photoelectric emission. The metric that quantifies its performance is

the spectral responsivity, which depends, at some level, on the quantum efficiency, but is mainly influenced by the detector's biasing and the properties of the ROC.

The following sections present an analytical discussion of three photo-sensor front-ends. They are the photodiode (PD), the avalanche photodiode (APD), and Geiger mode avalanche photodiode (GMAPD). All three comprise a p-n junction, but in each case, the junction is biased in a distinct reverse bias regime (Figure 2.2).

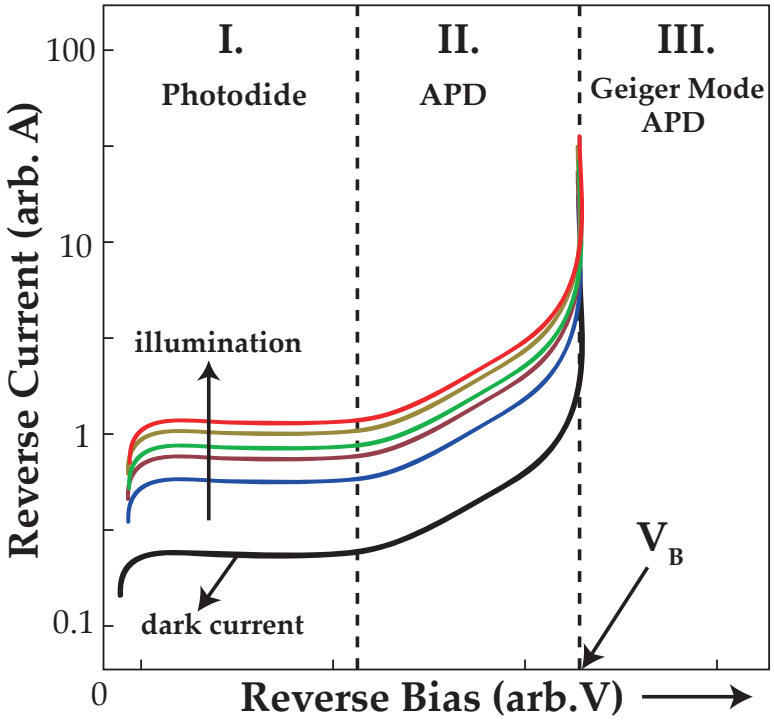

Figure 2.2: Arbitrary I-V curve showing three distinct p-n junction biasing regimes. Figure adapated from ref. [34].

Since deriving the spectral responsivity analytically requires a device physics-based model that takes into accounts dimensions as well as material properties, the discussion focuses rather on the signal-to-noise ratio (SNR) metric which can be computed from noise-equivalent circuit models; that is the case the first two front-

ends discussed. In case of the third one, i.e. the GMAPD, responsivity as well as SNR is easier determined experimentally. Appendix A and Appendix C both feature discussions on experimental techniques for estimating the spectral responsivity.

2.4 Photosensor Architectures

2.4.1 Photodiode Front-Ends

Photodiodes are p-n junctions biased at low reverse biases (Region I in Figure 2.2). In that regime, at most one free-carrier pair can be generated from an absorbed photon, that is, there is no internal gain mechanism through which a photo-generated carrier can create secondary electron-hole pairs. As shall be seen later on, this is not the case in Regions II and III.

Since the detector is biased, photogenerated carriers are accelerated by the applied electric field, and this gives rise to a photocurrent. As an ROC, for example, a transimpedance pre-amplifier may be used to convert the photocurrent into a voltage for further processing. A generic representation of a photodiode-based photosensor is shown in Figure 2.3.

2.4.1.1 Photodiode Signal-to-Noise Ratio

This section analyzes the photodiode's SNR utilizing the noise-equivalent circuit model shown in Figure 2.4. The derivation of the SNR metric from the photodiode noise-equivalent circuit model, as shown below, is credited to Still-

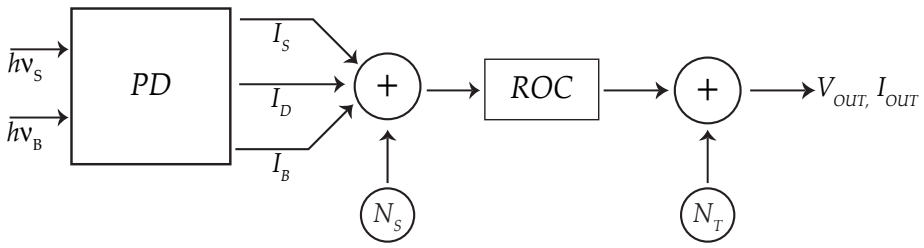

Figure 2.3: Model of a photodiode (PD) with its readout circuit (ROC). h is Planck's constant, and ν the frequency of the light. N_S and N_T denote shot noise and thermal noise terms, respectively. (Figure adapted from ref. [32].)

man and Wolfe [32].

The light incident on the junction has two components: one, of energy $h\nu_s$, which is the signal of interest, and the other, a background light signal of energy $h\nu_b$. Both components of the incoming light signal contribute to the photocurrent. In Figure 2.3, the mean values of these current components are denoted I_S and I_B, respectively.

Moreover, in the absence of light, a current can still be measured through the photodiode. That current is called the dark current, and it has a mean value denoted I_D. It is due to thermal energy in the junction and other leakage mechanisms from neighboring circuit components.

The dominant noise source in the ROC is thermal noise, and it can be modeled in its entirety as a two-port resistive impedance which has thermal noise current given by 4kT/R [35]. Accordingly, and utilizing the noise-equivalent circuit model shown in Figure 2.4, an expression for the SNR can be written as the ratio of the root mean-square (rms) signal power to that of sum of all the noise contributions [32]. These quantities are determined below.

The input signal power is assumed to be modulated as shown in Equation 2.2,

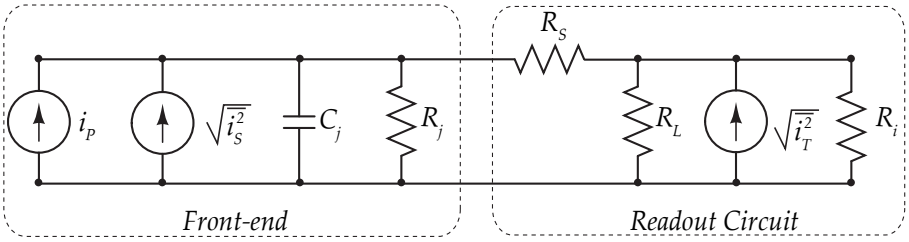

Figure 2.4: Noise equivalent small signal model of a photodiode with ROC. i_p is the root-mean-square photocurrent while, the other two current sources represent the mean-square shot noise and thermal noise terms. (Figure adapted from ref. [32].)

with modulation factor m, signal amplitude P_0, and angular frequency w. The root-mean-square signal power is shown in Equation 2.3.

$$P(wt) = P_0(1 + mcos(wt)) \tag{2.2}$$

$$\langle P \rangle^2 = \frac{mP_0}{\sqrt{2}} \tag{2.3}$$

The rms signal current is thus given by:

$$i_P(\lambda, w) = q\eta(\lambda, w)\frac{mP_0}{h\nu_S\sqrt{2}}. \tag{2.4}$$

The average photocurrent[3] is given by:

$$I_P(\lambda, 0) = q\eta(\lambda, 0)\frac{mP_0}{h\nu_S\sqrt{2}}. \tag{2.5}$$

The average background current, on the other hand, is the current produced over

[3] Here, we have changed the subscript from S to P to indicate that this component is due to the signal of amplitude P_0.

all wavelengths of light incident on the device. This is expressed mathematically as:

$$I_B = q\int_{\lambda} \frac{\left[\eta\left(\lambda^{'},0\right)P_B\left(\lambda'\right)\right]}{h\nu'}d\lambda^{'}. \tag{2.6}$$

The resistances in the equivalent circuit shown in Figure 2.4 can be lumped into one resistance R_{eq} at an effective temperature denoted by T_{eff}.

The SNR is:

$$\left(\frac{S}{N}\right) = \frac{\frac{1}{2}\left(\frac{q\eta P_0}{h\nu_S}\right)^2}{2q\left(I_P+I_B+I_D\right)\beta+\left(4kT_{eff}\left(\frac{1}{R_{eq}}\right)\beta\right)}. \tag{2.7}$$

Note that in the denominator, the first term of the sum is the additive shot noise obtained from Equation E.43 while the second term is the mean-squared thermal noise.

To analyze the photodiode's performance, it is more useful to solve Equation 2.7 for the optical power P_0 as a function of $\left(\frac{S}{N}\right)$. This yields:

$$P_0 = \frac{2h\nu_S\beta}{\eta}\left(\frac{S}{N}\right)\left\{1+\left[1+\frac{I_{eq}}{q\beta\left(\frac{S}{N}\right)}\right]^{\frac{1}{2}}\right\}, \tag{2.8}$$

where:

$$I_{eq} = I_B + I_D + \left(\frac{2kT_{eff}}{qR_{eq}} \right). \tag{2.9}$$

Equation 2.8 can be analyzed in two limiting regimes. In the first regime, the second term in the square brackets vanishes if the bandwidth is large. In that situation, the minimum power required to achieve a given SNR is limited only by the quantum efficiency. In reality, however, attaining such a limit is not possible because widening the bandwidth increases the thermal noise in the ROC (i.e. T_{eff} increases and R_{eq} decreases in Equation 2.9); this means means the term $\frac{I_{eq}}{q\beta\left(\frac{S}{N}\right)}$ may not go to zero.

In the other limiting case, the following condition holds:

$$\frac{I_{eq}}{q\beta\left(\frac{S}{N}\right)} \gg 1. \tag{2.10}$$

In this regime, design trade-offs are best understood utilizing the noise-equivalent power (NEP) metric, which is the optical power that is required to obtain an SNR of 1 in a 1 Hz measurement bandwidth [36]. A high performance detector has a low NEP.

The NEP is found from Equation 2.8 by setting the SNR term to 1, and by applying the limit condition of Equation 2.10 for further simplification.

$$NEP = \sqrt{2}\left(\frac{h\nu}{\eta}\right)\left[\frac{I_{eq}}{q}\right]^{\frac{1}{2}} = \sqrt{2}\left(\frac{h\nu}{\eta}\right)\left[\frac{I_B + I_D + \left(\frac{2kT_{eff}}{qR_{eq}}\right)}{q}\right]^{\frac{1}{2}}. \tag{2.11}$$

As Equation 2.11 shows, the NEP is minimized when R_{eq} is large. Unfortunately, however, large values of R_{eq} significantly reduce the 3dB cut-off frequency of the ROC, and thus lowers the bandwidth.

In conclusion, the photodiode front-end, equipped with a generic ROC, is best suited for applications that are background-limited (i. e. large I_B) and require small bandwidths [32]. As stated above, that limit can be reached by increasing R_{eq} at the expense of the bandwidth.

2.4.2 Avalanche Photodiode Front-Ends

This section considers a photosensor whose front-end is biased in Region II of Figure 2.2. In that regime, the front-end is said to be an avalanche photodiode. The applied field is so strong that it imparts enough kinetic energy to the photogenerated carriers; upon impacting a lattice atom as they are accelerated, they can create secondary carriers. These secondary carriers are in turn accelerated and give rise to additional free carriers via the same mechanism. This phenomenon is termed impact ionization, and it gives rise to an avalanche current, hence the APD denomination.

In Region II, the avalanche photocurrent is proportional to the photocurrent that would be generated without avalanche. The proportionality factor is finite, and it is called the multiplication factor, denoted M. This parameter is not only

wavelength-dependent but it is also influenced by the modulation frequency of the incident light signal [32].

A model of the APD with ROC is shown in Figure 2.5. Whereas the photocurrent is multiplied, the noise terms are also amplified. Intuitively, it would seem that an APD has a lot more noise than a photodiode front-end.

However, there are applications for which an APD is preferable to a photodiode because much lower NEPs can be achieved. As shown below, deriving the SNR and NEP metrics readily identifies the design trade-offs of the APD front-end.

2.4.2.1 Avalanche Photodiode Signal-to-Noise Ratio

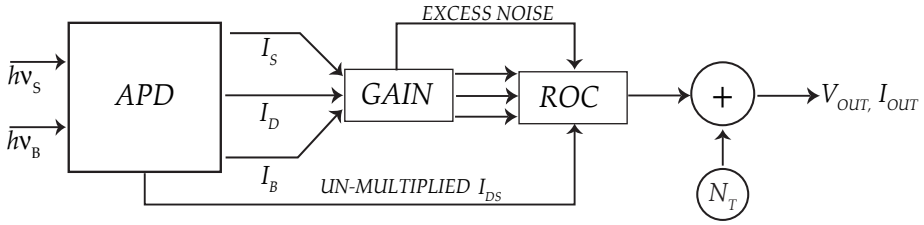

Figure 2.5: Model of an APD with ROC. The junction now has an internal gain mechanism which multiples the mean currents as well as the noise. Some of the dark current remains un-multiplied and the thermal noise term of the ROC is the same as in the case of the PD with ROC. (Figure adapted from ref. [32].)

The noise-equivalent circuit model for the APD-based photosensor is the same as that of the photiode-based sensor (shown in Figure 2.4). As before, shot noise, thermal noise, background, signal of interest, and dark current all couple to the ROC. The difference for an APD, however, is that, barring thermal noise in the ROC, all these components will be amplified by the internal gain mechanism. Moreover, statistical fluctuations in the gain mechanism itself introduce an excess noise which

couples to ROC. The excess noise factor is denoted F.

And lastly, dark currents originating from regions outside the multiplication region[4] also couple to the ROC. This term is denoted I_{DS}, where the subscript S denotes surface leakage currents.

Just as the avalanche photocurrent is proportional (by M) to the photocurrent without gain, the amplified noise is also proportional to the noise figure without gain.

In order to derive the SNR, the rms multiplied photocurrent and the shot noise term are written below as shown in ref. [32]. The thermal noise of the ROC is the same as before.

The multiplied rms photocurrent is:

$$i_P = \frac{q\eta P_0 M}{h\nu\sqrt{2}} \tag{2.12}$$

On the other hand, the shot noise, accounting for the effects of multiplication and excess noise, is given by:

$$\langle i_S^2 \rangle = 2q\left[\left(I + I_P F_P + I_B F_B + I_D F_D\right) M^2 + I_{DS}\right]\beta. \tag{2.13}$$

The SNR is:

$$\frac{S}{N} = \frac{\frac{1}{2}\left(q\eta P_0/h\nu\right)^2}{2q\left(I + I_P F_P + I_B F_B + I_D F_D\right)\beta + \left[2qI_{DS}\beta/M^2\right] + \left[4kT_{eff}\beta/R_{eq}M^2\right]} \tag{2.14}$$

[4] As shall be seen in Chapter 3, multiplication of photogenerated carriers is localized to specific regions of the p-n junction.

As Equation 2.14 shows, the SNR is maximized for large M values, which causes the last two terms of the sum in the denominator to zero.

Again, further insight can be gained by solving for the average power as a function of the SNR. This yields:

$$P_0 = \frac{2h\nu\beta F_P}{\eta}\left(\frac{S}{N}\right)\left\{1+\left[1+\frac{I_{eq}}{q\beta F_P^2\,(S/N)}\right]\right\}^{\frac{1}{2}}, \tag{2.15}$$

where

$$I_{eq} = I_B F_B + I_D F_D + \frac{I_{DS}}{M^2} + \frac{2kT_{eff}}{qR_{eq}M^2}. \tag{2.16}$$

The NEP is found by letting $\frac{S}{N} \rightarrow 1$ and $\beta \rightarrow 1$ in Equation 2.15.

$$NEP = \frac{2h\nu\beta F_P}{\eta}\left[\frac{I_{eq}}{qF_P^2}\right]^{\frac{1}{2}} \tag{2.17}$$

As Equation 2.16 shows, large multiplication factors minimize the NEP by eliminating the surface leakage-induced dark current and the thermal noise term.

This result implies that increasing the bandwidth does not adversely affect the NEP, unlike in the case of the photodiode. Consequently, APDs are suited for large bandwidth applications [32]. Furthermore, for inherently small R_{eq}, i.e. for high frequency operation, the internal gain mechanism also minimizes the NEP [32].

2.4.3 Geiger-mode Avalanche Photodiode Front-Ends

In Geiger mode, the APD is biased above the breakdown voltage (Region III in Figure 2.2). In that mode, the photosensor retains all the same features as the APD that we have just discussed. However, it exploits the discrete nature of photo-generation, and as such differs fundamentally from the two previous configurations. It does not measure a current, but rather produces curent pulses, the leading edges of which, corresponds to the primary carrier that triggered the diverging avalanche current. Its operation is explained below.

A readout circuit and GMAPD is shown in Figure 2.6. In the case of an APD, it is simply a discrete resistor. At quiescence, the cathode voltage sits at V_{DDA}. If the excess bias voltage (i.e. the voltage differential between the applied voltage and the breakdown voltage) is large enough, a sustainable avalanche current is produced when an electron or a hole is generated within the multiplication region or reaches it by minority carrier diffusion. As a result, the cathode voltage decreases exponentially with a time constant that depends on the reverse bias capacitance and the diode's series resistance R_S. The leading edge of the cathode voltage transient corresponds to the arrival of the avalanche's primary carrier within the multiplication region. For proper Geiger mode operation, the load resistor R_L is chosen to be large enough so that the avalanche current is quenched within a few hundred picoseconds following the onset of the avalanche process [37].

Following this transient decay in the cathode voltage the diode current is so low that the avalanche process can no longer be sustained; the avalanche current

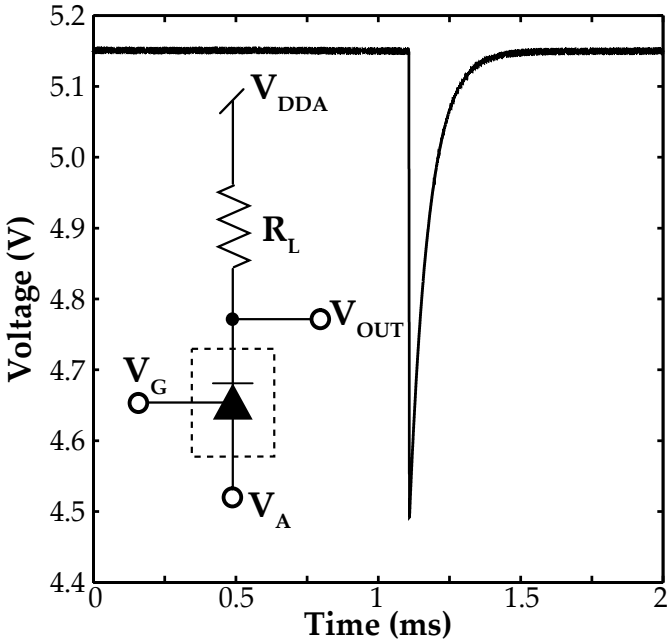

Figure 2.6: Measured data from a fabricated PGSPAD showing the cathode voltage transient resulting from passive (i.e. a resistor is used as the ROC) Geiger mode operation for V_G = -16 V, V_A = -13 V, V_{DDA} = 5 V , and R_L = 100 kΩ. (The control voltage V_G will be explained in Chapter 3.)

is thus said to be fully quenched and the voltage at which this happens is the *quenching threshold*. As stated previously, R_L must be large enough to reduce the net reverse bias voltage below the quenching threshold. Failure to do so results in partial quenching and yields increased noise and poor detection efficiency [37].

The quenching threshold is a significant parameter because it implies that the reverse bias voltage need not be reduced below the breakdown voltage in order to quench the avalanche current; this means faster device reset time and consequently faster device operation.

Once the APD is in the quench state, it can no longer detect photons through avalanche and is no longer in Geiger mode [38]. Thus it must be reset by bringing the cathode voltage to V_{DDA}. In the configuration shown in Figure 2.6, the leakage

current slowly recharges the parasitic capacitance of the APD once it is quenched. This recharge time is comparatively much longer than the quench time because its time constant is dominated by R_L as opposed to much smaller series resistance of the diode (R_S). For fast reset, a transistor can be used to quickly pull the cathode back towards V_{DDA} [37]. (This is demonstrated in Chapter 4).

2.4.3.1 Geiger Mode APD Noise

There are several important factors to consider when operating an APD as a SPAD. Firstly, the avalanche process is statistical. This means that the triggering of an avalanche event is associated with a probability measure. It has been shown that this probability increases with increasing excess bias voltage [37, 38]. Secondly, there avalanche events that occur in the absence of incident photons. These spurious events constitute the device's internal noise source. They are referred to as *dark counts*, and the dark count rate (DCR) strongly depends of the number of thermally generated carriers and on the number of carriers trapped from previously occurring avalanches [37, 38]. The latter mechanism is referred to as afterpulsing [37, 38], and in some instances it may be a significant component of the DCR.

2.5 Conclusion

In this chapter we have discussed the mechanisms through which light is converted into an electrical signal. We have reviewed three types of photosensor architectures, namely, the photodiode, the avalanche photodiode, and the Geiger

mode APD. The third configuration allows operation of the photosensor as a photon counter, and for that reason it's front-end is also called a single-photon avalanche diode (SPAD).

For the three photosensors discussed, the main differentiator was the biasing regime. While this is true, a photodiode cannot be operated as an APD or as a SPAD simply by changing the bias regime. There are structural features, for example, that impede proper Geiger mode operation of p-n junctions that work well as photodiodes. This is especially true in CMOS, where perimeter breakdown confines the multiplication region to the diodes periphery, which adversely affects the device's operation. This issue and its prevention is discussed in extensive detail in the remainder of the dissertation.

Chapter 3

Perimeter-Gated Single-Photon Avalanche Diodes†

3.1 Introduction

Traditionally, SPADs have been fabricated through dedicated processes [39], since achieving well controlled avalanche profiles in commercial CMOS processes is challenging. As a result of the planar nature of the junctions, electric field distributions show maxima at the diodes' periphery [40]. This means that in the high reverse bias regime, as is needed for SPAD operation, diodes are more susceptible to breakdown at the edges. When the device periphery enters breakdown prematurely, the device never reaches full volumetric breakdown. This adversely results in a reduced active area, and consequently, reduced photon detection efficiency. Therefore, perimeter breakdown is one of the most important obstacles in integrating SPADs into mainstream CMOS processes.

Several researchers have shown successful perimeter breakdown prevention in CMOS avalanche diodes. Rochas *et al.* have shown, in a twin-well CMOS technology, the use of lateral diffusion of donor atoms following n-well oxidation to effectively create a lighter n-doped region at the edge of the p-n junction [41]. Pauchard *et al.* have shown a CMOS compatible process for fabricating a photodiode with re-

†Originally published as: **M. Dandin**, A. Akturk, B. Nouri, N. Goldsman, and P. Abshire, "Characterization of Single-Photon Avalanche Diode in a 0.5μm Standard CMOS Process–Part 1: Perimeter Breakdown Suppression", IEEE Sens. J., vol. 10, No. 11, pp. 1682–1690, 2010

duced perimeter breakdown; the device comprised a field limiting guard ring placed at a distance d from the p^+ implant in conjunction with a control gate over the gap [42]. We have previously shown the combination of the lateral diffusion of n-wells, similar in spirit to that demonstrated by Rochas *et al.*, in combination with a depletion gate to further reduce premature edge breakdown [43]. All of these techniques stem from original works by Grove *et al.* and Temple *et al.* who studied the effects of dopant concentration modulation and junction curvature on the breakdown voltage [40], as well as the effects of field plates over high field regions [44]. Other architectures in deep-submicron CMOS technologies have made use of shallow trench isolation in order to favorably alter the junction's geometry to prevent edge breakdown [20].

In this paper, we present a thorough analysis of a device which was implemented in a 0.5 μm, single-well, 3-metal, 2-poly, CMOS process. In addition to characterizing the device's breakdown characteristics as a function of gate voltage and lateral diffusion distance, we describe a numerical model which identified regions in which the electron/hole generation rates were maximized, thus indicating locations susceptible to breakdown. This metric (the charge generation rate) allowed us to confirm that the application of the gate voltage, in conjunction with the lateral diffusion of adjacent n-wells, successfully prevented edge breakdown.

We begin with a review of the theory underlying avalanche breakdown in p-n junctions. We then introduce the device architecture and the rationale for the design. Finally, we present a thorough characterization of the device's DC response in the high-reverse bias regime. The empirical results are corroborated by the previously

mentioned numerical model.

3.2 Theory of Operation

3.2.1 Avalanche Breakdown

When a reverse bias applied across a p-n junction is increased beyond a critical potential, a swift rise in current occurs as a result of a charge multiplication process known as avalanche breakdown. This process is the result of free electrons (holes) attaining kinetic energies high enough in magnitude to ionize lattice atoms upon collisions. Because of the extremely strong electric field present across the junction, the newly generated carriers are in turn accelerated and, they too, reach energies high enough to cause impact ionization. This multiplication cycle continues, giving rise to an avalanche current. The reverse voltage beyond which this phenomenon occurs is the breakdown voltage, and its magnitude is denoted V_B in the remainder of this paper.

Avalanche breakdown is best described through the theory of impact ionization first postulated by McKay [45, 46]. The number of secondary carriers generated by a moving carrier in an electric field across the space-charge region is given by the following integral:

$$1 - \frac{1}{M} = \int_0^w \alpha_i dx, \tag{3.1}$$

where M is the multiplication factor that reflects the number of charges collected for each charge generated, α_i is the impact-ionization rate (electron (hole) $\times\ cm^{-1}$

, where the subscript i indicates the carrier type), and w is the width of the space-charge region at the applied reverse voltage. Avalanche occurs when, in Equation 3.1, $M \to \infty$. Miller subsequently showed the multiplication factor and the device's breakdown voltage to be related as follows:

$$M = \left[1 - \left(\frac{V_A}{V_B}\right)^n\right]^{-1}, \tag{3.2}$$

where V_A is the applied voltage and n and V_B are process dependent constants [47]. As can be seen from Equation 3.2, $M \to \infty$ as $V_A \to V_B$.

Subsequent works have developed a deeper understanding of breakdown mechanisms in semiconductor junctions, and there is a significant body of literature on the topic for a wide range of materials, [48–51].

3.2.2 Low-light Transduction

To make use of the avalanche phenomenon and transduce weak photon fluxes with high fidelity using an APD, a suitable readout mechanism must be implemented. One configuration with which this is attained is Geiger mode operation. In Geiger-mode APDs (GMAPDs), the bias point is well above the junction's breakdown voltage. (As previously mentioned, an APD in such configuration is a SPAD). In the absence of free carriers, there is no current and an extremely high field is present across the junction. Under these conditions, the generation of a free-carrier almost immediately triggers an avalanche current through the junction. This current is then quenched using an external circuit, consisting of either a passive ballast resis-

tor, or a set of transistors [52]. Quenching brings the bias voltage below the breakdown voltage and effectively stops the avalanche. The junction is then recharged for the detection of another avalanche event. In Geiger mode, the multiplication gain is infinite, and the device functions as a bi-stable circuit whose transitions are triggered by the generation of a single electron-hole pair. This paper focuses solely on the device's breakdown characteristics; we will consider its Geiger mode operation in a later publication (Part 2). For preliminary work showing Geiger mode operation of the device described herein, see [43, 53].

3.3 Device Architecture

3.3.1 Design

The physical implementation of a SPAD in a standard digital CMOS technology is shown in cross-sectional format in Figure 3.1 (bottom panel); the top panel illustrates the layout view. Some layers are drawn with half-symmetry for clarity. The avalanche junction is a p^+/n-well diode implanted in p-type bulk substrate material. As the layout indicates, a circular n-well is drawn to serve as the multiplication region. An additional annular n-well structure is drawn at its periphery at a distance denoted by β. Several structures were constructed with values of β varying from 0λ to 7.5λ, in increments of 0.5λ, where $\lambda = 0.35\mu m$ is half of the feature size of the CMOS technology. We also note that all values of β were smaller than the minimum spacing (8λ) between adjacent n-well regions as prescribed by the design rules. The anode (p^+ region) is implanted over the multiplication region

and extends laterally halfway to the inter-n-well gap. A polysilicon layer serving as a control gate extends from the edge of the anodic implant to partway over the annular n-well structure. A summary of the devices' dimensions is shown in Table 3.1.

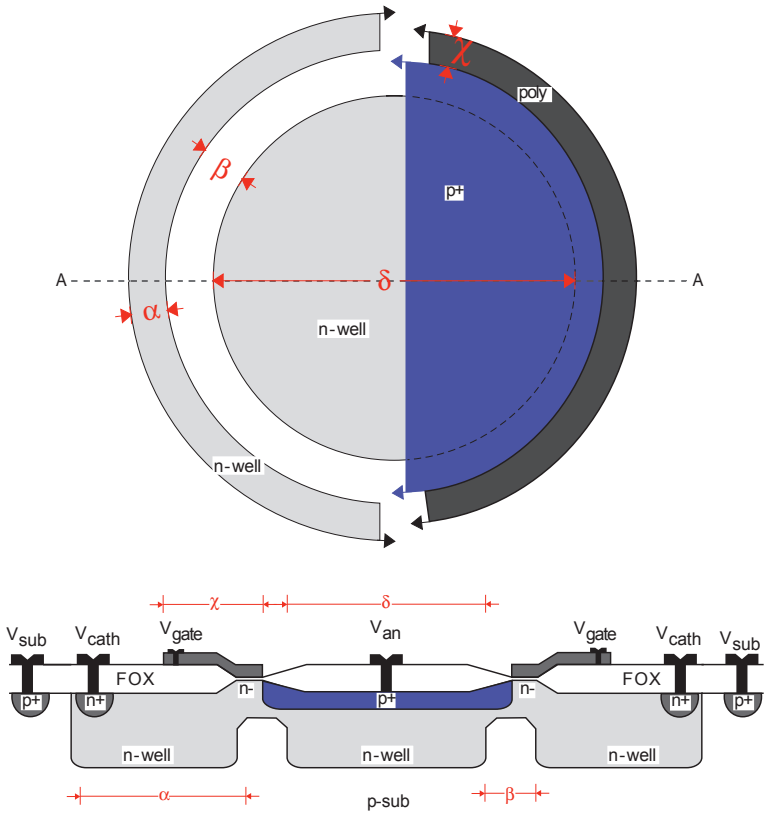

Figure 3.1: Layout and cross-sectional (along AA) views of the SPAD device. The diode consists of the p^+/n-well junction. A polysilicon gate is placed at the periphery. The adjacent n-wells diffuse into each other following high temperature steps of the CMOS fabrication process. This effectively forms an n-well region with doping concentration much lower at the periphery than at the center. The gate serves to deplete the corner region of electrons to further reduce the corner electric field. (Drawing not to scale.)

Table 3.1: PGSPAD Device Dimensions

$\alpha(\mu m)$	$\beta(\lambda)$	$\chi(\mu m)$	$\delta(\mu m)$
9	0:0.5:7.5	3.5	90

3.3.2 Rationale

The rationale for this design is two-fold; first, with the lateral diffusion of n-wells, a lighter n-doped region is created at the edge of the junction (following p^+ implantation). This effectively reduces the corner electric field when compared to the native diodes (devices with $\beta = 0\lambda$ and $V_G = 0V$). Second, the addition of a gate serves to deplete the corner regions of electrons when a negative bias is applied with respect to the cathode. This creates a field-induced junction which causes the corner electric field to be further reduced.

3.4 Breakdown Characteristics

3.4.1 Experimental Procedures

In this section, we describe the experimental methods that were used for characterizing the devices. We investigated the near-breakdown I-V characteristics of the SPADs as a function of the voltage applied to the control gate. We also sought to understand the effect of the n-well spacing on the I-V characteristics. To do so, devices with β ranging from 0λ to 7.5λ were tested. The voltages used to test the devices are shown in Table 3.2; we use the notation $V_{start} : V_{increment} : V_{end}$ to des-

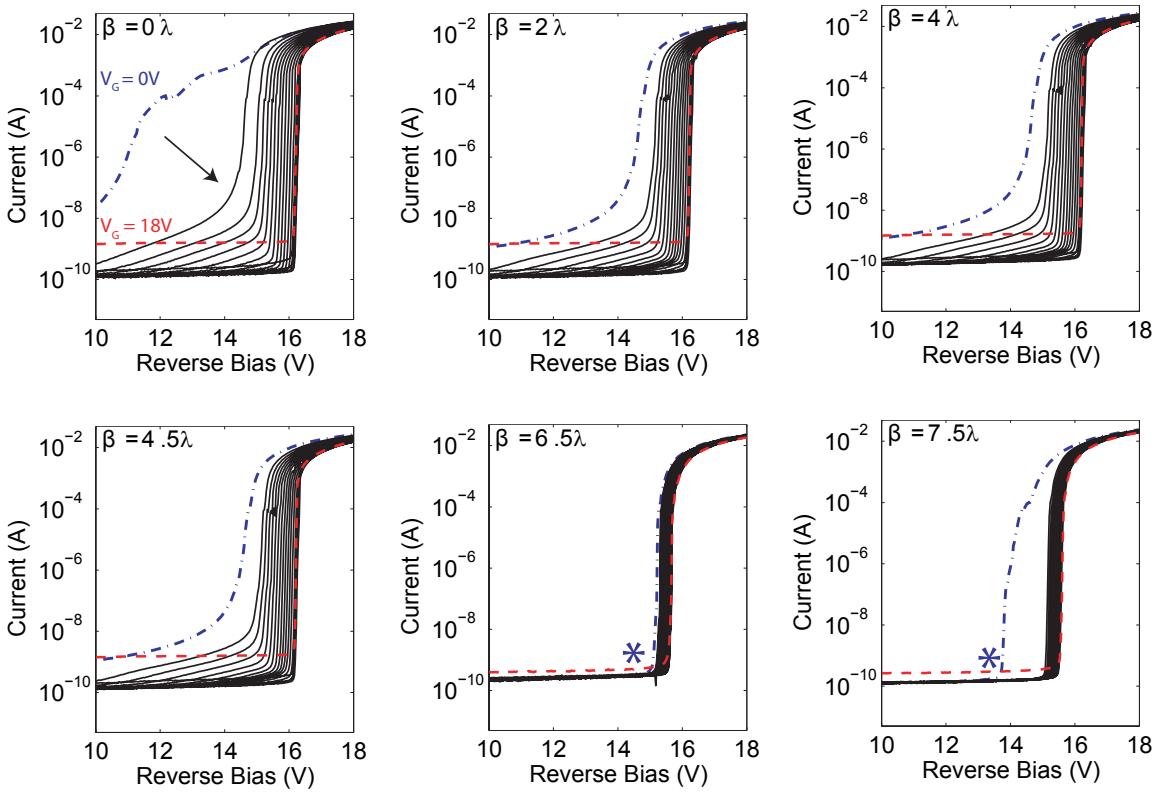

Figure 3.2: Current-voltage dependence for different devices. These results indicate the effect of both gate and lateral diffusion on the overall device characteristics. In each figure, the blue (dash-dotted) line indicates the I-V trace for $V_G = 0V$ and the red (dashed) line indicates the trace for $V_G = 18V$. The gate voltage is increased by increments of 1V in all cases in direction of the arrow shown on the first figure (top left). The figures with asterisks indicate cases for devices with $\beta \rightarrow 8\lambda$; at these values of β, the p+ anode tends to short with the substrate which implies that these I-V curves are likely that of the junction formed by the n+/n-well annulus and the p+/p-sub regions.

ignate sweep parameters. In the remainder of this paper, for the sake of simplicity, we shall refer to gate voltages, reverse bias voltages, voltage increments, and breakdown voltages in terms of their magnitudes. Note that the actual polarity of these voltages is negative, as indicated in Table 3.2.

We used two source-measure units (Keithley, 2400), one for biasing the gate and another for reverse-biasing the junction. In the latter case, a 4-wire connection

Table 3.2: Operational Parameters

V_{an}	V_{cath}	V_{sub}	V_{gate}
0:-0.03:-18	0	0	0:-1:-18

was used in order to minimize stray resistances arising from the leads thus ensuring accuracy when measuring weak currents. For a given device, voltages ranging from 0 to 18V, in 1V increments, were applied to the gate, and the I-V curve was collected. (In total, 19 I-V traces were collected.) For each trace, the reverse-bias potential across the junction was swept from 0 to 18V in increments of 30mV. This voltage increment was kept small in order to accurately resolve the avalanche current. Each measurement from the sweep was collected five times and the average current was recorded (all standard deviations were found to be in the pico-ampere regime). Data acquisition and processing were performed through an application-specific Matlab function which interfaced with Labview subroutines written for instrument control. In order to estimate the breakdown voltage, the Matlab function performed the computations described in further detail in Equations 3.3–3.6.

First, the raw current data is transformed into the log domain as $\log(I(V))$ as shown in Equation 3.3. Next, the derivative of the data was computed (Equation 3.4). The derivative was normalized (Equation 3.5) for display purposes, and the breakdown voltage was taken to be the reverse bias voltage at which the derivative was maximized (Equation 3.6). A moving average may be applied to the data in order to remove any measurement noise, but this was not found to be necessary for any of the data described here. This procedure has also been used for calculating

cutoff wavelengths of optical filters [54] and is illustrated graphically in Figure 3.3.

$$A_n = \log_{10} |I_n|, n = 1, \ldots, N \tag{3.3}$$

$$X_k = \frac{A_{k-1} - A_k}{V_{k-1} - V_k}, k = 2, \ldots, N \tag{3.4}$$

$$\Gamma_i = \frac{X_i}{max\,[X]} \tag{3.5}$$

$$V_B = arg\,[max\,[\Gamma]] \tag{3.6}$$

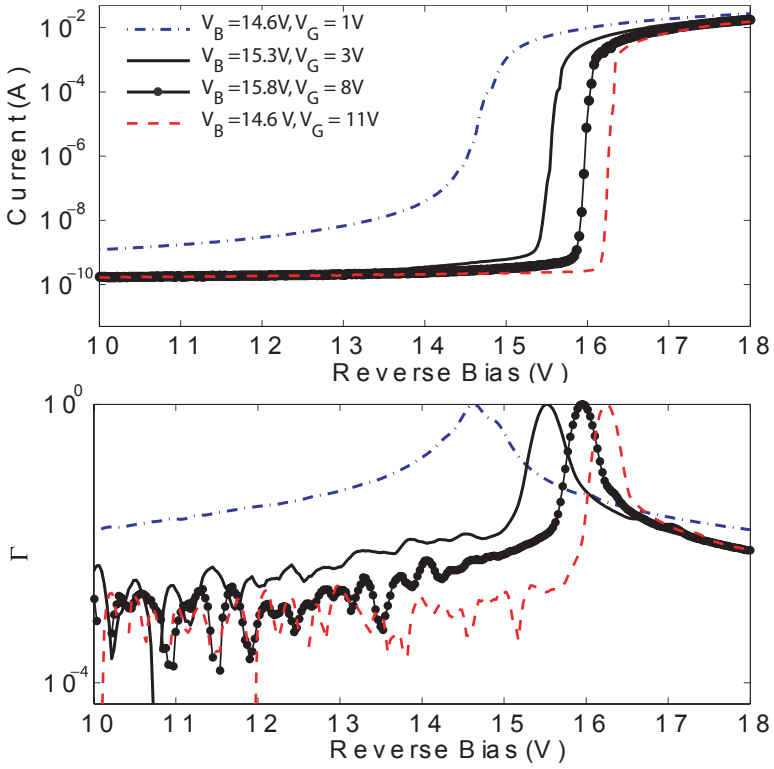

Figure 3.3: The top panel shows the current as a function of reverse bias. The bottom panel shows the normalized derivative Γ (see Equation 3.5) for several traces corresponding to the device with $\beta = 0$ for various gate voltages (also shown in Figure 3.2). In each case, Γ exhibits an extremum. The voltages at which this occurs are identified as the breakdown voltages (see legend in top panel).

3.4.2 Results

We collected I-V curves for devices with β ranging from 0λ to 7.5λ; we also varied the gate voltage in order to study its effect.

Holding the gate voltage at 0V allowed us to determine the effect of n-well lateral diffusion on the avalanche profile. Data for this experiment are indicated in Figure 3.2[1] by the dash-dotted lines. As the results show, the native junction, *i.e.* $\beta = 0\lambda$ and $V_G = 0V$, exhibits a gradual change in current as the reverse bias is increased. We attribute this excessive leakage to tunneling effects resulting from strong perimeter electric fields. These effects are mitigated as the inter-n-well gap is increased ($\beta = 2$, 4, and 4.5λ in Figure 3.2). However, at wider gaps ($\beta \rightarrow 8\lambda$), the p^+ anode tends to short with the substrate, causing another junction to form between the n^+/n-well annulus and the p^+/p-sub regions. This suggests that with the placement of the outer n-well (annulus of width α and inner diameter $\delta + 2\beta$ in Figure 3.1) alone, one can marginally improve the avalanche profile, as long as the gap is narrow enough to prevent anode to substrate shorting.

Another important implication of Figure 3.2 is that a large gate potential enhances the devices' rectifying efficiency. This is indicated by the increase in breakdown voltage as the gate voltage is increased (see Figure 3.4), as well as an increase in the rate of change of the current with reverse voltage. Nevertheless, the gate potential has a diminished effect for large β, *i.e.*, $\frac{\Delta V_B}{\Delta V_G}$ goes down as β is increased. As before, this is due to a conduction path forming from anode to substrate for devices with gaps approaching the technology's recommended minimum separation

[1] These I-V characteristics were measured in the dark.

distance.

Another salient issue is that for gate voltages greater than 17V, for all devices, there is a significant increase in the pre-breakdown current (red dotted lines). This finding suggests that at these voltages, although perimeter breakdown suppression is achieved, the overall generation rate is increased due to trap-assisted generation. This could lead to increased dark count rate in Geiger-mode operation.

For an overall view of the effect of both suppression techniques, we plotted the breakdown voltage as a function of n-well spacing for each of the gate biases applied in all 16 structures tested. This plot is shown in Figure 3.5. As the graph indicates, the maximum increase in breakdown voltage is observed in the 0λ case where the $\Delta V_B = 5.3$V for an 18V change in the gate potential.

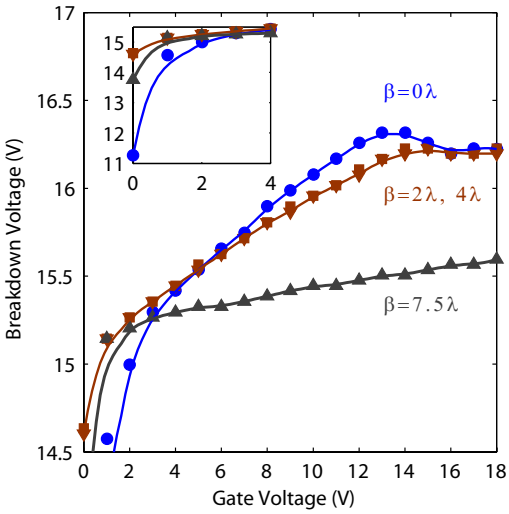

Figure 3.4: Breakdown voltage as a function of gate voltage for 4 different structures. The inset indicates a non linear relationship for gate voltages ranging from 0 to 4V. The relationship becomes linear and the breakdown voltage saturates for structures having $\beta = 0, 2, 4\lambda$. However, no saturation is observed for $\beta = 7.5\lambda$, indicating that the lateral diffusion is not as effective and that the two n-wells are more electrically isolated.

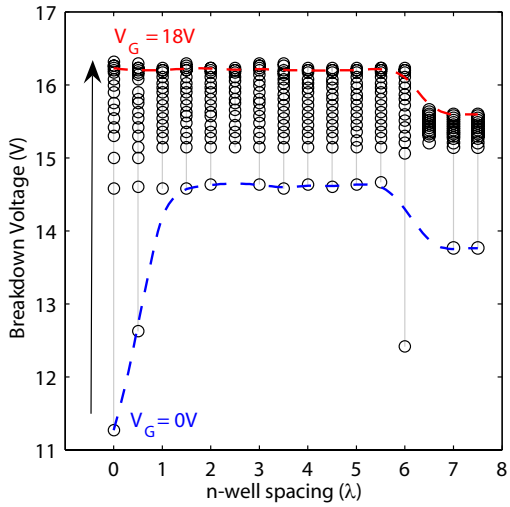

Figure 3.5: Breakdown voltage as a function of n-well spacing for the 8 structures tested. Each circle represents a gate voltage. The gate voltage is increased in magnitude in the direction shown by the arrow in increments of 1V. The blue trace represents averaged data for $V_G = 0$ and the red trace averaged data for $V_G = 18V$.

3.5 Avalanche Photodiode Modeling

3.5.1 APD Model

To corroborate the data presented thus far, and to identify regions susceptible to avalanche, we developed a drift-diffusion and impact ionization based two-dimensional device simulator. The simulator implements the following relationships to calculate electrostatic potential ϕ, electron concentration n and hole concentration p, respectively: Poisson (Equation 3.7), electron current continuity (Equation 3.8) and hole current continuity (Equation 3.9). These relationships are self-consistently solved.

$$\nabla^2\phi = -\frac{q}{\epsilon}(p - n + D) \tag{3.7}$$

$$\frac{\partial n}{\partial t} = \nabla \cdot (-n\mu_n \nabla\phi + \mu_n V_{th} \nabla n) + G_n \tag{3.8}$$

$$\frac{\partial p}{\partial t} = \nabla \cdot (p\mu_p \nabla\phi + \mu_p V_{th} \nabla p) + G_p \tag{3.9}$$

D represents the net ionized dopant density; V_{th} is the thermal voltage; q is the electronic charge; and ϵ is the dielectric constant of the medium. μ and G are the mobility and net generation-recombination rate of a carrier type indicated by the subscript, respectively. The G term incorporates trap-assisted as well as impact-initiated generation-recombination rates.

To characterize the operation and breakdown voltage of the avalanche devices, use of a predictive silicon impact generation rate formula is important. To this end, we employed recently published silicon impact coefficients [55] that are formulated using standard Chynoweth-type expressions with a temperature dependent exponent (Equations 3.10 and 3.11). Here, the local electric field E is the field along the total current density (J_t) and T is the absolute temperature. This field is calculated using $|J_t \cdot E_t|/|J_t|$ to remove the part of the local total electric field E_t that does not contribute to the current flow (especially the field normal to the semiconductor-insulator interface).

$$\alpha = n_1 \exp\left[-(n_2 + n_3 T)/E\right] \tag{3.10}$$

$$\beta = p_1 \exp\left[-(p_2 + p_3 T)/E\right] \tag{3.11}$$

To calculate electron (hole) impact rate, $n_1(p_1)$, $n_2(p_2)$ and $n_3(p_3)$ are taken as $4.43 \times 10^5 (1.13 \times 10^6)$ cm^{-1}, $9.66 \times 10^5 (1.71 \times 10^6)$ V$\cdot$cm^{-1} and $4.99 \times 10^2 (1.09 \times 10^3)$

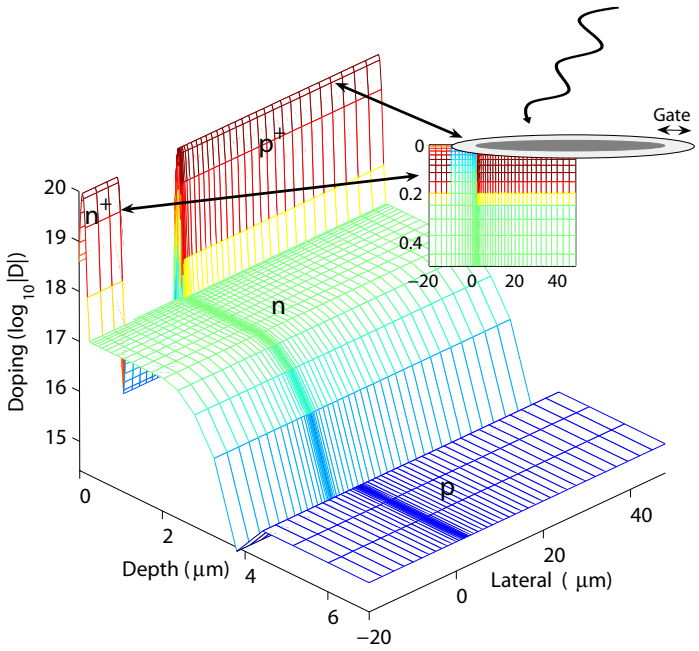

Figure 3.6: Cross section of half of the doping profile of the perimeter gated APD with adjacent n-wells (0λ case). Inset shows the location of the gate and an incoming photon, combining bird's eye and side views.

$V{\cdot}cm^{-1}K^{-1}$, respectively. These values were obtained empirically using silicon p-i-n diodes [55]. Furthermore, the band-to-band electron (hole) initiated impact rate used in the current continuity equations is calculated using the electron (hole) current density J_n (J_p) in $G_n = \alpha J_n/q$ ($G_p = \beta J_p/q$).

3.5.2 Doping Profile Model

Breakdown voltages, dark current levels, and multiplication efficiencies are all significantly affected by the doping profiles of the n-well and the p^+-n^+ terminals. As the doping on either side of a p-n junction increases, the breakdown voltage decreases due to higher associated built-in electric fields. The externally applied reverse bias results in a field that adds to this built-in field, and therefore gives rise

to increases in carrier kinetic energies and eventually impact ionizations.

To be able to predict performances of our APDs, we first need to estimate doping profiles of the wells and the substrate in the technology that our devices are fabricated in. As these doping details are proprietary information, we resort to empirical and numerical methods that give reasonable matches between calculated and measured data. Additionally, the extraction of a two-dimensional doping profile using experimental methods such as C-V measurements is often problematic as they provide a one-dimensional average doping map at a depletion region edge that is traced over the entire device by changing biases. In Figure 3.6, we show the inferred doping map of an APD with zero spacing between its two n-wells ($\beta = 0\lambda$ in Figure 3.1). This doping profile gives a good match between experimental and measured data, and is in line with doping profiles deduced for this process using other device configurations [56]. More specifically, the peak concentration in p^+ and n^+ regions is 1×10^{20} cm^{-3}, and this concentration drops with $\sigma = 50$ nm and $\sigma = 120$ nm in the depth and lateral directions assuming a shifted Gaussian profile where the mean is 0.1μm away from the surface. For the n-well, the empirically obtained maximum doping is 1.22×10^{17} cm^{-3}, and it also has a shifted Gaussian profile in the depth direction. These doping profiles result in a p-n junction at approximately 0.2μm depth for the p^+ terminal in an n-well. Here the substrate is set to 1×10^{15} cm^{-3}, and this gives rise to a doping crossover at roughly 3.5 μm depth for the n-well surrounded by the p substrate.

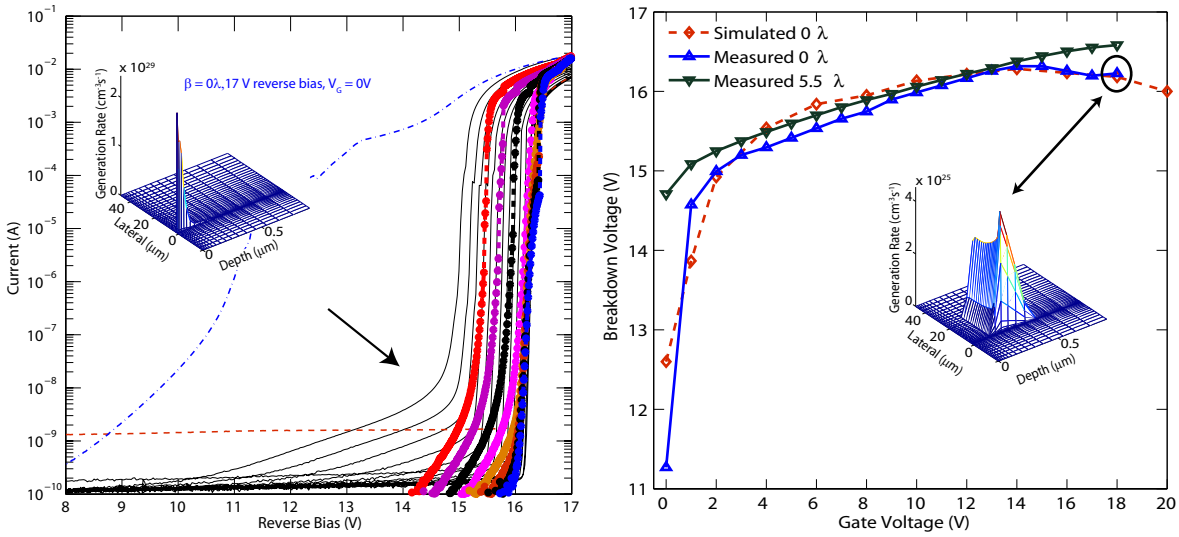

(a) (b)

Figure 3.7: (a) Current-voltage characteristics of an APD with a zero n-well spacing (0λ). The doping profile used in simulations is shown in Figure 3.6. The inset depicts the generation rate profile at 0V gate voltage and 17V reverse bias. For 0V gate bias, the generation rate peaks near the semiconductor-insulator interface in the depth direction and p^+-n edge in the lateral direction. (b) Room temperature breakdown voltage as a function of gate bias for the APD with zero n-well spacing, as well as another APD with a 5.5λ n-well spacing. We also compare experimental results with those calculated for a 0λ device. APDs with other well spacings show similar characteristics. Also, the inset shows that at gate biases higher in magnitude, breakdown moves away from the surface, and occurs at the p^+-n corner as well as laterally along the p^+-n edge away from the surface.

3.5.3 Simulation and Model Validation

To investigate the effects of the perimeter gate and doping profile on breakdown characteristics of our APD, we simulate a diode with the doping profile shown in Figure 3.6. The simulated current-voltage curves along with the generation rate profile at 17V reverse bias (*i.e.* -17V is applied to the p^+ anode, and the n^+ and substrate nodes are grounded) and 0V gate bias are shown in Figure 3.7a. Here the gate bias is changed by 2V increments from 0V to 18V. Comparison of measured and simulated currents shows a reasonable match. For the APDs designed and

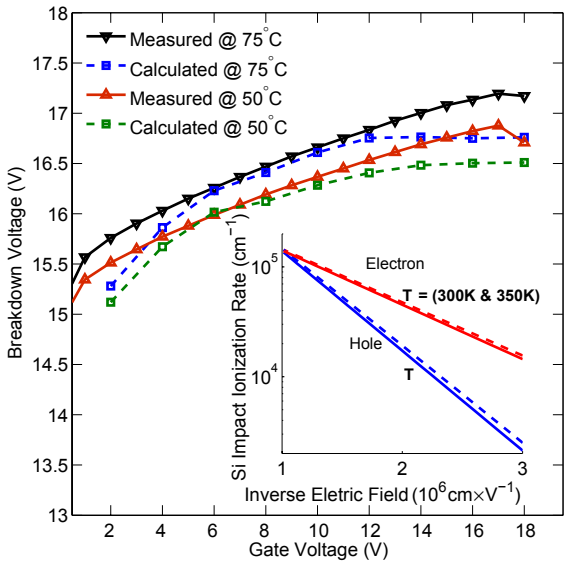

Figure 3.8: Experimental and calculated breakdown voltages as a function of gate bias at 50° and 75° C. We used a 5.5λ device for measurements. Inset shows that the silicon impact ionization coefficient decreases with rising temperature for both types of carriers.

tested, and also simulated, the spacing between the n-wells changes the breakdown voltage modestly (unless the n-wells are far apart and the channel under the gate shorts the p^+ tap to the substrate). However, the gate voltage noticeably affects the breakdown voltage, as well as the dark current level and the sharpness of the current change during breakdown. Thus, we performed simulations for the 0λ design under different gate and reverse biases, and temperatures.

As the reverse bias is changed from 0 to 10V, overall generation rate starts rising near the surface, as the lowest resistance path between p^+ and n^+ nodes runs parallel to the interface for low applied biases. However, the current as well as the generation rate is low for this bias range. For the 0V gate bias case, as the reverse bias is gradually increased, the field and generation rate near the silicon-silicon dioxide interface close to the p^+-n edge start increasing, and this eventually results

in avalanche breakdown near the surface, as shown in Figure 3.7a (inset).

Figure 3.7b shows experimental and simulated breakdown voltages as functions of gate biases. The breakdown voltage is calculated as the point where the curvature of the current-voltage curve changes sign[2], as previously described in Equations 3.3–3.6. The comparison shows a good match between calculated results for the 0λ device shown in Figure 3.2 and measured data for the 0λ and 5.5λ devices. For the gate voltages quoted in Figures 3.7a and 3.7b that are higher in magnitude, as the reverse bias voltage increases the lateral field at the surface decreases because the voltage bias between the gate and the p^+ anode is reduced. This causes current to spread outward through the edges, as well as through the corner of the p^+ anode. Thus, the highest electric field region is near the p^+ anode and n-well corner, since the corner shows a combination of both the lateral and vertical change in local electric field. When we further increase the reverse voltage, the corner electric field as well as the field in the normal direction of the p^+-n edge away from the interface rise rapidly. The generation rate at these locations due to current flow and high electric field gives rise to secondary carriers that are high enough in numbers to affect the terminal currents. A positive feedback between the current and multiplication rate is balanced by the slight reduction in electric field at the corner and along the deeper edge thus resulting in a finite current at the output. However, when there are abundant impact-generated carriers, the junction fields and the device's rectification efficiency drop significantly, giving rise to a resistive current-voltage behavior at very high reverse biases. For the high aforementioned gate biases, APDs

[2] This means where the derivative has a maximum.

break down at the p^+-n corner and along the p^+-n edge deeper into the substrate, as shown in Figure 3.7b (inset). The breakdown characteristics at gate biases higher in magnitude are in line with our initial design principles, which are verified by these simulations.

For a given negative gate bias, holes are attracted under the gate. We note that for gate biases lower than -18V, the channel under the gate has a large hole concentration. For a wide spacing between the n-wells, this channel results in an undesirable short between the p^+ tap and the substrate. Also, when gate biases greater than 18V are applied to devices with overlapping n-wells, breakdown voltages start decreasing as the lowering of the lateral field at the surface and the vertical field become less effective in pushing the current flow and breakdown region down into the substrate.

We further show in Figure 3.8 the simulated and measured gate bias breakdown voltages for a 5.5λ device at 50° and 75° C. The breakdown voltage increases with rising temperature, since the built-in electric fields as well as mobilities slightly decrease with an increase in intrinsic carrier concentration and phonon population at high temperatures. Figure 3.8 (inset) shows that the silicon electron and hole impact rates that are calculated using Equations 3.10 and 3.11 decrease with increasing temperature. This is consistent with high scattering rates which occur at higher temperatures.

3.6 Conclusion

We reported on the breakdown characteristics of a single-photon avalanche diode structure fabricated in a $0.5\mu m$ single-well CMOS process. Our investigation focused on two methods used for preventing edge breakdown in planar junctions; they were the placement of a field ring at the perimeter to create field-induced junctions and force the maximum electric field to be located at the middle of the junction, and the lateral diffusion of adjacent n-wells, through the deliberate violation of the design rules in the fabrication process. We first conducted a phenomenological study which revealed increases in breakdown voltages resulting from both methods independently.

Following this investigation, we showed that the charge generation rate was a suitable metric for identifying whether perimeter breakdown was prevented. We demonstrated its use through a self-consistently solved 2-D numerical model based on Poisson's equation and the hole and electron current continuity equations coupled with rate equations for carrier generation due to impact ionization. The model showed that the generation rate was maximized (a condition indicating susceptibility to avalanche) at the corner, confirming that in the native diodes, the lines of maximum electric fields are located at the corners. The model also confirmed that breakdown suppression techniques employed were adequate for curtailing edge breakdown in junctions fabricated in this process. Particularly, the field ring at the perimeter proved to be the most effective at preventing perimeter breakdown. This was evidenced by a spatial broadening (away from the surface and into the sub-

strate) of the charge generation function which implies that volumetric breakdown was achieved.

Chapter 4

High Signal-to-Noise Ratio Avalanche Photodiodes with Perimeter Field Gate and Active Readout†

This letter describes an avalanche photodiode (APD) fabricated in a 0.5 μm CMOS process. In Geiger mode, the APD had area-normalized dark count rate as low as 2 $Hz/\mu m^2$ at room temperature. Its signal-to-noise ratio (SNR) increased by an order of magnitude as a result of perimeter field gating. We demonstrate that under high illumination conditions perimeter field gating maximizes SNR, whereas under low-light conditions it maximizes sensitivity.

4.1 Introduction

When biased in the near-breakdown regime, CMOS p-n junctions suffer from premature edge breakdown (PEB), limiting their usefulness as Geiger mode avalanche photodiodes. Typically, PEB is averted by implanting a guard ring on the periphery of the photodiode in order to ensure breakdown at the volumetric junction instead of on the peripheral junction. Unfortunately, in small devices, the guard ring occupies a large portion of the photodiode's area which results in a significant reduction in pixel fill factor. Alternative PEB suppression methods which do not adversely affect

†Originally published as: **M. Dandin** and P. Abshire, "High Signal-to-Noise Ratio Avalanche Photodiodes with Perimeter Field Gate and Active Readout", IEEE Electron Device Lett., vol. 33, No. 4, pp. 570–572, 2012

fill factor have consisted of using shallow trench isolation (STI) to physically taper the periphery of the diode [20], or placing the avalanche junction in a retrograde buried n-well implant in order to widen the depletion regions at the boundary of the APD's anode [18].

We previously reported effective suppression of perimeter breakdown for a 90 μm-diameter avalanche photodiode fabricated in a 3-metal, 2-poly, 0.5 μm single-well mixed signal CMOS process [57]. The device featured two mechanisms for reducing peripheral electric fields: a laterally diffused n-well guard ring and a field gate over the perimeter of the diode. We found that the field gate proved most effective at reducing perimeter breakdown, and subsequently, that the technique scaled easily, with no fill factor loss, to a 25×25 μm^2 APD.

This letter features several original contributions. For the first time, we demonstrate the monolithic interfacing of active quenching and reset circuits with a perimeter-gated single-photon avalanche diode (PGSPAD) similar to the structure reported in ref. [57]. Secondly, we demonstrate a corollary effect of PEB suppression, namely, more than one order of magnitude reduction in dark count rate (DCR) which allows Geiger mode operation with high SNR. We show that a large negative bias on the perimeter gate allows the reliable detection of a continuous monochromatic beam of low intensity (16 nW/cm^2) with an SNR of 3; under high illumination conditions (5 $\mu W/cm^2$), the detector's SNR exceeds 300, corresponding to a 37 times higher SNR than for a bias voltage 6 V lower in magnitude applied on the perimeter gate.

4.2 Device Architecture

4.2.1 Front-end and Readout Circuit Design

The test chip comprised 16 channels operated in parallel. Each channel produced a digital pulse train, the number of pulses corresponding to the activity of the detector. Figure 4.1 shows the architecture and operation of a single channel which comprised a PGSPAD, a thresholding circuit with threshold set at V_T, active reset and active quenching transistors (MR and MQ), reset and quenching logic circuits (RLC and QLC), and an event generation circuit (EVG) for producing a digital pulse whose leading edge corresponds to an avalanche event.

4.2.2 Readout Circuit Operation

At quiescence, the cathode voltage (V_{CATH} in Fig. 4.1b)) is near V_R; V_{LOW} is set at -13 V which results in an 18 V reverse bias across the PGSPAD, corresponding to an excess bias voltage of $V_E = 1.15\,V$. Moreover, the gates of the reset and quenching transistors MR and MQ are tied to the outputs of the RLC and the QLC respectively. These two circuits are monostable in the off-state of each transistor, *i.e.* the output of the QLC sits at $0V$ and that of the RLC at $5\,V$, in the absence of an avalanche event.

When an event occurs, V_{CATH} drops exponentially towards ground. When it crosses the V_T threshold, the quenching signal is asserted. MQ is turned on and the cathode is pulled down to V_Q which is chosen so that the reverse bias of the diode in the quench state is below the junction's breakdown voltage. The cathode remains

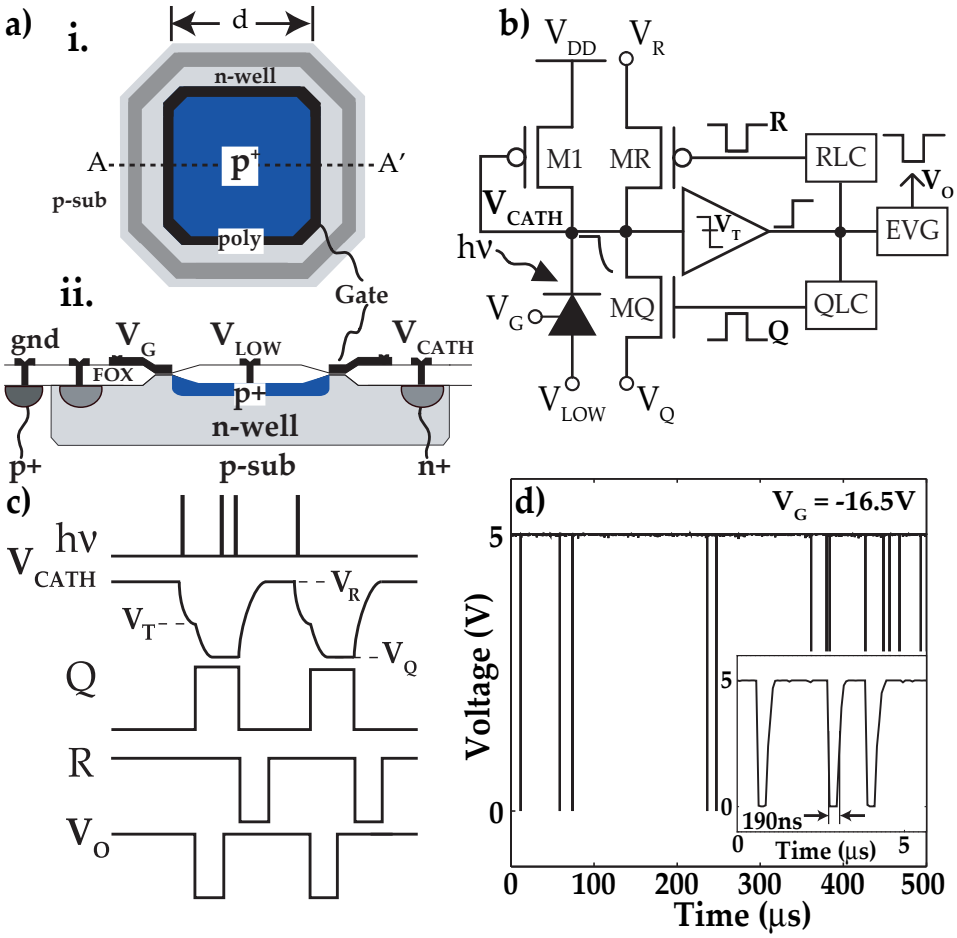

Figure 4.1: a) Structure of the p+/n-well PGSPAD [57] (top view shown in *i.* and cross-sectional view along AA' in *ii.*). $d = 25\mu m$. b) Circuit architecture. c) Timing diagram. ($V_R = 5V$, $V_Q = 2.5V$, and $V_T = 4.0V$) d) Sample output trace of a single channel in the dark (the inset shows the same data over a shorter time period).

at V_Q for a fixed time period after which the reset signal is asserted and MR pulls the cathode to V_R. The channel dead time is set by the EVG circuit's pulse width (190 ns), yielding a maximum achievable count rate of 5.3 MHz. Digital pulses corresponding to the channel's activity are shown in in Figure 4.1d).

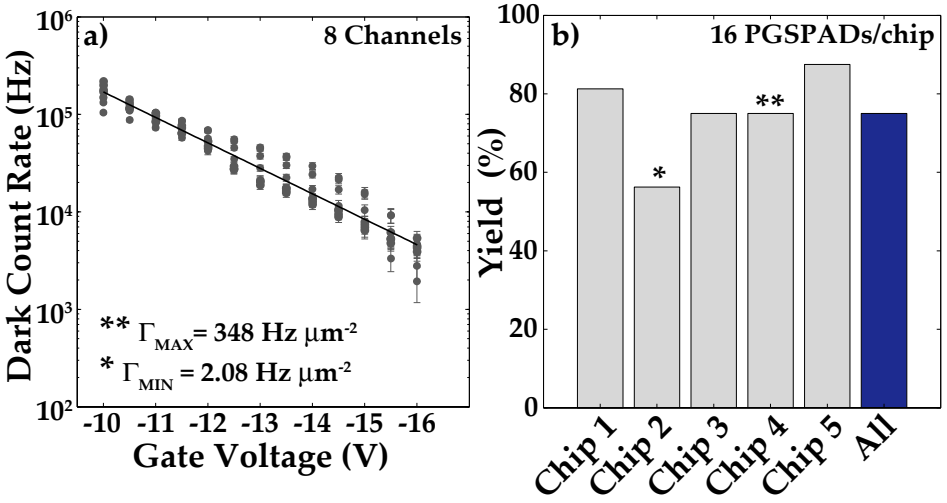

Figure 4.2: a) Dark count rate for 8 channels. The solid line is the mean dark count rate for 8 channels from 2 different test chips. b) Test sample lot yield. The asterisks indicate in which sample set the minimum ($*$) and maximum ($**$) area-normalized dark count rates occurred.

4.3 Experimental Results

4.3.1 Dark Count Rate Reduction with Perimeter Field Gate

The dark count rate was estimated by counting the average number of pulses in 500 consecutively acquired frames of data, each lasting 10 ms (i.e. 100 Hz measurement bandwidth). The measurements were performed for gate voltages ranging from $-10\,V$ to $-16\,V$ in steps of $-0.5\,V$.

A total of 80 devices, extending over 5 chips, were tested. Figure 4.2a) shows the dark count rate as a function of the perimeter gate voltage for 8 of the 80 channels characterized. The maximum DCR, measured at $V_G = -10V$, was 218 kHz ($\pm 26\,kHz$), and the minimum achievable DCR was 1.3 kHz ($\pm 0.18\,kHz$) at $V_G = -16V$. The area-normalized DCR corresponding to the aforementioned figures were $\Gamma_{MAX} = 348\ Hz\mu m^{-2}$ and $\Gamma_{MIN} = 2.08\ Hz\mu m^{-2}$, respectively.

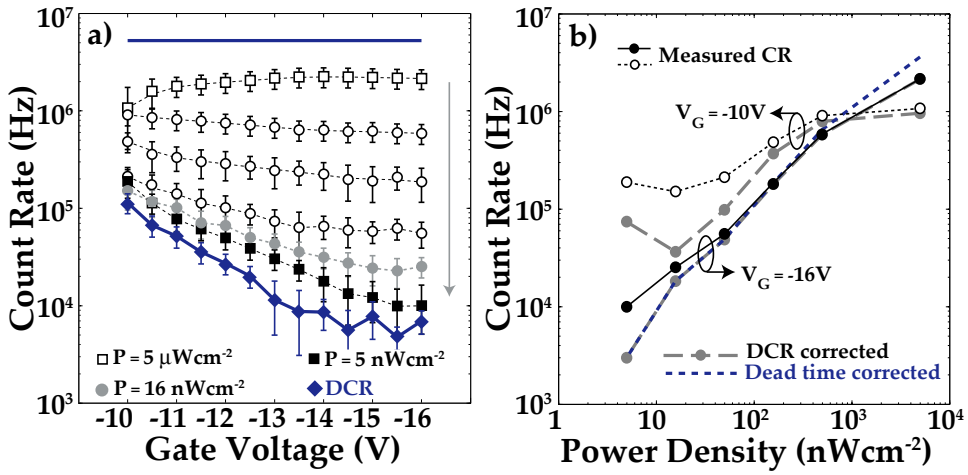

Figure 4.3: a) Count rate as a function of light intensity for a single channel. The arrow indicates the response for decreasing light intensity, and the horizontal line the maximum achievable count rate. b) Count rate as a function of optical power density for $V_G = -10\,V$ and for $V_G = -16\,V$. Also shown are, the DCR-corrected count rates (*i.e.* the mean DCR subtracted from the measured count rate under illumination), and the dead time (190 ns) corrected count rate for $V_G = -16\,V$ (see ref. [17] for correction procedure).

Figure 4.2b) shows the yield of the sample lot. A device was considered to be non-functional if its DCR at $V_G = -16\,V$ exceeded $10^5\ Hz$. Using this criterion, the overall yield was 75%. Devices exhibiting high DCR, in spite of the perimeter breakdown suppression, likely had a relatively larger defect density within the volumetric junction.

4.3.2 Signal-to-Noise Ratio

A grating monochromator was used to provide a narrow-band (2 nm) stimulus at 520 nm. The optical power of the stimulus was measured using a calibrated photometer, and the output beam of the monochromator was collimated onto a fiber bundle whose output was focused onto the test chip using a set of lenses.

In order to study the channels' response as a function of light intensity, neutral

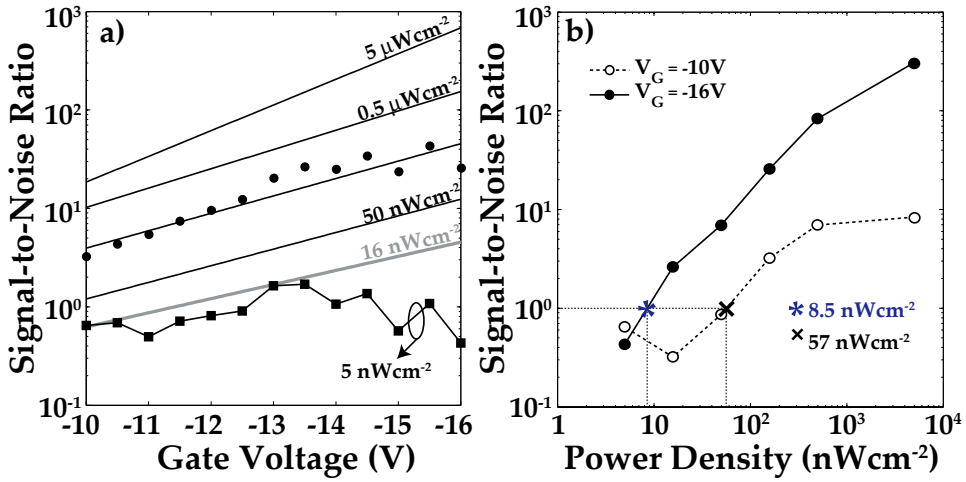

Figure 4.4: a) Exponential fits to the SNR data computed for 5 different light intensities. (For clarity, the fitted data is shown only for one trace). The raw SNR data for an optical power density below the noise floor (P = 5 $nWcm^{-2}$) is also shown (black squares). b) Signal-to-noise ratio as a function of optical power density for two gate voltages. At $SNR = 1$, the optical power densities ($\times$ and $*$) were extrapolated to find the minimum detectable signal for $V_G = -10\,V$ and $V_G = -16\,V$.

density filters were used to attenuate the monochromator's output signal. The optical power density before attenuation was 5 $\mu W/cm^2$.

Figure 4.3a) is a plot of a single channel's response under various illumination conditions, and Figure 4.3b) shows that each light level is readily discriminated when $V_G = -16\,V$; this is not the case at for $V_G = -10\,V$. These results imply that larger magnitude gate voltages serve to increase the dynamic range by allowing lower light levels to be detected.

At $V_G = -16\,V$ and with 2.5 orders of magnitude attenuation of the stimulus, the signal remained distinguishable from the noise, *i.e.* its mean was larger than 3 standard deviations of the mean DCR. This puts the optical power density of the weakest signal detected in our experiments at 16 nW/cm^2 which corresponds to a photon arrival rate of 2.5 $\times 10^5$ photons/sec. The probability of detecting a photon

was computed by dividing the measured count rate by the photon arrival rate; this calculation yielded a photon detection efficiency (PDE) of 10%.

The SNR was computed by dividing the DCR-corrected mean signal count rate by the mean DCR. Figure 4.4a) shows the SNR as a function of V_G and for different illumination levels. Except when the signal was below the noise floor, the SNR always increased with increasing gate voltage magnitudes.

At high illumination levels, the SNR showed an order of magnitude improvement (37-fold increase) over the gate voltage tuning range whereas the improvement was more moderate yet still appreciable at lower illumination levels (8-fold increase for a 16 nW/cm^2 stimulus).

Figure 4.4b) shows the SNR for $V_G = -10\,V$ and for $V_G = -16\,V$. The data show that lowering the perimeter gate voltage to -16V reduces the extrapolated minimum detectable optical power density from 57 nW/cm^2 to 8.5 nW/cm^2, thereby maximizing the sensor's sensitivity.

Table 4.1 compares the PGSPAD presented herein with recently published data from other CMOS SPAD architectures. The comparison is made on the basis of technology node, excess bias voltage V_E, measurement dead time t_D, DCR, area-normalized DCR, PDE, noise-equivalent power (NEP), and active area. Here, the dead time refers to the time required for a complete quench and reset cycle; it may also include a hold-off period in the quench state (for suppressing after-pulsing) and the latency of the readout chain.

The devices reported make use of several PEB suppression techniques. Palubiak [17], Marwick [58], Niclass [59], and Rochas [60] all used diffused guard rings,

and Finkelstein [20], Gerbasch [19], and Richardson [18] introduced techniques based on features available in modern process technologies, such as STI [20], passivated STI [19], and retrograde well doping [18]. As the table indicates, at $V_G = -16\,V$ the PGSPAD has area-normalized DCR (Γ_{MIN}) that is comparable with the state-of-the-art [18, 58, 60] despite having the largest area.

Table 4.1: Comparison with Recently Published Submicron CMOS SPADs

Reference	**CMOS Tech. (μm)**	**V_E (V)**	**t_D (ns)**	**DCR (Hz) ($T = 300\,°K$)**	**Γ_{MIN} (Hz μm^{-2})**	**PDE (%)**	**NEP^a ($fW/\sqrt{Hz}$)**	**SPAD Area (μm^2)**
Palubiak et al. [17]	0.13	0.5	12	1k	10	13 (570 nm)	–	100
Richardson et al. [18]	0.13	0.8	–	47	0.9	18 (440 nm)	–	50
Gersbach et al. [19]	0.13	1	180	90k	1.6k	–	–	58
Finkelstein et al. [20]	0.18	2.5	2	1M	26.3k	–	–	38
Marwick et al. [58]	0.18	0.5	–	100	1	14 (670 nm)	–	79
Niclass et al. [59]	0.35	3.3	100	646	17	35 (460 nm)	–	38
Rochas et al. [60]	0.80	2.5	<10	60	2	21 (440 nm)	0.025	30
This work	0.50	1.15 ***1.15***	190 ***190***	218k ($V_G = -10\,V$) ***1.3k ($V_G = -16V$)***	348 ***2***	14 (520 nm) ***10 (520 nm)***	35.6 ***5.30***	625

[a] The NEP was calculated by scaling the unity SNR optical power density by the active area and dividing by the square root of the measurement bandwidth.

4.4 Conclusion

In this letter we have shown that perimeter field gating reduces dark count rate. For high illumination this maximizes SNR, and for low illumination it maximizes sensitivity. Since the dark count rate increases strongly with excess bias voltage (V_E) and depends on the process technology, performance in specific applications will depend on the PDE and dead time (t_D). On that basis, the device reported by Rochas et al. [60] has the best performance due to its low DCR at relatively large V_E and short dead time. However, it was fabricated in an older CMOS process, limiting array density and fill factor. As fabrication technologies scale down, the trade-offs between DCR and excess bias voltage become significant; this explains the relatively higher DCR observed at smaller V_E for the other devices listed in Table 4.1.

Although STI techniques preserve fill factor, STI-based devices [19, 20] exhibit the highest DCR, suggesting that fill factor is improved at the expense of noise. Conversely, our data show ∼7-fold reduction in NEP using perimeter gating, a technique which also preserves fill factor. This suggests that a field-based PEB suppression method is viable for counteracting the degradation in noise performance observed in deep submicron CMOS technologies.

Chapter 5

Optical Filtering Technologies for Integrated Fluorescence Sensors[†]

Numerous approaches have been taken to miniaturizing fluorescence sensing, which is a key capability for micro-total-analysis systems. This critical, comprehensive review focuses on the optical hardware required to attenuate excitation light while transmitting fluorescence. It summarizes, evaluates, and compares the various technologies, including filtering approaches such as interference filters and absorption filters and filterless approaches such as multicolor sensors and light-guiding elements. It presents the physical principles behind the different architectures, the state-of-the-art micro-fluorometers and how they were microfabricated, and their performance metrics. Promising technologies that have not yet been integrated are also described. This information will permit the identification of methods that meet particular design requirements, from both performance and integration perspectives, and the recognition of the remaining technological challenges. Finally, a set of performance metrics are proposed for evaluating and reporting spectral discrimination characteristics of integrated devices in order to promote side-by-side comparisons among diverse technologies and, ultimately, to facilitate optimized designs of micro-fluorometers for specific applications.

[†]Originally published as: **M. Dandin**, P. Abshire, E. Smela, "Optical Filtering Technologies", Lab Chip, vol. 7, pp. 955–977, 2007

5.1 Introduction

Cost reduction is not the primary motivation behind efforts towards miniaturizing fluorescence sensing. Rather, it is increasing capability. Fluorescence spectroscopy will be a key component of future micro-total-analysis-systems (μTASs [9]) which will integrate the capabilities of entire laboratories onto compact devices consisting of microchips and other microfabricated elements. Such devices are already capable of performing complex chemical and biological experiments. Since the introduction of the first prototypes, these miniature systems have been demonstrated for numerous applications, ranging from immunoassays [61, 62] to pathogen detection and classification [63] to on-chip nucleic acid analysis [9, 64, 65]. State-of-the art μTASs also already automate steps such as sample preparation, handling, separation, and mixing [9, 64, 66].

However, despite the large number of microfabricated devices that make use of fluorescence spectroscopy as the detection modality [62, 65, 67–95], with only a few exceptions these microsystems still need to be interfaced with external, typically macro-scale equipment. Only high brightness samples can be used with existing micro-scale fluorometers. Fluorescence spectroscopy is still not μTAS-ready, in the sense of completely micro-scale modules, because of the numerous technological hurdles facing the development of high-sensitivity integrated fluorescence detection (although there has been some miniaturization to produce portable fluorescence sensors [96, 97]). Two of these challenges are low-noise optical detectors [98, 99] and optical filtering.

This article focuses on the second challenge: integrated[1] techniques for separating the fluorescence light from the excitation light. It covers demonstrated, as well as promising, optical filtering techniques that realize *at least partial separation on-chip*.

We begin with a brief overview of fluorescence sensing to lay the groundwork for evaluating the various filtering approaches. Each of the main technologies is then introduced in turn: interference filtering, absorption filtering, spectrally selective detectors, and controlling the path of the excitation beam. Each subsection begins with an overview of the physics behind the approach. This is followed by a description of the fabrication methods, since they determine the level of integration that is possible and since the techniques used in fabrication impact performance. The inherent advantages and limitations of the approach are then discussed, and representative micro-scale devices of that type are described. In the penultimate section, the performance metrics that have been achieved to date using the various approaches are compared, and suggested directions for future improvements are given. Finally, we end with a discussion of the performance standards that should be used to evaluate micro-scale fluorescence sensors.

5.2 Review of Fluorescence Spectroscopy

Fluorescence spectroscopy is well established and is the most powerful technique of molecular biology. Fluorescence assays are based on the excitation of par-

[1]By integration we mean either *heterogeneous* integration, which consists of the assembly of several modules to form a single device, or *monolithic* (sometimes called homogeneous) integration, where each component is micromachined (bulk or surface) on a single substrate.

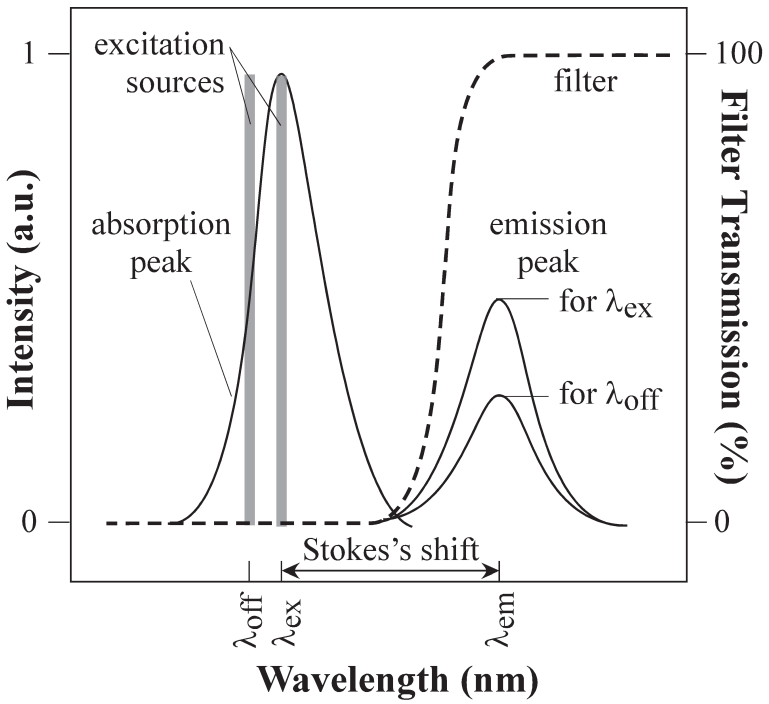

Figure 5.1: Typical peaks in the excitation (left) and emission (right) spectra. The wavelength filter (dashed line) must reject the excitation light and transmit the emitted fluorescent light. Excitation with off-peak (λ_{off}) wavelengths lowers the emission intensity.

ticular molecular groups called *fluorophores*, which can be intrinsic to the specimen under study, introduced into it, or chemically bound to it [100]. Fluorophores are organic dyes that absorb light in one range of wavelengths and re-emit the light, called the fluorescence, in a range of longer wavelengths.

Fluorescence spectroscopy is used for a wide variety of measurements, from simply detecting the presence of a species in a solution to monitoring complex biological processes like enzyme kinetics [100]. Its use in biomedical studies dates back to the late 1960s, when Herzenberg et al. introduced the fluorescence-based cell sorter [101], which allowed the sorting of live cells from dead ones using fluorophores as optical markers [102]. The next decade brought the capability of *single*

molecule detection, when Hirschfeld and his colleagues imaged a single antibody labeled with 100 fluorophores in a fluorescence microscope [103]. In the early 1980s, the field saw significant progress when Keller et al. detected a biomolecule labeled with a *single fluorophore* [104]. Today, fluorescence spectroscopy is ubiquitous in biomedical and biochemical analysis.

The absorption spectrum, illustrated for a generic fluorophore in Figure 5.1, has a peak at λ_{ex}, and the emission spectrum has a peak at λ_{em}; the distance between λ_{ex} and λ_{em} is called the Stokes shift. Stokes shifts can be as small as 10 nm (Amplex UltraRed) or as large as 150 nm (Fura-2), depending on the fluorophore[2]. Note that the emission and excitation spectra shown in the figure are mirror images of each other; this is true for the majority of fluorophores. If the fluorophore is excited at an off-peak wavelength λ_{off}, the resulting fluorescence spectrum will be unchanged but will have a lower amplitude than if it is excited at λ_{ex} [105]. The number of photons emitted is typically much smaller than the number absorbed, reflecting the existence of non-radiative pathways for the decay of the fluorophore from its excited state. The ratio of the emitted to absorbed photons is the *quantum yield* of the fluorophore.

Fluorescence can be detected visually, for example using a fluorescence microscope, or it can be converted to an electrical signal in a fluorescence spectrometer. Although spectrometers have greatly improved over the years, their basic operating principle has not changed. They comprise an excitation source, a wavelength fil-

[2]Amplex UltraRed and Fura-2 are trade names for commercially available synthetic fluorescent probes. The Stokes shift data were obtained from http://www.invitrogen.com. Stokes shifts of natural fluorophores can be found in ref. [100].

ter, and a detector [105]. The wavelength filter is of critical importance because it discriminates between excitation and emission photons by significantly reducing the excitation light intensity that reaches the detector while allowing through as much of the weak fluorescence signal as possible. This is essential because the excitation light is typically orders of magnitude brighter than the fluorescence signal. In conventional systems, the light directed at the sample is typically monochromatic at λ_{ex} and either comes from a laser or, more typically, is selected by a grating from a broadband source. In microsystems, however, the light source is often a broadband (40 to 90 nm FWHM[3]) light emitting diode (LED).

In fluorescence sensing, the primary choices for the wavelength filters are *dichroic filters*. An ideal dichroic filter completely reflects one or more ranges of wavelengths (*optical bands*) and transmits other wavelengths with a nearly zero coefficient of absorption (dashed line in Figure 5.1).

Four parameters that characterize optical filters are *rejection levels* in the stopband (the wavelengths that are blocked), *transmission levels* in the passband (the wavelengths that are transmitted), and the location and sharpness of the transition between them, respectively known as the *absorption edge* and the *absorption edge width*. The first two metrics are based on the *absorbance*, which is defined as the base 10 logarithm of the ratio of the output light intensity to the incident light intensity: $A = \log\left(\frac{I_o}{I_i}\right)$. The absorbance includes losses due to absorption, reflection, and scattering. Intensity is defined as power per unit area, so we report rejection

[3]The "full width half max" (FHWM) of an LED is a measure of the spread around its peak wavelength. Here the term broadband is used in comparison to laser sources which have FWHM below 1 nm.

and transmission levels in decibels (dB), i.e. $10 \times \log\left(\frac{I_o}{I_i}\right) = 10A$. A rejection level is a value of 10A in the stopband, and a transmission level is a value of 10A in the passband; since $\frac{I_o}{I_i} < 1$, these numbers are negative.

Because practitioners in this field are from various scientific and engineering backgrounds, no consistent units have been used when reporting filter spectra. For example, spectra are reported in absorbance units A, linear units, or in cm^{-1}. For the devices reviewed in this paper, units were converted to dB, and those that were already reported in dB were assumed to be in the $10A$ format.

Ideally, one would want the filter to transmit 0% ($-\infty$ dB) of the excitation light and 100% (0 dB) of the fluorescence, and the absorption edge to be perfectly vertical and located to the right of λ_{ex} and to the left of the entire emission spectrum. In reality, these levels are unattainable, and the stopband transitions to the passband over a range of wavelengths (the absorption edge width). The absorption edge width must be small enough to fit within the Stokes shift, as reported in ref. [106] and illustrated in Figure 5.1. Otherwise, the fluorophore cannot be excited at the absorption peak, or all the emitted light cannot be collected, both of which decrease sensitivity.

5.3 Multiple Layer Interference Filtering

The earliest types of filter used at the micro-scale were interference filters, since these are traditionally utilized with fluorescence spectrometers at the macro-scale. These filters are essentially mirrors that reflect the unwanted light. When a broad-

band light beam impinges on alternating layers of materials with different indices of refraction, wavelengths that undergo constructive interference are transmitted, and those that add destructively are reflected [107]. The number of layers and their thicknesses can be designed to create a filter that transmits a desired spectral range. Such wavelength filters are also called *distributed Bragg reflectors* (DBRs).

Three physical facts govern their design [107]. The first is that the amplitude of the reflected light at any boundary between two media is given by $\frac{1-\rho}{1+\rho}$, where ρ is the ratio of the optical admittances at the boundary. The second is that there is a phase shift of 180° when reflection occurs in a medium of lower refractive index, and zero phase shift otherwise. The third is that the reflected beam interferes destructively with the incident beam if the phase shift is 180° and constructively if the phase shift is 0°.

Interference filters often have a quarter-wave structure in which each layer has a thickness of $n\lambda/4$, where n is the refractive index of the material and λ is the center wavelength of the passband (set to the peak fluorescence wavelength) [107]. Such structures are known as *Bragg mirrors* or *Bragg reflectors*. Figure 5.2 shows the measured spectrum of a dichroic quarter-wave filter designed for use with the fluorophore FURA-2 (excitation: 365 nm, emission: 510 nm).

Band-pass filters can also be created. This is done by sandwiching a dielectric between two mirrors, which can be either Bragg mirrors or thin metal films, forming a solid Fabry-Perot cavity. For a guide to optimizing filter design, including how to determine the optimum number and thicknesses of the layers, how to deal with passband and stopband ripples (as are present in Figure 5.2, and how to minimize

angle dependence, refer to ref. [108].

5.3.1 Fabrication

Stacks of either dielectrics or semiconductors are used for quarter-wave filters that transmit in the visible. Their performance is generally comparable: although dielectrics do not attenuate optical wavelengths, and semiconductors do, the layers are so thin that absorption is negligible. A plethora of materials is available for the fabrication of interference filters, allowing one to achieve virtually any desired spectrum. Silicon dioxide, titanium dioxide, and silicon nitride are commonly used for visible light filters. Optical interference structures have also been made from

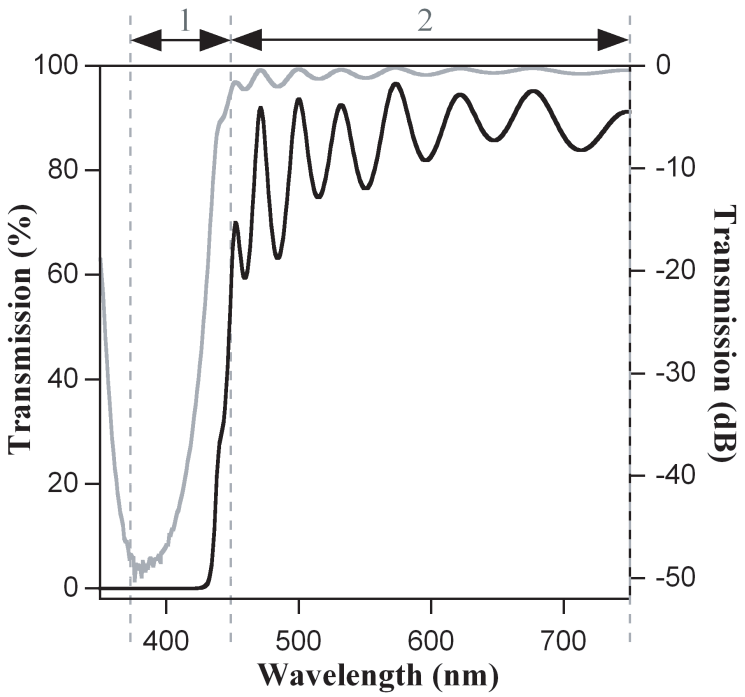

Figure 5.2: The spectrum, shown on both linear (black) and dB (gray) scales, of an interference filter with 39 alternating layers of PECVD-deposited silicon dioxide and silicon nitride, for a total thickness of 1.2 μm. Region 1 is the stopband of the filter and region 2 its passband.

compound semiconductors such as InGaAs, InP, and InGaN [107]. Metals, including Al and Au, are used in filters for infrared light.

The fabrication of interference filters is done with standard processes that can be performed at low temperature. Commonly used film deposition methods are plasma enhanced chemical vapor deposition (PECVD) for oxides and nitrides, sputtering or evaporation for metals, and molecular beam epitaxy (MBE) for compound semiconductors. Typically 40 layers are required to obtain reasonable rejection.

5.3.2 Advantages & Limitations

One of the most important advantages of interference filters is that, since they can be fabricated using standard, low-temperature processes, they are compatible with integrated circuitry, and can be readily integrated into larger micro-scale systems. Another is the aforementioned freedom in the design of the absorption spectrum. Arbitrary spectral profiles can be obtained using different layer arrangements. This flexibility is the most important feature of multilayer interference filters.

However, they also suffer from some serious drawbacks. One important limitation of interference filters is that variations of a few nanometers in the thicknesses of the layers can cause large errors in the cutoff wavelength, up to $\pm$ 50 nm. The thickness of each layer must be controlled to within 5% for a quarter-wave structure in order to preserve the targeted location of the absorption edge and achieve the desired transmission and rejection levels [107]. (Other structures such as half-wave stacks or Fabry-Prot interferometers require even tighter tolerances [107].) If the

fluorophore used in the assay has a small Stokes shift, with excitation and emission peaks close to the transition edge, exceeding the maximum allowable error is fatal to device performance. For example, the filter shown in Figure 5.2 was designed to have an absorption edge at 490 nm. Scanning electron micrographs of the stack revealed an average error of 12% ($\pm$ 5 nm) in the nominal thickness of each layer. This produced a filter with an absorption edge at 430 nm. For assays with Alexa Fluor Hydrazide (488 nm excitation and 30 nm Stokes shift), the excitation wavelength falls within the passband of this filter, rendering detection of fluorescence impossible. This highlights the need for stringent control during film deposition.

Moreover, the spectral response of these filters depends on the angle of incidence and the polarization of the incoming light, although design techniques can be used to minimize this [108]. The absorption edge of DBRs can shift by as much as 80 nm as the incidence angle is varied from 0 to 50° [106]. Another shortcoming, although not critical in most applications, is the presence of ripples in the transmission and stop bands, as illustrated in Figure 5.2. These ripples can be reduced by matching the optical admittance of the filter with that of the substrate.

Finally, it is not yet feasible to fabricate multiple filters of this type for different colors on one surface. Typically, the entire surface is coated and the filter is not patterned. This is because patterning is difficult if the layers are not etched by the same etchant. Given the effort required for deposition and patterning, interference filters remain the most challenging to integrate at the microscale.

5.3.3 Demonstrated Devices

This section highlights the systems microfabricated by Burns et al. [109], Adams et al. [110], Kim et al. [111], and Thrush et al. [112], [113]. Burnss device is one of the most highly cited in the literature because it beautifully illustrates not only integrated fluorescence, but also the lab-on-a-chip concept. Adams demonstrated the integration of filters and microfluidics with complementary metal oxide semiconductor (CMOS) imager chips, and Kim demonstrated the heterogeneous integration of detector, microfluidic channel, light source, and interference filter. Thrush accomplished the integration of the light source along with the filter and the photodetector.

5.3.3.1 Dielectric Quarter-Wave Stacks

Burns et al. fabricated a highly integrated μTAS for DNA analysis [109], [114], [115]. The fully automated system performed, on a single chip, several steps necessary for the sequencing of DNA. The device (Figure 5.3) consisted of the heterogeneous assembly of a nanoliter liquid injector, a sample positioning and mixing unit, a temperature-controlled reaction chamber, an electrophoretic separation system, air vents, and a fluorescence detector. The other components, including the light source and processing circuitry, were placed off-chip. A similar configuration was described by the same group for a capillary electrophoresis device integrated with a fluorescence detector [114].

The fluorescence sensor was a key component of this device, and it was used

to detect the fluorescently-tagged DNA. The filter was a quarter-wave dielectric interference structure that transmitted the fluorophore emission wavelength (515 nm) and rejected the excitation wavelength (under 500 nm). Neither the number of layers nor the spectrum of the optical filter were reported.

Sensor fabrication started with the formation of a photodiode detector in a silicon substrate. Silicon dioxide was subsequently thermally grown over the photodiode to electrically isolate it from the other parts of the device, while still allowing light to pass through. A quarter-wave interference filter, consisting of alternating layers of silicon dioxide and titanium dioxide was then deposited by the thin film coating company ZC& R Coatings for Optics Inc. (Carson, CA). Following this step, metal heaters were fabricated between two layers of vapor-deposited p-xylylene. These metal layers were used for temperature control and sensing. Platinum electrodes for electrophoretic separation were photolithographically defined on the surface of the upper p-xylylene layer. A glass chip containing etched microchannels was bonded to the surface to complete the assembly. Interfacing with off-chip control circuits was achieved via wirebonding of the pads to a printed circuit board.

This device demonstrated one of the benefits of μTAS: it performed DNA analysis with much smaller volumes than conventional fluorometers. In addition, the sensor could detect DNA at concentrations down to 10 ng/μL, which is impressive for a μTAS. Still, the authors acknowledged that one of the remaining technical challenges was to improve the sensitivity of the device. To address this issue, the authors later implemented more sensitive photodiodes that were able to detect a one hundred times lower concentration [114].

Adams et al. also made use of a quarter-wave dielectric filter, fabricating it on top of a CMOS imager [110]. This device is noteworthy because it integrated filters and fluidics with an on-chip camera, as opposed to discrete photodetectors. Such a configuration allows both quantitative and spatial analysis of fluorescence. This is an important feature for μTASs in which fluorescence is used not only as a detection mechanism but also as an imaging tool [116], such as is the case in microfabricated fluorescence-activated cell sorters (μFACS) [78].

The filter architecture was the same as that of Burns et al. The filter, which consisted of reactively sputtered silicon nitride and silicon dioxide, was deposited on top of the CMOS imager. Following this step, a layer of PDMS that had been patterned with analysis chambers and channels was reversibly bonded onto the surface of the filter. An off-chip LED was used for excitation. The authors reported detection of fluorescein dye and blocking of over 99% of the excitation light.

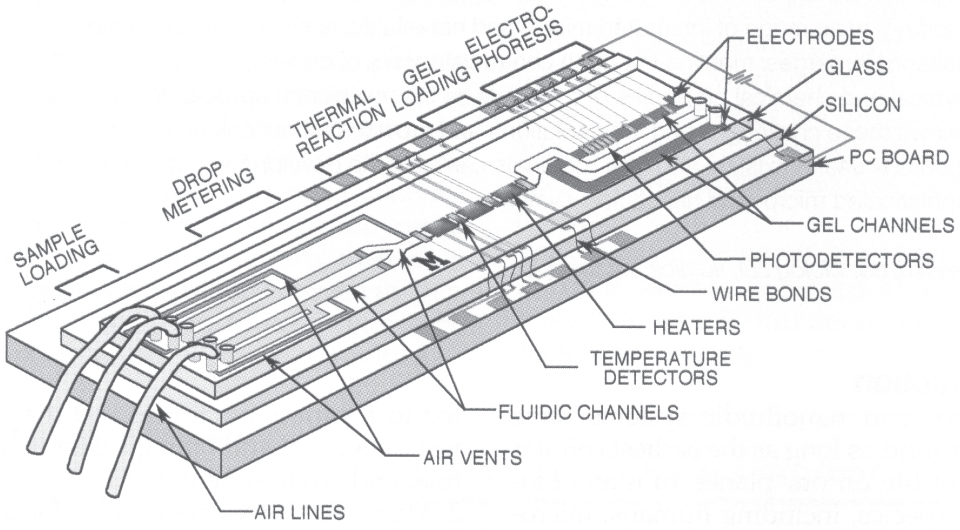

Figure 5.3: Schematic of a μTAS for DNA characterization that utilized a quarter-wave stack of SiO_2 and TiO_2 over the photodetectors. Reprinted with permission from 51. Copyright 1998 AAAS.

This device also stands out because it integrated filters and microfluidics with CMOS. Post-CMOS fabrication processes are often challenging because of the tiny (mm2) size of the microchips and because of more fundamental issues such as packaging, though these issues were not addressed by the authors.

Kim et al. [111] addressed both packaging and heterogeneous integration in their multi-module device, which included a detector, microfluidic channel, light source, and interference filter. The latter was a quarter-wave dielectric filter designed to attenuate 530 nm and to transmit 580 nm (the excitation and emission peaks, respectively, for tetramethylrhodamine (TAMRA)). While the spectrum showed a good transmission level of -1 dB at 580 nm, the decibel rejection level at 530 nm could not be determined from the given linear transmission spectrum.

The fabrication started by forming a p-i-n detector in a silicon wafer using photolithography and two cycles of ion implantation in order to obtain the desired doping levels. An interference filter comprising 32 layers of SiO2 and TiO2 with total thickness of 2.5 μm was then deposited over the surface. This photodetector substrate was then covered with a layer of PDMS. A microfluidic channel was defined in a second, soda-lime glass wafer, and on the back side of this wafer they fabricated an organic light emitting diode (OLED). The PDMS on the Si wafer was bonded to the soda-lime wafer to seal the microchannels, making a sandwich structure comprising the OLED light source, microchannels, filter, and detector.

This architecture illustrates the integration of all necessary components for on-chip fluorescence detection. It is noteworthy because the fabrication is simple and integration tolerances, such as alignment error during assembly, are not stringent.

The most challenging aspect of fabrication remains the control of layer thicknesses in the interference filter to achieve the desired spectral characteristics. The authors reported the detection of concentrations of TAMRA as low as 10 M. The authors also demonstrated a similar architecture for the detection of Rhodamine 6G which achieved a detection limit of 1 μM [117].

5.3.3.2 Semiconductor Quarter-Wave Stacks

Thrush et al. developed a sensor (Figure 5.4) for use in deep-red to near-infrared fluorescence studies [112], [113], [118–122]. It consisted of a light source, a wavelength filter, and a photodetector, all micromachined on a single substrate. A second module was used for the microfluidic network containing the DNA sample, formed in PDMS. A commercially-available miniature lens glued over the sample chamber focused the fluorescence back onto the photodetectors.

This design had several significant features, both from performance and fabrication standpoints. The authors used a vertical cavity surface emitting laser (VCSEL) as the on-chip light source, and they placed the detectors out of the direct optical path of the laser, thus combining interference and light-guiding spectral selection approaches. Because VCSELs emit exclusively in the direction normal to the surface, only the fluorescence focused by the lens (and a small amount of scattered excitation light) reached the detectors during the assay, allowing rejection levels of -40 dB [112].

DBRs served simultaneously as filters over the p-i-n photodetectors and as the

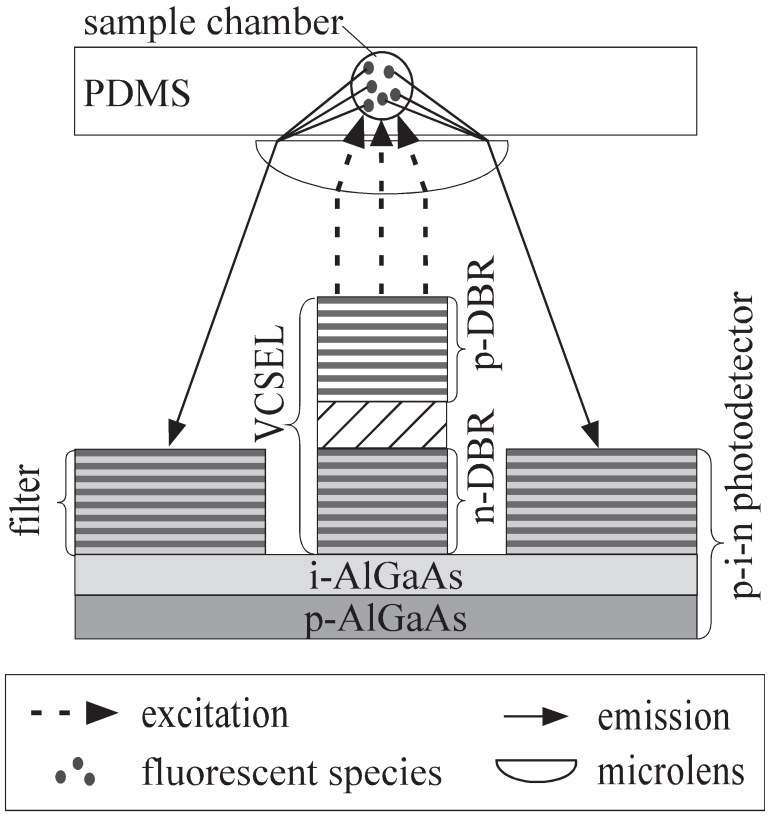

Figure 5.4: Integration of VCSEL light source, filter, and photodetectors (bottom) by Thrush et al. [112]. The microfluidics were housed in a separate module (top).

n-type material in the photodetector structure. The i-AlGaAs layer and the AlGaAs DBRs were deposited by metallo-organic chemical vapor deposition (MOCVD) onto a p-AlGaAs substrate. The deposition parameters were periodically varied to alter the stoichiometry of the compound. This produced a single layer of AlGaAs having 40 alternations in index of refraction forming the DBR, contrary to the previously described devices in which two dissimilar materials were used. There are several merits to producing a filter through index variations within a single material. The most important is that there is lower dispersion (the changes in index of refraction with frequency are similar for all layers), giving device performance that is easier to

model and closer to the designed spectrum. Another is that it facilitates patterning. Finally, there is no mismatch in the coefficients of thermal expansion between the layers.

It is important to mention that this type of filtering differs from absorption filtering with semiconductors, discussed below. Although the DBR filter utilized a material with non-zero absorption, filtration was achieved exclusively by interference because the thickness of each layer was an order of magnitude smaller than the wavelengths used (both excitation and emission) in the assay. (For techniques on designing resonant cavities for semiconductor lasers and for information on MEMS-based semiconductor lasers refer to ref. [123].)

A similar arrangement of components was used by Kamei et al. [124, 125]. However, there were separate modules for the detector and the filter, and an off-chip light source.

5.3.3.3 Porous Silicon Optical Filters

Another architecture for single-material interference filters is achieved by tailoring porous silicon. Porous silicon filters have been developed for other types of micro-spectrometers [126–129], but have not yet been demonstrated in fluorescence-based systems.

Pores ranging from nanometers to micrometers in diameter can be formed by bulk micromachining single crystal silicon through electrochemical etching [130–132]. The optical properties of porous silicon are controlled by varying the pore

size and density as a function of depth into the wafer [133]. Refractive indices have been varied between 1.6 and 3.4 by modulating the porosity [130], which has allowed fabrication of filters over a wide range of the electromagnetic spectrum.

This technology could have significant impact on future devices, since the porosity can in principle be varied across the surface of the Si, allowing different spectral characteristics to be produced adjacent to each other simply by altering the etch parameters at a given location. This would enable multi-wavelength spectroscopy. Multi-wavelength capability would allow fluorophores of different colors to be detected on the same device, and thus enable more sophisticated assays that examine correlations between measurements. Multi-wavelength capability would also allow emissions from a single fluorophore to be stimulated or detected at different wavelengths, providing improved accuracy through the use of ratiometric measurements[4] Such design freedom and ease of fabrication would significantly extend the capabilities of micro-scale fluorescence sensing systems.

As long as these filters can only be formed by bulk micromachining of single crystal material, monolithic integration with detectors and circuitry will not be possible. The technological hurdle to integrating such filters is producing porous silicon in thin films of amorphous or polycrystalline Si deposited onto a substrate. Promising attempts at producing porous silicon in films deposited on a substrate

[4]Ratiometric measurements rely on a differential response of the fluorophore at two wavelengths and can be done in one of two ways. In the first, two different frequencies are shone sequentially on the fluorophore, and the resulting emissions are measured. In the second, the emission at two wavelengths is monitored in response to a single excitation frequency. For a ratiometric dye, only one of these wavelengths is affected by the concentration of the analyte, so the ratio of intensities at the two wavelengths provides an estimate for the analyte concentration that is insensitive to changes in dye concentration, losses in the optical path, photobleaching, scattering, and background light.

were made by Link et al. [134], however its use as an optical filter for fluorescence has not yet been demonstrated.

5.3.3.4 Plasmonic Interference Filters

Interference filters may also be constructed using structured metallic surfaces that discriminate between different wavelengths of surface plasmons[5] , rather than of light directly. Plasmonic filters have been developed and characterized, but have not yet been demonstrated in fluorescence-based systems.

Many different plasmonic components have been demonstrated, including waveguides [135], mirrors [136, 137], interferometers [138], and Bragg gratings [138–141]. The Bragg gratings are typically realized in waveguide configurations using coupled metal-dielectric interfaces with periodic patterning imposed as gaps in a metal strip [140], changes in the thickness of a metal strip [139] or dielectric layer [142], changes in the width of a metal strip [140,141], or changes in the dielectric constant of the dielectric layer [143,144]. Although most existing plasmonic components have been developed and characterized at wavelengths relevant for telecommunications applications (λ = 1550 nm) [135, 139–144], a few components have been designed for operation at visible and near-IR wavelengths that are more appropriate for applications in fluorescence measurements [136, 145, 146].

This technology could have significant impact on future fluorescence sensing devices, since there is good potential for compact filters with different spectral char-

[5]Surface plasmons are electromagnetic waves that propagate along the surface of a conductor, with exponentially decaying fields on either side of the interface. They arise from resonant interactions between a light wave and free electrons at the surface of the conductor and thus are confined spatially at the interface.

acteristics to be implemented on the same substrate [147, 148]. This would enable multi-wavelength spectroscopy, as described above. Additionally, surface plasmons enhance fluorescence emission intensity [149–153]. This implies that it might be possible to create plasmonic devices that simultaneously enhance fluorescent emissions and filter excitation light [154, 155].

The primary drawback of plasmonic devices for spectral filtering is that the technology is not as mature as the other techniques discussed here. While the basic physical mechanisms have been known for several decades, the creation of such devices relies on nanostructured metal-dielectric interfaces, and fabrication of such structures has begun to be practical only within the last few years. Additionally, in order to use plasmonic filters for fluorescence, it must be possible to efficiently couple light into and out of surface plasmons. This is difficult because the momentum of surface plasmon waves is higher than the momentum of free space photons of the same frequency [147].

5.4 Absorption Filtering

An alternative to multiple-layer interference filters are single layers that have high absorption at the excitation wavelength but low absorption at the emission wavelength, known as *absorption filters*. The absorption process is governed by the Beer-Lambert law: $I = I_0 e^{-\alpha x}$, where I is the intensity of the light exiting the filter, I_0 the intensity of the incident beam, α the *absorption coefficient*, a wavelength-dependent constant, and x the filter thickness. If the absorption spectrum of a

material is known, the Beer-Lambert law can be used to find the absorbance A for a given thickness, and subsequently, the decibel representation of the transmission across the spectrum. Figure 5.5 shows absorption coefficient and transmission spectra for a few semiconductors and an organic chromophore that have been used for filtering.

There are two types of absorption filters, bandgap and organic, and both have been demonstrated at the micro-scale. Semiconductors make good absorption filters because of the energy gap between their valence and conduction bands [31,156]: impinging photons with energies lower than the bandgap pass through, while photons with higher energies are strongly absorbed. Direct bandgap semiconductors (such as CdS, GaAs) have steeper drops in absorption coefficient (narrower absorption edge widths) in comparison with indirect bandgap semiconductors (such as Si).

Organic absorption filters are chromophore-based. *Chromophores* are molecular groups that absorb light with no subsequent re-emission. Polymer filters contain chromophores either as part of their molecular structure (intrinsic) or as guests (extrinsic) in the polymer host [30].

5.4.1 Fabrication

Essentially all semiconductor deposition methods can be employed to deposit thin films for absorption filtering. CVD, low pressure CVD (LPCVD), PECVD, pulsed laser deposition (PLD), and MBE are the most common [159]. For some materials, the absorption edge can be tailored by controlling the deposition conditions.

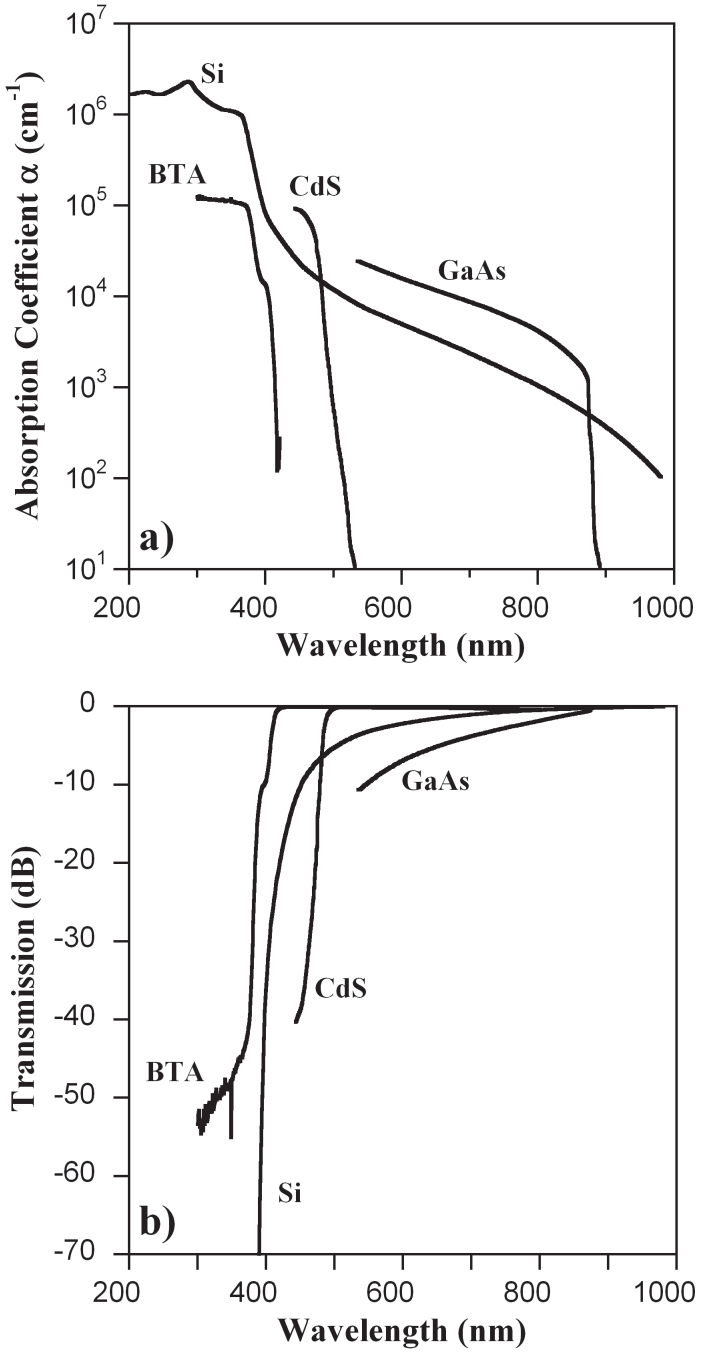

Figure 5.5: a) Absorption coefficient spectra of some common semiconductors and a chromophore, BTA, in an acrylic polymer host. Semiconductor data adapted from [31, 157, 158]. Data for 37 vol% BTA in acrylic are experimental results from our laboratory. b) Transmission spectra calculated from the absorption coefficient spectra.

For example, the bandgap of hydrogenated amorphous silicon has been varied from 1.2 eV to 3.3 eV by adjusting pressure and gas flow rates during PECVD [160].

The main advantage of polymer filters is that they can be deposited and patterned simply and at low cost by a wide variety of methods, usually at room-temperature, with minimal residual stress even in thick films. Polymers can be deposited by spin-coating or casting (for thicker layers) when the polymer is either a precursor that requires a curing step or a polymer dissolved in a solvent that evaporates. Curing methods vary depending on the polymer: some are cured by ultraviolet exposure, whereas others require a thermal cycle or the addition of a cross-linking agent.

5.4.2 Advantages & Limitations

Fabrication is more straightforward for absorption filters than for interference filters, since it requires only a single layer and no tight tolerances. Another advantage is that, unlike for multi-layer filters, the response of the filters is independent of the angle of incidence. On the other hand, a disadvantage of absorption filters is their limited tailorability compared with interference filters; instead, the material must be chosen to be compatible with a specific fluorophore, which can entail complete changes in fabrication methods for different applications of the same device.

Semiconductors show a remarkable ability to absorb ultraviolet light. For example, high energy ultraviolet light (200 nm) is reduced by a factor of 3 in only 10 nm of silicon. However, a major drawback is their lack of dichroism. As can

be seen in Figure 5.5, the absorption coefficient for some materials is non-zero from the ultraviolet to the infrared regions of the electromagnetic spectrum. This means that 0 dB transmission of short Stokes shifted fluorescence emissions is impossible with most semiconductor filters. Though this is not an issue for high brightness applications, it is in assays with low fluorophore concentrations.

For polymeric filters based on absorption by a chromophore mixed into the polymer matrix, the spectrum can be modified through the choice of the chromophore, but the dye must be soluble in the host. Extrinsic chromophores loaded into an optically clear matrix can offer high rejection, as shown in Figure 5.5. Rejection can be increased without increasing film thickness by adding more chromophore to the host, until it saturates. Dandin et al. [161] demonstrated the loading of *2-(2-hydroxy-5-methylphenyl) benzotriazole*, BTA, which is a photo-stable UV-absorbing chromophore, into several polymers. They were able to achieve -45 dB rejection of excitation wavelengths and -1.5 dB transmission of emission wavelengths in only 1 μm thick films. In addition, the chromophore exhibits dichroic behavior, so the absorption edge was steep. It should be mentioned that loading of photo-active organic compounds into polymers has previously been proven to be effective in other commercial applications, such as thin-film polymer displays [27], [25], multi-wavelength photoresists [26], photostabilization of polymers for sunlight protection [30], [28], and cataract surgery [29].

5.4.3 Demonstrated Devices

Several devices in the literature have made use of single-layer absorption filters. The first that we review in this section, developed by Chediak et al. [106], integrated the light source, detector, and filter. These authors also presented a useful quantitative comparison of single layer semiconductor filters versus DBRs. The second, developed by Iordanov et al. [162], stands out because it integrated filters and microfluidics and, like Adams [110], used a CMOS imager.

Chabinyc et al. [163] demonstrated a device that used a polymeric filter, and similarly Kruger et al. [164] used a commercially-available gelatin filter. Hofman et al. used a millimeter-thick dye-doped PDMS film both as a microfluidic network and as a fluorescence filter [23]. These devices are not discussed further here because of the thicknesses of the polymer filter films; however, they do illustrate the technique of loading chromophores into optically clear polymers for fluorescence sensing applications.

5.4.3.1 Cadmium Sulfide Filters

Chediak et al. [106] demonstrated a micro-fluorometer based on the heterogeneous integration of CdS filters with InGaN LEDs Figure 5.6. CdS was used because of its sharp absorption edge at 513 nm (20 nm wide): the device was used to detect blue-excited, green-emission fluorophores.

This device configuration was essentially the same as the one in Figure 5.4, but without a lens. It consisted of two modules. The sensing module included a

silicon photodetector onto which the CdS filter was deposited by PLD. An InGaN LED (primarily blue emission) grown on sapphire was bonded to an aluminum bondpad that had been deposited and patterned over the filter to provide electrical connection. The aluminum served a critical secondary role as a reflector of the weaker green emission of the LED: these wavelengths lay in the transmission band of the filter and had to be blocked. A separate sample-containing module consisted of analysis chambers and a microfluidic network formed in PDMS. The PDMS was bonded to a glass substrate and positioned 2 mm above the LED.

The authors characterized a 2.4 μm CdS film. It had -60 dB rejection of the excitation light at 470 nm (i.e. 99.9999% of the light blocked, or 10^{-6} of the light transmitted) and -4 dB (40%) transmission of the fluorescent wavelength (513 nm). However, only a 1.2 μm film was used in the prototype, and its rejection and transmission metrics were not provided. From Figure 5.5 and the Beer-Lambert law we estimate the transmission to be -30 dB at the excitation wavelength and -0.05 dB at the emission wavelength of the fluorophore. The device was able to detect a concentration of fluorescein as low as 0.12 μM. The authors likely used a thinner film in order to enhance transmission of the fluorescence and increase device sensitivity.

5.4.3.2 Poly-Si Filters

Iordanov et al. used a single layer of poly-crystalline silicon (polySi) to filter ultraviolet light but transmit light at 450 nm to a custom-made CMOS imaging array (Figure 5.6) [162]. They fabricated a microfluidic network over the sensor

and used the device to perform enzymatic analyses, specifically monitoring NADH concentration. They used the imager for monitoring fluorescence on different areas of the chip.

After completion of the CMOS fabrication process, the polySi thin film filter was deposited using LPCVD over the passivation layer. Filtering characteristics were improved if the grains of the polySi were enlarged through a subsequent pulsed XeCl excimer-laser annealing step. A microfluidic network was built on top of the filter using the negative photoresist SU-8. Packaging and integration issues must have been challenging but were not explicitly addressed. The authors reported that the device detected fluorescence with 35 dB selectivity (ratio of the signal from the fluorescence to the signal from the excitation light). Unfortunately, they did not

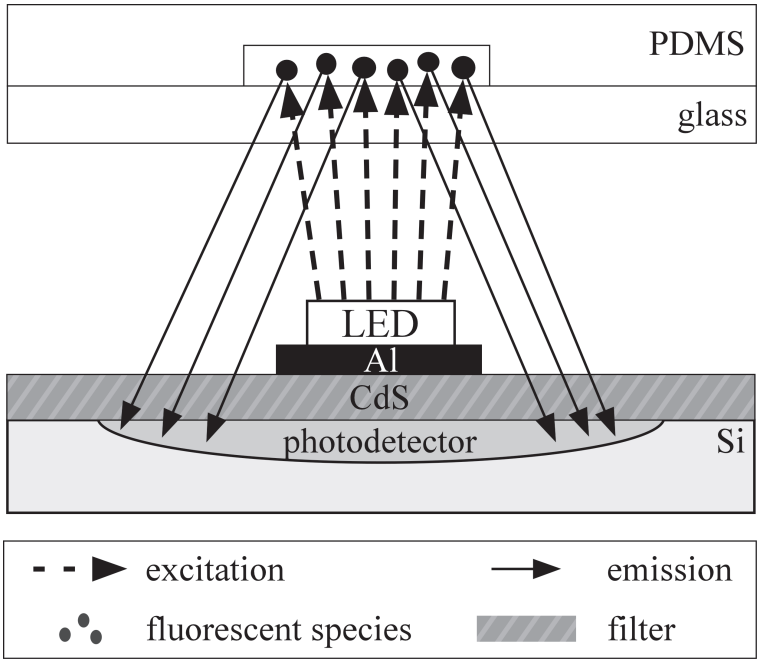

Figure 5.6: A microfluidic channel module assembled with a detector chip that has a CdS filter and Si photodetector onto which an LED has been mounted over an Al bond pad [106].

provide results characterizing the performance of the filter alone.

5.4.3.3 Polymer-Based Filters

Chabinyc et al. demonstrated a simple fluorescence sensing system that employed polycarbonate as a filter [163]. This system was not integrated, but rather used a multimode optical fiber inserted into a microchannel fabricated in PDMS to couple light into the microchannel. A commercial micro-scale avalanche array detector was embedded into the PDMS at the other end of the channel. The avalanche array detector was coated with 80 μm of polycarbonate.

The device was calibrated by filling the channel with known concentrations of the fluorophore in water. The sensor was able to reproducibly detect concentrations as low as 25 nM. No data were reported on the spectral characteristics of the polymer filter.

5.4.3.4 Aqueous Filters

Schueller et al. [165] and Chen et al. [166] demonstrated absorption filters using water-soluble dyes that were spatially patterned using an array of parallel microfluidic channels. These systems have the advantage of being able to reconfigure the filter during operation for different desired characteristics by filling the channels with fluids having different optical densities and different spectral characteristics. However, this technique has not yet been demonstrated in fluorescence-based systems.

5.5 Spectrally Selective Detectors

Thus far we have reviewed filtering approaches that prevent the excitation light from reaching the detector by either reflection (through interference) or absorption. A relatively new approach is to collect both fluorescence and excitation components and discriminate between the two electronically. This is possible because semiconductor detectors are spectrally selective, as implied by the absorption coefficient curves shown in Figure 5.5. Multi-color sensors can be obtained by exploiting this spectral selectivity.

The physical principles are identical with those responsible for the operation of absorption filters namely, that absorption is a function of both material composition and wavelength. Absorption of photons above a critical energy in a semiconductor creates electron-hole pairs that can be separated and collected. These carriers may be used to produce a current, charge, or voltage signal that is directly proportional to the intensity of the incident light. Three devices that use these principles are described in this section.

One method for realizing spectrally selective sensors is by using a variety of different semiconductors. Clearly, different semiconductor materials can exhibit distinctly different spectral responses as a result of the underlying differences in their electronic properties.

The second approach makes use of the fact that light of different wavelengths is absorbed at different depths in a semiconductor photosensor, giving spectral selectivity within a single material. Shorter wavelength photons are absorbed at the

surface, longer wavelength photons deeper in the material, although both decrease exponentially by the Beer-Lambert law. Spectral components can be separated by collecting photo-generated carriers at different depths using, for example, three vertically-stacked p-n junctions as illustrated in Figure 5.7 [167]. The p-n junctions of such a pixel have different, broad spectral responses, or selectivities, similar to the responses found in cones, the photosensitive cells of the retina. Even if each junction is sensitive to all of the incident wavelengths, it is differently sensitive to each, and so to identify the intensities of the 3 known wavelengths from the 3 broad spectral bands is a simple matter of solving a set of algebraic equations.

5.5.1 Fabrication

Layered semiconductor structures can be constructed using standard CMOS fabrication techniques, a significant benefit for integration. These architectures are not limited to silicon, though: the deposition processes discussed previously for other semiconductor materials can also be applied to the construction of spectrally selective detectors.

5.5.2 Advantages and Limitations

Multi-color sensors are of significant importance to micro-scale fluorescence-based systems. The architectures discussed so far targeted specific applications and are limited because they can only accommodate specific fluorophores. Multi-color sensors offer more versatility because they can detect several emission wavelengths.

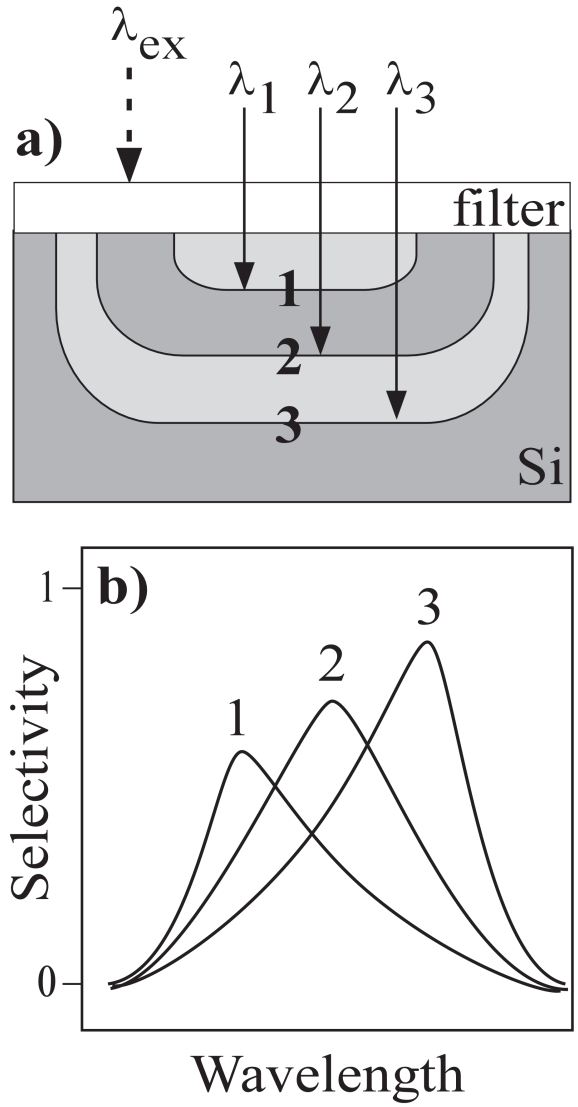

Figure 5.7: Multiple p-n junctions at different depths collect different spectral components of the fluorescence, λ_1, λ_2, λ_3. The excitation light (λ_{ex}) is blocked by the filter. b) Spectral selectivities of each of the three coincident p-n junctions. Figure adapted from [168].

Unfortunately, the spectral components collected by a multi-color sensor might not match the fluorescent wavelengths for a specific application, which could reduce the accuracy of the intensity estimation. This would occur because the spectral selectivity is determined primarily by the material properties, rather than by components in the system design such as readout circuits or physical layout. Therefore, it is necessary to tightly control film deposition parameters and it may be necessary to tweak the fabrication process. In most cases this is impractical or prohibitively expensive for CMOS technologies. For this reason, it may be advantageous to combine the fabrication of such sensors with the micro-machining of the optical filters.

5.5.3 Demonstrated Devices

Two macro-scale devices that demonstrate the use of spectrally selective detectors for fluorescence sensing can be found in the literature; this concept has not yet been used in an integrated device. The first, by Starikov et al. [169] used several MBE-grown diodes in order to obtain a wide range of spectral characteristics. This work is remarkable because it also made use of the detectors as light sources. The second device, developed by Maruyama et al. [170], [171], is important because it shows the use of a CMOS-fabricated photogate pixel to achieve fluorescence detection. Neither of these devices made use of an optical filter.

5.5.3.1 Heterojunction Detectors

Starikov et al. [169] demonstrated the use of spectrally selective photodetectors in detecting multi-wavelength fluorescence. The photodiodes were p-n heterojunctions of the wide bandgap semiconductors AlGaN and InGaN, which were fabricated by molecular beam epitaxy. Optical selectivity was achieved by varying the composition of the AlGaN/InGaN alloy to achieve different emission and photoresponse spectra in different devices. The diodes could be toggled on or off to serve either as photodetectors or light sources.

Multi-wavelength fluorescence detection was achieved by placing 8 diodes, with spectral characteristics ranging from the ultraviolet to red, in a circular pattern around an analysis chamber containing the analyte. The diodes were used for either excitation or collection of the fluorescence. Assays with several fluorophores (fluorescein, chlorophyll, pyrene, green fluorescence protein (GFP), and red fluorescence protein (RFP)) were conducted as a proof of concept. A detection limit of 2 nM of fluorescein was achieved.

5.5.3.2 Photogate CMOS Pixel

Maruyama et al. [170], [171] extended the concept of Figure 5.7 by using a photogate pixel for collection of fluorescence. Rather than stacking a series of junctions, the depth of the sensing region was controlled by the voltage applied to the photogate. A photogate is a single-element surface-channel charge-coupled device. Photo-generated charges are collected in a depletion area formed underneath

the photogate, which in this case was formed using poly-Si over a p-n junction formed by a moderately doped p-type region (p-well) in a lightly doped n-type substrate.

By varying the gate voltage, these authors were able to vary the collection depth, and thus to modulate the spectral responsivity of the device. The pixel was fabricated using standard CMOS technology and was able to discriminate between blue and green wavelengths without the use of a filter. The sensor was used to detect a solution containing double-stranded DNA labeled with the fluorescent nucleic acid stain SYBR-Green, with an estimated detection limit of 10 μM.

5.6 Light Guiding Elements

Thus far, we have reviewed on-chip filtering and detection techniques based on optical interference and light absorption. A completely different approach consists of exploiting ray optics to achieve separation of excitation and fluorescence, either with waveguides or with microfabricated free-space optical elements. The basic idea in both cases is to use geometry and optics to prevent the excitation light from falling on the detector. This is possible because the excitation light is collimated, and can therefore be guided, while the fluorescence is emitted in all directions. Lenses, gratings, mirrors, and prisms have been miniaturized for this purpose. A wealth of information is available on the fabrication and integration of these elements for other types of micro-spectrometers [16], [172]. In this section, we review those devices that have used light-guiding elements to achieve at least some degree of on-chip filtering.

5.6.1 Fabrication

The fabrication methods used to produce miniature fluorescence sensors based on filterless techniques vary greatly because of the large variety of implementations. Thus, fabrication information is provided below, together with each of the demonstrated devices.

5.6.2 Advantages and Limitations

Filtration of excitation light without a thin film filter is attractive because it can be achieved using free-space optical elements simply by collimating the excitation and positioning the detector away from the optical path. The waveguiding schemes provide the same advantage, but can be limited by the performance of the waveguide. Non-idealities due to fabrication imperfections, such as waveguide sidewall roughness, or to misalignment in coupling the excitation light into the waveguide affect the extent to which the fluorescence is guided without loss and the extent to which the excitation light is excluded from the detector.

Another attractive feature, if not the most important, is the ability to combine this filtering approach with those previously discussed. We presented the Thrush and Chediak devices as architectures using thin-film filters, but positioning played an important role in preventing the excitation light from falling on the detector. Thrush (Figure 5.4) used the vertical emission of the VCSEL to ensure that minimal excitation light reached the filter-protected detectors and a microlens to focus maximum fluorescence light onto the detectors. In later work, Thrush incorporated metal

sidewalls on the detector to enhance optical isolation and rejection levels [120, 122]. Similarly, the Chediak architecture (Figure 5.6) used positioning to avoid saturating the fluorescence collected by the CdS-protected detector.

Unfortunately, measurements that describe the extent to which rejection has been achieved or to which fluorescence has been collected with miniaturized light-guiding technologies have not been reported: metrics analogous to absorption and transmission for filters have not been developed to characterize the performance of filterless devices. Rather, it has been more common to report the signal to noise ratio (SNR). This makes comparison among different device types difficult, since the SNR depends not only on fluorescence signal, but also on the photodetector characteristics, such as the dark current level or other sources of electronic noise.

5.6.3 Demonstrated Devices

The light-guiding approach has been popular, with quite a few devices reported in the literature [173–190]. The majority of these devices make use of orthogonal or angled positioning of the waveguides to obtain some degree of spectral separation. However, most of them still rely on off-chip filters or spectrometers to completely isolate the fluorescence from the background excitation light.

Another approach is to use micromachined free-space optical elements to achieve on-chip filtering. Two of these that demonstrate the free-space optical element approach are reviewed here as representatives of the types of architectures that have been employed. The first, by Roulet et al. [180–182], integrated microlenses

with microfluidic modules. The second, by Zeller et al. [178], demonstrated excitation and sensing with a single microfabricated grating.

5.6.3.1 Waveguides and Fiber Optics

The classical definition of the term waveguide is any structure that routes electromagnetic energy. An optical fiber is a special type of waveguide that guides electromagnetic energy in the visible range by total internal reflection. In the integrated fluorescence sensing literature, the term waveguide has been used to refer to microfabricated light conduits. The principle of operation of both waveguides and optical fibers in fluorescence sensing is the same, i.e. the separation of fluorescence from excitation light is achieved in the same manner.

Quite a few researchers have used microfabricated waveguides to achieve separation of fluorescence from excitation light [68–70, 72, 86, 94, 174, 183–189] while several others have used optical fibers [80, 176, 178, 179]. There are two types of waveguide/fiber-based architectures in the literature. The first confines both the excitation and the fluorescence in the plane of the microfluidic channel as shown in Figure 5.8a). The second excites perpendicularly to the plane of the microfluidic channel and collects the fluorescence laterally through a waveguide as illustrated in Figure 5.8b).Alternatively, it is also possible to excite fluorophores in-plane and collect the fluorescence out of plane (Figure 5.8c)).

Fabrication of these devices is typically achieved through soft lithography[6]. However, the procedure is dictated by the choice of the substrate. Other machining

[6]Soft lithography is a micromachining technique utilizing soft materials (polymers).

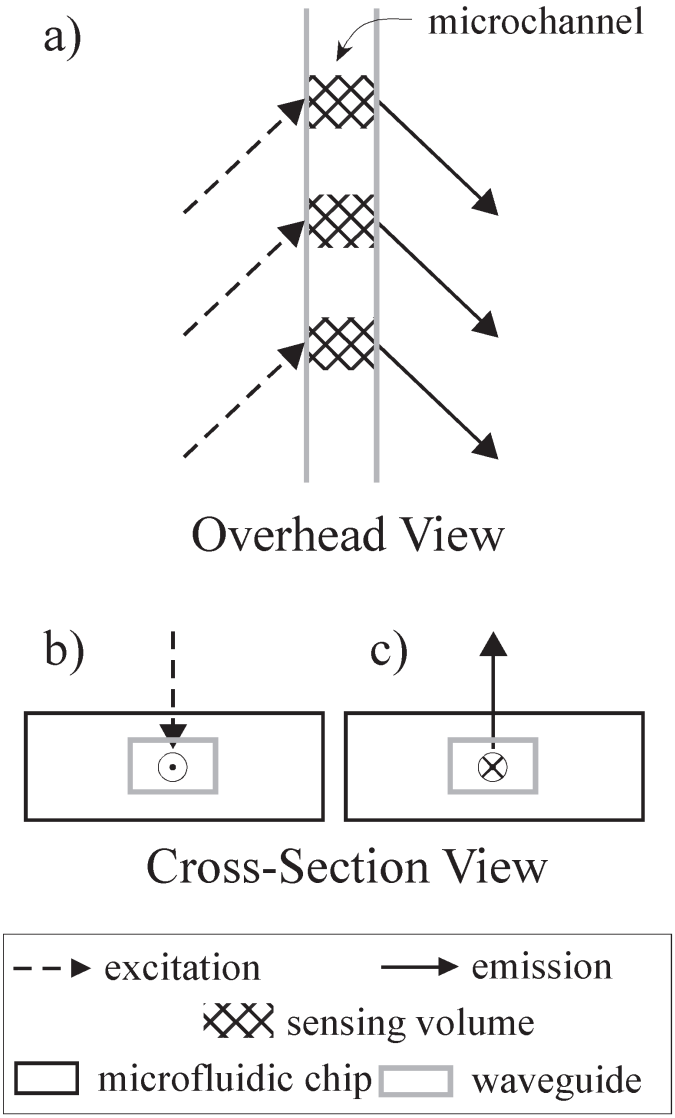

Figure 5.8: Sketch of geometries typically used in waveguide-based devices. a) Fluorescence and excitation are confined in-plane, but the fluorescence is collected at a different angle than the collimated excitation. b) Fluorophores are excited from the top, and fluorescence is collected laterally (out of the page). c) Fluorophores are excited laterally (into the page) and fluorescence is collected perpendicularly.

techniques, such as wet and dry etching, can also be used.

The separation obtained using waveguide-based approaches is only partial. One can never position the waveguides in such a way as to achieve complete isolation between wavelengths. Therefore, these devices often require an off-chip filter or spectrometer to increase sensitivity.

5.6.3.2 Micro-Lenses

The concept behind the Roulet device [180–182] was combining illumination at an angle (geometry) with focusing by lenses (optics) to direct the excitation beam onto the sample and then away from the detector. The first set of lenses was placed on one side of a glass substrate containing microfluidic channels to converge the excitation beam onto the sample (Figure 5.9). The second set was placed on the opposite surface of the substrate, behind the channels, to deflect the excitation beam away from the photodetector. A fraction of the omnidirectionally-emitted fluorescence light reached the detector, which was on another substrate.

The microlenses were fabricated by patterning layers of photoresist on both sides of a previously micromachined Pyrex microfluidic chip. The chip was placed in an oven to melt the resist, which contracted into lens shapes by surface tension. The authors adjusted the process parameters to produce the desired focal lengths. Nearly 30% of the fluorescence light, the portion that heads into the substrate and toward the detector, was collected with this configuration; the detector yielded an SNR of 21 dB. The authors demonstrated the successful detection of 10 nM of the

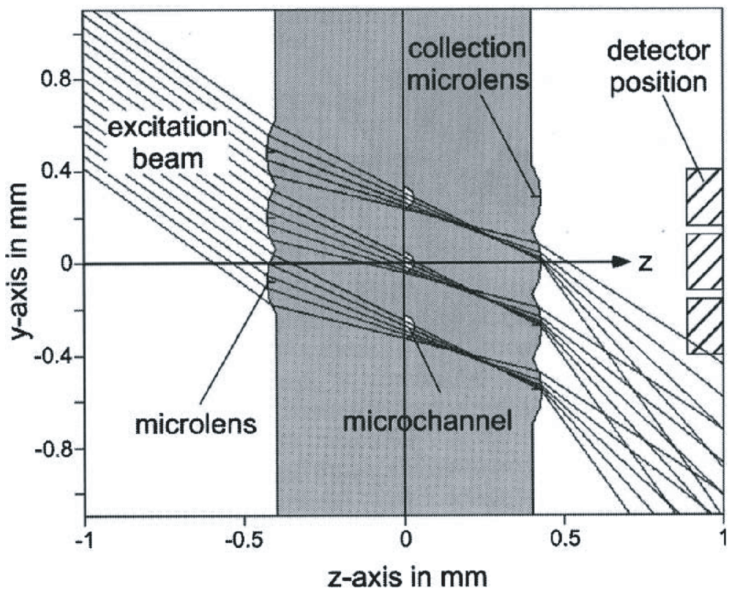

Figure 5.9: Cross-sectional sketch of a device based on free-space optical elements, showing a mechanism for separating fluorescence light from the excitation beam using lenses 132. Photoresist lenses were microfabricated on the top and bottom faces of a glass substrate (gray) containing microfluidic channels, which run perpendicular to the page. Copyright ref. [181]

fluorophore Cy5.

5.6.3.3 Microfabricated Diffraction Gratings

Zeller et al. [178] demonstrated that filterless fluorescence could be realized with only a single grating. The fabrication of this device began with the fabrication of a mold by etching the grating pattern into a silica substrate and coating it with gold; this served as a mold for producing an electroplated nickel stamp. The resulting stamp was used to transfer the grating pattern onto a polycarbonate sheet. Subsequently, a titanium oxide waveguide was formed on the back side of the sheet, on top of the grating.

The operation of the device is illustrated in Figure 5.10. TM[7] polarized light from a laser was coupled into the waveguide via the grating. Molecules adsorbed on top of the waveguide were illuminated by the TM mode of the laser beams evanescent tail. The fluorescent light emitted by these molecules was coupled into TM and TE modes in the waveguide. These modes were again coupled out by the same grating, at different angles of diffraction for the different modes and wavelengths. The detector was placed at the diffraction angle for the TE mode of the fluorescent light in order to collect the fluorescence signal and not the excitation light from the laser, which appeared at the diffraction angle for the TM mode of the excitation light. The authors demonstrated the successful detection of 10 nM of Cy5-tagged species. No detection limit or SNR were reported.

5.7 Summary of Achieved Device Performance

The performance metrics of the various miniature fluorescence sensors are summarized in Table 5.1.[8] Two fundamental metrics are given when they were provided by the authors: the rejection and transmission levels [9] of the filters which we reported in decibels (on a $10 \times \log_{10}$ basis). In the following two subsections, attractive features of each of the technologies are summarized based on their rejection and transmission levels, and then on the fabrication methods.

[7]Transverse magnetic (TM) and transverse electric (TE) modes are solutions to Maxwells equations which specify the intensity patterns of a propagating electromagnetic field. For TM modes there is no magnetic field in the direction of propagation, and for TE modes there is no electric field in the direction of propagation.

[8]The numbering of the references follow that of the original paper [54].

[9]As previously mentioned, we are referring to the intensity of the light that is rejected/transmitted.

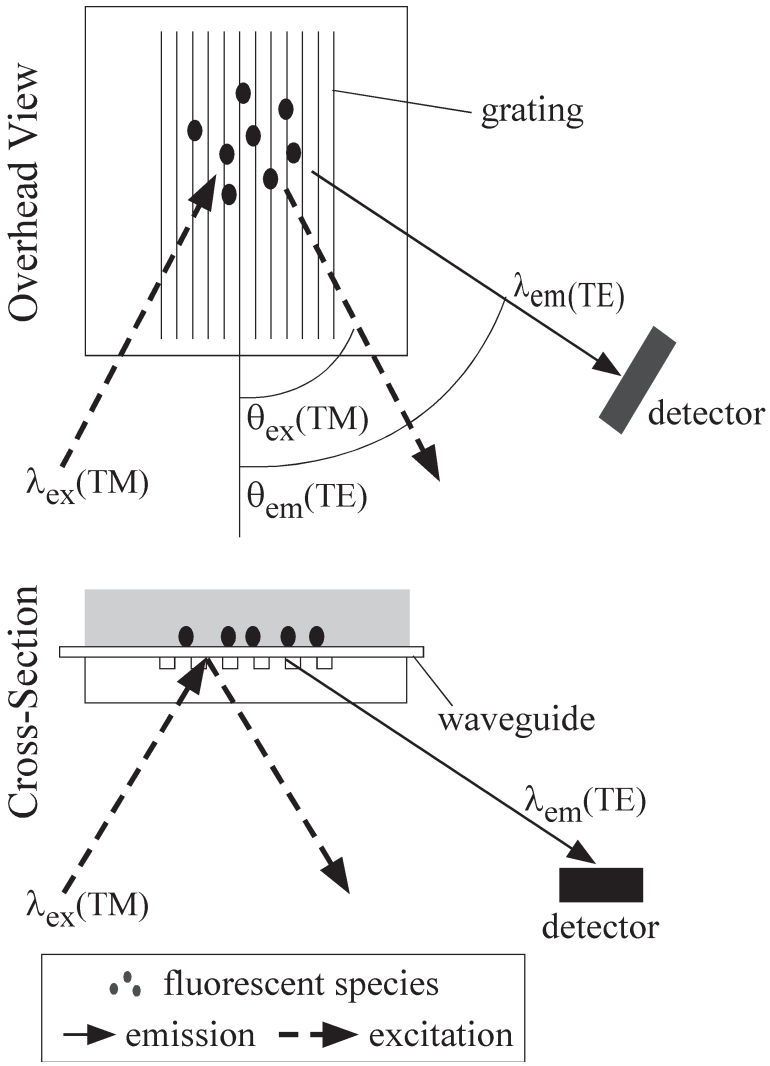

Figure 5.10: Polarized TM excitation light at wavelength λ_{ex} is incident at an angle θ_{ex}(TM) on fluorescently tagged molecules immobilized above a grating. The incident beam is diffracted through an angle $2\theta_{ex}$(TM), away from the detector, while the fluorescent emissions are coupled into the waveguide and diffracted out of the waveguide at an angle θ_{em}(TE) [178].

Reported detection limits are also included in Table 5.1: these indicate the performance of the devices in the assays for which they were designed. However, these figures cannot be used as a metric for comparison between sensors if the fluorophore is different, or in fact even if the fluorophore is the same since the emission intensity of the fluorophores depends on conditions such as pH and temperature. Therefore comparing sensors based on their detection limits is inappropriate unless care has been taken to reproduce exactly the same conditions.

The most valuable feature of interference filters is the tailorability of the stopband, which can be placed in arbitrary ranges of the electromagnetic spectrum. Furthermore, their steep absorption edges allow the highest percentage of fluorescence photons to be collected and make this the only type of filter that can be used with fluorophores having small Stokes shifts. However, the angular sensitivity of their spectral characteristics may further limit their applications.

Semiconductor bandgap filters, on the other hand, have shown excellent rejection levels in the ultraviolet. While their non-zero absorption at fluorescent wavelengths is less than ideal for applications with low fluorescence intensity, it is preferable to the loss in sensitivity from insufficient rejection. The 2.4 μm CdS filter developed by Chediak et al. [106], for example, rejected the excitation light to -60 dB while still transmitting 40% of the fluorescence. For absorption filters in general, transmission levels are best for long Stokes shifted dyes.

Spectrally selective detectors also exploit the absorption characteristics of

Table 1 Performance synopsis for demonstrated miniaturized fluorescence sensors

Filter characteristics						Performance				
Materials or architecture	Thickness/ μm	Excitation wavelength/nm	Emission wavelength/nm	Absorption edge location/nm	Absorption edge width/nm	Rejection/dB	Transmission/dB	Fluorophore	Detection limit/nM	References
Interference only										
SiO_2, TiO_2		490	515			−13	−1.05			Burns[51,56,57]
SiO_2, Si_3N_4		488	515	500	15	−20		fluorescein	85 000	Adams[52]
SiO_2, TiO_2		530	580				−1	TAMRA	10 000	Kim[53]
SiO_2, TiO_2	2.3	530	580			−30	−1	rhodamine 6G	1000	Shin[59]
Absorption										
PolySi	1.5	365	450					NADH, DiFMUP		Iordanov[111]
Polycarbonate	80	360	510			−20	−1.05	fluorescein	25	Chabinyc[112]
Dye-loaded PDMS	3000			560	30	−40	−1.6			Hofmann[114]
Ray optics										
Micro-lenses	N/A			N/A	N/A			Cy5	3.3	Roulet[131–133]
Microfabricated grating	N/A			N/A	N/A			Cy5	10	Zeller[129]
Waveguides and fiber optics	N/A			N/A	N/A			Cy5	24 000	Ruano[128]
Waveguides and fiber optics	N/A	635	650	N/A	N/A			Alexa Fluor 633		Powers[127]
Microprism	N/A	543		N/A	N/A			Cy3		Huang[28]
Orthogonal geometry		540						Albumin Blue 580	1200	Hofmann[124]
Spectrally selective detectors										
Photogate CMOS pixel	N/A	470	520	N/A	N/A			SYBR Green	10 000	Maruyama[120,121]
Multi-wavelength III–V detectors	N/A	371–651		N/A	N/A			fluorescein, chlorophyll, pyrene, GFP, RFP	2	Starikov[119]
Filter + ray optics										
Interference + directional source + lens		780				−60[b]				Thrush[54,55,60–64]
Bandgap absorption filter + directional source	1.2	475	510			−30[a]	−0.05[a]		120	Chediak[48]

[a] By our calculations. [b] Best value is reported.

semiconductors, since they are a function of wavelength: the absorbance at energies above the bandgap increases monotonically with frequency. However, rejection is only moderate: -25 dB in experiments by Maruyama [170, 171] (this was demonstrated with LEDs rather than in fluorescence measurements).

It is clear that no one of these filtering approaches alone yields the high rejection in the stopband with the high transmission in the passband that will be necessary for the next generation of devices. There are two approaches to improving the performance. One its to combine interference or spectrally selective filtering with additional absorption filtering, as done in Starikov [169]. Another is to combine these approaches with light separation methods that employ positioning, micro-optical elements, and/or light guiding to achieve the bulk of the rejection.

5.8 Proposed Performance Standards

In the interest of furthering progress in the field, we propose a set of performance standards for characterizing the spectral selectivity of miniaturized fluorescence sensors. Such metrics will permit the fair comparison of widely disparate approaches in order to allow better design of micro-fluorometers at the system-level for μTAS applications.

Fluorescence sensing systems can be divided into three parts: the optical components that determine how much of the excitation and fluorescence light falls on the area of the detector, the filter over the detector, and the detector itself. The overall performance of the sensing system is determined by the responsivity R and

the noise N. Responsivity is a general term for an input-output characteristic, and in the case of photodetectors it has the specific meaning of the electrical output produced in response to a particular optical input intensity; which typically has units of A/W or V/W. The overall noise power N is the sum of photon shot noise and detector noise. The arrival of photons is a random Poisson process, so both noise power and signal-to-noise power ratio are proportional to the flux of photo-electrons in the detector. Photon noise sets a lower bound on the overall noise power [157].

The overall responsivity R of the system is the product of the detector responsivity with the composite transfer efficiency for the system components (defined in the following sections)

$$R_{system}(\lambda) = R_{detector}(\lambda) \times 10^{0.1\times\left[H_{filter}(\lambda)+H_{geometry}(\lambda)+H_{loss}(\lambda)\right]} \tag{5.1}$$

where the responsivities are represented on a linear scale and the composite transfer efficiency is the sum of individual transfer efficiencies , which are represented on a log scale as $10 \times \log_{10}$(output intensity / input intensity)[10]. In order to allow comparison of different systems without reference to specific fluorophores, these responsivities and transfer efficiencies should be given as a function of wavelength.

At a minimum, if it is impossible to obtain these spectra, the responsivities and transfer efficiencies should be provided for the excitation and peak fluorophore emission frequencies. In the case that only the overall R_{system} can be obtained, $R_{system}(\lambda_{ex})$ and $R_{system}(\lambda_{em})$ can always be found using a standard procedure (Sec-

[10]The composite transfer efficiency would be the product of the individual transfer efficiencies if they were expressed on a linear scale, but it is the sum when expressed in dB.

tion 5.8.5).

5.8.1 Detector Metrics

Since all detectors are spectrally selective, at least to a certain extent, the detector itself performs some spectral filtering. (This effect is exploited in the multi-wavelength spectrally selective detectors, Section 5.5.) A metric that represents this phenomenon is the quantum efficiency (QE) of the detector, defined as the probability that an incident photon creates a photo-electron. The way in which each photo-electron contributes to the detector output signal varies according to the details of the detector; a metric that represents the overall conversion from incident photon to detector output is the responsivity $R_{detector}$, defined as the ratio between the electrical output signal and the incident optical intensity. The responsivity of the detector should be provided as a function of wavelength, $R_{detector}(\lambda)$.

$$R_{detector}(\lambda) = \frac{electrical\ output\ signal}{incident\ optical\ power} \tag{5.2}$$

There are standard methodologies for experimentally determining quantum efficiency and responsivity [191,192]. The general approach to measuring responsivity is to provide a known optical intensity at a known wavelength as input to the detector and to measure the detector response. For different detectors the electrical output response may be in the form of voltage, current, or charge, which may be sampled using standard techniques. The optical intensity may be calibrated using another detector whose response is calibrated in the spectral range of interest. Because light

beams diverge (i.e., increase in diameter) as they propagate, it is important to ensure that the distance between the light source and the detector remains the same for different measurements. In order to obtain reliable measurements it is also necessary to ensure spatial uniformity of the light source; for best results this is done using an integrating sphere[11] but in many cases simple diffusers may be adequate. The intensity of the light source should be adjusted by setting the source at its maximum intensity and inserting neutral density filters into the light path rather than by using electronic controls, since in general the spectral characteristics of a light source vary with bias conditions.

Whereas quantum efficiency reflects the probability that an incident photon generates a photo-electron, responsivity reflects the overall conversion from optical input to electrical output. Thus the responsivity is the quantum efficiency multiplied by the internal gain of the photodetector. Typically, responsivity can be measured directly from the detector output, but determining quantum efficiency requires an estimate of the internal gain from generated photo-electrons to output response, which usually cannot be measured directly and must be estimated using statistical methods. Reviewing these methods is outside the scope of this paper, but they are detailed in ref. [191, 192].

The minimum detectable signal is determined by the noise and is commonly taken to be the root mean square (RMS) noise, the square root of the noise variance. Signals in real detectors will be degraded by photon shot noise as well as noise sources

[11] An integrating sphere is an optical component consisting of a hollow cavity with its interior coated for diffuse high reflectance, having relatively small holes for entrance and exit ports. It serves as an ideal diffuser, scattering and distributing incident light rays so that the outgoing light is spatially uniform.

including shot noise from bias currents, flicker noise (also known as $1/f$ noise), and thermal noise from thermal agitation of charge carriers. At low intensities, the noise is typically dominated by dark noise resulting from leakage currents in the detector [25]. Ideally, the power spectral density of the detector noise should be provided as a function of both temporal frequency and intensity [193]. The RMS noise is the square root of the spectral density integrated over all temporal frequencies and can be determined from measurements of the detector output using standard techniques [194]. The power spectral density can be measured using a spectrum analyzer, and the RMS noise can be estimated as the standard deviation of an ensemble of samples of the output signal from the detector. At a minimum, the RMS noise $\sigma_{detector}(\Gamma)$ as a function of input intensity Γ should be provided (under the assumptions that the detector is a linear system, and that detection is performed using a single measurement with no temporal filtering or signal modulation). In order to allow comparison of different systems without reference to temporal filtering and signal modulation strategy, the power spectral density of the detector noise should be provided as a function of temporal frequency f and intensity, $N_{detector}(f, \Gamma)$.

5.8.2 Filter Metrics

Table 5.1 shows that few authors report the characteristics of the filters used in their systems. We recommend that such information always be provided by reporting the transmission spectrum of the filter. This is an important design parameter that allows one to estimate the performance of a micro-fluorometer with a wide

variety of fluorophores. In addition, it allows devices to be categorized by their transition wavelengths and their rejection and transmission levels.

Because it is difficult to discern variations in low-transmission regions in spectra reported in linear units or from absorption coefficient data, transmission measurements should be reported in decibel units. As mentioned previously, this has not been the norm, since in other fields absorption spectra have traditionally been reported in a variety of other units. For detecting low fluorescence levels, however, it is necessary to distinguish levels below 20 dB, such as between 30 and 50 dB, which appear as zero on a linear scale. Also, the dB representation better shows the passband to stopband transitions than does the absorption coefficient (Figure 5.5a).

The transfer efficiency of the filter is equal to its transmission, given by

$$H_{filter}(\lambda) = T(\lambda) = 10 \log_{10} \left(\frac{I(\lambda)}{I_0(\lambda)} \right) \tag{5.3}$$

where $I(\lambda)$ is the intensity of light ($\mu W/cm^2$) after filtering and $I_0(\lambda)$ is the intensity of light incident on the filter.

The absorption edge or cutoff wavelength λ_c and the absorption edge width w define the transition between stopband and passband. The former determines the excitation sources and fluorophores that can be employed, while systems with large w are restricted to use with fluorophores that have large Stokes shifts. The standard definition for λ_c for an electronic long-pass filter is the wavelength at which the transmission is -3 dB. The upper frequency limit of the passband is defined as a given fraction of λ_c , and the stopband is defined as the frequency range for which the

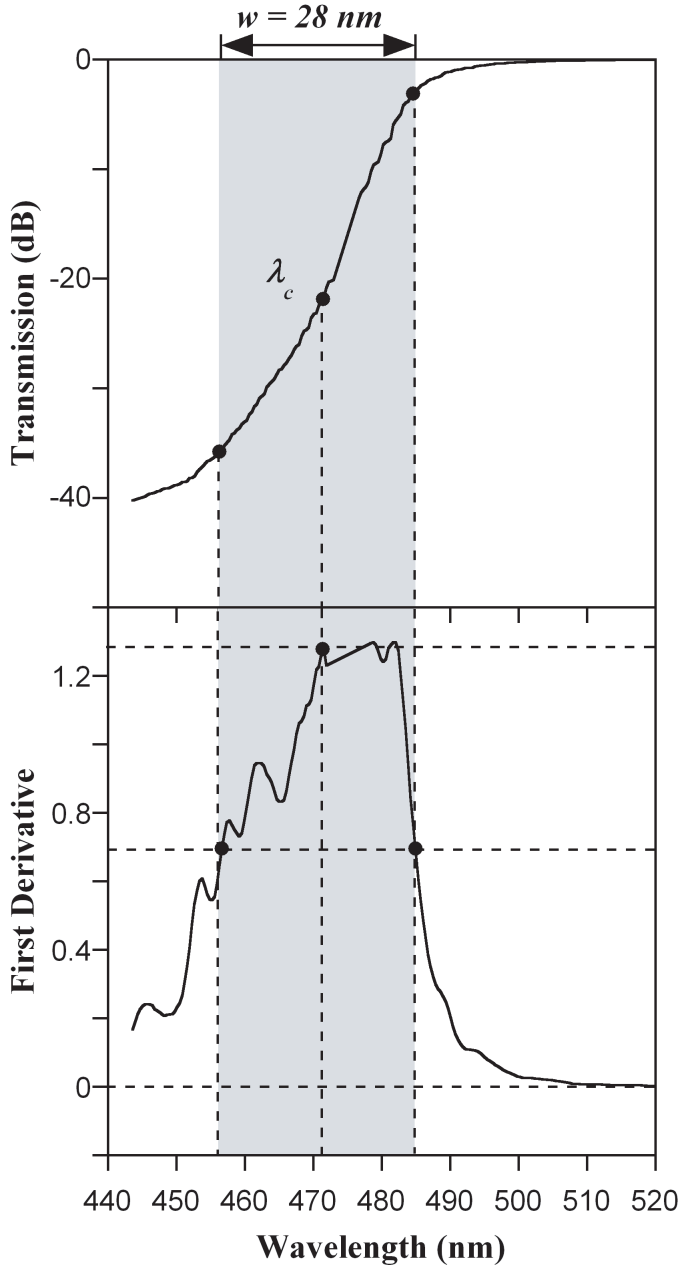

Figure 5.11: a) The transmission spectrum of a 1 μm thick CdS film. The solid circles and shaded region indicate the absorption edge width w and cut-off wavelength λ_c. b) The application of the FWHM technique to the first derivative of the transmission spectrum (in dB).

transmission is less than a specified arbitrary value, such as -20 or -40 dB. However, these definitions are problematic for optical filter transmission spectra, which do not have the ideal characteristics illustrated for a long-pass filter by the dashed line in Figure 5.1, and which do not have specified roll-off slopes but varying slopes that we wish to characterize.

We propose an algorithm that determines the absorption edge and the absorption edge width from measured data. The technique extends to all types of optical filters. The absorption edge λ_c is specified as the wavelength at which the first derivative of the transmission spectrum is maximized. The absorption edge width is specified as the full width at half maximum (FWHM) of the first derivative. Thus, the lower and upper limits of the absorption edge width, λ_s and λ_p , are the wavelengths on either side of λ_c at which the first derivative is half of its maximal value (in dB). These definitions are illustrated in Figure 5.11 and Figure 5.12, in which these procedures have been applied to data from absorption and interference filters. The definitions of absorption edge λ_c , absorption edge width w, and transmission and rejection levels T_{pb} and T_{sb} are described by the following equations.

$$\lambda_c \equiv arg_\lambda max \frac{dT(\lambda)}{d\lambda} \tag{5.4}$$

$$\frac{dT(\lambda_s)}{d\lambda} \equiv \frac{1}{2} max_\lambda \frac{dT(\lambda)}{d\lambda}, \quad \lambda < \lambda_c \tag{5.5}$$

$$\frac{dT(\lambda_p)}{d\lambda} \equiv \frac{1}{2} max_\lambda \frac{dT(\lambda)}{d\lambda}, \quad \lambda > \lambda_c \tag{5.6}$$

$$w \equiv \lambda_p - \lambda_s \tag{5.7}$$

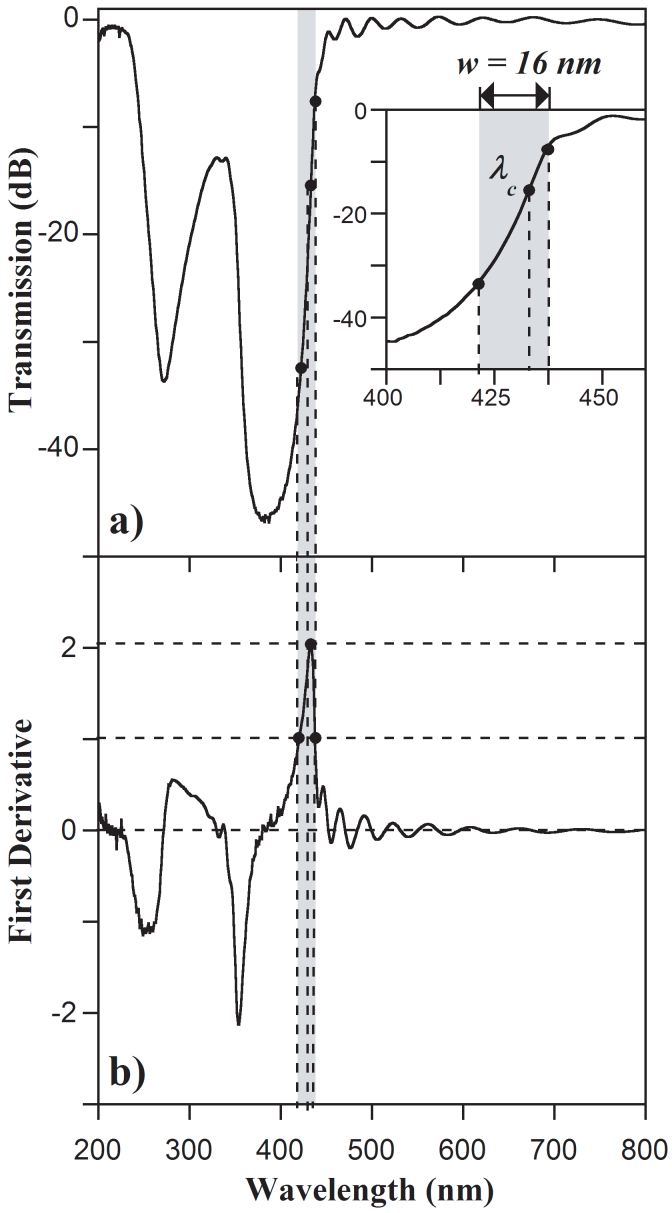

Figure 5.12: a) The transmission spectrum of a 1.2 μm-thick interference filter. The solid circles and shaded region indicate the absorption edge width w (shaded region) and cut-off wavelength λ_c. The inset shows a finer view of λ_c and w. b) The application of the FWHM technique to the first derivative of the transmission spectrum (in dB).

$$T_{sb} \equiv T(\lambda_s) \tag{5.8}$$

$$T_{pb} \equiv T(\lambda_p) \tag{5.9}$$

However, these computations are problematic when the curve is not smooth. Under these circumstances it may be necessary to apply a smoothing operation to the data prior to computing the derivative. For example, a 5-point smoothing average was performed on the transmission data shown in Figure 5.11. Smoothing should be kept to a minimum, since it artificially broadens the spectrum.

If the system has multiple filtering stages (i.e. from packaging materials such as PDMS), their individual as well as cumulative responsivities should ideally be provided. Note that $H_{filter}(\lambda)$ may be somewhat different for the excitation and fluorescent light, since the they travel through different optical paths in the system. For example, sometimes a spectral filter is placed in the excitation light path in order to restrict the spectral bandwidth of the excitation light, so that this filter is included in H_{filter} for the excitation light, but this additional filter is irrelevant for the fluorescent light because it is not positioned between the sample and the detector. After the sample, the spectral filtering is identical for both.

5.8.2.1 Absorption Filter Spectra

For absorption filters, it is difficult to specify the absorption edge location and width from absorption coefficient spectra (Figure 5.5). Absorption coefficients typically decrease monotonically as the wavelength increases, never reaching zero and with variations in the slope. This is true for the spectrum of CdS (Figure 5.5a), to

which the proposed algorithm is applied in Figure 5.11 (computed from the absorption coefficient spectrum using the Beer-Lambert law for a hypothetical 1 μm film). The top panel shows the transmission spectrum alongside computed locations of the edge and edge width, and the bottom panel shows the first derivative from which these metrics were obtained. The wavelength at which the first maximum occurs in the first derivative is the absorption edge λ_c. The half-maximum wavelengths define the boundaries, and thus the width, of the absorption edge.

5.8.2.2 Interference Filter Spectra

Interference filters often have large ripples in the transmission band (Figure 5.2), with peak-to-peak ripple heights that can be tens of percent. The ripple positions are highly sensitive to fabrication variations, so using absolute criteria such as magnitude (i.e., -3 dB) to define absorption edge location and width might arbitrarily shift these values by tens of nm. In Figure 5.12, our suggested algorithm has been applied to the transmission spectrum for a 1.2 μm silicon nitride/silicon dioxide interference filter.

Thus far the absorption edge has been specified by a single wavelength for one stopband-passband pair, but interference filters or micromachined fluorescence sensors for multi-wavelength spectroscopy would have several absorption edge locations. In this case the definition of absorption edge and absorption edge width may be extended to describe the multiple wavelengths and widths w_1, w_2, w_3,... associated with the stopbands and passbands of the system. These wavelengths may be speci-

fied using the same algorithm, applied in different spectral bands to capture all the absorption edges and absorption widths of the system.

5.8.2.3 Single Number Metrics

Using the proposed technique, passbands and stopbands can be explicitly determined. Therefore we suggest that the following single-number metrics be reported for the filter if the entire transmission spectrum cannot be obtained: 1) the rejection in the stopband at λ_{ex},

$$T_{sb} = 10 \log_{10} \left(\frac{I(\lambda_{ex})}{I_0(\lambda_{ex}} \right) \tag{5.10}$$

and 2) the transmission in the passband at λ_{pb}, T_{pb}, defined analogously. Although this will not allow comparison of the filter with those in other systems, it will give an indication of the effectiveness of the filter with a particular fluorophore.

In addition to providing the ability to easily determine the filter metrics, the FWHM method also provides the capability to quantitatively compare the absorption edges of different systems. We define the attenuation factor $\gamma(dBnm^{-1})$associated with an absorption edge as the measure of the rate of change of transmission at that edge. This metric is computed by dividing the change in transmission across the transition between passband and stopband by the absorption edge width.

$$\gamma = \frac{T_{sb} - T_{pb}}{w} \tag{5.11}$$

For example, the attenuation factor of the interference filter in Figure 5.12 is $\gamma = 1.6$ dB/nm, whereas the attenuation factor for the CdS filter in Figure 5.11 is $\gamma = 1.1$ dB/nm. Although this metric does not offer any insights on the absolute rejection and transmission levels around that edge, it does allow the designer to determine the relative rejection and transmission levels near the edge. This is particularly important when designing systems to detect emissions from fluorophores having small Stokes? shifts. Note that the attenuation factor γ as defined above (in $dB\ nm^{-1}$) is distinct from the transmission loss (typically expressed in $dB\ cm^{-1}$). Although the units are similar, the former quantifies the steepness of an optical filter's absorption edge whereas the latter is commonly used to denote the magnitude of transmission across material of a given thickness.

5.8.3 Optical Path Filtering: Coupling Efficiency

The optical part of the fluorescence sensor also requires metrics equivalent to transmission, rejection, and absorption edge location and width, since the prevalent SNR metric not only incorporates the detector performance, but also the brightness of the sample, and is thus an extrinsic rather than intrinsic quantity.

The optical path of the sensor system includes the placement of the detector relative to the light source, free-space optical elements such as lenses, and light-guiding components. For these, metrics such as λ_c and w may be ambiguous. Instead, the optimal wavelength for the device should be provided together with the range of usable wavelengths.

Ideally, curves showing the fraction of light falling on the detector as a function of wavelength should be provided for both the excitation light source and the fluorescent probes. This may be difficult in practice. In order to quantify the collection efficiency, we adapt the notion of *coupling efficiency* (CE), which is widely used in fiber optics to denote the efficiency of power transfer between two optical components. We quantify geometrical effects on collection efficiency by defining coupling efficiency as the fraction of light that is able to impinge on the detector area. This analysis should be performed for the excitation light source in order to quantify the degree to which the photodetector is shielded from excitation light and for light emitted by the fluorophores in order to quantify what fraction of the emitted fluorescence is able to fall upon the photodetector. The CE can be employed as a design tool to maximize collection of emitted fluorescence and to minimize collection of excitation light.

For the optical path filtering, the transfer efficiency in dB is given by

$$H_{geometry,ex}(\lambda) = 10 \log_{10} [CE_{ex}(\lambda)] \tag{5.12}$$

$$H_{geometry,em}(\lambda) = 10 \log_{10} [CE_{em}(\lambda)] \tag{5.13}$$

for the excitation light and fluorescent emissions, respectively. Ideally, the CE should be given as a function of wavelength, but if this is not possible the CE should be determined for the excitation and peak fluorophore emission wavelengths. Note that the optical path filtering is inherently different for excitation light and fluorescent light, since the two sources of light travel through different optical paths

in the system.

5.8.3.1 CE for Fluorescence Light

For emitted fluorescence, the system geometry factor quantifies geometrical effects on collection efficiency that result from differences in the fraction of the total solid angle received by the detector. Typically fluorescence is emitted isotropically, so the solid angle of emission is 4π. The maximum solid angle subtended by a planar detector is 2π, which occurs for the special case of a detector that is large and in direct contact with the sample. Design constraints might not allow positioning of the detector in such proximity, and in many cases the solid angle subtended by the detector is significantly less than 2π.

If the system has lenses to collect or redirect the light, as in Figure 5.4, their effects should be included in the CE. In the case of collection, focusing increases the amount of fluorescent light impinging on the detector, so the CE is greater than that for the detector alone. For the ideal case of a lens that focuses all the light falling on it onto the detector, the solid angle subtended by the lens may be taken as the effective detector area. (It may be possible to collect emissions from more than 2π of the total solid angle using reflective surfaces, but this has not yet been demonstrated for a micro-fluorometer.)

The CE can be determined for any system geometry. For generality, we define a function Q which represents the relative light intensity as a function of the angular spherical coordinates θ and ϕ. The function Q is normalized so that

$$\int_0^{2\pi}\int_0^{\pi} 2\,Q(\theta,\phi,\lambda)\,\sin\phi d\phi d\theta = 4\pi \tag{5.14}$$

For the special case of a fluorescent point source with isotropic emission, the fluorescence intensity is constant: $Q(\theta,\phi,\lambda) = 1$.

The fluorescence CE is the ratio between the fluorescent photons impinging on the detector and the total number of fluorescent photons emitted, given by:

$$CE_{em} = \frac{\oint_{\Omega_d} Q(\theta,\phi,\lambda)\sin\phi d\phi d\theta}{4\pi} \tag{5.15}$$

where Ω_d is the solid angle subtended by the detector.

Determining the fluorescence CE is straightforward for fluorescent point sources with circular or square detectors (Figure 5.13), which are the most commonly used. For an ideal circular detector centered at $\phi = 0$, the polar angle α subtended by the detector is related to the detector diameter a and distance d to the fluorophores via a trigonometric relation:

$$\alpha = 2\cos^{-1}\left(\frac{d}{\sqrt{\frac{a^2}{4}+d^2}}\right) \tag{5.16}$$

The solid angle subtended by the detector is then given by:

$$\int_0^{2\pi}\int_0^{\frac{\alpha}{2}} \sin\phi d\phi d\theta = 2\pi\left[1-\cos\left(\frac{\alpha}{2}\right)\right] = 2\pi\left[\frac{\sqrt{\frac{a^2}{4}+d^2}-d}{\sqrt{\frac{a^2}{4}+d^2}}\right] \tag{5.17}$$

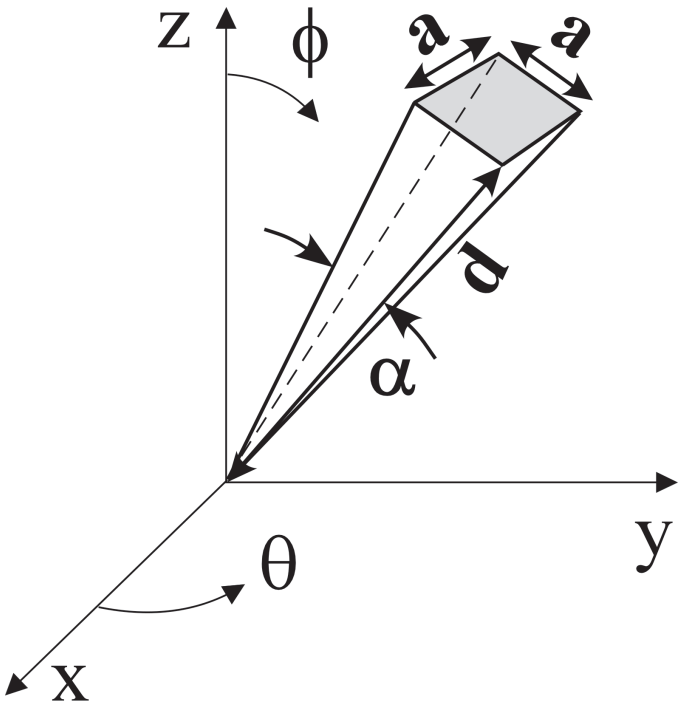

Figure 5.13: Solid angle α for emission from a fluorophore located at the origin and intercepting a square detector a distance d away with an area as indicated by the gray shading.

The fluorescence CE for this detector is thus:

$$CE_{em} = \frac{1 - \cos\left(\frac{\alpha}{2}\right)}{2} = \frac{\sqrt{\frac{a^2}{4} + d^2} - d}{2\sqrt{\frac{a^2}{4} + d^2}} \tag{5.18}$$

This function exhibits the expected asymptotic behavior, since:

$$\lim_{\alpha \to \infty} CE_{em} \to \frac{1}{2} \tag{5.19}$$

and,

$$\lim_{d\to 0} CE_{em} \to \frac{1}{2}. \tag{5.20}$$

Likewise, the fluorescence CE for an ideal square detector centered at $R = d$, $\phi = 0$ with side length a is:

$$CE_{em} = \frac{\alpha}{2\pi}\sin\left(\frac{\alpha}{2}\right) = \frac{a}{2\pi\sqrt{\frac{a^2}{4}+d^2}}\cos^{-1}\left(\frac{d}{\sqrt{\frac{a^2}{4}+d^2}}\right) \tag{5.21}$$

This function exhibits the same asymptotic behavior.

The fluorescence CE can just as readily be calculated for more complex geometries. For the case of an annular detector (such as in Figure 5.4), the CE is found by subtracting the CEs of two circular detectors with radii equal to the inner and outer diameters of the ring.

5.8.3.2 CE for Excitation Light

For excitation light, the coupling efficiency quantifies geometrical effects on rejection that result from differences in the fraction of excitation light that reaches the detector. For the excitation light, the function Q (Equation 5.14) would be replaced by the emission intensity I, which would not generally be isotropic but would depend on position (excitation light is usually directional) and wavelength.

The excitation CE is the ratio between the excitation photons reaching the detector and the total number of photons from the excitation source, given by:

$$CE_{em} = \frac{\oint_{\Omega_d} I(\rho, \theta, z, \lambda)\rho d\rho d\theta dz}{\oint_{\Omega_{4\pi}} I(\rho, \theta, z, \lambda)\rho d\rho d\theta dz} \tag{5.22}$$

where Ω_d is the solid angle subtended by the detector, is the total solid angle, and the excitation intensity is defined in cylindrical coordinates due to its directionality.

Most lasers emit beams that have a Gaussian profile. A Gaussian beam has a time-averaged intensity given by

$$I(\rho, z) = I_0 \left(\frac{w_0}{w(z)}\right)^2 \exp\left(\frac{-2\rho^2}{w^2(z)}\right) \tag{5.23}$$

where ρ and z denote the axial and radial location of the detector in polar coordinates, $w(z) = w_0\sqrt{1 + \left(\frac{z}{z_0}\right)^2}$ is the beam width, and w_0 is the radius of the beam waist which occurs at $z = 0$ [195]. For an ideal circular detector of diameter a positioned at the center of a Gaussian beam, this leads to a CE_{ex} of:

$$CE_{ex} = 1 - \exp\left[\frac{-a^2}{2w^2(z)}\right] \tag{5.24}$$

This function exhibits the expected asymptotic behavior, since

$$\lim_{a\to\infty} CE_{ex} \to 1, \tag{5.25}$$

and

$$\lim_{z\to\infty} CE_{ex} \to 0. \tag{5.26}$$

Similarly, the CE_{ex} for an ideal square detector of diameter a positioned at the center of a Gaussian beam is:

$$CE_{ex}(\lambda) = erf\left(\frac{a}{\sqrt{2}w(z)}\right)^2 \tag{5.27}$$

Again, this function exhibits the expected asymptotic behavior.

5.8.4 Optical Path Losses

In real optical systems, additional losses will play a role in determining overall system performance. In a full description of the optical path of the system, absorption and scattering would have to be taken into account, as would focusing and numerical aperture effects. For example, two types of scattering commonly occur for the excitation light: large angle scattering due to side wall roughness of a waveguide

and small angle scattering due to interaction of the excitation light with the sample itself [105]. Both can result in unwanted excitation light falling on the detector. Also, the intensity of the fluorescence light will be attenuated as it is scattered and absorbed by materials within the system before it reaches the detector. Numerical aperture comes into play because when light exits a waveguide, it expands in the lower index of refraction medium, which would most typically be air or water. This may reduce the amount of light reaching the sample, which will reduce the excitation light as well as fluorescent light hitting the detector. These effects are difficult to model accurately, so H_{loss} will usually be determined experimentally, and will represent a correction to the other components of the composite transfer efficiency and overall system responsivity as given in Equation 5.1.

For optical path losses, the transfer efficiencies in dB are given by

$$H_{loss,\,ex}\,(\lambda) = 10\log_{10}\left[\frac{I_{ex}(\lambda)}{I_{ideal,\,ex}(\lambda)}\right] \tag{5.28}$$

for the excitation light and

$$H_{loss,\,em}\,(\lambda) = 10\log_{10}\left[\frac{I_{em}(\lambda)}{I_{ideal,\,em}(\lambda)}\right] \tag{5.29}$$

for the fluorescent emissions. Ideally, $H_{loss,\,ex}$ and $H_{loss,\,em}$ should be given as a function of wavelength, but if this is not possible then they should be determined for the peak excitation and emission wavelengths of the fluorophore. Note that the

optical path losses are inherently different for excitation and fluorescent light, since the two may travel through different optical paths in the system. The optical losses are expected to increase transmission in the stopband and decrease transmission in the passband, reducing the overall sensitivity of the fluorescence measurement.

5.8.5 Minimal System Metrics and Calibration

It is clear from the preceding discussion that the overall performance of a micro-fluorometer depends on many factors. For fair comparison of widely disparate approaches, it is necessary to quantify the effects of each of these factors separately, as functions of wavelength and intensity. However, it may not be practical or possible to carry out such exhaustive analysis and empirical characterization.

A minimal set of system metrics that should be reported if it is impossible to obtain the metrics described above are $R_{system,mx}(\lambda_{em})$, $R_{system,\,ex}(\lambda_{ex})$, and $\sigma_{detector}$ (see Section 5.8.1) as functions of incident intensity Γ. $R_{system,\,ex}(\lambda_{ex})$ represents the overall system response to light at the excitation wavelength, with the input optical intensity determined at the input to the micro-fluorometer (or at the light source if the light source is part of the micro-fluorometer). The reference location for calibration of excitation intensity is therefore at the input to the system. The input intensity can be determined by placing a reference optical detector, which has been calibrated at the excitation wavelength, at the same position with respect to the light source as the micro-fluorometer. (This may not be feasible in the case of an integrated light source, in which case a free-standing version of the same

light source should be used.) The distance from the light source to the calibrated detector should be the same as in the standard measurement configuration, and the optically sensitive area of the reference detector should be matched to the optically sensitive area of the micro-fluorometer (or the measured intensity should be adjusted to account for any differences). The intensity of the light source should be adjusted using neutral density filters rather than electronic controls, as described above.

$R_{system,\,em}(\lambda_{em})$ represents the overall system response to light at the peak emission wavelength, with the input optical intensity being the fluorescence intensity. (Note this system metric includes the effects of all the component metrics, such as the fluorescence CE.) Fluorescence intensity depends on the absorbance and quantum yield of the fluorophore as well as the intensity of the excitation light, and absorbance, in turn, depends on the molar extinction coefficient and concentration of the fluorophore as well as the optical path length through the sample. For dilute solutions and low excitation intensities, fluorescence intensity is proportional to each of these parameters. At higher concentrations and intensities, the relationship becomes nonlinear due to effects such as self-absorption, quenching, and photobleaching. Both the molar extinction coefficient and the quantum yield are sensitive to environmental conditions.

The reference location for calibration of fluorescence intensity is inside the sample chamber. The purpose is to calibrate what the detector reads in response to a particular fluorescence intensity. There are three alternative strategies for calibration of the intensity: calibration from the input of the system to the sample chamber, or calibration from the sample chamber to the output of the system,

and use of a calibrated fluorophore. The choice of which method to use depends primarily on the relative difficulty of modifying the micro-fluorometer for the desired measurement.

The first method is useful for any micro-fluorometer. A reference light source with calibrated intensity at the peak emission wavelength is placed at the same position with respect to the detector as the sample chamber, and the output of the detector is monitored. This may be accomplished by modifying a representative micro-fluorometer so that the reference light source can be placed in the appropriate location (i.e., in the sample chamber).

The second method requires two measurements, which are combined to calibrate the intensity. The first measurement is the responsivity of the detector alone for a reference light source at the emission wavelength, with the intensity calibrated at the detector. The other measurement is the transfer efficiency of the micro-fluorometer between specific locations within the system. A calibrated light source at the peak emission wavelength is applied at the input to the system. The intensity is measured, using a reference optical detector that has been calibrated at the emission wavelength, at two places: with the detector in its usual position, and with the detector placed at the same position with respect to the light source as the sample chamber. This may be accomplished by modifying the micro-fluorometer so that the reference detector can be placed in the appropriate location (i.e., in the sample chamber). Dividing the source-detector responsivity by the source-chamber responsivity gives the transfer efficiency between chamber and detector, then multiplying the detector responsivity by this chamber-detector transfer efficiency accounts for

losses in the optical path between the sample chamber and the detector.

Finally, a third option for calibrating the fluorescence intensity is the use of a calibrated fluorophore solution. The National Institute of Standards and Technology has developed a method to quantify fluorescence radiance in terms of *molecules of equivalent soluble fluorophores* (MESF). NIST provides a standard reference solution (SRM 1932) of fluorescein with well-controlled pH and concentration for quantification of fluorescence intensity. Unfortunately, the technique has been developed only for fluorescein, so assays with other fluorophores require reference solutions to be prepared in-house. For details on the MESF quantification of fluorescence, refer to [196, 197]. There are, however, several difficulties with this method. First, the *fluorescence quantum yield*, which is the number of fluorescence photons emitted per incident excitation photon, varies significantly with changes in the microenvironment, so great care must be taken to ensure that the pH and temperature of the reference solution are matched to the system under test. Second, it is well known that the quantum yield of a fluorophore varies, depending on whether it is dissolved in solution, immobilized on a surface, or conjugated to a biological specimen.

5.9 Conclusions

A wide variety of spectral discrimination schemes have been demonstrated, but none has been established as a paradigm for miniaturized fluorescence sensors. This is a consequence of the trade-offs between performance and complexity. For more demanding applications in which the fluorescence signal is weak, some increase in

complexity is inevitable since none of the current technologies can be used alone; a combination of methods will be required to increase sensitivity while also achieving strong rejection of the excitation light.

The micro-scale fluorometers that have been demonstrated to date work well with high brightness samples. The challenge for the next generation of devices is improving the sensitivity so that these systems can accomplish low-light tasks such as single-molecule detection. This will require more attention to the filter performance than has been paid so far, including device design and fabrication details, as well as the measurement of the metrics achieved by the various device components. Without such metrics, it is impossible to compare the widely disparate approaches in order to improve overall system design and performance.

Collection efficiency also needs to be considered if detection of single molecules is to be achieved in μTAS. The issue of collecting more of the fluorescent light using optical elements has not yet been addressed. Furthermore, no systems have been made that focus the totality of the emitted light onto the detector to increase the signal strength.

Although it can be argued that monolithic integration of all the components is desirable for achieving the highest reliability and smallest size, it is usually not possible and may come with too high a cost in terms of fabrication complexity, individual component performance, and system design constraints. As can be seen from this review, none of the reported devices has integrated light source, detector, and microfluidics all on one substrate. Some of the devices integrated the microfluidics, filter, and detector, but could not integrate the light source due to

the device configuration [109, 114, 115]. Alternatively, the light source, filter, and detector were integrated, and the microfluidics were placed off-chip [106]. The latter configuration allows the device to be reused by simply replacing the microfluidic network. In addition, using a ray-optics based microsystem with no integrated light source [178, 180–182] offers versatility: the system is not constrained to any particular light source and can therefore be used with any fluorophore. Integration choices will thus continue to be influenced by the intended device application.

Chapter 6

Polymer Filters for Integrated Fluorescence Sensing†

Optical filters for blocking ultraviolet (UV) light were fabricated by doping various polymer hosts with a UV absorbing chromophore. The polymers were polydimethylsiloxane (PDMS), a silicone elastomer frequently used in microfluidics, SU-8, a photopatternable epoxy, and Humiseal 1B66, an acrylic coating used for moisture protection of integrated circuits. The chromophore was 2-(2'-hydroxy-5'-methylphenyl) benzotriazole (BTA), which has a high extinction coefficient between 300 nm and 400 nm. We demonstrate filters 5 μm thick that exhibit high ultraviolet rejection (nearly -40 dB at 342 nm) yet pass visible light (near 0 dB above 400 nm), making them ideal for ultraviolet-excited fluorescence sensing within microsystems. Unexpectedly, the absorbance of the BTA depended on the host polymer. These filters are promising for integrated fluorescence spectroscopy in bioanalytical platforms because they can be patterned by dry etching, molding, or exposure to ultraviolet light.

6.1 Introduction

Researchers are attempting to harness the benefits of fluorescence-based analyses in micro-scale total analysis systems (μTAS). Integrated (i.e. on-chip) flu-

†Manuscript in preparation for submission to the *Journal of Micromechancis & Microengineering* as: **M. Dandin**, P. Abshire, E. Smela, "Polymer Filters for Ultraviolet-Excited Integrated Fluorescence Sensing", 2012.

orescence sensing [11, 21, 22], combined with existing μTAS technologies such as microfluidics [198] and capillary electrophoresis [115], could lead to compact devices capable of performing complex biochemical assays.

There are, however, challenges in achieving integrated fluorescence sensing. One of these is improving the performance of microscale filters for separating the fluorescence from the excitation light [54] (thus improving the fluorescence-to-background ratio). In macro-scale spectrometers, optical filtering is achieved with the aid of free-space optical elements having relatively long pathlengths (on the order of cm). However, the integration of detectors, analysis chambers, and optical filters in close proximity for μTAS leads to inherently short optical paths (μm - mm), which presents difficulties for optical filtering [54].

Several on-chip filtering approaches have been demonstrated, as reviewed in our previous publication [54]. They include thin film interference filtering [109,199], absorption filtering [106,163,199], spectrally selective detectors [169,170], microfabricated optical elements [178,180], waveguides [200,201], and optical fibers [70,183]. Nevertheless, none of these approaches has been established as a paradigm for microscale fluorescence spectrometers. Rather, the choice of filtering technology depends on the application for which the device is intended and its overall architecture.

For sensors having an isotropic, off-chip excitation source, absorption filters are preferable because they exhibit no angular dependence in their transfer efficiency (log of the ratio of the output to the input intensity). In this paper, we demonstrate the implementation of absorption filters using dye-doped polymer films. The doping of polymer matrices with light-absorbing molecules (chromophores) is par-

ticularly attractive for integrated devices [202] since performance can be optimized by changing the dopant concentration without increasing the filters thickness, a key advantage that allows the placement of fluorescently-labeled samples close to the detectors' active area without compromising the ability to reject the excitation light.

Chromophore-doped polymer films have previously been demonstrated in integrated fluorescence spectroscopy [21–24] and other applications [25–30]. There are two original contributions in the work reported here. First, the filters were specifically designed for ultraviolet (UV) excited fluorescence in μTAS, and the filters exhibit high rejection (-43 dB at 342 nm) in films as thin as 5 μm. Second, several microfabrication procedures for patterning the filters were developed, and they were based on standard photolithographic and dry subtractive processes, thus allowing selective placement over solid state detector arrays.

6.2 Filter Fabrication & Patterning

6.2.1 Materials

The chromophore was 2-(2-hydroxy-5-methylphenyl) benzotriazole (BTA), obtained in powder form (Great Lakes Chemical Corporation). BTA (Figure 6.1) belongs to the family of 2-hydroxybenzotriazoles [203], whose main use has been for protecting polymers from degradation due to UV radiation. Host materials were SU-8 (Microchem Corp.), a negative photosensitive epoxy, 1B66 (Humiseal), a polymerized acrylic diluted in methyl-ethyl ketone and toluene, and PDMS (Sylgard

184), a silicone elastomer.

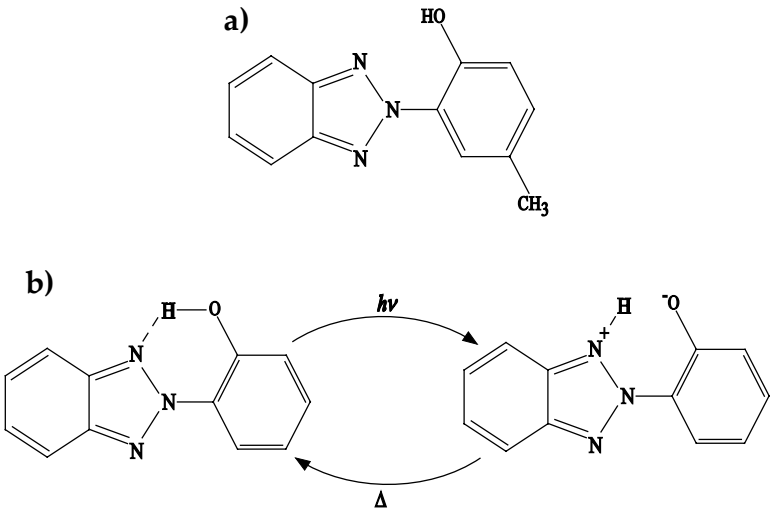

Figure 6.1: a) Molecular structure of 2-(2-hydroxy-5-methylphenyl) benzotriazole. b) UV absorption mechanism. [203].

6.2.2 Fabrication Procedures

Doping was carried out by manually mixing aliquots of a solution of BTA dissolved in toluene into the pre-polymer resins. For 1B66 and PDMS-based composites, air bubbles introduced by the mixing were removed by spinning the mixture in a centrifuge. For SU-8-BTA composites, a 50°C ultrasonic bath was instead used to remove the air bubbles; exposure to ultrasonic energy was more effective because of the SU-8's higher viscosity.

6.2.2.1 PDMS-BTA Filters

Curing

The PDMS hardening agent was manually mixed in a 1:10 ratio with the BTA-loaded

pre-polymer. The composites were cast in Petri dishes and cured in a convection oven for 3 hours at 75°C.

Patterning

The viscosity of the PDMS-BTA pre-polymer was not significantly different from that of undoped PDMS, and the composite was patterned by casting and curing it over a mold. Alternatively, PDMS may be patterned using a combination of wet and dry etching utilizing a hard etch mask [204], and this technique is also expected to work for the composites, although it was not tested.

6.2.2.2 1B66-BTA Filters

Curing

1B66 is a polymer dissolved in a solvent that is cured simply by driving off the solvent. This was done either by placing the composites at 95°C for two hours in a convection oven or by placing them in a well-ventilated area at room temperature for over 24 hours.

Patterning

The 1B66-BTA films were patterned by reactive ion etching (RIE) (150 mT, 100 sccm O_2, 75 W). Two different masking materials were used: thick positive photoresist (Shipley SPR 220 7.0, Figure 6.3b for a 1B31-BTA composite[1]) and resistively evaporated aluminum (not shown). The masking materials were photolithographically patterned. The etch mask was removed with either photoresist stripper (Nano

[1]1B31 and 1B66 have the same chemical formulation. However, 1B31 contains an optical brightener that causes increased background emission in the BTA passband. Filters of this type were not reported in this work, but the same patterning procedures were also applied to 1B66-based composites and produced the same results shown in Figure 6.3b.

PG, Microchem Corp.) or aluminum etchant (CH3COOH:HNO3:H3PO4, 20:3:77, room temperature [159])).

6.2.2.3 SU-8-BTA Filters

Pre-Exposure Thermal Cycle

Prior to exposure, the BTA-doped SU-8 films were soft-baked at 65°C for 25 minutes on a contact hotplate. The temperature was then ramped to 95°C at a rate of 300°C/hr, and the sample was held for 30 minutes at the final temperature. The sample was brought back to room temperature at a rate of 300°C/hr.

Photocuring

Although SU-8 shows a broad absorption spectrum below 400 nm (see Figure 6.4b)), curing is typically conducted utilizing the i-line wavelength of a mercury vapor lamp, i.e. 365 nm. This wavelength falls within the absorption band of BTA. This means that in SU-8-BTA composites, the endogenous chromophores in the resist that absorb UV energy and initiate photopolymerization receive less energy than required to cure the SU-8, particularly at high doping concentrations. Therefore, the exposure dose must be adjusted to compensate for the introduction of the dopant.

We have developed an analytical model for determining the exposure dose to cure an SU-8-BTA composite based on the film thickness and dopant concentration. This model can be generalized to other photosensitive matrices containing extrinsic light quenching chromophores, as long as the exposure dose for polymerizing the undoped pre-polymer and the molar extinction coefficient of the doping material

are known. The derivation of this model is given in Appendix B. The minimum exposure dose needed for polymerizing the composite is given by:

$$E_d^*(\delta) \geq E_u(\delta)e^{\alpha n_{SU8}\delta} = E_u(\delta)e^{\left(\frac{\epsilon_i c_{BTA}}{M}\right)n_{SU8}\delta} \tag{6.1}$$

where $E_d^*(\delta)$ is the energy required for curing a doped film of thickness δ, $E_u(\delta)$ is the energy required for curing an undoped film of that thickness, α is the absorption coefficient, ϵ_i is the i-line molecular extinction coefficient, c_{BTA} is the BTA concentration, M is the molecular weight of the dopant, and n_{SU8} is the refractive index of the SU-8. In the term at the right-hand side of the equal sign, the expressions in parentheses in the exponent is the macroscopic absorption coefficient expressed as a function of the physical properties of the species in the material that absorbs the incident radiation.

The i-line extinction coefficient ϵ_i was obtained experimentally (see Figure 6.2 inset) using the Beer-Lambert law for stock solutions of known concentration. The chromophore concentration was calculated using the molarity of the stock solution, the doping aliquot volume, and the pre-polymer volume (V_p). Each line in Figure 6.2 represents the calculated dose-thickness relationship for a different c_{BTA} value, obtained by varying the aliquot volume used for doping a $10mL$ pre-polymer solution.

Post-Exposure Thermal Cycle

Following exposure, a second thermal cycle was performed. The films were heated

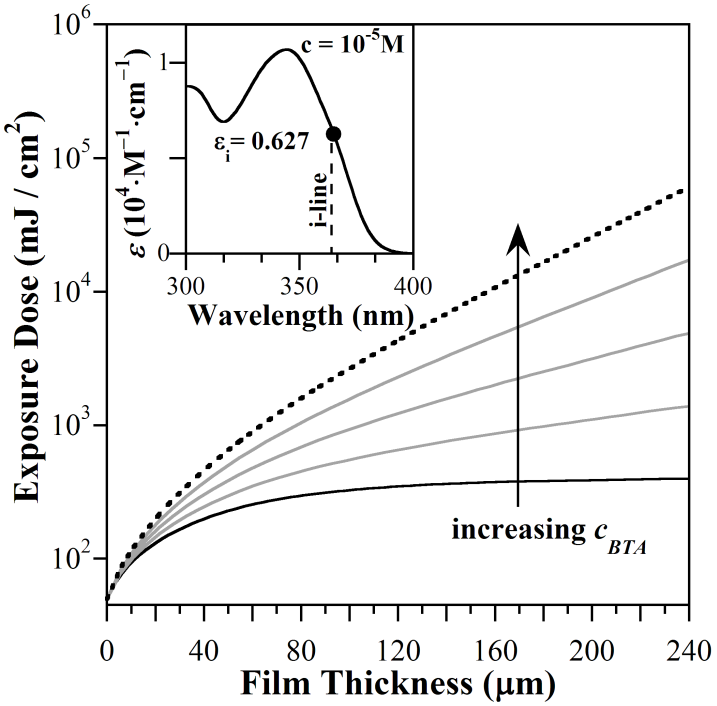

Figure 6.2: Adjusted exposure dose versus film thickness required for curing BTA-doped SU-8 films. The solid black line is the exposure dose curve for undoped SU-8, whereas the solid gray lines are for doped films (5 mM increments), and the dotted black line is the surface exposure dose for a 20 mM doping concentration. The inset shows the extinction coefficient of BTA as a function of wavelength in toluene obtained by averaging the spectra of five solutions at $c = 10^{-5}M$. The i-line ($\lambda = 365\,nm$) extinction coefficient is $\epsilon = 0.627 \times 10^4 M^{-1}cm^{-1}$.

on a hotplate at 65°C for 5 minutes, the temperature was ramped to 95°C at a rate of 200°C/hr, the samples were held at 90°C for 30 minutes, and the samples were cooled to room temperature at a rate of 100°C/hr.

Patterning

Filter patterning was achieved using a photolithographic mask during exposure followed by developing in SU-8 developer (Microchem Corp.) for up to 6 minutes with mild agitation. The samples were rinsed in isopropyl alcohol and dried under ni-

trogen. As shown in Figure 6.3d-f, pattern transfer was successful only when the optimum exposure dose (1442 mJ/cm^2 for a 20 mM doping concentration), as predicted by the model, was used. Figure 6.3c shows an undoped SU-8 film of the same thickness cured with the manufacturers recommended exposure dose.

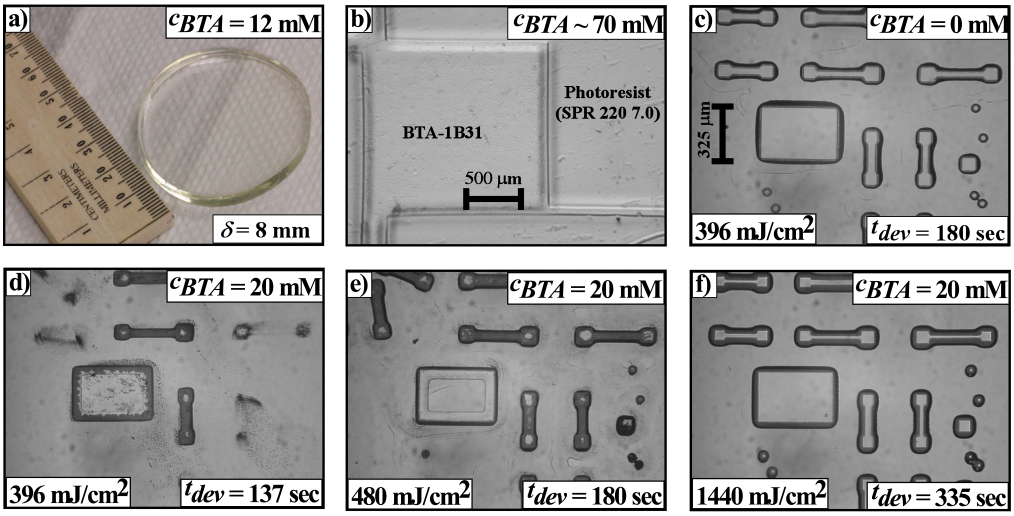

Figure 6.3: a) 8 mm-thick BTA-doped PDMS substrate fabricated by casting. b) Acrylic polymer (1B31) doped at c_{BTA} = 70 mM patterned with RIE and a photolithographically defined SPR 220 7.0 layer as an etch mask. c) Undoped SU-8 structures (75 μm thick) patterned on a silicon wafer using a transparency mask. d)-e) Unsuccessful development of 75 μm thick BTA-SU-8 structures (c_{BTA} = 20 mM) exposed at 396 mJ/cm^2 and 480 mJ/cm^2, respectively. f) Successful patterning utilizing an exposure dose prescribed by the photopolymerization model (Equation 6.1). model.

6.3 Optical Characterization

6.3.1 Chromophore and Host Transmission Spectra

The independent contributions of the chromophore and the host matrices to the overall transmission efficiency were evaluated. The transmission spectrum of the

chromophore as a function of loading concentration was obtained in a liquid matrix (toluene). The spectra of the undoped host matrices were obtained from films of these polymers, ranging in thickness from 5 μm to 1 mm, that were cured on glass substrates.

Transmission spectra were collected, in reference to air, using a Cary 5000 UV-Vis-NIR spectrophotometer (Varian). Scans were performed from 300 nm to 450 nm at 1 nm increments. The light source change-over point was 350 nm. The scan rate was 600 nm/min, and a 2 nm spectral bandwidth was used. The slit height was set to full. All spectra were baseline corrected to remove contribution from the substrate.

As Figure 6.4a shows, the transmission of UV wavelengths dropped significantly as the concentration of chromophore in the toluene increased. This is a direct result of the Beer-Lambert law. On the other hand, the host materials exhibited almost 0 dB transmission over the range of interest (Figure 6.4b) with the exception of SU-8, which showed significant rejection (approximately -20 dB at 310 nm) in a film only 30 μm thick (Figure 6.4b inset).

6.3.2 Filter Spectra

According to the Beer-Lambert law, there is a linear relationship between absorbance A and the concentration of the absorber c and the film thickness l,

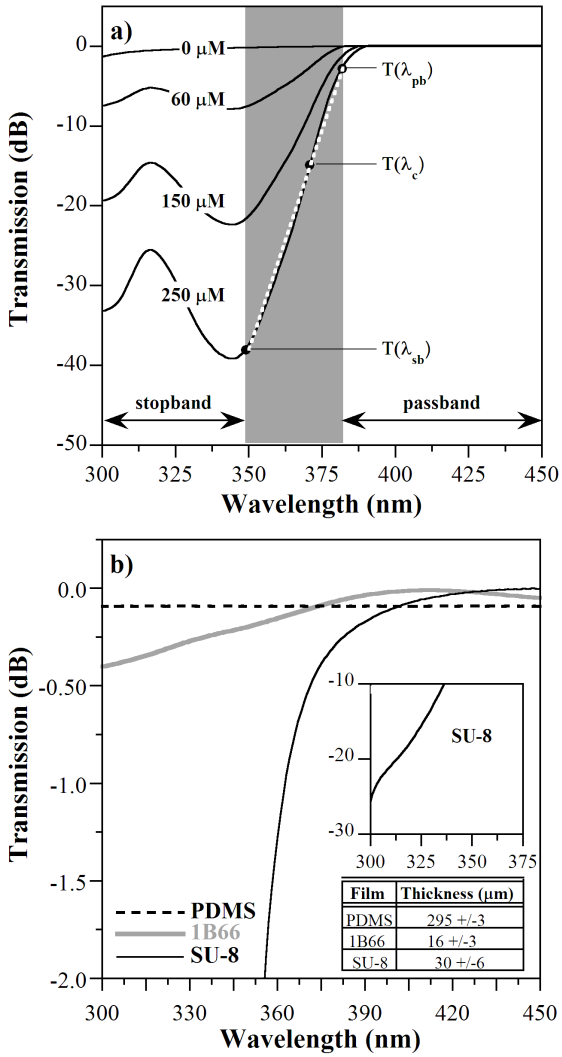

Figure 6.4: a) Transmission spectrum T(λ) of BTA dissolved in toluene measured at different loading concentrations across a 1 cm optical path length. The 0 μM spectrum is that of the solvent, and it was subtracted from the spectra of the loaded samples. The shaded region indicates, for high loading concentrations, the transition from stopband to passband. The dashed line illustrates a linear approximation of the filter transition; the points are defined in Section 6.3.3. b) Transmission spectra of the undoped host materials. (inset) Expanded view of the transmission of the same SU-8 film at the shorter wavelengths.

$$A = \epsilon(\lambda) \times l \times c = -\log\left(\frac{I}{I_0}\right) \tag{6.2}$$

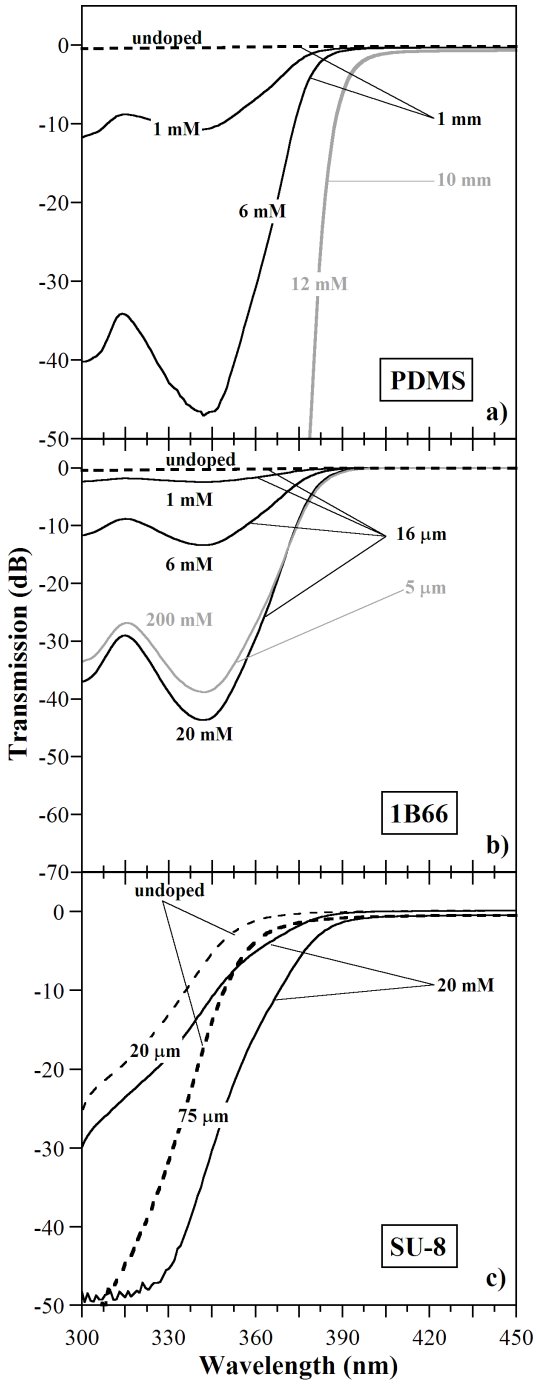

Figure 6.5: Transmission spectra of the polymer films and filters.

where λ is the wavelength, $\epsilon(\lambda)$ is the wavelength-dependent extinction coefficient, I_0 is the incident light intensity, and I is the intensity of the light exiting the film.

The measured transmission spectra of BTA-doped PDMS, 1B66, and SU-8 films are shown in Figure 6.5. The precursor solutions for these films were prepared by mixing aliquots of a doping solution into 10 mL of the pre-polymer. The doping solution was saturated with BTA at 250 mM in order to deliver the highest possible concentration in the aliquot, and the aliquot volume (and hence c_{BTA}) was held constant (800 μL). For PDMS and 1B66, the chromophore concentration (c_{BTA}) was varied by changing the number of aliquots loaded in the pre-polymer solutions. SU-8 was treated differently because adding solvent to the pre-polymer changed its flow properties, so the film thickness was varied instead of c_{BTA}. PDMS-based composites were cast into Petri dishes, while the doped 1B66 and SU-8 pre-polymers were spin-coated onto microscope cover slips.

Once the instruments lower limit of detection was reached (50 dB for the settings used in these measurements), further decreases in transmission in the stop-band could not be registered. These results show that thin films can have good filter performance if the dopant concentration is sufficiently high, and that high concentrations can be readily achieved. The spectra for SU-8 show that doping did, as expected, result in even greater absorption in the UV. (In order to confirm that the increase in rejection was caused by the BTA rather than the greater thickness, each filters transmission spectrum was compared to that of its undoped counterpart, which was an SU-8 layer mixed with 800 μL of toluene. Transmission efficiencies at

specific wavelengths for these films are reported in Table 6.1.)

6.3.3 Performance Metrics

We now evaluate the performance of the filters using a set of metrics that include the *stopband rejection*, *passband transmission*, *absorption edge*, *absorption edge width*, and *attenuation factor* [54]. Equations for computing these metrics using measured data are given below.

A filters *transfer efficiency*, denoted here as T(λ) [54], is equal to ten times the absorbance spectrum. The absorption edge or cut-on wavelength λ_c is the wavelength at which the transfer efficiency function transitions from stopband to passband. It is the wavelength at which the numerical derivative of the transfer efficiency is maximized:

$$\lambda_c \equiv arg\, max_\lambda \frac{dT(\lambda)}{d\lambda} \tag{6.3}$$

For filters with long-pass characteristics such as the ones featured in this paper, the derivative of the transmission efficiency yields a bell-shaped curve with a maximum occurring at λ_c. The absorption edge width w_c is found by subtracting the two wavelengths (λ_{pb} and λ_{sb}) on either side of λ_c at which the full-width half maximum (FWHM) points of the bell curve lie [54]:

$$w_c \equiv \lambda_{pb} - \lambda_{sb} \tag{6.4}$$

The stopband rejection (T_{sb} = T(λ_{sb})) and the passband transmission (T_{pb} = T(λ_{pb})) are used to compute the attenuation factor γ (in $dB\,nm^{-1}$), which is a measure of the sharpness of the transition. It is given by the rate of change of the transmission at the absorption edge:

$$\gamma \equiv \frac{T_{sb} - T_{pb}}{w_c} \tag{6.5}$$

Equations 6.3,6.4, and 6.5 are used to model a long-pass filters transfer efficiency as a linear function of wavelength with positive slope γ over the wavelength range λ_{pb} to λ_{sb}, and the cut-on wavelength λ_c is used to uniquely situate the filters' transition region. Table 6.1 summarizes these performance metrics computed for the filters reported in this paper.

As can be seen in Table 6.1, the absorption edges λ_c of the PDMS and 1B66 filters were located at λ_c = 370 nm, irrespective of doping concentration or film thickness. This is the same wavelength at which the spectrum of BTA transitions from stopband to passband (Figure 6.4a) because both host polymers have negligible UV attenuation. Thus, Equation 6.3 yielded the same cut-on wavelength for the filters as that of the chromophore, confirming that the UV rejection was due solely

Table 6.1 Performance of BTA-doped absorption filters.

	Thickness (μm)	c_{BTA} (mM)	λ_{sb} (nm)	$T_{sb}(\lambda_{sb})$ (dB)	λ_{pb} (nm)	$T_{pb}(\lambda_{pb})$ (dB)	λ_c (nm)	w_c (nm)	γ (dB/nm)
PDMS	10^3	0	N/A	N/A	N/A	N/A	N/A	N/A	N/A
		1	347	-10.20	379	-1.12	370	32	0.28
		6	347	-46.0	379	-3.95	370	32	1.31
1B66	16	0	N/A	N/A	N/A	N/A	N/A	N/A	N/A
		1	350	-2.21	380	-0.25	370	30	0.07
		6	349	-12.5	379	-1.37	370	30	0.37
		20	352	-38.3	382	-2.83	370	30	1.18
	5	200	352	-35.3	382	-3.88	370	30	1.05
SU-8	20	0	307	-21.7	352	-2.74	337	45	0.42
	20	20	318	-22.5	360	-5.10	340	42	0.42
	55	0	314	-33.0	353	-4.34	337	39	0.74
	55	20	314	-43.8	372	-5.46	340	58	0.66
	75	0	323	-38.6	353	-7.10	338	30	1.10
	75	20	330	-45.4	380	-3.64	346	50	0.84

to the addition of BTA.

This was not the case for the SU-8 filters, whose absorption edges were around 340 nm, close to that of undoped SU-8. This shows that the UV rejection was dominated by the hosts intrinsic chromophores, rather than by the extrinsic chro-

mophore, BTA. Furthermore, doping broadened the absorption edge widths w_c and consequently reduced the attenuation factors γ; this was more pronounced for thicker films. For assays that utilize fluorophores that have small Stokess shifts it is desirable to use a filter that has a small absorption width. In such a case, BTA should be loaded in in a photosensitive matrix that exhibits less intrinsic rejection than SU-8, such as, for example, a photopatternable formulation of PDMS [205].

For all the filters, rejection increased with dopant concentration and film thickness, as expected, allowing comparable rejection levels to be achieved with the different composites by adjusting these parameters. In Figure 6.6, the absorbance at 342 nm is plotted as a function of the product of the BTA concentration and the film thickness, $c_{BTA} \times l$, to show how the absorbance varied with these two parameters. The absorbance points were calculated from the measured transmission data (Figure 6.5)[2] Linear fits confirmed that the absorbance was linear with $c_{BTA} \times l$, as expected from Equation 6.2).

The slopes of the lines in Figure 6.6 give the extinction coefficient ϵ (units of $10^4 M^{-1} cm^{-1}$), which quantifies how well the materials absorb energy at 342 nm. Unexpectedly, ϵ differed for each host and differed from that of the BTA. This finding has important implications in filter design because it suggests an interaction between the BTA and the host that makes the BTA more (1B66) or less (PDMS) effective than it is in solution. The 1B66 data from samples 16 μm thick loaded with c_{BTA} between 0 and 20 mM had a different extinction coefficient than that from the 5 μm-thick film (asterisk-labeled) doped at 200 mM, indicating that this interaction

[2]The absorbance was computed using $A(\lambda) = -\frac{T_{dB}(\lambda)}{10}$, where $\lambda = 342\, nm$.

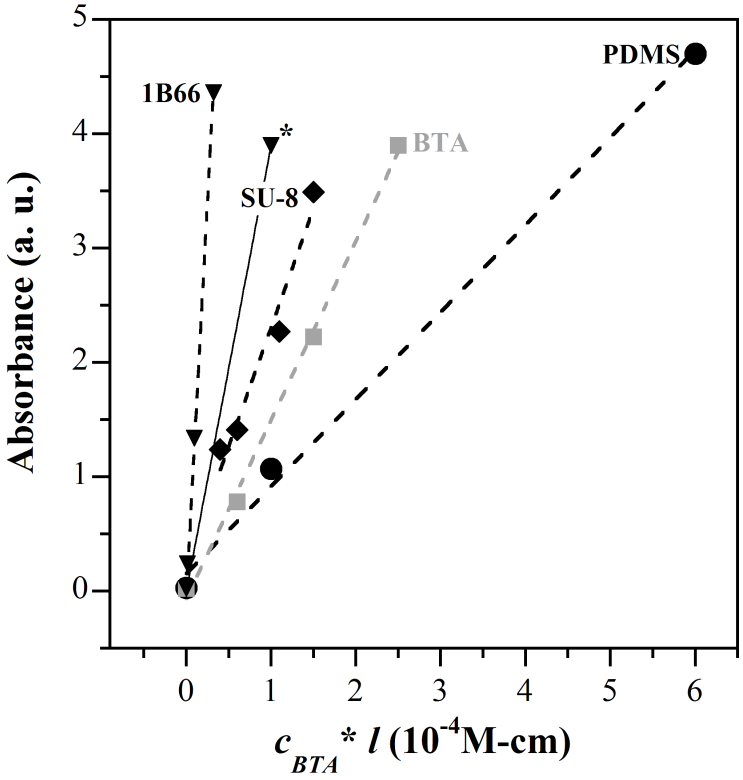

Figure 6.6: Measured absorbance at 342 nm as a function of the product of the BTA concentration and the film thickness, $c_{BTA} \times l$. During the measurements, one parameter was varied (either c_{BTA} or l) and the other held fixed. The gray squares are for BTA dissolved in toluene, and the asterisk-labeled data point is from a sample of different thickness (5 μ) than the other 1B66 samples (16 μ) . The dashed lines are linear fits, and the solid line is an extrapolation from the asterisk-labeled point to zero.

is doping level dependent.

6.3.4 Autofluorescence

Autofluorescence is the emission of light from fluorophores other than the ones of interest, and this background signal can overwhelm the desired fluorescent signal[3]. Some of the polymers used as host matrices in this work are known to autofluoresce

[3]Note that autofluorescence may also originate from microsystem components other than the filter, including the sample under study.

in specific regions of the electro-magnetic spectrum, so this issue must be considered.

To verify that the BTA dopant did not autofluoresce, its spectrum was recorded with a Cary 50 Eclipse fluorescence spectrophotometer (Varian Inc.). A toluene solution containing a high concentration of BTA was exposed to monochromatic light of wavelengths between 300 and 600 nm, and no signal above the instrument's noise floor was recorded. (The toluene also did not autofluoresce in this range.)

The autofluorescence of SU-8 and PDMS have been reported previously. Piruska et al. [206] showed that the relative autofluorescence of PDMS with respect to BoroFloat (Schott) glass was the lowest among three other polymers (cyclic olefin copolymer (COC), poly(methyl-methacrylate) (PMMA), and polycarbonate). The autofluorescence level dropped as the excitation wavelength increased from 403 nm to 633 nm. Wang et al. [207] reported that SU-8 autofluoresced with a peak at 465 nm when excited at 400 nm, but the autofluorescence decreased rapidly with longer excitation wavelengths. They also reported that the autofluorescence of SU-8 was 8-fold higher than that of PDMS at 465 nm. These results are consistent with our measurements for PDMS and SU-8 at an excitation wavelength of 400 nm (Figure 6.7).

To our knowledge, no data has been published on 1B66 autofluorescence. Figure 6.7 compares the measured autofluorescence response of 1B66 with that of SU-8 and PDMS. The excitation wavelength was 400 nm, and the film thicknesses were kept the same in order to determine the relative auto-fluorescence levels. The 1B66 autofluorescence was 260 times higher than that of SU-8. A direct comparison could not be made with PDMS since its signal was within the noise of the detector. Thus,

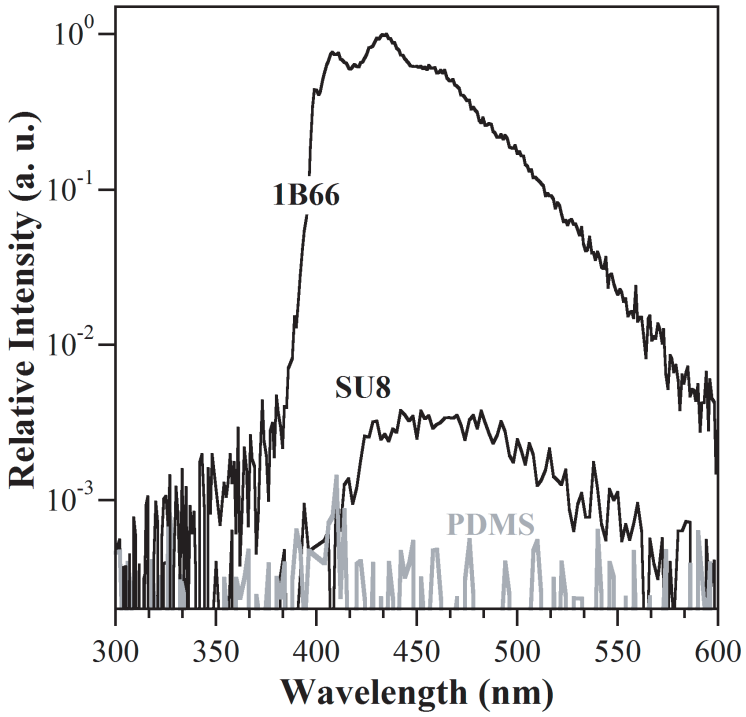

Figure 6.7: Autofluorescence spectra of the host matrices at an excitation wavelength of 400 nm.

autofluorescence is an issue that must be considered when using 1B66 as a host material, and even SU-8 might be problematic. PDMS is the best choice on this basis.

Autofluorescence can be mitigated by keeping film thicknesses to a minimum. Moreover, collimating the excitation signal to limit it to the sample under study and placing the detectors at an offset path from the excitation source should minimize the background signal.

6.4 Proof-of-Concept: Filter Integration in a Hand-held Fluorometer[‡]

This section describes the integration of a BTA-based PDMS filter into a portable fluorescence sensor. Furthermore, it reports on several bioassays that were conducted utilizing the hand-held sensor.

Figure 6.8 (a) shows how the various components of the device fit together. A data acquisition system was used to display the sensor output on a computer screen. The integrated sensor (i.e the photodetector integrated with the emission filter) was mounted onto a PCB housed in a light-proof case. The sensor output was captured by a PC-based DAQ system, and a custom LABVIEW program that recored the data and displayed the sensor's output was used for post-processing. (For an even more compact and portable device, the PC-based data acquisition may be integrated onto the same PCB, effectively replacing the laptop and DAQ card with a microcontroller and an LCD screen.)

6.4.1 Sample Holder & Excitation Source

A photograph of the integrated fluorescence sensor is shown in Figure 6.8 (b). The sample under study was held in a standard 4 mL methacrylate cuvette for which a custom fixture was machined using a 3-D printer. Most of the light collected by the detector originated from the portions of the sample volume that are located directly in the region subtended by the detector; thus a viewing window was cut out

[‡] Excerpts from a journal article originally published as: N. Nelson, D. Sander, **M. Dandin**, S. B. Prakash, A. Sarje, and P. Abshire, "Handheld Fluorometers for Lab-on-Chip Applications", *IEEE Trans. Biomed. Circuits Syst.*, vol. 3, pp. 99–107, 2009.

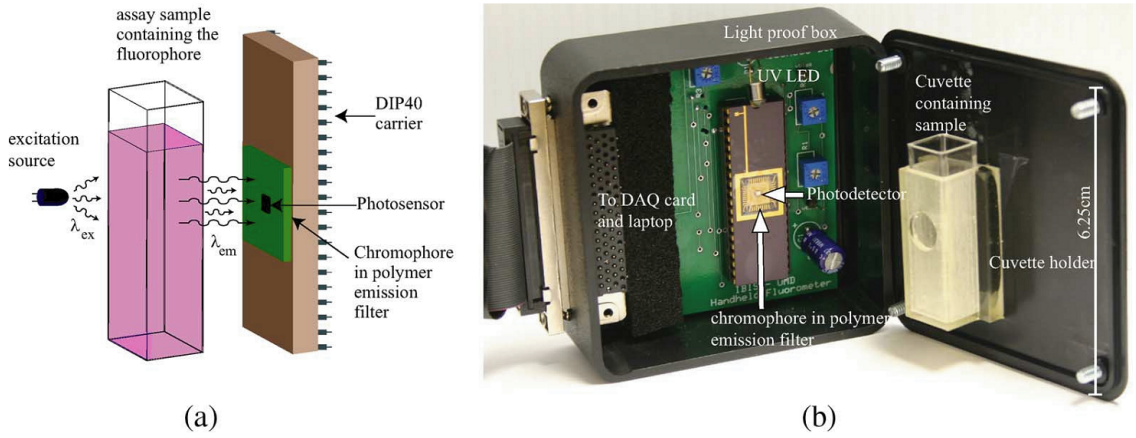

Figure 6.8: (a) Handheld fluorometer components. (b) Photograph of handheld fluorometer for use with a standard cuvette and 400 nm long pass filter.

of the fixture to allow the fluorescent light to reach the detector's active area.

Although it is possible to use small footprint surface-mount LEDs as a light source, a discrete UV LED packaged in a 2-leg metal can (Nichia Inc.) was used; the LED had a narrow emission band around 375 nm. It was placed orthogonal to the optical path of the detector (Figure 6.8 (b)). This provided a means for geometrically filtering the excitation light (as was discussed in Chapter 6). However, preliminary data suggested that scattered excitation light still reached the detector and that an emission filter was required, despite the intrinsic rejection achieved by the placement of the source relative to the detector.

6.4.2 Detector: Differential Active Pixel Sensor

For the bioassays described in the following sections, a SPAD detector was not necessary since there was no need for photon counting. Rather, a CMOS active pixel sensor (APS) was used (Figure 6.9), and it provided a voltage reading corresponding

to the *average* fluorescent light intensity over a short integration period. The circuit was designed by my colleague, Dr. Honghao Ji.

However, as in the case of the CMOS SPAD front-end, noise reduction is a central issue in using the APS as a fluorescence detector. To reduce noise, in-pixel correlated double sampling (CDS) was used. This technique allowed the reduction of correlated and environmental noise, but at the expense of increased thermally generated noise, as was demonstrated by my colleague, Dr. David Sander, in ref. [208].

As was shown in Chapter 2, noise sources include shot noise and thermal noise. In an APS, however, two additional noise sources exist. They are: the *reset* noise and the *readout* noise. The reset noise is due to random fluctuation of carriers at the integration node and is given by kT/C, where C is the capacitance at the integration node (estimated to be 300 fF for the detector in Figure 6.9). The readout noise is composed of the flicker and thermal noise of the MOSFETs of the source follower and subsequent stages in the readout path. The flicker noise component is due to the mobile charges that are randomly trapped and released from interface traps at the silicon-oxide interface.

Most importantly, however, environmental noise coupled into the signal path due to power supply fluctuations and stray electromagnetic fields may exceed the noise generated from the sources mentioned previously. Given that the sensor shown in Figure 6.8 is for use in situations where environmental noise shielding is poor, i.e. in in-field applications, power supply and environmental fluctuations are expected to be significant.

Fortunately, power supply noise and environmental noise couple evenly to different parts of the circuit. So a differential signal representation of the output signal can greatly improve the circuit's immunity to these noise sources; this differential readout feature was incorporated in the circuit (Figure 6.9).

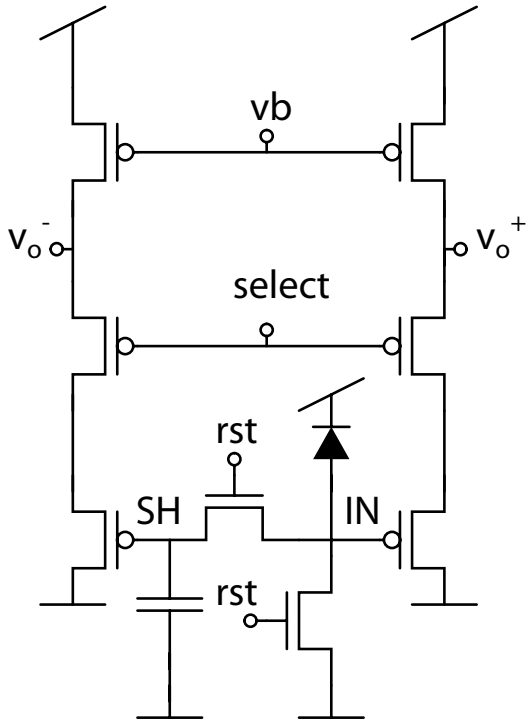

Figure 6.9: Sensor circuit schematic showing integration and S-H nodes for differential readout. (Figure by Dr. David Sander.)

The photodetector (the diode in Figure 6.9) was a 33.6 μm x 33.6 μm p^+/nwell diode. The photo-circuit comprised integration (labeled IN in Figure 6.9) and sample-and-hold (labeled SH in Figure 6.9) nodes which were buffered differentially. During the reset cycle, the switches labeled *rst* reset the integration and S-H nodes to ground. Once these switches are turned off, the capacitor stores the reset value and the sensor is allowed to integrate for a predetermined integration time. The

output is taken as the difference between nodes V_o^+ and V_o^-.

In addition to removing temporally correlated environmental noise, the differential readout removes offsets due to threshold voltage mismatches, clock feedthrough, and charge injection, all of which introduce noise to the readout path. The sensor was fabricated in the same CMOS process mentioned in Chapters 3 through 5. The measured electrical performance metrics of the APS circuit are reported in Table 6.2. The readout and reset noise were experimentally estimated by examining the statistics of many sample paths as demonstrated by Fowler et al. [209].

Table 6.2: Summary of Differential Active Pixel Sensor Characteristics

Metric	**Measured Data**
Readout noise	175.3 μV
Reset noise	360 μV
Supply voltage	5 V
Power consumption	68 μW
Dynamic range	59 dB
Maximum signal	3.5 V
Dark signal	4.1 mV/s
Conversion gain	530 nV/e^-
Detection limit	2.2$\times$ 10 ^{8} photons/cm^2

The spectral responsivity of the differential APS was obtained experimentally (Figure 6.10(a)) using the test bench described in Chapter 4; the only difference being the manner in which the responsivity was computed since the PGSPAD and the APS function in two fundamentally different modes. In the case of the former, responsivity was estimated from the measured photo-current and expressed in units of $A \times W^{-1}$, whereas for the latter, the metric was estimated from the integrated photo-generated charge during a finite integration time and expressed in units of

$V \times s^{-1} \times W^{-1}$.

The linearity of the sensor as a function of light intensity, and for wavelengths

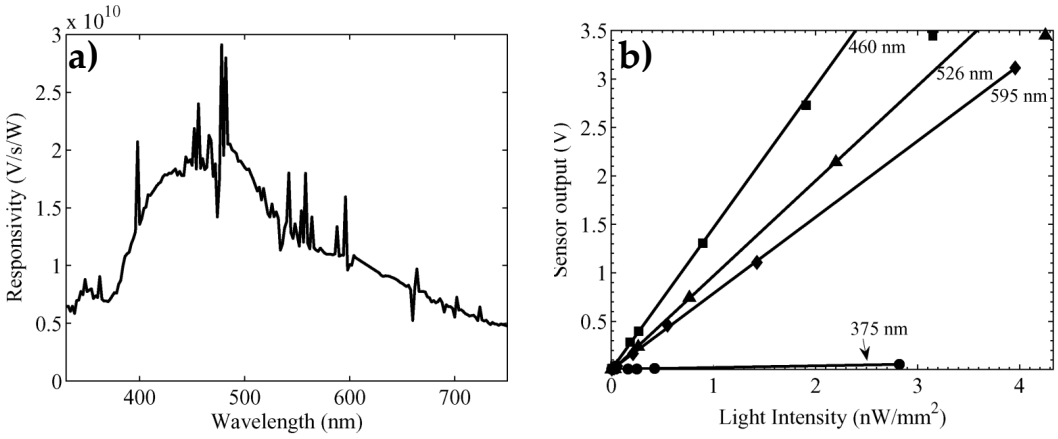

Figure 6.10: (a) Spectral responsivity of the differential active pixel sensor, showing highest responsivity for blue wavelengths. (b) Sensor output as a function of light intensity for a chip with integrated UV rejection filter shows excellent linearity. The integrated sensor shows very little response for 375 nm (the filter attenuates wavelengths below 400 nm).

above and below the filter cut-on, was measured (Figures 6.10 (a) and (b)). The data showed that the sensor's output remained linear for an increase in light intensity extending from 0 to 4 nW/mm^2 , a range of intensities typical to fluorescence assays conducted in this integrated sensor.

6.4.3 BTA-doped PDMS Emission Filter

The BTA-doped PDMS pre-polymer was prepared as described in Section 6.2.2.1. The concentration of BTA in the doping solution was 111 mM (Figure 6.11(a)). The composite was cast directly in the DIP40 cavity package in which the wire-bonded microchip was mounted. The filter was cured at 70° C for two hours. A lower temperature than that reported in Section 6.2.2.1was used in order to maintain the

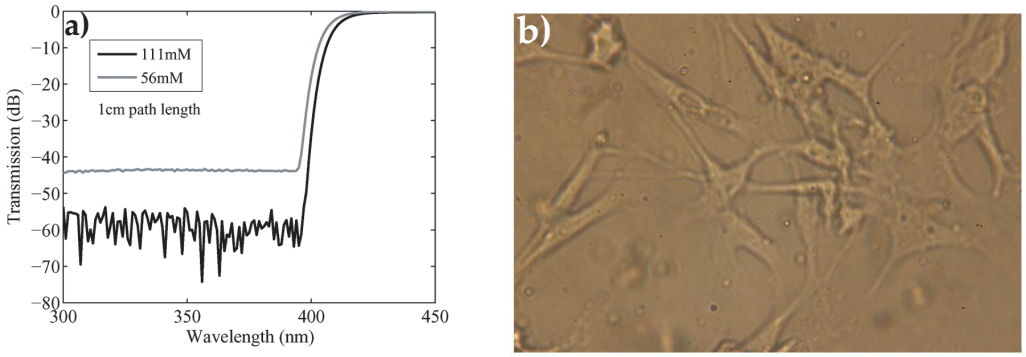

Figure 6.11: (a) Transmission characteristics of 2-(2'-hydroxy 5'-methylphenyl) benzotriazole in Toluene. (b) Photomicrograph of Bovine Aortic Smooth Muscle cells growing on a cured BTA-PDMS filter.

integrity of the wire-bonds. The resulting filter was 3-mm thick. Figure 6.11(b) shows BAOSM cells proliferating on the filter, indicating that the filter was biocompatible and thus cannot compromise the viability of the specimens under study.

6.5 Bioassays

This section reports results from two types of bioassays that were conducted using the integrated fluorescence sensor of Figure 6.8. The motivation for these assays and the experimental procedures used are summarized.

6.5.1 PAMAM Cytotoxicity Assay

Nano-particles can be used as a delivery system for transporting specific molecules to target locations in the body via absorption through the gastrointestinal (GI) tract. This requires that the nano-particles have no adverse effects on surrounding tissues and act merely as carriers. Thus, prior to conjugating the drug of interest onto the

nano-particle carrier, one must ensure that it is not cytotoxic, particularly to the GI tract.

IFS is a key technology for aiding in the discovery of nano-particle-mediated therapeutics. Since integrated fluorescence sensors can be pixelated, high-throughput assays can be used to conduct combinatorial cytotoxicity studies on a wide variety of nano-particles simultaneously. Thus, IFS platforms can help speed-up the the discovery of a lead compounds during the drug discovery process.

Poly-(amidoamine) (PAMAM) dendrimers are a family of highly branched macromolecules defined by their mass, shape, size and surface chemistry, and they have been found to have potential uses in oral drug delivery. Studies on PAMAM dendrimers have demonstrated that the surface chemistries of different dendrimer families influence their transport across the epithelial lining of the GI tract thereby resulting in differing degrees of cytotoxicity [210, 211]. The experiment featured herein demonstrates the effectiveness of using an IFS platform for assessing the cytotoxicity of two types of PAMAM dendrimers. Human intestinal adenocarcinoma cells (Caco-2 cell line, ATCC) were used as an in vitro model of the GI tract, as previously shown by Gandeheri et al. [210, 211].

In order to study the effects of the dendrimers on the Caco-2 cells, the AQUA live/dead stain (Invitrogen), with excitation at 375 nm and emission above 526 nm, was used to conduct a fluorimetric cytotoxcity assay. AQUA live/dead fluoresces only when it is bound to amine groups. Since healthy cells have a high degree of membrane integrity, the fluorophore reacts exclusively with amine groups situated on the the outer surface of the cell membrane. Conversely, compromised cell membranes

let the dye through, and it can thus be bound with intra-cellular amine groups, in addition to those located on the outer cell membrane. Thus, in the presence of cytotoxic agents, a cell culture stained with AQUA live/dead will show increased fluorescence.

In order to have a calibration curve relating the sensor's output voltage with fluorescence intensity (and thus with bound fluorophore concentration), a titration experiment was conducted. The sensor's output voltage was recored as a function of known concentrations of AQUA stain dissolved in HBSS-BSA. All concentrations were normalized by the manufacturer's recommended dosage.[4]

For the titration, the solution's concentration was repeatedly halved and measurements (for 5 samples) were made and averaged. This yielded the calibration curve shown in Figure 6.12. As the data show, the sensor was able to quantifiy the AQUA stain fluorescence with a high degree of linearity. The smallest detectable quantity was 12% of the manufacturer's recommended concentration.

The Caco-2 cells were exposed to two types of PAMAM dendrimers (G3.5 and G4, Sigma-Aldrich), and their viability was determined using the hand-fluorometer shown in (Figure 6.8), and using the the above-mentioned calibration curve as an indicator of bound AQUA stain concentration. The experiments showed that the G4 family was cytotoxic, whereas the G3.5 family was not, confirming results previously shown by Gandheri et al. [210, 211]. The cell culture, staining protocols, and

[4]Since the assay is proprietary, concentrations used in the experiments are reported as a percentage of the manufacturer's recommended dosage.

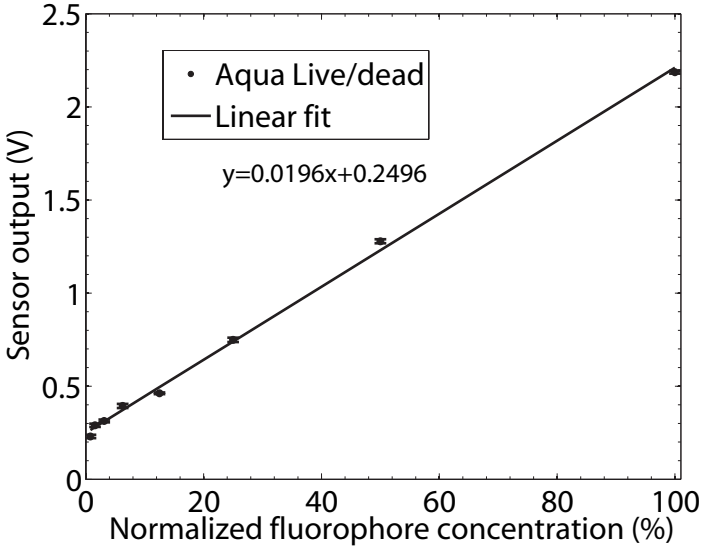

Figure 6.12: Sensor output is a linear function of AQUA live/dead stain concentration.

bioassays were conducted by my colleague Dr. Nicole McFarlane, née Nelson, and additional experimental procedures are reported in detail in ref. [202].

6.5.2 Metabolic Activity Assay

The assay described in the previous section is an end-point measurement, i.e, all measurements are made at the end of the experiment. With the sensor of Figure 6.8, it is also possible to measure fluorescence in real time, though not with the tens of nanosecond resolution offered by the PGSPAD. This feature was demonstrated by conducting an experiment that consisted of monitoring the fluorescence intensity of nicotinamide adenine dinucleotide (NADH in reduced form, NAD^+ in oxidized form) of a germinating yeast culture under various environmental conditions.

NADH is an autofluorescent compound that is a by-product of cellular respi-

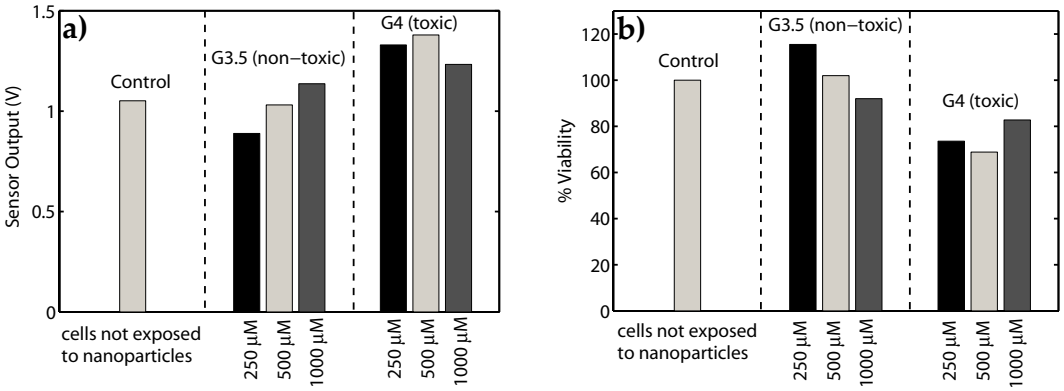

Figure 6.13: Fluorimetric cytotoxicity assay using AQUA live/dead: (a) as function of sensor output voltage, (b) as a function ofthe percentage of viable cells in the culture..

ration (Figure 6.14(a)). It is present in all metabolically active cells. NADH can also be found in the medium surrounding the cells as it is a small molecule which passes freely across the cellular membrane. Although not a specific marker, positive detection of NADH, when other means of ensuring specificity are used, can indicate the presence a pathogen in a medium. NADH has a peak excitation at 380 nm and peak emission at 460 nm in the blue region of the spectrum, making it possible to conduct a bioassay that monitors this compound using the IFS of Figure 6.8.

Similar to what was done in the cytotoxicity assay reported in the previous section, a sensor calibration curve was first obtained. To do so, β-NADH (Sigma-Aldrich) was dissolved in a 1X TRIS-EDTA solution (pH 8), and the mixture was successively diluted into aliquots of concentrations ranging from 11.012 mM to 0.672 μM. The detector's output was then measured for each test aliquot. The resulting calibration curve is shown in Figure 6.14(b). A similar curve derived using a spectrophotometer is shown as a reference (with both curves normalized to their respective maxima).

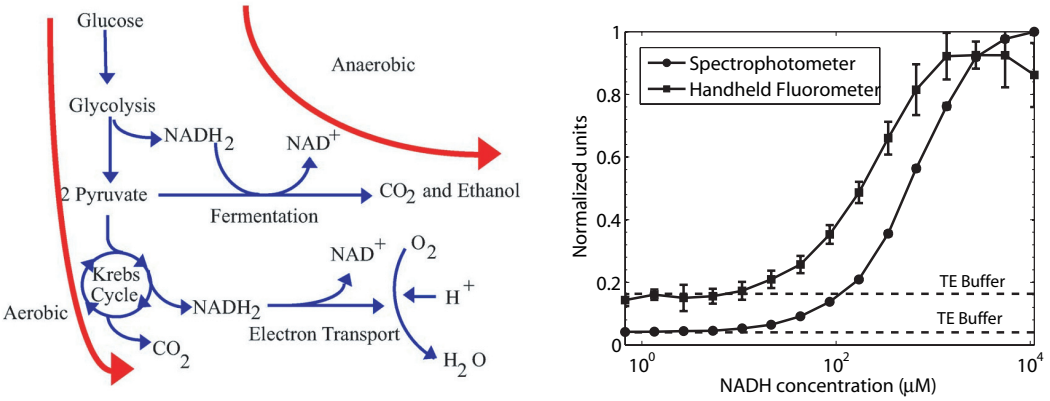

Figure 6.14: a) Metabolic pathways for glucose in yeast cells. NADH is repeatedly recycled and its concentration depends on the type of respiration occurring. b) Sensor output as a function of β-NADH concentration. Units are normalized to allow comparison with results from standard spectrophotometer, where normalized units = sensor output/max output..

As the data show, the hand-held IFS was capable of detecting as low as 10 μM of NADH. Since the fluorophore self-quenches at high concentrations, the amount of fluorescence will be reduced. This phenomenon was also observed in the IFS as indicated in Figure 6.14(b).

Figure 6.14(a) suggests that the intracellular NADH concentration changes over time, depending on whether the cell is respiring anaerobically or aerobically. Thus, the measured fluorescence will reflect these changes in the NADH concentration if conditions are changed to cause the cells to respire anaerobically or aerobically.

This implies that yeast spores germinating in the test cuvette start with a low NADH concentration. As the cells deplete the available dissolved oxygen, electron transport is impeded, and the end-result of the metabolic cycle is a build-up of NADH within the cell. As the cell switches to anaerobic respiration, the intensity of the fluorescence decreases again as fermentation starts to occur [212, 213].

In addition to oxygen availability, the amount of glucose also influences the

NADH cycle. So once the dextrose supply is depleted, the entire metabolic cycle will shut down, and the quantity of glucose available will influence the rate of NADH production. Thus, the germination rate is highest when the spores are placed in a warm environment.

This was verified experimentally. Three mL of 1 g/mL dextrose solution was

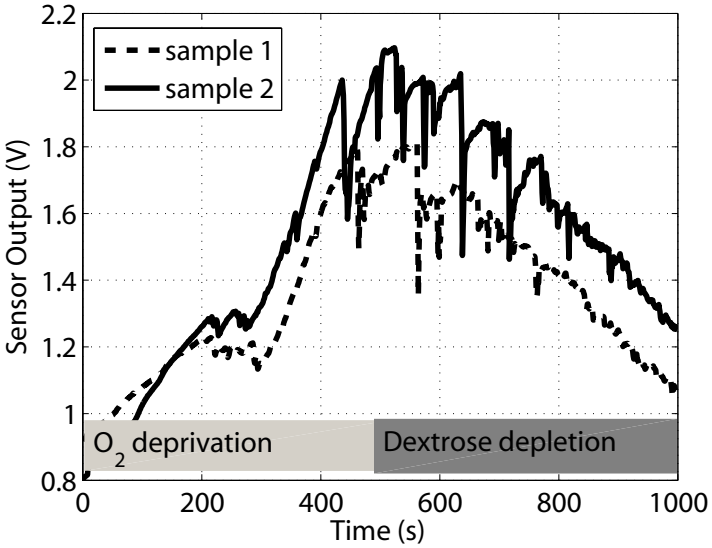

Figure 6.15: Sensor output versus time as yeast cells germinate in dextrose solution, reflecting the change in fluorescence due to changing NADH levels [214].

warmed in a water bath for approximately 5 minutes and 0.03 g of dry yeast spores were subsequently added to the solution. The mixture was loaded into the test cuvette of the IFS. The sensor's output was monitored for approximately 17 minutes (Figure 6.15). The output voltage was triangular-shaped as a function of time, as expected. The increasing portion of the curve indicated oxygen deprivation while the decreasing leg suggested a depletion in the dextrose supply. It was assumed that the signal measured in Figure 6.15 originated from extra-cellular fluorescent NADH. Confirmation of this assertation would require flushing the medium and an-

alyzing the cells separately. Nevertheless, the result was consistent with the NADH metabolic cycle.

6.6 Conclusions

This chapter demonstrated the use of BTA, an ultraviolet absorbing dye, as an additive to polymers that are typically used in microsystem fabrication to create high rejection optical filters. These filters can be used in integrated fluorescence sensors utilizing ultraviolet-excited fluorophores, as was shown by our group in ref. [202].

The chromophore was embedded in films that required different fabrication and patterning procedures: casting and soft lithography (PDMS), spin coating and dry etching (1B66), and photopatterning (SU-8). However, for the latter two polymers, autofluorescence should be taken into consideration when designing the sensing system, and with SU-8, its strong UV absorption should also be considered.

Furthermore, the data revealed discrepancies between the extinction coefficient of the composites and that of the chromophore when dissolved in an organic solvent. This result means that interactions between BTA and the host matrices affect the chromophore's ability to attenuate UV light. Thus, extinction coefficient data are insufficient for predicting the behavior of a chromophore in a given host matrix (even if the latter has little or no intrinsic UV rejection). Accordingly, designing a high-performance UV-blocking filter utilizing the approach presentend herein will require initial empirical investigations.

The latter part of the chapter showed a meso-scale fluorometer that utilized a

millimeter-thick BTA-PDMS filter. The integrated sensor exhibited nearly the same detection limit (less than 100 μM) for β-NADH as a bench-top spectrophotometer, a figure which is adequate for monitoring metabolically-active cell populations as we have shown in the experiments reported above.

This agreement in the readings from both instruments (i.e. the IFS and the spectrophotometer) was unexpected since the bench-top instrument has better dynamic range and hence can theoretically detect much lower concentrations of fluorophores. There is likely a range of concentrations for β-NADH for which an optimum fluorescence yield is obtained: outside that range the fluorophore either self-quenches or it does not produce enough photons that either instruments can register.

Chapter 7

Conclusion

In this dissertation I have presented a body of work that addresses the two most pressing challenges in the field of integrated fluorescence sensing, namely, the design of integrated optical photon counting sensors and the fabrication of high-rejection micro-scale optical filters. I have introduced two novel technologies that each address these unmet needs. They are: the perimeter-gated single-photon avalanche diode (PGSPAD), for on-chip photon counting, and the benzotriazole-based thin-film polymer filter, for on-chip ultraviolet light rejection.

Furthermore, I have presented the development of theoretical and experimental frameworks for the evaluation of performance metrics that pertain to both technologies, and as a result, identified the trade-offs that exist when designing the detector and the filter components of integrated fluorescence sensors. Consequently, the primary contribution of this work is a rigorous approach towards integrated microsystem development that focuses on achieving low-noise optical sensing front-ends as well as high-rejection filtering across extremely short optical path lengths; these two features are necessary for transducing fluoresent light with high signal-to-noise ratio in lab-on-a-chip platforms.

In the following sections, I summarize each chapter of the dissertation while highlighting key findings and their significance. I end the dissertation with a dis-

cussion of the next steps that need to be undertaken in this research and with an exhaustive list of archival publications that resulted from this effort.

7.1 Perimeter-Gated Single Photon Avalanche Diodes

Chapter 2 covered the theory of phototransduction and common solid-state photo-sensors architectures. Several performance metrics were discussed. The single-photon avalanche diode architecture was introduced, and the issue of perimeter breakdown was identified as one of the major impediment to implementing SPADs in CMOS technologies.

Chapter 3 addressed that issue and sought to determine the most effective method for curtailing perimeter breakdown. Several test SPADs were designed and fabricated in a commercial CMOS process for the purpose of studying edge breakdown effects. The devices' architecture had two structural features that contributed to reducing the high electric fields at the periphery, the primary cause of perimeter breakdown. These features were a poly-silicon gate, placed over the high-field regions, and a laterally diffused peripheral n-well guard ring surrounding the diode's active area.

The experimental data showed that a combination of the above-mentioned methods was not requisite for fully suppressing perimeter breakdown. Rather, the data revealed that while both methods independently reduced peripheral electric fields, the field-effect resulting from a large magnitude negative bias on the gate produced the maximum obtainable suppression. The study thus concluded that

perimeter gating was sufficient as a stand-alone method for mitigating edge breakdown. These experimental results were supported by a 3-D numerical model that tracked the charge generation rate in the junction's x, y, and z directions, confirming that large negative perimeter gate voltages caused a spatial broadening of the charge generation rate at the volumetric junction, a condition indicating that perimeter breakdown was curtailed.

Chapter 3 is a major contribution to the field of CMOS SPAD design. It demonstrated, for the first time, a viable edge breakdown suppression method that is independent of process technology parameters, i.e. the technique is portable to *any* CMOS process. Moreover, in contrast to SPADs that use the traditional suppression method (i.e the laterally diffused n-well guard ring) perimeter-gated SPADs are scalable, which means that smaller devices can be fabricated without compromising the front-end's fill factor. While shallow-trench isolation (STI) suppression techniques offer the same scalability, perimeter gating achieves two orders of magnitude improved performance (as was shown in Chapter 5) and is thus a superior method.

Another merit of perimeter gating lies in the ability to increase the breakdown voltage of native diodes. For example, in the 0.5 μm process used in this dissertation, a 4 V increase in breakdown voltage was observed for an 18 V change in the perimeter gate voltage. Thus, perimeter gating can be used to produce high-voltage diodes in processes that are inherently designed for low-voltage junctions. For example, this may be a significant advantage in developing low-cost ICs for MEMS actuation and control applications which often require high-voltage circuits.

Chapter 4 featured experimental results from actively quenched and rest PGSPAD. The test results showed that the PGSPAD, when interfaced with adequate active readout mechanisms, can be operated at high SNR in the high count rate regime, and at maximum sensitivity in the low count rate regime. This important finding implies that perimeter gating, in addition to suppressing perimeter breakdown, extends the dynamic range.

The chapter ended with a comparison of the actively readout PGSPAD with state-of-the-art CMOS SPADs of different architectures. The comparison revealed that the PGSPAD achieved equal or better dark count rate, area-normalized dark count rate, and similar photon detection efficiency, despite having the largest active area. This means that further scaling of the PGSPAD will greatly improve these performance metrics.

7.2 Micro-scale Integrated Optical Filtering

Chapter 5 laid the ground work for understanding the challenges in optical filtering in microsystems. State-of-the-art micro-scale filtering technologies were reviewed, putting an emphasis on materials systems, fabrication methods, and the potential for integration. The literature survey revealed that there was no established paradigm for integration of optical filters in lab-on-a-chip devices. Rather, it was found that the method of integration depended on the application at hand and on the other system components.

Consequently, for the purpose of comparing optical filters and integrated flu-

orescence sensors of disparate architectures, a set of single-number and spectrum-based metrics was developed. This novel analytical framework is extremely important in the development of new devices since it applies to any integrated fluorescence sensors, irrespective of the materials used and the intended application. As such, this set of metrics is the most important contribution of Chapter 5. It represents the first step in the field towards the development of a mathematical formalism that will facilitate the integration of fluorescence sensors in a wide variety of lab-on-a-chip systems.

Chapter 6 focused on the development of an integrated absorption filter for ultraviolet-excited fluorescence assays, utilizing the above-mentioned set of metrics for design and evaluation. Several polymer composites were demonstrated as being suitable micro-scale filters. Each used the high-extinction coefficient UV-absorbing chromophore 2–(2'–hydroxy-5'-methylphenyl) benzotriazole (BTA) as the active filtering agent. In addition, custom-developed dry subtractive and photo-patterning processes were demonstrated, and they were found to be viable fabrication methods for integrating the filters into lab-on-a-chip devices. Furthermore, a novel photo-polymerization model for incorporating the chromophore into photo-sensitive polymer hosts.

The work featured in Chapter 6 is an important step towards fabrication of integrated filters specifically designed to attenuate UV light over short optical path lengths; filters 5 μm-thick with nearly -40 dB rejection at 342 nm were demonstrated, making them one of the highest performing filters currently available in a thin-film format. The use of these filters in nanoparticle cyto-toxicity and metabolic

activity assays was demonstrated at the end of the chapter. These experiments established the proof-of-concept for BTA-based micro-scale optical filtering in UV-excited integrated fluorescence sensing.

7.3 Future Work

As was shown in the block diagram of Figure 1.2, an integrated fluorescence sensor comprises several subsystems, namely, the optics, the filter, the detector, and the microfluidics hardware. Moreover, as illustrated by the arrows interconnecting each subsystem, the overall sensor performance not only depends on the ability to discriminate fluorescence from excitation (i.e. the filter's performance) but also on minimizing cross-talk from neighboring integrated sensors and minimizing background emissions from the sample under study, the microfluidics, or any other system component that may exhibit autofluorescence. In addition, the electronic noise in each integrated fluorescence sensor "pixel" needs to be minimized at the local level in order to avoid cross-talk.

There are two research tracks that can be extended from this dissertation to address the above-mentioned concerns. The first track consists of a system level design approach in which the interactions between each subsystem are mapped out and understood. The obstacle in reaching that goal is the development of the packaging and assembly know-how for integrating all the components shown in Figure 1.2. During the course of my PhD, I contributed substantially to the development of post-CMOS packaging methods for various integrated bioanalytical microchips. (A

summary of that effort is reported in Appendix D.) However, the application of these methods to integrated fluorescence sensors has yet to be shown.

The second research track consists of a component-level design approach, in line with the one presented in this dissertation, in which performance metrics are further analyzed and optimized. For example, considering the detector, additional techniques for noise reduction, such as cooling, can be investigated. For the filter, one can investigate other chromophores with different spectral characteristics for fabricating filters with different absorption edges, thereby allowing multi-color fluorescence assays on the same IFS platform. Moreover, for multiplexing assays and increasing throughput, higher density arrays need to be designed. As was shown in Chapter 4, the yield in a lot of 80 detectors was 75%.

One strategy for achieving high yield in high density arrays would be to scale the device area down in order to reduce the probability of having regions of high defect concentration within the multiplication volume of the PGSPAD. Determining the adequate sizing of the detector that maximizes yield in a given CMOS process can be done empirically using test structures with different sizes.

7.4 Archival Publication Record

This section features a list of publications that span over 6 years of graduate study. I am indebted to the various co-authors listed below for a fruitful collaboration and for many intellectually rewarding discussions. I am particularly thankful to my advisors, Dr. Elisabeth Smela and Dr. Pamela Abshire, for their support.

7.4.1 Refereed Journal Articles

1. **M. Dandin** and P. Abshire, "High Signal-to-Noise Ratio Avalanche Diodes with Perimeter Field Gate and Active Readout," *IEEE Electron Device Lett.*, vol. 33, No. 4, pp. 570–572, 2012.

2. **M. Dandin**, A. Akturk, B. Nouri, N. Goldsman, and P. Abshire, "Characterization of Single-Photon Avalanche Diodes in a 0.5 μm Standard CMOS Process–Part 1: Perimeter Breakdown Suppression," *IEEE Sens. J.*, vol. 10, No. 11, pp. 1682–1690, 2010.

3. N. Nelson, D. Sander, **M. Dandin**, S. B. Prakash, A. Sarje, and P. Abshire, "Handheld fluorometers for lab-on-a-chip applications," *IEEE Trans. Biomed. Circuits Syst.*, vol. 3, pp. 99–107, 2009.

4. **M. Dandin**, P. Abshire, and E. Smela, "Optical filtering technologies for integrated fluorescence sensing," *Lab Chip*, vol. 7, pp. 955–977, 2007.

7.4.2 Journal Articles in Preparation

1. **M. Dandin** and P. Abshire, "Characterization of Single-Photon Avalanche Diodes in a 0.5 μm Standard CMOS Process–Part 2: Optoelectronic Performance," for submission to *IEEE Sens. J.*, 2012.

2. **M. Dandin**, P. Abshire, and E. Smela, "Polymer filters for ultraviolet-excited integrated fluorescence sensing," for submission to *J. Micromech. Microeng.*, 2012.

7.4.3 Refereed Conference Proceedings & Abstracts

1. A. Akturk, **M. Dandin**, A. Vert, S. Soloviev, P. Sandvik, S. Potbhare, N. Goldsman, P. Abshire,"*Silicon Carbide Ultraviolet Photodetector Modeling, Design and Experiments*," in *International Conference on Silicon Carbide and Related Materials*, Cleveland, Ohio, USA, 2011. (4 pages).

2. P. Abshire, A. Bermak, R. Berner, G. Cauwenberghs, S. Chen, J. B. Christen, T. Constandinou, E. Culurciello, **M. Dandin**, T. Datta, T. Delbruck, P. Dudek, A. Eftekhar, R. Etienne-Cummings, G. Indiveri, M. K. Law, B. Linares-Barranco, J. Tapson, W. Tang, Y. Zhai,"*Confession session: Learning from others' mistakes*," in *IEEE International Symposium on Circuits and Systems*, Limerick, Ireland, 2011, pp. 1149–1162.

3. **M. Dandin**, A. Akturk, A. Vert, S. Soloviev, P. Sandvik, S. Potbhare, N. Goldsman, P. Abshire, and K. P. Cheung, "*Optoelectronic Characterization of 4H-SiC Avalanche Photodiodes Operated in DC and in Geiger Mode*,"in *IEEE International Semiconductor Device Research Symposium*, College Park, Maryland, USA, 2011. (2 pages).

4. A. Akturk, **M. Dandin**, N. Goldsman, and P. Abshire, "*Modeling of perimeter-gated silicon avalanche diodes fabricated in a standard single-well CMOS process*," in *IEEE International Semiconductor Device Research Symposium*, College Park, Maryland, USA, 2009. (2 pages).

5. B. Nouri[†], **M. Dandin**[†], and P. Abshire,"*Characterization of single-photon avalanche diodes in standard CMOS*," in *IEEE Conference on Sensors*, Christchurch, New Zealand, 2009, pp. 1889–1892 ([†]contributed equally).

6. **M. Dandin**, I. D. Jung, M. Piyasena, J. Gallagher, N. Nelson, M. Urdaneta, C. Artis, P. Abshire, and E. Smela, "*Post-CMOS packaging methods for integrated biosensors*," in *IEEE Conference on Sensors*, Christchurch, New Zealand, 2009, pp. 795–798. (Invited paper).

7. I. Weinberg, P. Stepanov, A. S. Weinberg, P. Abshire, and **M. Dandin**, "*Improvement of energy resolution in Geiger-mode APD arrays using curve-fitting of signal decay*," in *IEEE Nuclear Science Symposium*, Dresden,Germany, 2008, pp. 1416–1418.

8. N. Nelson, D. Sander, **M. Dandin**, A. Sarje, S. B. Prakash, H. Ji, and P. Abshire, "*A handheld fluorometer for measuring cellular metabolism*," in *IEEE International Symposium on Circuits and Systems*, Seattle, Washington, USA, 2008, pp. 1080–1083.

9. I. Weinberg, P. Stepanov, P. Abshire, D. Sander, A. Weinberg, and **M. Dandin**, "*Improving SNR of radiation detector readout electronics*," *Journal of Nuclear Medicine*, vol. 49, p. S1, 2008 (abstract only).

10. N. Nelson, S. Prakash, D. Sander, **M. Dandin**, A. Sarje, H. Ji, and P. Abshire, "*A handheld fluorometer for UV-excitable fluorescence assays*," in *IEEE Biomedical Circuits and Systems Conference*, Montréal, Québec, Canada, 2007, pp. 111–114.

11. **M. Dandin**, N. M. Nelson, H. Ji, and P. Abshire, "*Single-photon avalanche detectors in standard CMOS*," in *IEEE Conference on Sensors*, Atlanta, Georgia, USA, 2007, pp. 585–588.

12. D. Sander, **M. Dandin**, H. Ji, N. Nelson, and P. A. Abshire, "*Low-noise CMOS fluorescence sensor*," in *IEEE International Symposium on Circuits and Systems*, New Orleans, Louisiana, USA, 2007, pp. 2007–2010.

13. E. Smela, M. Christophersen, S. Prakash, M. Urdaneta, **M. Dandin**, and P. Abshire, "*Integrated cell-based sensors and cell clinics utilizing conjugated polymer actuators*," in *SPIE Conference on Smart Structures and Materials: Electroactive Polymer Actuators and Devices*, San Diego, California, USA, 2007. (10 pages).

14. I. Weinberg, P. Cheng, K. H. Wong, K. Cleary, P. Abshire, V. Saveliev, **M. Dandin**, L. G. Gruionu, "*PET-Enabled Glove for Molecular Image-Guided Surgery*," *Journal of Nuclear Medicine*, vol. 48, p. S2, 2007 (abstract only).

15. H. Ji, **M. Dandin**, E. Smela, and P. Abshire, "*Integrated Fluorescence Sensing for Lab-on-a-chip Devices*," in *IEEE/NLM Life Science Systems & Applications Workshop*, Bethesda, Maryland, USA, 2006. (2 pages).

Appendix A

Experimental Methods for Estimating APS Spectral Responsivity

A.1 Introduction

The spectral responsivity spectra of the detectors featured in this dissertation (APS and PGSPAD) were estimated experimentally. An illustration of the custom-designed responsivity measurement test bench is shown in Figure A.1. It comprised a monochromator (Newport Cornerstone 260 1/4M, model 74100) which was used to illuminate the sensors with a monochromatic light beam obtained using an internal diffraction grating and a 150W Hg-Xe light source. The wavelength of the test beam was variable, and it could be changed (with a 2 nm resolution) to any wavelength in the range extending from 200 nm to 1100 nm. The intensity of the light incident on the detectors could be was varied using neutral density filters at the output of the monochromator. An integrating sphere was used to obtain spatially homogeneous light. For reference, the light intensity was measured on the top exit port of the integrating sphere while the detector was illuminated through another port. The optical power measurement was performed using a calibrated photometer (Newport 818-UV) fitted with a 5-mm diameter pinhole and an optical power meter (Newport 1830-C).

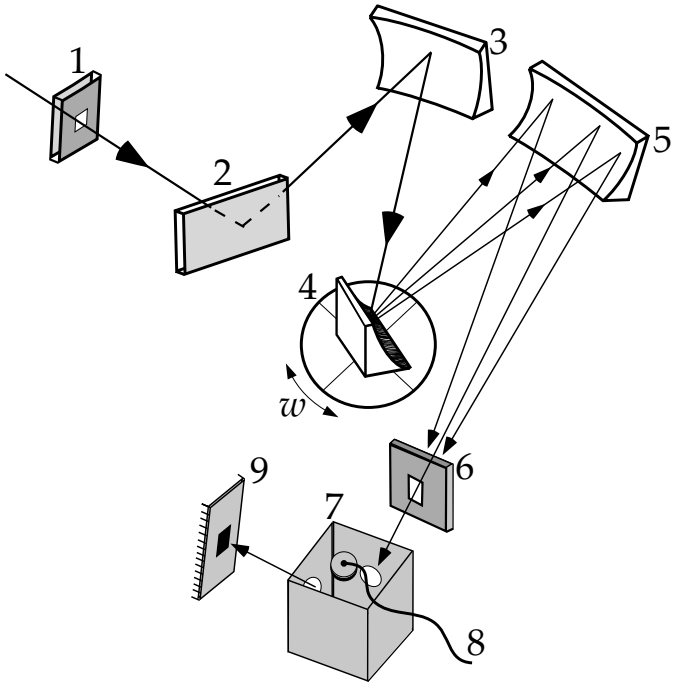

Figure A.1: Experimental setup for spectral characterization. The monochromator comprised the following components: entrance and exit slits (1, 6), mirrors (2, 3, and 5), and diffraction grating (4). The additional hardware used were: an integrating sphere (7) , and a calibrated photometer head (8). The DUT (9) was placed at the output of the integrating sphere. (The light source is not pictured. It was fitted to the monochromator's entrance slit (1) using a flange system.

A.2 Algorithm for APS Spectral Responsivity Measurements

This section describes the procedure that was used for computing the spectral responsivity of the APS front-end discussed in Section 6.4.2 and whose topology is depicted in Figure 6.9. Ideally, the responsivity for a known illumination intensity can be estimated by computing the slope of the sensor's output voltage (corrected for the dark current's slope) and normalizing that result by the optical power received by the detector's active area. However, in the case of an APS, the sensor's front-end gain non-linearity introduces significant non-linearities in the output voltage slope as shown in Figure A.2a) and Figure A.2b). This means that the responsivity also

depends on the temporal dynamics of the readout chain. Thus, only a temporally-averaged responsivity measure can be obtained for a non-linear APS such as the one shown in Figure 6.9.

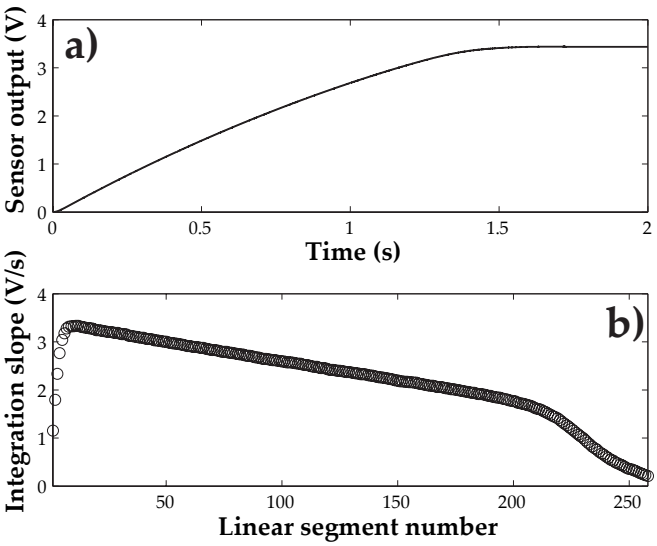

Figure A.2: (a) A sample integration path (shown until saturation). (b) Temporal evolution of the integration path slope (the responsivity follows the same trend).

In addition to front-end gain non-linearity, the presence of noise during the integration period also adversely affects the spectral responsivity. For an ensemble of integration paths, integrated noise (mainly photocurrent shot noise) will cause large deviations in the output voltage; these fluctuations translate to large errors when estimating spectral responsivity.

In order to reduce the effect of noise on the responsivity computation, the following algorithm, developed by Fowler et al. [209], was used[1]. An ensemble (500 experiments) of integration paths were recored, each lasting 2 seconds. Each path in the ensemble was partitioned into segments, thus approximating the path as a

[1]This algorithm can also be used to estimate readout and reset noise parameters. See ref. [209]

set of piece-wise linear signals. The last data point of each segment was subtracted from all the data points of the following segment. This removed any offsets which may have accumulated during the integration, particularly integrated shot noise. (Recall that the differential APS filters out correlated noise, however shot noise is still present and is thus integrated.) The responsivity was taken as the average of the responsivities of each segment. The algorithm is shown graphically in Figure A.3.

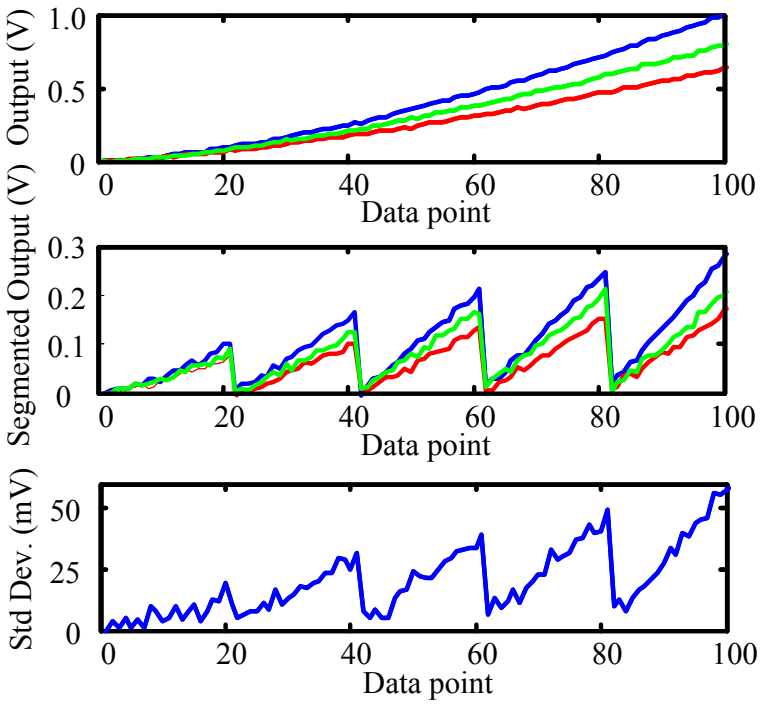

Figure A.3: Signal paths diverge as a result of photon shot noise. The ensemble was broken into short linear segments, and the last data point from previous segments were subtracted from following segments. (data collected and processed by Dr. David Sander.)

A.3 Measurement Results

This section shows several responsivity studies conducted utilizing the methods stated above. Figure A.4a) shows the responsivity spectra of the filtered and that of the un-filtered differential APS of Section 6.4.2.

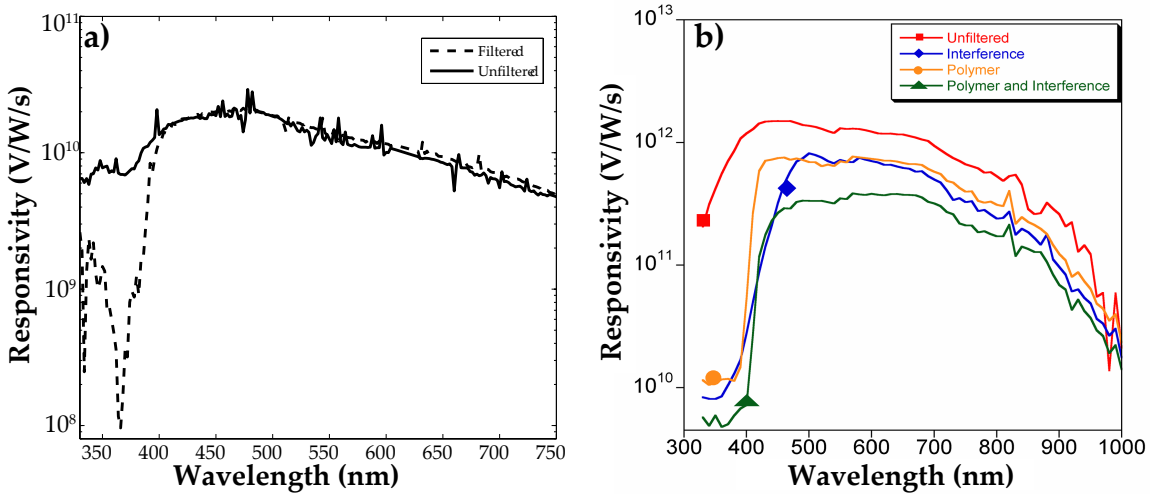

Figure A.4: a) Responsivity of filtered and un-filtered 0.5 μm CMOS differential APS. b) Responsivity of filtered and un-filtered 0.18 μm CMOS singled-ended APS.

Figure A.4b) shows the spectra for a 3-transistor single-ended APS fabricated in a 0.18 μm CMOS process. Four identical detectors were tested. The first was un-filtered. The second was coated with SiO_2/TiO_2 interference filter (with cut-on at 395 nm). The third was equipped with a cast BTA-doped 1B66 filter, and the fourth consisted of a detector coated with the same interference fitler mentioned above but onto which a BTA-doped 1B66 filter was subsequently deposited. These results that absorption and interference filters can be combined to achieve even greater rejection than either one filter can achieve alone. This concept was explored in greater detail by Charette et al. in ref. [199].

Appendix B

Photopolymerization Model for Curing BTA-Doped Polymers

We begin by calculating the exposure dose, i.e. the energy, required for photopolymerization. To do so, we first consider the penetration depth D_p. This parameter is defined as the location at which the ultraviolet energy incident on a photosensitive film decays to a value of $1/e$ of its maximum value. The thickness of the film that is cured is related to the penetration depth as follows:

$$C_p = D_p \, ln\left(\frac{E_{max}}{E_c}\right) \tag{B.1}$$

where E_{max} is the energy at the surface of the film and E_c is the minimum energy required to induce photopolymerization [215].

Furthermore, the energy absorbed as a function of film thickness follows the Beer-Lambert law:

$$E_u(z) = E_{max} \, \exp\left[-\frac{z}{D_p}\right] \tag{B.2}$$

The subscript u indicates the case of an undoped film. Substituting Equation B.1 into Equation B.2 yields:

$$E_u(z) = E_{max} \times exp\left[-z\frac{1}{C_p}ln\left(\frac{E_{max}}{E_c}\right)\right] \tag{B.3}$$

.

The term $\frac{1}{C_d}ln\left(\frac{E_{max}}{E_c}\right)$ has inverse length units. Thus, this term can be considered as an effective absorption coefficient and Equation B.3 can be re-written as:

$$E_u(z) = E_{max}\exp\left[-\alpha_{eff}z\right], \tag{B.4}$$

where

$$\alpha_{eff} = \frac{1}{C_d}ln\left(\frac{E_{max}}{E_c}\right) \tag{B.5}$$

The parameter α_{eff} differs from the cured and uncured absorption coefficients. Rather, it is a dynamic variable that depends on photoinitiator concentration and polymerization initiation and termination rates, and is thus a function of exposure time. Gaudet et al. have shown the temporal dependence of the absorption coefficient of thick SU-8 films during i-line exposure, and they used their findings to control the process time in order to create bridge-like membranes [216].

Put simply, Equation B.4 evaluated at $z = n \times \delta$, where δ, is the physical

thickness of the film and n its refractive index, is the minimum energy required to fully cure the film. The total exposure dose (E_u) as a function of film thickness is typically supplied by the manufacturer.

Let us now consider the case of a doped photosensitive pre-polymer film. With the addition of a UV-absorbing compound such as BTA, the film will absorb more of the incoming radiation. This effect is additive in terms of the absorption coefficient. The energy equation becomes

$$E_d(z) = E_{max} \exp\left[-\left(\alpha_{eff} + \alpha_d\right)\right] = E_u\left(z\right) \exp\left[-\alpha_d z\right] \tag{B.6}$$

where the subscript d denotes the energy for a doped film. The parameter is the additional attenuation resulting from introducing the dopant. Re-arranging Equation B.6 yields:

$$E_d(z) = E_{max} \exp(-\alpha_{eff} z) \exp(-\alpha_d z) \tag{B.7}$$

With further simplification, we obtain:

$$E_d(z) = E_u(z) \exp\left(-\alpha_d z\right). \tag{B.8}$$

As Equation B.6 shows, for large α_d as in the case for BTA, $E_d << E_u$.

This implies that the energy received by the film, E_d, will not be sufficient to induce polymerization. The loss of energy resulting from BTA absorption must be compensated by increasing the exposure time.

Thus, the energy required to cure the doped film, $E_d^*(\delta)$, where the subscript '$*$' denotes the adjustment in exposure time, is:

$$E_d^*(\delta) = I_{max}\left(t_E + \Delta t\right)\exp\left[-\left(\alpha_{eff} + \alpha_d\right)\right] \tag{B.9}$$

is the irradiance of the UV lamp, is the time it would take to cure an undoped film of optical thickness , and is the additional time by which exposure must be extended.

Simplifying Equation B.9 we obtain:

$$E_d^*(z) = I_{max}t_E e^{-\alpha_{eff}z}e^{-\alpha_d z} + I_{max}\Delta t e^{-\alpha_{eff}z}e^{-\alpha_d z} \tag{B.10}$$

Since $E_{max} = I_{max}t_E$, we can write:

$$E_d^*(z) = E_{max}e^{-\alpha_{eff}z}e^{-\alpha_d z} + \frac{E_{max}}{t_E}\Delta t e^{-\alpha_{eff}z}e^{-\alpha_d z} \tag{B.11}$$

$$E_d^*(z) = E_{max}e^{-\alpha_{eff}z}e^{-\alpha_d z}\left(1 + \frac{\Delta t}{t_E}\right) = E_u(z)e^{-\alpha_d z}\left(1 + \frac{\Delta t}{t_E}\right). \tag{B.12}$$

Recall that for polymerization to occur, the film must be exposed with a

minimum dosage of E_u. In order to have $E_d^* \geq E_u$, the condition required for curing the BTA-doped film, the following condition must hold:

$$e^{-\alpha_d z}\left(1+\frac{\Delta t}{t_e}\right) \geq 1. \tag{B.13}$$

Thus, the additional time required for successful curing must satisfy $\Delta t \geq t_E\left(e^{\alpha_d z}-1\right)$. The total exposure time is thus:

$$t_d^* = t_E + \Delta t \geq t_E e^{\alpha_d z} \tag{B.14}$$

The parameter α_d is a concentration and wavelength dependent absorption coefficient and it is given by the following formula:

$$\alpha_d = \frac{\epsilon c}{M}, \tag{B.15}$$

where ϵ is the extinction coefficient, M is the molecular weight of the doping chromophore, and is its concentration in the pre-polymer. For a model particular to the photolithography of SU-8-BTA composites at the i-line wavelength, we re-write Equation B.14 as

$$t_d^* \geq t_E e^{\left(\frac{\epsilon_i c_{BTA}}{M}\right) n_{SU8}\delta}. \tag{B.16}$$

The i-line extinction coefficient ϵ_i is obtained experimentally using the molecular formulation of the Beer-Lambert law, namely, $A = \epsilon_i cl$, where A is the absorbance of the chromophore in solution at concentration c across an optical thickness l. The chromophore c_{BTA} concentration is obtained by dividing the number of moles of BTA in the doping aliquot by the pre-polymer volume. (The solvent volume can be neglected because it evaporates during curing).

Scaling Equation B.16 by yields the minimum exposure dose needed for polymerizing the composite:

$$E_d^*(\delta) \geq E_u(\delta) e^{\left(\frac{\epsilon_i c_{BTA}}{M}\right) n_{SU8} \delta}. \tag{B.17}$$

Appendix C

Silicon Carbide Avalanche Photodiode Spectral Responsivity Measurements[†]

C.1 Introduction

Silicon carbide has attracted a lot interest in the power electronics arena due to its advantageous properties over other semiconductor materials; it has high thermal conductivity, a wide bandgap, and a high breakdown electric field, all of which are properties that make it suitable for high voltage and high current density devices capable of operating in extremely harsh environments. Another noted advantage of SiC is its capability to transduce photons in the ultraviolet band of the electromagnetic spectrum. Due to the large energy gap, SiC p-n junctions exhibit high UV responsivity and negligible response beyond 400 nm. This makes SiC ideal for solar-blind UV imaging, and as a result there has been significant efforts towards optimizing the performance of SiC avalanche photodiodes (APDs).

In this work, we have developed experimental techniques to characterize the deep-UV spectral response of 4H-SiC avalanche photodiodes, and we are working towards implementing a functional SPICE model which contains spectral respon-

[†]Originally published as: **M. Dandin**, A. Akturk, A. Vert, S. Soloviev, P. Sandvik, S. Potbhare, N. Goldsman, P. Abshire, and K. P. Cheung, "*Optoelectronic Characterization of 4H-SiC Avalanche Photodiodes Operated in DC and in Geiger Mode*,"in *IEEE International Semiconductor Device Research Symposium*, College Park, Maryland, USA, 2011. (2 pages).

sivity parameters as well as built-in capabilities for Geiger mode simulation. The model will enable circuit simulations of complex imaging systems which comprise SiC APDs as a front-end phototransducer.

C.2 Photocurrent Measurements

The first set of experiments we conducted consisted of measuring the devices I-V characteristics in the reverse bias regime. A Keithley 237 source-measure unit (SMU) was used to source voltages from 0 V to 350 V in steps of 2.5 V. The output of the SMU was connected to the cathode, and the anode was grounded. The structural features of the APD under test are reported in ref. [217]. The current was measured in the dark, and under different illumination conditions. Figure C.1 shows the I-V behavior of the SiC APD.

As can be seen on the figure, the device breaks down around 325 V in the dark, and at a slightly lower reverse bias voltage under illumination conditions (traces labeled photocurrent). To generate photon stimuli at different wavelengths, a monochromator fitted with a laser-driven light source was used. In order to ensure a high optical power throughput in the deep-UV region, both the light source and the monochromator were operated under a nitrogen-purged environment. A picture of a similar setup is shown in Figure C.2. The chip was characterized from 200 nm to 400 nm using facilities at the National Institute of Standards and Technology (NIST); the optical power density incident on the APD during the experiment is shown in Figure C.3.

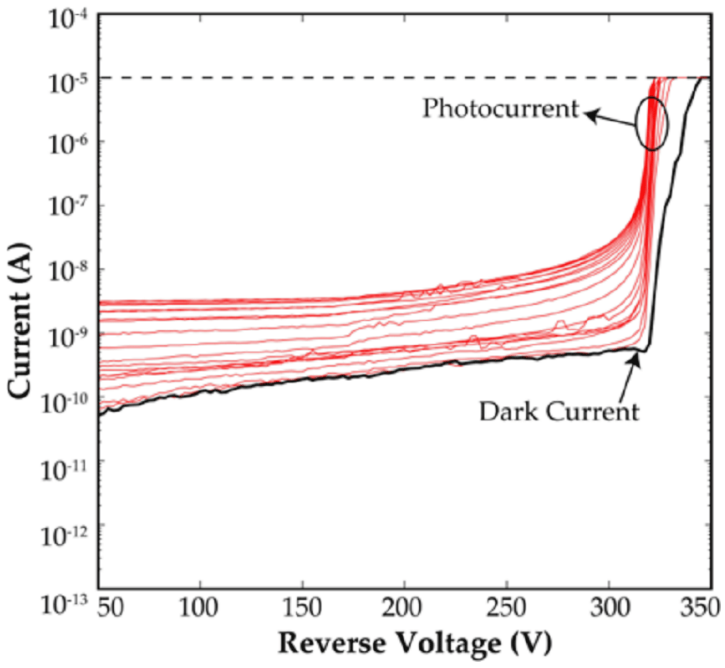

Figure C.1: I-V characteristics of the devices in the dark along with measured photocurrent for different wavelengths. The dotted line indicates the compliance level on the measurement.

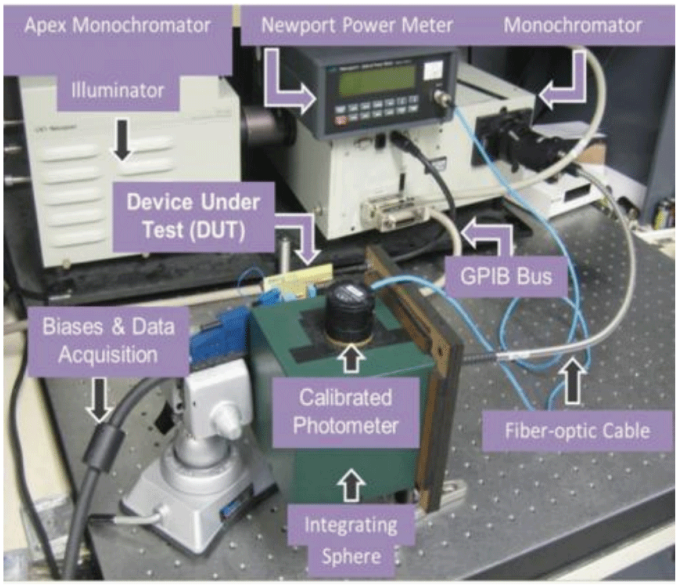

Figure C.2: Example of a typical experimental setup used in characterizing the device. In this case, a calibrated photometer head coupled to an integrating sphere is used to measure the optical power incident on the DUT.

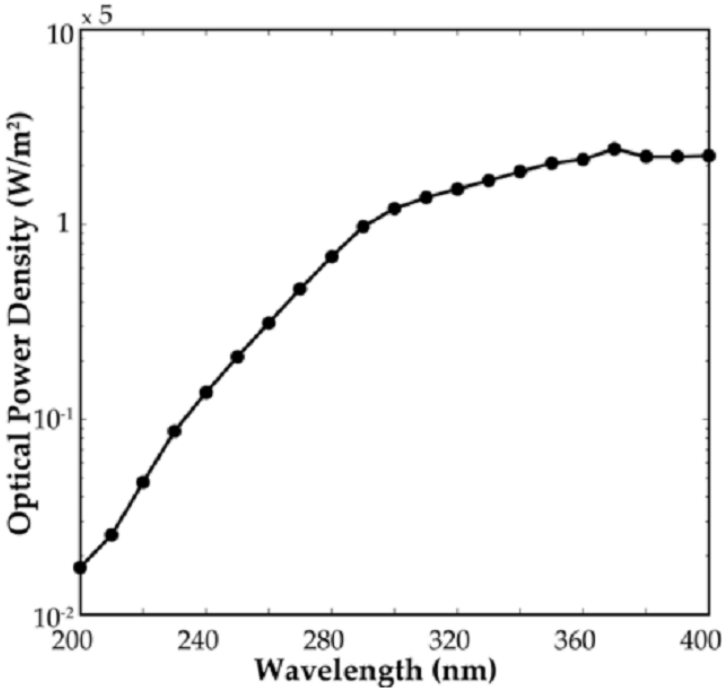

Figure C.3: Laser-driven light source power density.

C.3 Spectral Responsivity Measurement

The spectral responsivity (Figure C.4a) and b)) was calculated by dividing the photocurrent by the incident optical power. That ratio was then scaled by the ratio of the area of the photometer-head (see Figure C.2) to that of the active area of the APD. The responsivity was found to be maximum at 280 nm; this finding was consistent with previously published spectra collected for the same structure at low reverse-biases. However, for a fully-functional SPICE model, the responsivity must be measured over a wide range of biasing conditions. To do so, we repeated the above-mentioned experiment for biases ranging from 0 V to 350 V. The peak responsivity was found to be of the order of 60 A/W at a reverse bias of 320 V, which suggest that there can be a significant gain in responsivity at the lower end

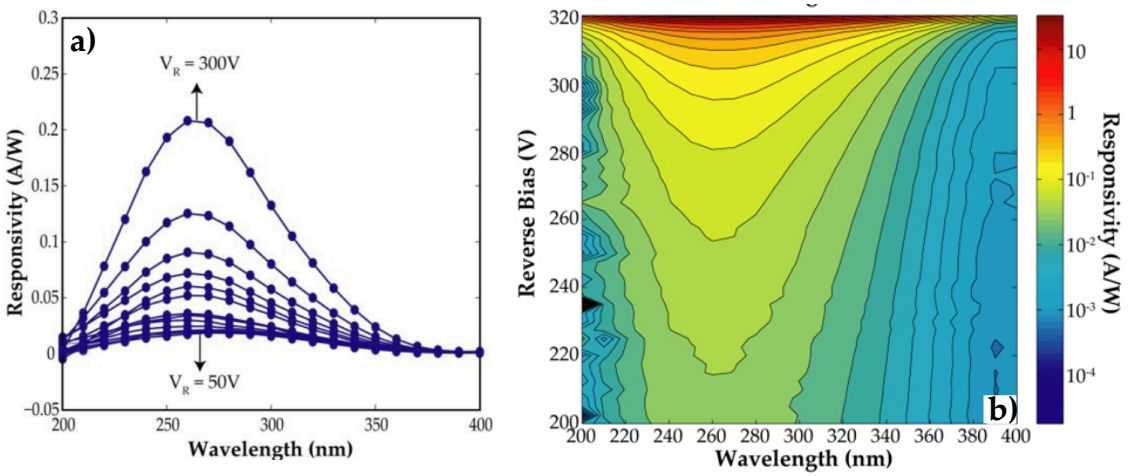

Figure C.4: a) Spectral responsivity curves of the SiC APD measured at reverse biases ranging from 50V to 30 V in steps 12.5 V (other bias conditions mentioned in the text not shown.) b) Spectral responsivity contour plot.

of the spectrum if the device is operated in the high-field region. Operating the high-field region, however, also amplifies the dark current, and in Geiger mode, this yields a high dark count rate.

C.4 Geiger Mode Operation

We performed a study on the Geiger mode operation of the above-mentioned SiC APD for different reverse voltages. The APD was tested in Geiger mode using a load resistor of 130kΩ and a termination resistor of 100Ω. The dark count rate (Figure C.5) increased an order of magnitude for a 5 V increase in the reverse bias voltage magnitude before saturation. The saturation of the count rate was due to the long reset transient typically observed in passive quenching.

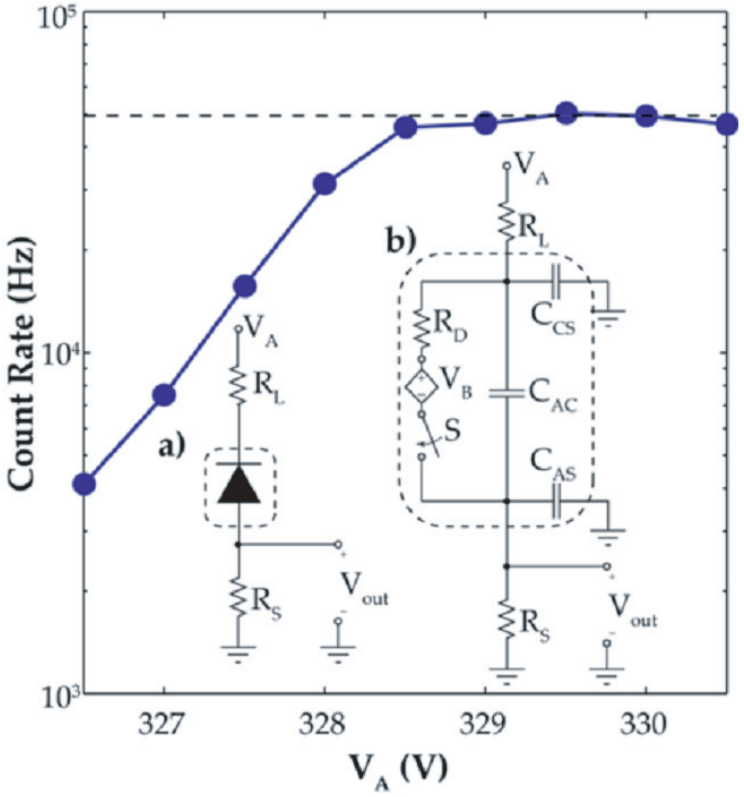

Figure C.5: Dark count rate of the SiC APD as a function of reverse voltage (V_A). The insets show the Geiger mode circuit and its equivalent circuit model.

Appendix D

Post-CMOS Packaging Methods for Integrated Biosensors†

We report on several techniques that have been pursued in our laboratories for packaging complementary metal-oxide semiconductor (CMOS) sensors for use in biological environments, such as cell medium. These techniques are suited for single CMOS die ranging from $1.5 \times 1.5\ mm^2$ to $3 \times 3\ mm^2$ in area. The first method consisted of creating high aspect ratio structures from negative-tone photocurable resins to simultaneously encapsulate wirebonds from the chip to a ceramic package and create a cell culture well. The second technique used a photolithographically defined barrier on the die to allow the use of non-photocurable resins as encapsulants. The third method consisted of re-routing the die padframe using photolithographically defined, planar leads to a much larger padframe; this will allow the chip to be integrated with microfluidic networks. Finally, we show a method in which the encapsulant was also used as an optical filter and as a base for integrating more complex structures.

D.1 Introduction

Packaging is one of the most important features of any sensor design; the package must permit the transducer module to be interfaced with the sensing medium

†Originally published as: **M. Dandin**, I. D. Jung, M. Piyasena, J. Gallagher, N. Nelson, M. Urdaneta, C. Artis, P. abshire, and E. Smela, "Post-CMOS Packaging Methods for Integrated Biosensors", in IEEE Conference on Sensors, Chirstchurch, New Zealand, pp. 795–798, 2009.

without affecting the functioning of the other components. In the case of biosensors, the package must allow the introduction of liquid analytes to the sensing surface while preserving the sensor's electrical integrity.

Several investigators have demonstrated fabrication sequences for creating biosensor packages. These steps are usually application-specific, although they are all based on conventional microfabrication techniques, namely, photolithography, anodic bonding, electroplating, and injection molding. Velten *et al.* have provided a thorough review of microfabrication and rapid prototyping techniques that are typically utilized for biosensor packaging [218].

In this paper, however, we focus on a problem not often considered in the packaging literature; we aim to package *single* and *tiny* CMOS chips with sensing micro-electrode arrays for use in bio-fluids, with the longer-term aim of integrating microfabricated elements such as micro-vials and microfluidic networks. CMOS chips are expected to confer significant capability to biosensor platforms by providing on-board transduction, signal processing, and control.

Packaging of these CMOS sensors is difficult because the diced chips are only $1.5 \times 1.5\ mm^2$ or $3 \times 3\ mm^2$ in area. Because of the large cost associated with acquiring full CMOS wafers, many university groups submit their designs for fabrication on shared multi-project wafers, and thus only diced samples are available. As a result, one is limited to developing packaging solutions for single units. Handling, as well as photolithography, is thus challenging.

In developing a suitable package for our CMOS sensors, we have investigated four different approaches. The first consisted of casting negative-tone *photocurable*

epoxy over the chip and photolithographically defining an opening to the sensing structures (see Fig. D.1 and ref. [219]). The second method made use of a photolithographically defined ring structure on the die, added prior to wirebonding, that served as a barrier to epoxy flow. This allowed the use of *non-photocurable* epoxy for encapsulating the wirebonds. In the third we fabricated a redistribution platform with planar leads in order to allow microfluidic integration with the chips; this method consisted of redistributing the die padframe to a much larger one, thereby allowing wirebonds to be placed further away from the active area of the chip. Finally, we showed a simple method for encapsulating wirebonds with a polymeric material that simultaneously served as an optical filter.

D.2 Experimental Results

In this section we briefly describe the CMOS sensors and circuits that have been designed, and also how the function of each design influences the choice of packaging method. We also describe a test structure that was designed for the purpose of assessing package viability. We then provide the experimental procedures for packaging the various sensors.

D.2.1 CMOS Suite

We have demonstrated several CMOS-based biosensors. They are: a bioamplifier, which is an active electrode array, for recording the spiking activity of electrogenic cells [220]; a differential photodetector for transducing low level biosig-

nals such as bio-chemiluminescence and fluorescence [202]; a capacitive sensor for monitoring cell proliferation and cell adhesion [221]. We have also shown an integrated potentiostat circuit for actuating the lids of microfabricated vials [222, 223].

Of the sensors mentioned above, the active electrode array, the capacitive sensor, and the integrated potentiostat require a package that provides direct access of an aqueous medium to the chip surface, since the sensors require close proximity of the cells for transduction. For instance, cells must be in direct contact with the electrodes for transducing action potentials. Similarly, cells must be in close proximity for adhesion strength to be monitored as a change in capacitance. In the case of the potentiostat, the medium must be in direct contact with the actuators because the actuation mechanism is electrochemical.

The optical sensors, on the other hand, do not require direct access to the chip surface. Therefore, encapsulation materials can be simply cast over the chip. Nevertheless, this must be done in such a way as to prevent unwanted signal attenuation. Packaging of these sensors is less challenging, since there is no need for patterning the encapsulant.

D.2.2 Test Structure

A test structure used for assessing package lifetime is shown in Fig. D.2d. It consisted of a 3 x 3 mm^2 oxidized piece of Si with an aluminum pattern replicating the top-metal layer of our bio-amp chip. On the periphery of the test chip each bond pad was shorted with the adjacent one to form pairs. Once the chip was mounted

and bonded to a ceramic package and the epoxy applied, these shorted bondpads provided a means to monitor failures in wire bond attachment: an open loop (infinite resistance) showed that there was a discontinuity between the wirebonds.

D.2.3 High-aspect ratio patterning of photocurable materials[‡]

In order to encapsulate the bond wires while leaving an opening above the sensors (see Fig. D.1(a)), we used Loctite^{TM} 3340, a photopatternable polymer which has the advantage of being cured upon exposure to ultraviolet light [219]. The polymer was cast over the entire chip, which had previously been glued into the ceramic package cavity and wirebonded. A mask was applied directly over the Loctite to block the light over the center, active area of the chip. (The mask was 5×5 mm^2 and consisted of a black square of dimensions 1.2×1.2 mm^2 or 2.5×2.5 mm^2 printed with a high-resolution printer on a mylar sheet.)

Due to the dimensions the mask, it was easily manipulated under a light microscope, and accurate placement could be achieved. The chip was exposed to UV light for 6 minutes, and the unexposed portions were rinsed with alternating streams of ethyl acetate and water, leaving the active chip surface available for interfacing with cells. As Fig. D.1 shows, the encapsulation could be done in multiple steps to create multiple layers of the polymer with increasingly larger openings (Figure D.1). The chip was left at ambient temperature and pressure for 24 hours to ensure that any remaining solvent had evaporated prior to cell plating. There was no noticeable

[‡] Procedure developed by my colleagues R. Delille, M. Urdaneta, S. Moseley, and E. Smela (ref. [219]).

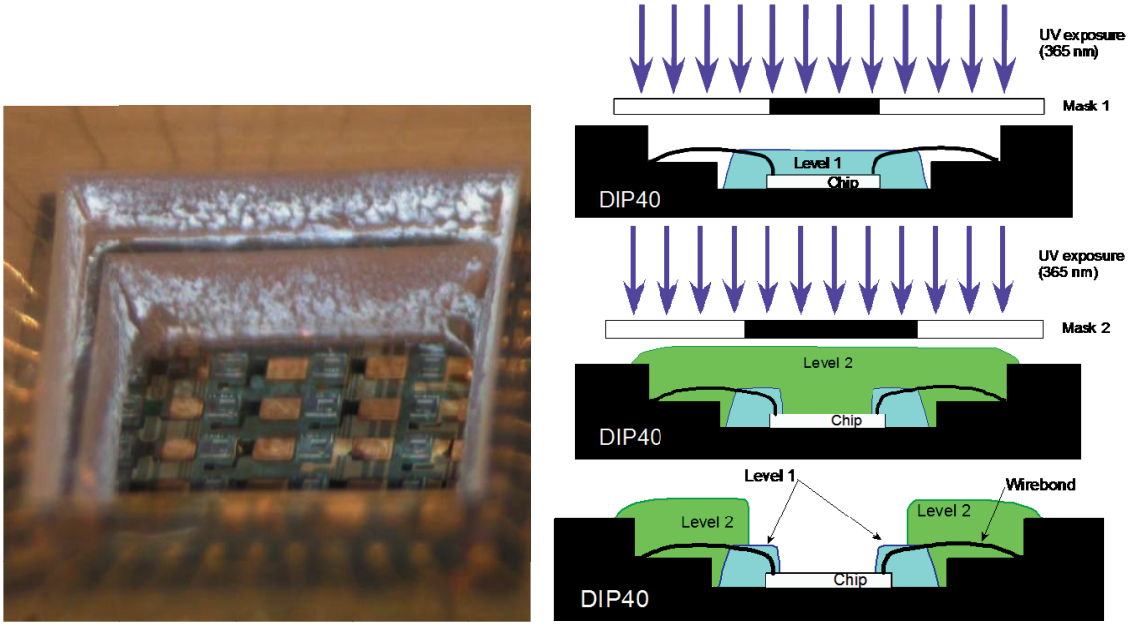

(a) (b)

Figure D.1: (a) Encapsulation of bond wires with two layers of Loctite. (b) Overview of Loctite encapsulation process.

shrinkage of the Loctite^{TM} after it had cured.

One disadvantage of the method is that it must be done individually, chip by chip. Another disadvantage is that exposure to ethanol, used for sterilization in standard cell culture practice, causes package failure. The main disadvantage, however, is that the package fails at unpredictable times. While chips packaged with Loctite 3340 have been used for cell sensing experiments for up to one week at 100% humidity in 5% CO_2 at 37 °C, packages may fail as soon as the first day, typically due to bond wire detachment from the chip. The reason for this is most likely swelling of the polymer in the cell medium.

D.2.4 Photolithographically defined epoxy barriers

To be able to work with polymers that swell less upon immersion in aqueous media, we also investigated a second packaging method, which was first proposed by Martin et al. [224]. It involves the use of an SU-8 dam and relies upon the surface tension of the epoxy to stop at this dam.

The SU8 dam is in the form of a square ring between the active area of the chip and the bond pads. The SU-8 is used with an adhesion promoter to ensure that it does not delaminate after prolonged immersion in cell medium. Epoxy is introduced outside the dam and allowed to flow through the bond wires. If the surface tension of the epoxy is just right, then it stops flowing at the dam and cures covering the wires but not the chip active area. The requirements on the epoxy, other than the right flow characteristics and surface tension, are that is biocompatible, has a sufficiently rapid cure time, and adheres well to the chip surface. If the cure time is too long, then the epoxy overflows the dam, and if the adhesion is not strong, then it delaminates.

Biocompatibility tests of the epoxy with SU-8 were performed according to standard procedures. Bovine aortic smooth muscle cells (BAOSMC)were plated into culture wells defined by the SU-8 and epoxy on oxidized silicon surfaces. The proliferation of the cells was monitored visually over a four-day period and compared with growth rates in cell culture flasks.

A range of epoxies was examined for biocompatibility, adhesion, and curing. Some absorbed the cell medium (as evidenced by it turning red after immersion in

a bath containing phenyl red), others overflowed the dam, others proved not to be biocompatible, and still others did not flow between and around the wires. Three epoxies met those initial criteria. They were used to package the test structures described in section B. After encapsulation of the bonded chips, the packages were surmounted by wells that were filled with cell medium and put into an incubator at 37 °C. The wire bonds were tested daily for several weeks. Unfortunately, bond wire failures were recorded within a few days for every one of those materials. We therefore conclude that this packaging method is insufficiently reliable for our purposes.

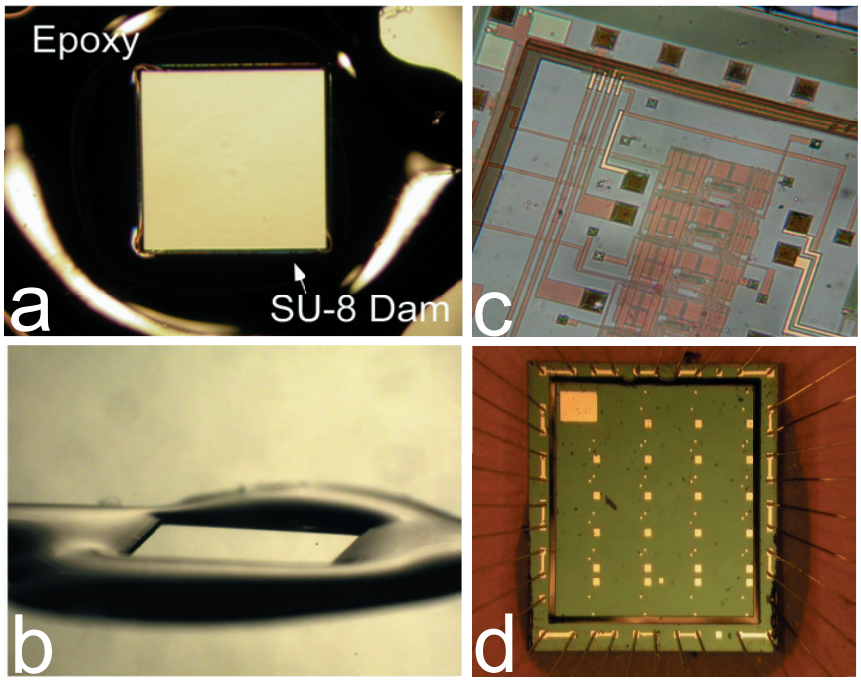

Figure D.2: (a) Top view of an encapsulant flown around a photolithographically defined SU-8 dam. (b) Bird's eye view. In this example, the encapsulating epoxy successfully flowed around the wires and stopped at the dam. (c) Dam fabricated on an electrolessly plated 3 × 3 mm^2 CMOS chip. (d) Wirebonded test chip, 3 ×s 3 mm^2, with an SU8 barrier.

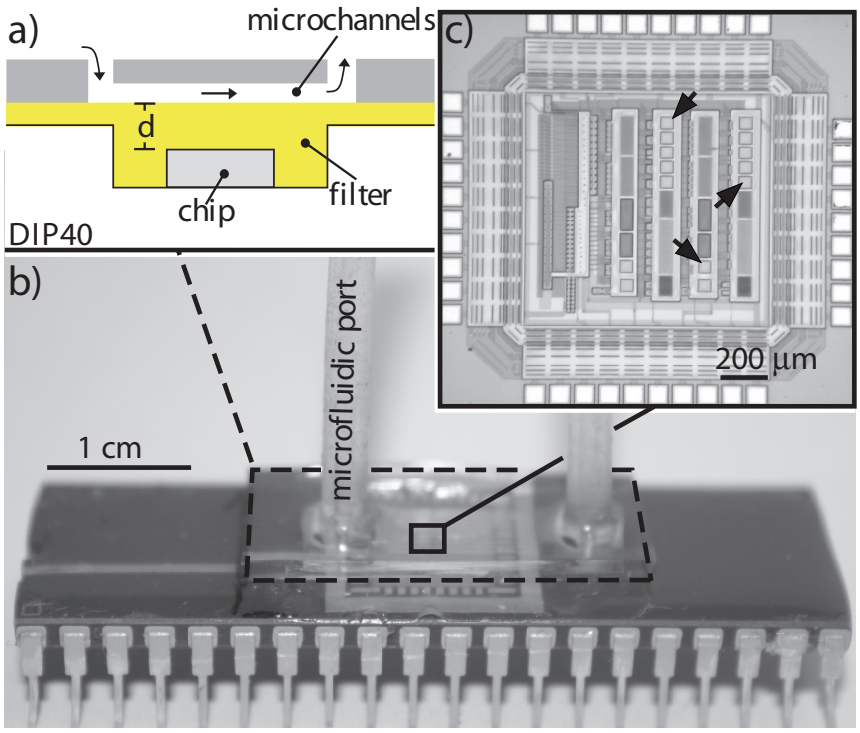

Figure D.3: (a) Cross-sectional view of an optical sensor with a cast filter/encapsulant (b) Integration of the encapsulated chip with a microfluidic network. (c) Photomicrograph of the die (arrows indicate location of photodiodes).

D.2.5 Micromachined redistribution padframes (MRP)

Like the previous two methods, the MRP method was designed for chips for which direct access to the chip surface is necessary, but with the aim of allowing later integration of microfluidics. The process starts by bulk micromachining a cavity into a silicon wafer using deep reactive ion etching (DRIE) in an inductively coupled plasma etcher. The cavity is as deep as the chip is thick (between 250 and 300 μm). This is to ensure that the chip surface is flush with the wafer surface after the chip is inserted into the cavity.

The DRIE step was performed with the following settings on the etcher. The pressure, for both passivation and etching cycles, was set at 15 mT, the bias power

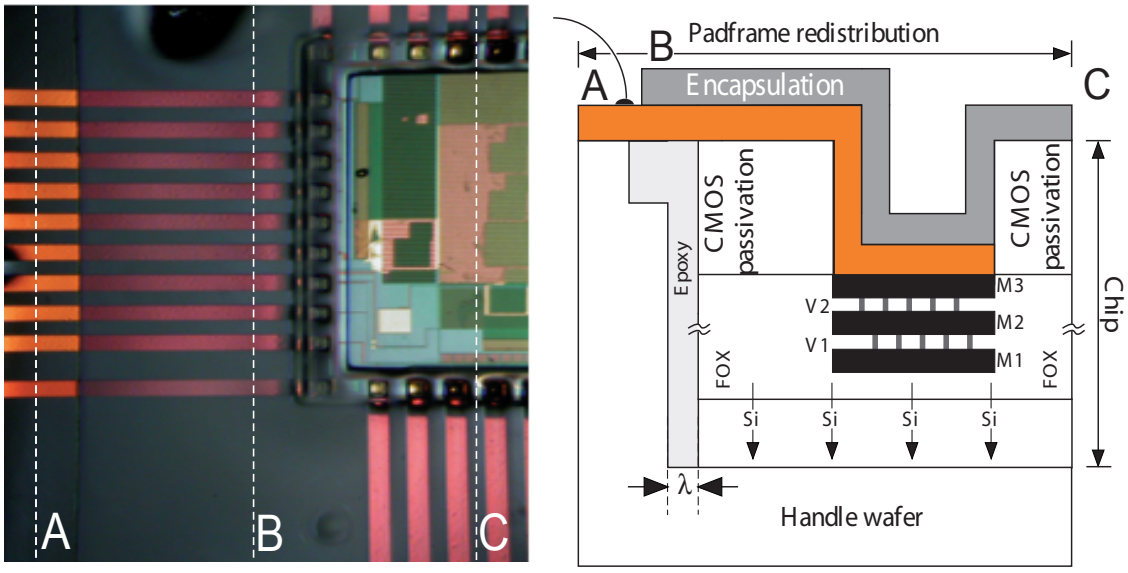

(a) (b)

Figure D.4: (a) Photomicrograph of a chip packaged using the MRP method. (b) Cross-sectional view of both the MRP platform and the CMOS chip. A, B, and C indicate crossectional views of regions shown in (a).

for the etch power was set as 14 W for the etch cycle and 0 W for the passivation cycle, and the RF power was set at 600 W for both cycles. The flow rates of SF_6, C_4F_8, and O_2 were set at 130, 0, and 13 sccm, respectively for the etch cycle. These flow rates were set at 0, 85, and 0 sccm for the passivation cycle. An overlap of two seconds was chosen for the two cycles. This yielded an average etch rate of 1.90 μm/min and a selectivity of 30:1 for the etch mask, which was the photoresist AZ4620. A photograph of the redistributed chip and a diagram of its cross-sectional area are shown in Fig. D.4.

Following the bulk micromachining step, a thin layer of epoxy was applied to the back side of the chip, and the chip was mounted in the cavity. A microscope slide was used to apply an even force on the chip to ensure that it was properly adhered to the cavity. Subsequently, SU-8 was uniformly coated on the wafer. This

first layer of encapsulation ensured that any gaps between the cavity walls and the chips were bridged (denoted by the gray area labeled "Epoxy" on Fig. D.4(b)). The next step consisted of photolithographically defining the planar metal leads. Finally, a second SU-8 coating was deposited and patterned in order to open a window for access to the chip surface while passivating the metal lines.

Several encapsulation materials are now being investigated for enhancing protection of the bondpads. This packaging method has not yet been tested in cell medium.

D.2.6 Packaging of optical CMOS sensors

The easiest sensors to package, as previously stated, were the optical sensors. As shown in Fig. D.3, an encapsulant can easily be cast within the ceramic package cavity and cured, since no patterning is required. The cured film can be used as a substrate for integrating additional structures provided it has a flat enough surface. Figure D.3 shows a chip onto which a PDMS film, doped with 2-2-hydroxy 5-methyl-phenyl benzontrizole (BTA), was cast. A microfluidic structure was subsequently bonded onto the cured PDMS using O_2 plasma bonding. This package allowed the sensor to be used over a period of several weeks for multiple 10-hour long experiments.

D.3 Conclusion

In this paper we have shown several methods that have been tried in our labs for packaging single CMOS dice obtained from multi-project wafer fabrication runs, with varied levels of success. Ultraviolet curing of thick polymer precursor layers cast over the chip allowed successful operation of the CMOS chip for 1 to 2 weeks in the best cases, but immediate failure in the worst. The method of photolithographically defining a ring at the periphery of the die to segregate the active area from the perimeter pad frame and then applying epoxy suffered from several failure mechanisms, and was found to be too unreliable. A third method, which is still under investigation, consisted of placing the chip in a cavity and re-routing the padframe, allowing the integration of microfluidics. The reliability of this packaging method is being investigated using the test platform that we specifically developed to study bond wire integrity. Finally, we reported on the packaging of an optical sensor. In this method, the encapsulant consisted of a chromophore-doped PDMS layer, which also functioned as an optical filter. This packaging method was straightforward and successful, allowing long-term use of the sensor.

Appendix E

Poisson Statistics of Photoelectron Emission

E.1 Introduction

In an optical sensor front-end, the photo-generated current exhibits random fluctuations that are independent of the ROC noise sources and of thermal energy. These fluctuations are known as the shot noise, and they arise from the discrete and random removal of energy quanta from the incident radiation field. For this reason, shot noise is a quantum mechanical random process, and it is the fundamental noise which underlies all light detection and measurement applications.

In a detector that integrates photo-generated charge, like an APS for example, the shot noise manifests itself as an uncertainty in the source follower-buffered voltage of the integration node. On the other hand, in a detector that performs photo-electric counting, like the PGSPAD, it can be estimated from the uncertainty in the count rate.

Thus, the number of photo-electrons generated in a detector is a random process, irrespective of the detector's mode of operation and architecture. The distribution that describes this random process can be derived by considering photo-electron emission in an ideal vacuum photocathode (shown in Figure E.1a)). (This analysis is credited to Davenport and Root. [225])

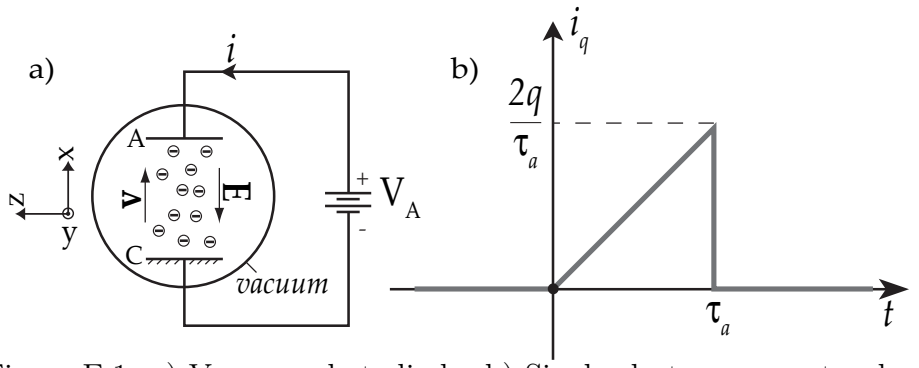

Figure E.1: a) Vacuum photodiode. b) Single electron current pulse.

E.2 Single-Electron Current in a Vacuum Diode

In Figure E.1 the plate (or anode) is biased at a constant voltage denoted V_A and the photocathode is held at ground. This systems is governed by the following electrostatic and classical kinematic equations:

$$\mathbf{F_m} = m\mathbf{a} \tag{E.1}$$

$$\mathbf{F_l} = -q\mathbf{E} \tag{E.2}$$

$$\mathbf{E} = -\boldsymbol{\nabla} V \tag{E.3}$$

$$\boldsymbol{\nabla^2} V = -\frac{\rho}{\epsilon} \tag{E.4}$$

$$\mathbf{J} = \rho \boldsymbol{v}. \tag{E.5}$$

Here , $\mathbf{F_m}$ is the Newtonian force that a moving electron is subjected to as a result of its acceleration through the electric field $\boldsymbol{E}$ resulting from the potential difference between the two electrodes, ρ is the charge density, $\boldsymbol{J}$ the current density, and $\boldsymbol{v}$ the velocity of the electron. $\mathbf{F_l}$ is the Lorentz force in the absence of a magnetic field ($\boldsymbol{B} = 0$).

We first solve for the potential as a function of distance. We restrict our

analysis to only one dimension, that is the y and z components of the E-field are zero. We further assume that the temperature is constant and that there are no space charge effects. The latter assumption means that the electron does not interact with other electrons during its motion and that its initial velocity, in comparison to its terminal velocity (at the plate) is negligible. Consequently, the Poisson's equation (E.4) simplifies to Laplace's equation ($\boldsymbol{\nabla^2} V = 0$). This yields the boundary value problem (Equations E.6,E.7, and E.8) whose solution is shown in Equation E.9.

$$\frac{\delta^2 V}{\delta x^2} = 0 \tag{E.6}$$

$$V(0) = 0 \tag{E.7}$$

$$V(d) = V_A \tag{E.8}$$

$$V(x) = \frac{V_A}{d} x \tag{E.9}$$

The electric field is obtained using Equation E.3. In Equation E.10, the vector $\hat{\mathbf{i}}$ indicates the basis vector in the x-direction in a Cartesian reference frame.

$$\mathbf{E} = -\frac{V_A}{d} \hat{\mathbf{i}} \tag{E.10}$$

We may now find a second order differential that describes the motion of the electron by using a force balance equation. This is done by equating the Lorentz

force to the Newtonian force. This yields:

$$\mathbf{F_l} = \mathbf{F_m} \tag{E.11}$$

$$q\frac{V_A}{d}\hat{\mathbf{i}} = m\frac{d^2x}{dt^2}\hat{\mathbf{i}} \tag{E.12}$$

$$q\frac{V_A}{dm} = \frac{d^2x}{dt^2} \tag{E.13}$$

By integrating Equation E.13 once, we obtain the velocity. Recall that we assume the initial velocity of the electron to be negligible compared to terminal velocity; this means v(0) = 0. Further integration yields a closed form solution (Equation E.15) for the position of the electron as it travels towards the plate.

$$\mathbf{v(t)} = \frac{qV_A}{dm}t \tag{E.14}$$

$$\mathbf{x(t)} = \frac{1}{2}\frac{qV_A}{dm}t^2 \tag{E.15}$$

The transit time, i.e. the time it takes the electron to travel a distance equal to d is found by solving for t in equation E.15.

$$\tau_a = \sqrt{\frac{2m}{qV_A}}d \tag{E.16}$$

We have now all the equations that are needed in order to find the current induced on the plate as a result of the motion of the single charge. This is done by setting up an energy balance equation that relates the potential energy of the

moving electron and the work that need to be done to induce a net charge Q at the plate.

$$U = q\frac{V_A}{d}x \tag{E.17}$$

$$W = QV_A \tag{E.18}$$

$$q\frac{V_A}{d}x = QV_A \tag{E.19}$$

$$i_e(t) = \frac{dQ}{dt} \tag{E.20}$$

$$i_e(t) = \frac{q}{d}\frac{dx}{dt} \tag{E.21}$$

$$\tag{E.22}$$

Expressing Equation E.21 in terms of the transit time, we obtain the final expression for the current pulse resulting from pulling a single charge from the cathode, and it is plotted in Figure E.1b).

$$i_e(t) = \left(\frac{2q}{\tau_a}\right)\left(\frac{t}{\tau_a}\right), \ for\ 0 \leq t \leq \tau_a \tag{E.23}$$

E.3 Photo-electron Emission Probability in a Time Interval τ

Equation E.23 suggest that each electron emitted from the photocathode creates a current pulse of duration τ_a. In this section, we derive the statistical distribution that accounts for the number of these current pulses in a time interval of duration τ, where $\tau \geq \tau_a$. We begin by deriving the probability that no pulses are

emitted in time window τ; using that result, we subsequently derive the probability of having k events in that same time interval.

In order to arrive at the latter, we assume that, in an incremental increase $\Delta\tau$, there can either be only one event, or no event at all. Mathematically, this is written as shown in Equation E.24, with p, denoting the probability measure.

$$p\left(0, \Delta\tau\right) + p\left(1, \Delta\tau\right) \quad = \quad 1 \tag{E.24}$$

We now assume that the probability of obtaining one event in the incremental time window is proportional (by a constant) to the length of the time window. That is:

$$p\left(1, \Delta\tau\right) \quad = \quad a\Delta\tau \tag{E.25}$$

If we further assume that the emission of one electron is independent of previous emissions, then statistical independence allows us to write:

$$p\left(0, \tau + \Delta\tau\right) \quad = \quad p\left(0, \tau\right) p\left(0, \Delta\tau\right) \tag{E.26}$$

Substituting in Equation E.25 and Equation E.24 in Equation E.26, we find an expression for $p\left(0, \Delta\tau\right)$. Taking the limit of $\Delta\tau \rightarrow 0$ in Equation E.27 yields

a first order difference equation whose solution is shown in Equation E.28. The difference equation was solved using the boundary condition shown in Equation E.29, which implies that when the time window $\Delta\tau$ is vanishingly small, there can be no emissions. In other words, the probability of having no emissions in a zero-width time interval is equal to 1.

$$\frac{p\left(0,\tau+\Delta\tau\right)-p\left(0,\tau\right)}{\Delta\tau} = -ap\left(0,\tau\right) \tag{E.27}$$

$$p\left(0,\tau\right) = e^{-a\tau} \tag{E.28}$$

$$p\left(0,0\right) = \lim_{\Delta\tau\rightarrow 0} p\left(0,\Delta\tau\right) = 1 \tag{E.29}$$

We now derive the probability of having K events in a time interval of duration τ. This probability, denoted $P(K,\tau)$, is a general expression for calculating the likelihood of having an arbitrary number of electron emissions in a given time window. The derivation begins by considering a time interval of duration $\tau+\Delta\tau$ and by again assuming that emissions times are statistically independent.

We write the following, with the latter assumption permitting the expansion of the left-hand side of equation E.30 as a product of probabilities:

$$p\left(k,\tau+\Delta\tau\right) = p\left(k,\tau\right)\times p\left(k,\Delta\tau\right). \tag{E.30}$$

However, it is more convenient to expand the left-hand side of Equation E.30 as a sum of conditional probabilities by virtue of the assumed statistical independence of the emission times. Equation E.30 is becomes:

$$p\left(k,\tau+\Delta\tau\right) \;=\; p\left(k-1,\tau;1,\Delta\tau\right)+p\left(k,\tau;0,\Delta\tau\right). \tag{E.31}$$

Furthermore,

$$p\left(k,\tau+\Delta\tau\right) \;=\; p\left(k-1,\tau\right)p\left(1,\Delta\tau\right)+p\left(k,\tau\right)p\left(0,\Delta\tau\right). \tag{E.32}$$

Substituting in the values previously derived for $P\left(0,\tau\right)$ and $P\left(1,\tau\right)$ into Equation E.32 and dividing through by $\Delta\tau$ yields:

$$\frac{p\left(k,\tau+\Delta\tau\right)+p\left(k,\tau\right)}{\Delta\tau}+ap\left(k,\tau\right) \;=\; p\left(k-1,\tau\right). \tag{E.33}$$

For $\Delta\tau\rightarrow 0$, Equation E.33 becomes a recursive differential equation which establishes a relation between $p\left(k,\tau\right)$ and $p\left(k-1,\tau\right)$. Utilizing an appropriate integrating factor and the initial value $p\left(0,0\right)=0$, the solution of equation E.33 was found to be:

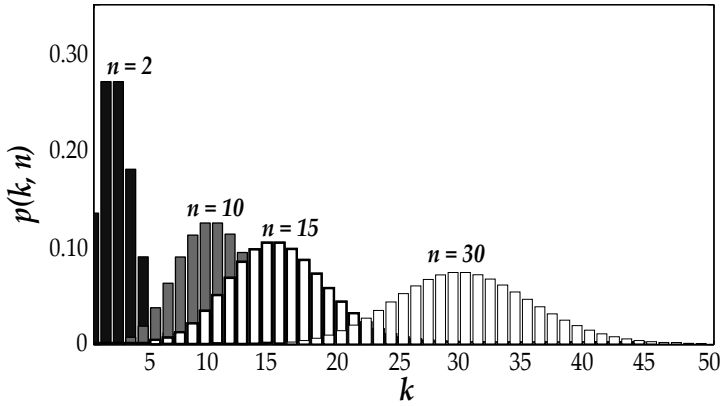

Figure E.2: Poisson distribution for $n = 2, 10, 15, 30$.

$$p\left(k,\tau\right) \;=\; ae^{-a\tau}\int_0^\tau e^{at}p\left(k-1,t\right)dt. \tag{E.34}$$

Using mathematical induction and $p\left(0,\tau\right) = e^{-a\tau}$ the following general expression is obtained:

$$p\left(k,\tau\right) \;=\; \frac{\left(a\tau\right)^k e^{-a\tau}}{k!} = \frac{\left(n\right)^k e^{-n}}{k!} \tag{E.35}$$

The above equation is none other the well-known Poisson probability mass function, $p\left(k,n\right)$, which describes arrival processes with mean $n = a\tau$. As expected, the normalization condition $(\sum_{k=0}^{\infty} p\left(k,n\right) = 1)$ is satisfied and for large values of k, the limit is Gaussian.

Equation E.35 is plotted in Figure E.2 for various n.

E.4 Shot Noise

Equation E.35 implies that the current I through the vacuum diode during time τ is proportional to the number of k electrons emitted at a fixed rate $r = \frac{k}{\tau}$ (Equation E.36). However, the *mean square* current is given by Equation E.37.

$$I = \frac{kq}{\tau} \tag{E.36}$$

$$\langle \Delta I^2 \rangle = \langle I^2 \rangle - \langle I \rangle^2 \tag{E.37}$$

The first term in the right-hand-side of Equation E.37 is computed directly from Equation E.36:

$$\langle I^2 \rangle = \langle k^2 \rangle \left(\frac{q}{\tau} \right)^2 . \tag{E.38}$$

Similarly, the second term is:

$$\langle I \rangle^2 = \langle k \rangle^2 \left(\frac{q}{\tau} \right)^2 . \tag{E.39}$$

Substituting Equations E.38 and E.39 into Equation E.37 yields:

$$\langle \Delta I^2 \rangle = \left(\frac{q}{\tau}\right)^2 \left(\langle k^2 \rangle - \langle k \rangle^2\right) \tag{E.40}$$

The second factor in Equation E.40 can be re-written as[1]:

$$\left(\langle k^2 \rangle - \langle k \rangle^2\right) \;=\; \left(\langle k^2 \rangle - n^2\right) = n. \tag{E.41}$$

Thus Equation E.40 yields:

$$\langle \Delta I^2 \rangle = n \left(\frac{q}{\tau}\right)^2 = \left(\frac{\langle I \rangle q}{\tau}\right). \tag{E.42}$$

Re-writing $\langle \Delta I^2 \rangle$ as $\overline{i^2}$ and $\dfrac{1}{\tau}$ as 2β, where β is the single-sided measurement bandwidth, yields the well-known equation for shot noise:

$$\overline{i^2} = 2q\langle I \rangle \beta. \tag{E.43}$$

[1]This is done by subtracting the first and second central moments of Equation E.35 and subsequently making use of the normalization condition [33].

Bibliography

[1] J. Bardeen and W. Brattain, "Three-electrode circuit element utilizing semiconductor materials," *U.S. Patent 2,524,035*, October, 3^{rd}, 1950.

[2] J. Bardeen and W. Brattain, "The transistor, a semi-conductor triode," *Phys. Rev.*, vol. 74, pp. 230–231, 1948.

[3] W. Shockley, "Circuit element utilizing semiconductive material," *U.S. Patent 2,569,347*, June, 26^{th}, 1948.

[4] W. Shockley, "The theory of p-n junctions in semiconductors and p-n junction transistors," *Bell System Technical Journal*, vol. 28, pp. 435–489, 1949.

[5] J. E. Lilienfeld, "Method and apparatus for controlling electric currents," *U.S. Patent 1,745,175*, January, 18^{th}, 1930.

[6] J. E. Lilienfeld, "Device for controlling electric current," *U.S. Patent 1,900,018*, March, 7^{th}, 1933.

[7] R. S. Muller, T. I. Kamins, and M. Chan, *Device Electronics for Integrated Circuits*. New York: John Wiley & Sons, 2006.

[8] J. Bryzek, K. Peterson, and W. McCulley, "Micromachines on the march," *IEEE Spectr.*, vol. 31, pp. 20–31, 1994.

[9] A. Manz, N. Graber, and H. M. Widmer, "Miniaturized chemical analysis systems – a novel concept for chemical sensing," *Sens. Actuators, B*, vol. 1, pp. 244–248, 1990.

[10] T. Thorsen, S. Maerkl, and S. Quake, "Microfluidic large-scale integration," *Science*, vol. 298, p. 580, 2002.

[11] C. Weisbuch, M. Rattier, L. Martinelli, H. Choumane, J. Avarre, Y. Marcy, G. Cerovic, M.-L. Miramon, and H. Benistys, "Towards portable, real-time, integrated fluorescence microarray diagnostics tools," *TBM-RBM*, vol. 28, pp. 216–223, 2007.

[12] K. Tainaka, R. Sakaguchi, H. Hayahsi, N. S., F. F. Liew, and T. Morii, "Design strategies of fluorescent biosensors based on biological macromolecular receptors," *Sensors*, vol. 10, pp. 1355–1376, 2010.

[13] L. Zhu, Q. Zhang, H. Feng, S. Ang, F. S. Chau, and W.-T. Liu, "Filter-based microfluidic device as platform for immunofluorescent assay of microbial cells," *Lab Chip*, vol. 4, pp. 337–341, 2004.

[14] P. S. Dittrich and P. Schwille, "An integrated microfluidic system for reaction, high-sensitivity detection, and sorting of fluorescent cells and particles," *Anal. Chem.*, vol. 75, pp. 5767–5774, 2003.

[15] M. A. McClain, C. T. Culbertson, S. C. Jacobson, and J. M. Ramsey, "Flow cytometry of *Escherichia coli* in microfluidic devices," *Anal. Chem.*, vol. 73, pp. 5334–5338, 2001.

[16] R. F. Wolffenbuttel, "State-of-the-art in integrated optical microspectrometers," *IEEE Trans. Instrum. Meas.*, vol. 53, no. 1, pp. 197–202, 2004.

[17] D. Palubiak, M. M. El-Desouki, O. Marinov, M. J. Deen, and Q. Fang, "High-speed, single-photon avalanche-photodiode imager for biomedical applications," *IEEE Sensors J.*, vol. 11, pp. 2401–2412, 2011.

[18] J. A. Richardson, E. A. G. Webster, L. A. Grant, and R. K. Henderson, "Scaleable single-photon avalanche diode structures in nanometer CMOS technology," vol. 58, pp. 2028–2034, 2011.

[19] M. Gersbach, C. Niclass, E. Charbon, J. Richardson, R. Henderson, and L. Grant, "A single photon detector implemented in a 130nm CMOS imaging process," in *Solid-State Device Research Conference, 2008. ESSDERC 2008. 38th European*, sept. 2008, pp. 270 –273.

[20] H. Finkelstein, M. Hsu, and S. Esener, "STI-bounded single-photon avalanche diode in a deep submicrometer CMOS technology," *IEEE Electron Device Lett.*, vol. 27, pp. 887–889, 2006.

[21] Y. Dattner and O. Yadid-Pecht, "Low Light CMOS Contact Imager with an Integrated Poly-Acrylic Emission Filter for Fluorescence Detection," *Sensors*, vol. 10, no. 5, pp. 5014–5027, 2010.

[22] M. Beiderman, T. Tam, A. Fish, G. A. Jullien, and O. Yadid-Pecht, "A Low-Light CMOS Contact Imager With an Emission Filter for Biosensing Applications," vol. 2, no. 3, pp. 193–203, 2008.

[23] O. Hofmann, X. H. Wang, A. Cornwell, B. Stephen, A. Raja, D. Bradley, A. deMello, and J. deMello, "Monolithically integrated dye-doped pdms long-pass filters for disposable on-chip fluorescence detection," *Lab Chip*, vol. 6, pp. 981–987, 2006.

[24] A. Llobera, S. Demming, H. N. Joensson, J. Vila-Planas, H. Andersson-Svahn, and S. Buettgenbach, "Monolithic PDMS passband filters for fluorescence detection," *Lab Chip*, vol. 10, no. 15, pp. 1987–1992, 2010.

[25] T. Graves-Abe, F. Pschenitzka, H. Z. Jin, B. Bollman, J. C. Sturm, and R. A. Register, "Solvent-enhanced dye diffusion in polymer thin films for polymer light-emitting diode application," *J. Appl. Phys.*, vol. 96, no. 12, pp. 7154–7163, 2004.

[26] D. J. Guerrero, B. DiMenna, T. Flaim, R. Mercado, and S. Sun, "Dyed red, green, and blue photoresist for manufacture of high resolution color filter arrays for image sensors," in *Sensors and Camera Systems for Scientific, Industrial and Digital Photography Applications IV*, vol. 5017. SPIE, 2003, pp. 298–306.

[27] K. Long, F. Pschenitzka, M. H. Lu, and J. C. Sturm, "Full-color oleds integrated by dry dye printing," *IEEE Trans. Electron Devices*, vol. 53, no. 9, pp. 2250–2258, 2006.

[28] M. Muasher and M. Sain, "The efficacy of photo stabilizers on the color change of wood filled plastic composites," *Polym. Degrad. Stabil.*, vol. 91, no. 5, pp. 1156–1165, 2006.

[29] G. A. Peyman, H. Sloan, and J. Lim, "Ultraviolet light absorbing pseudophakos," *J. Am. Intraocul. Implant. Soc.*, vol. 8, no. 4, pp. 357–360, 1982.

[30] J. Rabek, *Photostabilization of Polymers*, 1st ed. Stockholm: Elsevier Applied Science, 1990.

[31] R. Muller, T. Kamins, and M. Chan, *Device Electronics for Integrated Circuits*, 3rd ed. John Wiley & Sons, 2003.

[32] G. E. Stillman and C. M. Wolfe, *Semiconductors and Semimetals – Infrared Detectors II*. New York: Academic Press, 1977, vol. 12, ch. 5.

[33] R. H. Kingston, *Optical Sources, Detectors, and Systems: Fundamentals and Applications*. Academic Press, 1995.

[34] G. M. Williams and A. S. Huntington, "Probabilistic analysis of linear mode vs. Geiger mode APD FPAs for advanced LADAR enabled interceptors," in *Proceedings of the SPIE*, vol. 6220, 2006, p. 622008.

[35] A. Van der Ziel, *Noise in measurements*. New York: John Wiley & Sons, 1976.

[36] R. H. Kingston, *Optical Sources, Detectors, and Systems*. San Diego, CA, USA: Academic Press, 1995.

[37] A. Gallivanoni, I. Rech, and M. Ghioni, "Progress in quenching circuits for single photon avalanche diodes," *IEEE Trans. Nucl. Sci.*, vol. 57, pp. 3815–3826, 2010.

[38] S. Cova, M. Ghioni, A. Lotito, I. Rech, and F. Zappa, "Evolution and prospects for single-photon avalanche diodes and quenching circuits," *J. Mod. Opt.*, vol. 51, pp. 1267–1288, 2004.

[39] B. Aull, A. Loomis, D. Young, *et al.*, "Geiger-mode avalanche photodiodes for three dimensional imaging," *Linc. Lab. J.*, vol. 13, pp. 335–345, 2002.

[40] V. A. K. Temple and M. S. Adler, "Calculation of the diffusion curvature related avalanche breakdown in high-voltage planar p-n junctions," vol. 22, pp. 910–916, 1975.

[41] A. Rochas, A. R. Pauchard, P.-A. Besse, *et al.*, "Low-noise silicon avalanche photodiodes fabricated in conventional CMOS technologies," vol. 49, pp. 387–394, 2002.

[42] A. Pauchard, P.-A Besse, and R. S. Popovic, "Simulations of a new CMOS compatible method to enhance the breakdown voltage of highly-doped shallow PN junctions," in *International Conference on Modeling and Simulation of Microsystems*, 1998.

[43] M. Dandin, N. Nelson, V. Saveliev, *et al.*, "Single photon avalanche detectors in standard CMOS," in *IEEE Sensors Conference*, 2007.

[44] A. S. Grove, O. Leistiko, Jr., and W. W. Hooper, "Effect of surface fields on the breakdown voltage of planar silicon p-n junctions," vol. 14, pp. 157–162, 1967.

[45] K. G. McKay and K. B. McAfee, "Electron multiplication in silicon and germanium," vol. 91, pp. 1079–1084, 1953.

[46] K. G. McKay, "Avalanche breakdown in silicon," vol. 94, pp. 877–884, 1954.

[47] S. L. Miller, "Ionizaton rates for holes and electrons in silicon," vol. 105, pp. 1246–1249, 1957.

[48] J. Y. Tang and K. Hess, "Impact ionization of electrons in silicon (steady state)," *J. Appl. Phys.*, vol. 54, pp. 5139–5144, 1983.

[49] A. G. Chynoweth, "Ionization rates for electrons and holes in silicon," vol. 109, pp. 1537–1540, 1958.

[50] R. A. Kokosa and R. L. Davies, "Avalanche breakdown of diffused silicon p-n junctions," vol. 13, pp. 874–881, 1966.

[51] S. L. Miller, "Avalanche breakdown in germanium," vol. 99, pp. 1234–1241, 1955.

[52] H. Finkelstein, M. J. Hsu, S. Zlatanovic, and S. Esener, "Performance tradeoffs in single-photon avalanche diode miniaturization," *Rev. Sci. Instrum.*, vol. 78, 2007.

[53] B. Nouri, M. Dandin, and P. Abshire, "Characterization of single photon avalanche diodes in standard CMOS," in *IEEE Sensors Conference*, 2009, pp. 1889–1892.

[54] M. Dandin, P. Abshire, and E. Smela, "Optical filtering technologies for integrated fluorescence sensors," *Lab Chip*, vol. 7, no. 8, pp. 955–977, 2007.

[55] D. J. Massey, J. P. R. David, and G. J. Rees, "Temperature dependence of impact ionization in submicrometer silicon devices," vol. 53, pp. 2328–2334, 2006.

[56] A. Akturk, J. Allnutt, Z. Dilli, N. Goldsman, and M. Peckerar, "Device modeling at cryogenic temperatures: effects of incomplete ionization," vol. 54, pp. 2984–2990, 2007.

[57] M. Dandin, A. Akturk, B. Nouri, N. Goldsman, and P. Abshire, "Characterization of single-photon avalanche diodes in a $0.5\mu m$ standard CMOS process–Part 1: Perimeter breakdown suppression," *IEEE Sens. J.*, vol. 10, pp. 1682–1690, 2010.

[58] M. A. Marwick and A. G. Andreou, "Single photon avalanche photodetector with integrated quenching fabricated in TSMC 0.18 μm 1.8v CMOS process," *Electronics Letters*, vol. 44, 2008.

[59] C. Niclass, C. Favi, T. Kluter, M. Gersbach, and E. Charbon, "A 128 $\times$ 128 single-photon imager with on-chip column-level 10 b time-to-digital converter array capable of 97 ps resolution," *IEEE J. Solid-State Circuits*, vol. 43, pp. 2977–2989, 2008.

[60] A. Rochas, P.-A. Besse, and R. S. Popovic, "Actively recharged single photon counting avalanche photodiode integrated in an industrial CMOS process," *Sens. Actuators A: Phys.*, vol. 110, pp. 124–129, 2004.

[61] N. Chiem and D. J. Harrison, "Microchip-based capillary electrophoresis for immunoassays: Analysis of monoclonal antibodies and theophylline," *Anal. Chem.*, vol. 69, no. 3, pp. 373–378, 1997.

[62] Z. H. Liang, N. Chiem, G. Ocvirk, T. Tang, K. Fluri, and D. J. Harrison, "Microfabrication of a planar absorbance and fluorescence cell for integrated capillary electrophoresis devices," *Anal. Chem.*, vol. 68, no. 6, pp. 1040–1046, 1996.

[63] N. V. Zaytseva, V. N. Goral, R. A. Montagna, and A. J. Baeumner, "Development of a microfluidic biosensor module for pathogen detection," *Lab Chip*, vol. 5, no. 8, pp. 805–811, 2005.

[64] P. A. Auroux, D. Iossifidis, D. R. Reyes, and A. Manz, "Micro total analysis systems. 2. analytical standard operations and applications," *Anal. Chem.*, vol. 74, no. 12, pp. 2637–2652, 2002.

[65] P. A. Auroux, Y. Koc, A. deMello, A. Manz, and P. J. R. Day, "Miniaturised nucleic acid analysis," *Lab Chip*, vol. 4, no. 6, pp. 534–546, 2004.

[66] T. Vilkner, D. Janasek, and A. Manz, "Micro total analysis systems. recent developments," *Anal. Chem.*, vol. 76, no. 12, pp. 3373–3385, 2004.

[67] C. H. Lin, G. B. Lee, L. M. Fu, and S. H. Chen, "Integrated optical-fiber capillary electrophoresis microchips with novel spin-on-glass surface modification," *Biosens. Bioelectron.*, vol. 20, no. 1, pp. 83–90, 2004.

[68] A. Hanning, P. Lindberg, J. Westberg, and J. Roeraade, "Laser induced fluorescence detection by liquid core waveguiding applied to dna sequencing by capillary electrophoresis," *Anal. Chem.*, vol. 72, no. 15, pp. 3423–3430, 2000.

[69] S. L. Wang, X. J. Huang, Z. L. Fang, and P. K. Dasgupta, "A miniaturized liquid core waveguide-capillary electrophoresis system with flow injection sample introduction and fluorometric detection using light-emitting diodes," *Anal. Chem.*, vol. 73, no. 18, pp. 4545–4549, 2001.

[70] C. H. Lin, G. B. Lee, S. H. Chen, and G. L. Chang, "Micro capillary electrophoresis chips integrated with buried su-8/sog optical waveguides for bioanalytical applications," *Sens. Act. A*, vol. 107, no. 2, pp. 125–131, 2003.

[71] H. F. Li, Z. W. Cai, and J. M. Lin, "Separation of catecholamines by microchip electrophoresis with a simple integrated laser-induced fluorescence detector," *Anal. Chim. Acta*, vol. 565, no. 2, pp. 183–189, 2006.

[72] A. Hanning, J. Westberg, and J. Roeraade, "A liquid core waveguide fluorescence detector for multicapillary electrophoresis applied to dna sequencing in a 91-capillary array," *Electrophoresis*, vol. 21, no. 15, pp. 3290–3304, 2000.

[73] X. L. Zhang, H. B. Yin, J. M. Cooper, and S. J. Haswell, "A microfluidic-based system for analysis of single cells based on ca^{2+} flux," *Electrophoresis*, vol. 27, no. 24, pp. 5093–5100, 2006.

[74] A. T. Woolley and R. A. Mathies, "Ultra-high-speed dna sequencing using capillary electrophoresis chips," *Anal. Chem.*, vol. 67, no. 20, pp. 3676–3680, 1995.

[75] P. C. Simpson, D. Roach, A. T. Woolley, T. Thorsen, R. Johnston, G. F. Sensabaugh, and R. A. Mathies, "High-throughput genetic analysis using microfabricated 96-sample capillary array electrophoresis microplates," *Proc. Natl. Acad. Sci. U. S. A.*, vol. 95, no. 5, pp. 2256–2261, 1998.

[76] L. C. Waters, S. C. Jacobson, N. Kroutchinina, J. Khandurina, R. S. Foote, and J. M. Ramsey, "Microchip device for cell lysis, multiplex pcr amplification, and electrophoretic sizing," *Anal. Chem.*, vol. 70, no. 1, pp. 158–162, 1998.

[77] E. T. Lagally, P. C. Simpson, and R. A. Mathies, "Monolithic integrated microfluidic dna amplification and capillary electrophoresis analysis system," *Sens. Act. B*, vol. 63, no. 3, pp. 138–146, 2000.

[78] A. Y. Fu, C. Spence, A. Scherer, F. H. Arnold, and S. R. Quake, "A microfabricated fluorescence-activated cell sorter," *Nat. Biotechnol.*, vol. 17, no. 11, pp. 1109–1111, 1999.

[79] C. M. Chang, S. K. Hsiung, and G. B. Lee, "A micromachine-based flow cytometer chip integrated with micro-pumps/valves for multi-wavelength detection applications," *Mater. Sci. Forum*, vol. 505-507, pp. 637–642, 2006.

[80] Y. C. Tung, M. Zhang, C. T. Lin, K. Kurabayashi, and S. J. Skerlos, "Pdms-based opto-fluidic micro flow cytometer with two-color, multi-angle fluorescence detection capability using pin photodiodes," *Sens. Act. B*, vol. 98, no. 2-3, pp. 356–367, 2004.

[81] L. Cui, T. Zhang, and H. Morgan, "Optical particle detection integrated in a dielectrophoretic lab-on-a-chip," *J. Micromech. Microeng.*, vol. 12, no. 1, pp. 7–12, 2002.

[82] J. Voldman, M. L. Gray, M. Toner, and M. A. Schmidt, "A microfabrication-based dynamic array cytometer," *Anal. Chem.*, vol. 74, no. 16, pp. 3984–3990, 2002.

[83] D. Sander, M. Dandin, H. Ji, N. Nelson, and P. Abshire, "Low-noise cmos fluorescence sensor," in *IEEE Int. Symp. Circuits and Systems (ISCAS07)*, New Orleans, LA USA, 2007.

[84] E. J. Cho and F. V. Bright, "Optical sensor array and integrated light source," *Anal. Chem.*, vol. 73, no. 14, pp. 3289–3293, 2001.

[85] P. Neuzil, J. Pipper, and T. M. Hsieh, "Disposable real-time micropcr device: lab-on-a-chip at a low cost," *Mol. Biosyst.*, vol. 2, no. 6-7, pp. 292–298, 2006.

[86] P. Hua, J. P. Hole, J. S. Wilkinson, G. Proll, J. Tschmelak, G. Gauglitz, M. A. Jackson, R. Nudd, H. M. T. Griffith, R. A. Abuknesha, J. Kaiser, and P. Kraemmer, "Integrated optical fluorescence multisensor for water pollution," *Opt. Express*, vol. 13, no. 4, pp. 1124–1130, 2005.

[87] S. H. Huang and F. G. Tseng, "Development of a monolithic total internal reflection-based biochip utilizing a microprism array for fluorescence sensing," *J. Micromech. Microeng.*, vol. 15, no. 12, pp. 2235–2242, 2005.

[88] A. Cleary, S. Garcia-Blanco, A. Glidle, J. S. Aitchison, P. Laybourn, and J. M. Cooper, "An integrated fluorescence array as a platform for lab-on-a-chip technology using multimode interference splitters," *IEEE Sens. J.*, vol. 5, no. 6, pp. 1315–1320, 2005.

[89] A. Zanzotto, P. Boccazzi, N. Gorret, T. K. Van Dyk, A. J. Sinskey, and K. F. Jensen, "In situ measurement of bioluminescence and fluorescence in an integrated microbioreactor," *Biotechnol. Bioeng.*, vol. 93, no. 1, pp. 40–47, 2006.

[90] A. Zanzotto, N. Szita, P. Boccazzi, P. Lessard, A. J. Sinskey, and K. F. Jensen, "Membrane-aerated microbioreactor for high-throughput bioprocessing," *Biotechnol. Bioeng.*, vol. 87, no. 2, pp. 243–254, 2004.

[91] L. J. Golonka, T. Zawada, J. Radojewski, H. Roguszczak, and M. Stefanow, "Ltcc microfluidic system," *Int. J. Appl. Ceram. Technol.*, vol. 3, no. 2, pp. 150–156, 2006.

[92] L. J. Golonka, H. Roguszczak, T. Zawada, J. Radojewski, I. Grabowska, M. Chudy, A. Dybko, Z. Brzozka, and D. Stadnik, "Ltcc based microfluidic system with optical detection," *Sens. Act. B*, vol. 111, pp. 396–402, 2005, sp. Iss. SI.

[93] R. Irawan, C. M. Tay, S. C. Tjin, and C. Y. Fu, "Compact fluorescence detection using in-fiber microchannels - its potential for lab-on-a-chip applications," *Lab Chip*, vol. 6, no. 8, pp. 1095–1098, 2006.

[94] D. Kelly, K. M. Grace, X. Song, B. I. Swanson, D. Frayer, S. B. Mendes, and N. Peyghambarian, "Integrated optical biosensor for detection of multivalent proteins," *Opt. Lett.*, vol. 24, no. 23, pp. 1723–1725, 1999.

[95] A. Neubauer, D. Pum, U. B. Sleytr, I. Klimant, and O. S. Wolfbeis, "Fibre-optic glucose biosensor using enzyme membranes with 2-d crystalline structure," *Biosens. Bioelectron.*, vol. 11, no. 3, pp. 317–325, 1996.

[96] J. A. Fruetel, R. F. Renzi, V. A. VanderNoot, J. Stamps, B. A. Horn, J. A. A. West, S. Ferko, R. Crocker, C. G. Bailey, D. Arnold, B. Wiedenman, W. Y. Choi, D. Yee, I. Shokair, E. Hasselbrink, P. Paul, D. Rakestraw, and D. Padgen, "Microchip separations of protein biotoxins using an integrated hand-held device," *Electrophoresis*, vol. 26, no. 6, pp. 1144–1154, 2005.

[97] A. E. Bruno, S. Barnard, M. Rouilly, A. Waldner, J. Berger, and M. Ehrat, "All-solid state miniaturized fluorescence sensor array for the determination of critical gases and electrolytes in blood," *Anal. Chem.*, vol. 69, no. 3, pp. 507–513, 1997.

[98] R. A. Yotter and D. M. Wilson, "A review of photodetectors for sensing light-emitting reporters in biological systems," *IEEE Sens. J.*, vol. 3, no. 3, pp. 288–303, 2003.

[99] M. Wells, "Advances in optical detection strategies for reporter signal measurements," *Curr. Opin. Biotechnol.*, vol. 17, no. 1, pp. 28–33, 2006.

[100] N. Vekshin, *Photonics of Biopolymers*. New York: Springer-Verlag, 2002.

[101] L. A. Herzenberg, D. Parks, B. Sahaf, O. Perez, and M. Roederer, "The history and future of the fluorescence activated cell sorter and flow cytometry: A view from stanford," *Clin. Chem.*, vol. 48, no. 10, pp. 1819–1827, 2002.

[102] S. Weiss, "Fluorescence spectroscopy of single biomolecules," *Science*, vol. 283, no. 5408, pp. 1676–1683, 1999.

[103] T. Hirschfeld, "Optical microscopic observation of single small molecules," *Appl. Optics*, vol. 15, no. 12, pp. 2965–2966, 1976.

[104] R. A. Keller, W. P. Ambrose, P. M. Goodwin, J. H. Jett, J. C. Martin, and M. Wu, "Single molecule fluorescence analysis in solution," *Appl. Spectrosc.*, vol. 50, no. 7, pp. A12–A32, 1996.

[105] J. R. Lakowicz, *Principles of Fluorescence Spectroscopy.* New York: Plenum Publishing Corporation, 1983.

[106] J. A. Chediak, Z. S. Luo, J. G. Seo, N. Cheung, L. P. Lee, and T. D. Sands, "Heterogeneous integration of cds filters with gan leds for fluorescence detection microsystems," *Sens. Act. A*, vol. 111, no. 1, pp. 1–7, 2004.

[107] H. A. Macleod, *Thin Film Optical Filters.* London: Institute of Physics Publishing, 2001.

[108] J. Karunamuni, K. E. Stitzer, D. Eastwood, K. J. Albert, D. R. Walt, S. B. Brown, and M. L. Myrick, "Interference filter refinement for artificial nose fluorescence sensing," *Opt. Eng.*, vol. 40, no. 6, pp. 888–895, 2001.

[109] M. A. Burns, B. N. Johnson, S. N. Brahmasandra, K. Handique, J. R. Webster, M. Krishnan, T. S. Sammarco, P. M. Man, D. Jones, D. Heldsinger, C. H. Mastrangelo, and D. T. Burke, "An integrated nanoliter dna analysis device," *Science*, vol. 282, no. 5388, pp. 484–487, 1998.

[110] M. Adams, M. Enzelberger, S. Quake, and A. Scherer, "Microfluidic integration on detector arrays for absorption and fluorescence micro-spectrometers." *Sens. Act. A*, vol. 104, pp. 25–31, 2002.

[111] Y.-H. Kim, K.-S. Shin, J.-Y. Kang, E.-G. Yang, K.-K. Paek, D.-S. Seo, and B.-K. Ju, "Poly(dimethylsiloxane)-based packaging technique for microchip fluorescence detection system applications," *J. Microelectromech. Syst.*, vol. 15, no. 5, pp. 1152–1158, 2006.

[112] E. Thrush, O. Levi, W. Ha, K. Wang, S. J. Smith, and J. S. Harris Jr., "Integrated bio-fluorescence sensor," *J. Chromatogr. A*, vol. 1013, no. 1-2, pp. 103–110, 2003.

[113] E. Thrush, O. Levi, K. Wang, J. J. S. Harris, and S. Smith, "Integrated semiconductor fluorescent detection system for biochip and biomedical applications," in *2nd Annual International IEEE-EMBS Special Topic Conference on Microtechnologies in Medicine & Biology*, Madison, Wisconsin USA, 2002.

[114] V. Namasivayam, R. S. Lin, B. Johnson, S. Brahmasandra, Z. Razzacki, D. T. Burke, and M. A. Burns, "Advances in on-chip photodetection for applications in miniaturized genetic analysis systems," *J. Micromech. Microeng.*, vol. 14, no. 1, pp. 81–90, 2004.

[115] J. R. Webster, M. A. Burns, D. T. Burke, and C. H. Mastrangelo, "Monolithic capillary electrophoresis device with integrated fluorescence detector," *Anal. Chem.*, vol. 73, no. 7, pp. 1622–1626, 2001.

[116] H. Ji, D. Sander, A. Haas, and P. Abshire, "Contact imaging: simulation and experiment," *IEEE Trans. Circuits Syst. I-Regul. Pap.*, 2007, submitted.

[117] K. S. Shin, Y. H. Kim, K. K. Paek, J. H. Park, E. G. Yang, T. S. Kim, J. Y. Kang, and B. K. Ju, "Characterization of an integrated, fluorescence-detection hybrid device with photodiode and organic light-emitting diode," *IEEE Electron Device Lett.*, vol. 27, no. 9, pp. 746–748, 2006.

[118] E. Thrush, O. Levi, L. J. Cook, J. Deich, A. Kurtz, S. J. Smith, W. E. Moerner, and J. S. Harris Jr., "Monolithically integrated semiconductor fluorescence sensor for microfluidic applications," *Sens. Act. B*, vol. 105, no. 2, pp. 393–399, 2005.

[119] E. Thrush, O. Levi, L. J. Cook, J. J. S. Harris, S. J. Smith, J. Deich, and W. E. Moerner, "Integrated semiconductor bio-fluorescence sensor integrated on micro-fluidic platform," in *Conference on Lasers and Electro-Optics (CLEO) 2004*, vol. 2, San Francisco, CA, 2004.

[120] E. Thrush, O. Levi, L. J. Cook, S. J. Smith, and J. J. S. Harris, "Greater than 10^6 optical isolation in integrated optoelectronic fluorescence sensor," in *26th Annual International Conference of the IEEE Engineering in Medicine and Biology Society (EMBS '04)*, vol. 3, San Francisco, CA, 2004, pp. 2080–1.

[121] E. Thrush, O. Levi, W. Ha, G. Carey, L. J. Cook, J. Deich, S. J. Smith, W. E. Moerner, and J. J. S. Harris, "Integrated semiconductor vertical-cavity surface-emitting lasers and pin photodetectors for biomedical fluorescence sensing," *IEEE J. Quantum Electron.*, vol. 40, no. 5, pp. 491–8, 2004.

[122] E. P. Thrush, O. Levi, L. J. Cook, J. Deich, S. J. Smith, W. E. Moerner, and J. J. S. Harris, "Laser background characterization in a monolithically integrated bio-fluorescence sensor," in *SPIE Conference on Advanced Biomedical and Clinical Diagnostic Systems II*, vol. 5318, San Jose, CA, 2004, pp. 59–65.

[123] H. D. Summers and P. A. Porta, "Resonant-cavity optoelectronic devices for fluorimetry," *IEEE J. Sel. Top. Quantum Electron.*, vol. 11, no. 4, pp. 854–857, 2005.

[124] T. Kamei, B. M. Paegel, J. R. Scherer, A. M. Skelley, R. A. Street, and R. A. Mathies, "Integrated hydrogenated amorphous si photodiode detector for microfluidic bioanalytical devices," *Anal. Chem.*, vol. 75, no. 20, pp. 5300–5305, 2003.

[125] T. Kamei, B. M. Paegel, J. R. Scherer, A. M. Skelley, R. A. Street, and R. A. Mathies, "Fusion of a-si : H sensor technology with microfluidic bioanalytical devices," *J. Non-Cryst. Solids*, vol. 338-40, pp. 715–719, 2004.

[126] G. Lammel and P. Renaud, "Free-standing, mobile 3d porous silicon microstructures," *Sens. Act. A*, vol. 85, no. 1-3, pp. 356–360, 2000.

[127] G. Lammel, S. Schweizer, and P. Renaud, "Microspectrometer based on a tunable optical filter of porous silicon," *Sens. Act. A*, vol. 92, no. 1-3, pp. 52–59, 2001.

[128] G. Lammel, S. Schweizer, S. Schiesser, and P. Renaud, "Tunable optical filter of porous silicon as key component for a mems spectrometer," *J. Microelectromech. Syst.*, vol. 11, no. 6, pp. 815–828, 2002.

[129] E. Lorenzo, C. J. Oton, N. E. Capuj, M. Ghulinyan, D. Navarro-Urrios, Z. Gaburro, and L. Pavesi, "Porous silicon-based rugate filters," *Appl. Optics*, vol. 44, no. 26, pp. 5415–5421, 2005.

[130] S. Langa, J. Carstensen, M. Christophersen, K. Steen, S. Frey, I. M. Tiginyanu, and H. Foll, "Uniform and nonuniform nucleation of pores during the anodization of si, ge, and iii-v semiconductors," *J. Electrochem. Soc.*, vol. 152, no. 8, pp. C525–C531, 2005.

[131] S. Lolkes, M. Christophersen, S. Langa, J. Carstensen, and H. Foll, "Selforganized formation of crystallographically oriented octahedral cavities during electrochemical pore etching," *Mater. Sci. Eng. B-Solid State Mater. Adv. Technol.*, vol. 101, no. 1-3, pp. 159–163, 2003.

[132] H. Ouyang, M. Christophersen, R. Viard, B. L. Miller, and P. M. Fauchet, "Macroporous silicon microcavity for macromolecule detection," *Adv. Funct. Mater.*, vol. 15, no. 1851, 2005.

[133] H. Ouyang, M. Christophersen, and P. M. Fauchet, "Enhanced control of porous silicon morphology from macropore to mesopore formation," *Phys. Status Solidi A-Appl. Mat.*, vol. 202, pp. 1396–1401, 2005.

[134] J. R. Link and M. J. Sailor, "Smart dust: Self-assembling, self-orienting photonic crystals of porous si," *Proc. Natl. Acad. Sci. U. S. A.*, vol. 100, no. 19, pp. 10 607–10 610, 2003.

[135] M. Hochberg, T. Baehr-Jones, C. Walker, and A. Scherer, "Integrated plasmon and dielectric waveguides," *Opt. Express*, vol. 12, no. 22, pp. 5481–5486, 2004, 1094-4087.

[136] M. U. Gonzalez, J. C. Weeber, A. L. Baudrion, A. Dereux, A. L. Stepanov, J. R. Krenn, E. Devaux, and T. W. Ebbesen, "Design, near-field characterization, and modeling of 45 circle surface-plasmon bragg mirrors," *Phys. Rev. B*, vol. 73, no. 15, 2006, 1098-0121.

[137] J. C. Weeber, Y. Lacroute, A. Dereux, E. Devaux, T. Ebbesen, C. Girard, M. U. Gonzalez, and A. L. Baudrion, "Near-field characterization of bragg

mirrors engraved in surface plasmon waveguides," *Phys. Rev. B*, vol. 70, no. 23, 2004, 1098-0121.

[138] J. R. Krenn, H. Ditlbacher, G. Schider, A. Hohenau, A. Leitner, and F. R. Aussenegg, "Surface plasmon micro- and nano-optics," *J. Microsc.-Oxf.*, vol. 209, pp. 167–172, 2003, 0022-2720 Part 3.

[139] A. Boltasseva, S. I. Bozhevolnyi, T. Nikolajsen, and K. Leosson, "Compact bragg gratings for long-range surface plasmon polaritons," *J. Lightwave Technol.*, vol. 24, no. 2, pp. 912–918, 2006, 0733-8724.

[140] S. Jette-Charbonneau, R. Charbonneau, N. Lahoud, G. Mattiussi, and P. Berini, "Demonstration of bragg gratings based on long-ranging surface plasmon polariton waveguides," *Opt. Express*, vol. 13, no. 12, pp. 4674–4682, 2005, 1094-4087.

[141] S. Jette-Charbonneau, R. Charbonneau, N. Lahoud, G. A. Mattiussi, and P. Berini, "Bragg gratings based on long-range surface plasmon-polariton waveguides: Comparison of theory and experiment," *IEEE J. Quantum Electron.*, vol. 41, no. 12, pp. 1480–1491, 2005, 0018-9197.

[142] Z. H. Han, E. Forsberg, and S. L. He, "Surface plasmon bragg gratings formed in metal-insulator-metal waveguides," *IEEE Photonics Technol. Lett.*, vol. 19, no. 2-4, pp. 91–93, 2007, 1041-1135.

[143] A. Hosseini and Y. Massoud, "A low-loss metal-insulator-metal plasmonic bragg reflector," *Opt. Express*, vol. 14, no. 23, pp. 11 318–11 323, 2006, 1094-4087.

[144] A. Hosseini and Y. Massoud, "Subwavelength plasmonic bragg reflector structures for on-chip optoelectronic applications," in *IEEE Int. Symp. Circuits and Systems (ISCAS07)*, New Orleans, LA, 2007, pp. 2283–2286.

[145] J. A. Dionne, L. A. Sweatlock, H. A. Atwater, and A. Polman, "Planar metal plasmon waveguides: frequency-dependent dispersion, propagation, localization, and loss beyond the free electron model," *Phys. Rev. B*, vol. 72, no. 7, 2005, 1098-0121.

[146] J. A. Dionne, L. A. Sweatlock, H. A. Atwater, and A. Polman, "Plasmon slot waveguides: Towards chip-scale propagation with subwavelength-scale localization," *Phys. Rev. B*, vol. 73, no. 3, 2006, 1098-0121.

[147] W. L. Barnes, A. Dereux, and T. W. Ebbesen, "Surface plasmon subwavelength optics," *Nature*, vol. 424, no. 6950, pp. 824–830, 2003, 0028-0836.

[148] E. Ozbay, "Plasmonics: Merging photonics and electronics at nanoscale dimensions," *Science*, vol. 311, no. 5758, pp. 189–193, 2006, 0036-8075.

[149] R. R. Chance, A. Prock, and R. Silbey, "Comments on classical theory of energy-transfer," *J. Chem. Phys.*, vol. 62, no. 6, pp. 2245–2253, 1975, 0021-9606.

[150] H. Ditlbacher, J. R. Krenn, N. Felidj, B. Lamprecht, G. Schider, M. Salerno, A. Leitner, and F. R. Aussenegg, "Fluorescence imaging of surface plasmon fields," *Appl. Phys. Lett.*, vol. 80, no. 3, pp. 404–406, 2002, 0003-6951.

[151] S. C. Kitson, W. L. Barnes, J. R. Sambles, and N. P. K. Cotter, "Excitation of molecular fluorescence via surface plasmon polaritons," *J. Mod. Opt.*, vol. 43, no. 3, pp. 573–582, 1996, 0950-0340.

[152] M. Kreiter, T. Neumann, S. Mittler, N. Knoll, and J. R. Sambles, "Fluorescent dyes as a probe for the localized field of coupled surface plasmon-related resonances," *Phys. Rev. B*, vol. 64, no. 7, 2001, 1098-0121.

[153] O. Stranik, H. M. McEvoy, C. McDonagh, and B. D. MacCraith, "Plasmonic enhancement of fluorescence for sensor applications," *Sens. Act. B*, vol. 107, no. 1, pp. 148–153, 2005, 0925-4005.

[154] M. Tuma and R. Gruhlke, "Integrated fluorescence," Patent 5 841 143, November 24^{th}, 1998.

[155] G. C. Giakos, K. Meehan, and M. Tuma, "Exploitation of enhanced fluorescence via cross-coupling principles toward the design of an optical integrated thin-film sensor for nanotechnology and biomedical applications," *IEEE Trans. Instrum. Meas.*, vol. 51, no. 5, pp. 970–975, 2002.

[156] S. Ninomiya and S. Adachi, "Optical properties of wurtzite cds," *J. Appl. Phys.*, vol. 78, no. 2, pp. 1183–1190, 1995.

[157] O. Yadid-Pecht and R. Etienne-Cummings, Eds., *CMOS Imagers: From Phototransduction to Image Processing.* Norwell, MA: Kluwer Academic Publishers, 2004.

[158] D. R. Lide, Ed., *CRC Handbook of Physics and Chemistry*, 87th ed. Boca Raton: CRC Press, 2006.

[159] G. Kovacs, *Micromachined Transducers Sourcebook*, ser. McGraw-Hill Series in Electrical and Computer Engineering. McGraw-Hill, 1998.

[160] A. H. Mahan, R. Biswas, L. M. Gedvilas, D. L. Williamson, and B. C. Pan, "On the influence of short and medium range order on the material band gap in hydrogenated amorphous silicon," *J. Appl. Phys.*, vol. 96, no. 7, pp. 3818–3826, 2004.

[161] H. Ji, M. Dandin, E. Smela, and P. Abshire, "Integrated fluorescence sensing for lab-on-a-chip devices," in *IEEE/NLM Life Science Systems and Applications Workshop*, Bethesda, Maryland, 2006.

[162] V. P. Iordanov, J. Bastemeijer, R. Ishihara, P. M. Sarro, A. Bossche, and M. J. Vellekoop, "Filter-protected photodiodes for high-throughput enzymatic analysis," *IEEE Sens. J.*, vol. 4, no. 5, pp. 584–588, 2004.

[163] M. L. Chabinyc, D. T. Chiu, J. C. McDonald, A. D. Stroock, J. F. Christian, A. M. Karger, and G. M. Whitesides, "An integrated fluorescence detection system in poly(dimethylsiloxane) for microfluidic applications," *Anal. Chem.*, vol. 73, no. 18, pp. 4491–4498, 2001.

[164] J. Kruger, K. Singh, A. O'Neill, C. Jackson, A. Morrison, and P. O'Brien, "Development of a microfluidic device for fluorescence activated cell sorting," *J. Micromech. Microeng.*, vol. 12, no. 4, pp. 486–494, 2002.

[165] O. J. A. Schueller, D. C. Duffy, J. A. Rogers, S. T. Brittain, and G. M. Whitesides, "Reconfigurable diffraction gratings based on elastomeric microfluidic devices," *Sens. Act. A*, vol. 78, no. 2-3, pp. 149–159, 1999, 0924-4247.

[166] C. C. Chen, D. Hirdes, and A. Folch, "Gray-scale photolithography using microfluidic photomasks," *Proc. Natl. Acad. Sci. U. S. A.*, vol. 100, no. 4, pp. 1499–1504, 2003, 0027-8424.

[167] R. B. Merrill, "Color separation in an active pixel cell imaging array using a triple-well structure," Patent 5 965 875, October 12^{th}, 1999.

[168] R. Lyon and P. Hubel, "Eyeing the camera: into the next century," in *Tenth Color Imaging Conference: Color Science and Engineering Systems, Technologies, Applications*, vol. 10, Scottsdale, Arizona, 2002, pp. 349–355.

[169] D. Starikov, F. Benkabou, N. Medelci, and A. Bensaoula, "Integrated multi-wavelength fluorescence sensors," in *Sensors for Industry Conference, 2nd ISA/IEEE*, 2002, pp. 15–18.

[170] Y. Maruyama, K. Sawada, H. Takao, and M. Ishida, "The fabrication of filterless fluorescence detection sensor array using cmos image sensor technique," *Sens. Act. A*, vol. 128, no. 1, pp. 66–70, 2006.

[171] Y. Maruyama, K. Sawada, H. Takao, and M. Ishida, "A novel filterless fluorescence detection sensor for dna analysis," *IEEE Trans. Electron Devices*, vol. 53, no. 3, pp. 553–558, 2006.

[172] R. F. Wolffenbuttel, "Mems-based optical mini- and microspectrometers for the visible and infrared spectral range," *J. Micromech. Microeng.*, vol. 15, no. 7, pp. S145–S152, 2005, sp. Iss. SI.

[173] O. Hofmann, X. H. Wang, J. C. deMello, D. D. C. Bradley, and A. J. deMello, "Towards microalbuminuria determination on a disposable diagnostic microchip with integrated fluorescence detection based on thin-film organic light emitting diodes," *Lab Chip*, vol. 5, no. 8, pp. 863–868, 2005.

[174] V. Lien, K. Zhao, Y. Berdichevsky, and Y. H. Lo, "High-sensitivity cytometric detection using fluidic-photonic integrated circuits with array waveguides," *IEEE J. Sel. Top. Quantum Electron.*, vol. 11, no. 4, pp. 827–834, 2005.

[175] G. M. Yee, N. I. Maluf, P. A. Hing, M. Albin, and G. T. A. Kovacs, "Miniature spectrometers for biochemical analysis," *Sens. Act. A*, vol. 58, no. 1, pp. 61–66, 1997.

[176] M. A. Powers, S. T. Koev, A. Schleunitz, H. Yi, V. Hodzic, W. E. Bentley, G. F. Payne, G. W. Rubloff, and R. Ghodssi, "A fabrication platform for electrically mediated optically active biofunctionalized sites in biomems," *Lab Chip*, vol. 5, no. 6, pp. 583–586, 2005.

[177] J. M. Ruano, A. Glidle, A. Cleary, A. Walmsley, J. S. Aitchison, and J. M. Cooper, "Design and fabrication of a silica on silicon integrated optical biochip as a fluorescence microarray platform," *Biosens. Bioelectron.*, vol. 18, no. 2-3, pp. 175–184, 2003.

[178] P. N. Zeller, G. Voirin, and R. E. Kunz, "Single-pad scheme for integrated optical fluorescence sensing," *Biosens. Bioelectron.*, vol. 15, no. 11-12, pp. 591–595, 2000.

[179] K. Miyaki, Y. L. Guo, T. Shimosaka, T. Nakagama, H. Nakajima, and K. Uchiyama, "Fabrication of an integrated pdms microchip incorporating an led-induced fluorescence device," *Anal. Bioanal. Chem.*, vol. 382, no. 3, pp. 810–816, 2005.

[180] J. C. Roulet, R. Volkel, H. P. Herzig, E. Verpoorte, N. F. de Rooij, and R. Dandliker, "Fabrication of multilayer systems combining microfluidic and microoptical elements for fluorescence detection," *J. Microelectromech. Syst.*, vol. 10, no. 4, pp. 482–491, 2001.

[181] J. C. Roulet, R. Volkel, H. P. Herzig, E. Verpoorte, N. F. de Rooij, and R. Dandliker, "Microlens systems for fluorescence detection in chemical microsystems," *Opt. Eng.*, vol. 40, no. 5, pp. 814–821, 2001.

[182] J. C. Roulet, R. Volkel, H. P. Herzig, E. Verpoorte, N. F. de Rooij, and R. Dandliker, "Performance of an integrated microoptical system for fluorescence detection in microfluidic systems," *Anal. Chem.*, vol. 74, no. 14, pp. 3400–3407, 2002.

[183] M. Zourob, S. Mohr, B. J. T. Brown, P. R. Fielden, M. McDonnell, and N. J. Goddard, "The development of a metal clad leaky waveguide sensor for the detection of particles," *Sens. Act. B*, vol. 90, no. 1-3, pp. 296–307, 2003, sp. Iss. SI.

[184] M. Zourob, S. Mohr, B. J. T. Brown, P. R. Fielden, M. B. McDonnell, and N. J. Goddard, "An integrated metal clad leaky waveguide sensor for detection of bacteria," *Anal. Chem.*, vol. 77, no. 1, pp. 232–242, 2005.

[185] M. Zourob, S. Mohr, B. J. T. Brown, P. R. Fielden, M. B. McDonnell, and N. J. Goddard, "An integrated optical leaky waveguide sensor with electrically induced concentration system for the detection of bacteria," *Lab Chip*, vol. 5, no. 12, pp. 1360–1365, 2005.

[186] M. Zourob, S. Mohr, B. J. T. Brown, P. R. Fielden, M. B. McDonnell, and N. J. Goddard, "Bacteria detection using disposable optical leaky waveguide sensors," *Biosens. Bioelectron.*, vol. 21, no. 2, pp. 293–302, 2005.

[187] M. Zourob, S. Mohr, P. R. Fielden, and N. J. Goddard, "Small-volume refractive index and fluorescence sensor for micro total analytical system (μ-tas) applications," *Sens. Act. B*, vol. 94, no. 3, pp. 304–312, 2003.

[188] M. Zourob, S. Mohr, P. R. Fielden, and N. J. Goddard, "An integrated disposable dye clad leaky waveguide sensor for μtas applications," *Lab Chip*, vol. 5, no. 7, pp. 772–777, 2005.

[189] M. Zourob, A. Simonian, J. Wild, S. Mohr, X. D. Fan, I. Abdulhalim, and N. J. Goddard, "Optical leaky waveguide biosensors for the detection of organophosphorus pesticides," *Analyst*, vol. 132, no. 2, pp. 114–120, 2007.

[190] J. Seo and P. L. Lee, "Fluorescence amplification by self-aligned integrated microfluidic optical systems," in *Transducers*, Boston, USA, 2003, pp. 1136–1139.

[191] T. Daud, J. R. Janesick, K. Evans, and T. Elliott, "Charge-coupled-device response to electron beam energies of less than 1 kev up to 20 kev," *Opt. Eng.*, vol. 26, no. 8, pp. 686–91, 1987.

[192] B. Fowler, A. E. Gamal, D. Yang, and H. Tian, "A method for estimating quantum efficiency for cmos image sensors," in *SPIE Conference on Solid State Sensor Arrays: Development and Applications II. , USA*, vol. 3301, San Jose, CA, 1998, pp. 178–85.

[193] A. v. d. Ziel, *Noise in Solid State Devices and Circuits*. New York, NY: John Wiley & Sons, Inc., 1986.

[194] C. D. Motchenbacher and J. A. Connelly, *Low Noise Electronic System Design*. New York, NY: John Wiley & Sons, Inc., 1993.

[195] B. E. A. Saleh and M. C. Teich, *Fundamentals of Photonics*. New York , NY: John Wiley & Sons, Inc., 1991.

[196] A. Schwartz, L. Wang, E. Early, A. Gaigalas, Y.-z. Zhang, G. E. Marti, and R. F. Vogt, "Quantitating fluorescence intensity from fluorophore: The definition of MESF assignment," *J. Res. Natl. Inst. Stand. Technol.*, vol. 107, no. 1, pp. 83–91, 2002.

[197] A. K. Gaigalas, L. Wang, A. Schwartz, G. E. Marti, and J. R. F. Vogt, "Quantitating fluorescence intensity from fluorophore: assignment of MESF values," *J. Res. Natl. Inst. Stand. Technol.*, vol. 110, no. 2, pp. 101–14, 2005.

[198] D. Psaltis, S. R. Quake, and C. Yang, "Developing optofluidic technology through the fusion of microfluidics and optics," *Nature*, vol. 442, no. 7101, pp. 381–386, 2006.

[199] C. Richard, A. Renaudin, V. Aimez, and P. G. Charette, "An integrated hybrid interference and absorption filter for fluorescence detection in lab-on-a-chip devices," *Lab Chip*, vol. 9, no. 10, pp. 1371–1376, 2009.

[200] C. L. Bliss, J. N. McMullin, and C. J. Backhouse, "Integrated wavelength-selective optical waveguides for microfluidic-based laser-induced fluorescence detection," *Lab Chip*, vol. 8, no. 1, pp. 143–151, 2008.

[201] K. S. Lee, H. L. T. Lee, and R. J. Ram, "Polymer waveguide backplanes for optical sensor interfaces in microfluidics," *Lab Chip*, vol. 7, no. 11, pp. 1539–1545, 2007.

[202] N. Nelson, D. Sander, M. Dandin, S. B. Prakash, A. Sarje, and P. Abshire, "Handheld Fluorometers for Lab-on-a-Chip Applications," *IEEE Trans. Biomed. Circuits Syst.*, vol. 3, no. 2, pp. 97–107, 2009.

[203] R. E. Lee, C. Neri, V. Malatesta, R. M. Riva, and M. Angaroni, *in Specialty Polymer Additives, ch. 7.* Blackwell Publishing, Inc., 2001.

[204] B. Balakrisnan, S. Patil, and E. Smela, "Patterning PDMS using a combination of wet and dry etching," *J. Micormech. Microeng.*, vol. 19, no. 4, 2009.

[205] P. Jothimuthu, A. Carroll, A. A. S. Bhagat, G. Lin, J. E. Mark, and I. Papautsky, "Photodefinable PDMS thin films for microfabrication applications," *J. Micromech. Microeng.*, vol. 19, no. 4, 2009.

[206] A. Piruska, I. Nikcevic, S. Lee, C. Ahn, W. Heineman, P. Limbach, and C. Seliskar, "The autofluorescence of plastic materials and chips measured under laser irradiation," *Lab Chip*, vol. 5, no. 12, pp. 1348–1354, 2005.

[207] Y. Wang, G. Young, P. C. Aoto, J.-H. Pai, M. Bachman, G. P. Li, C. E. Sims, and N. L. Allbritton, "Broadening cell selection criteria with micropallet arrays of adherent cells," *Cytom. Part A*, vol. 71A, no. 10, pp. 866–874, 2007.

[208] N. N. D. Sander and P. Abshire, "Noise model, analysis and characterization of a differential active pixel sensor," in *IEEE Int. Symp. Circuits and Systems*, Seattle, WA, USA, 2008, pp. 1780–1783.

[209] B. Fowler, A. El Gamal, D. Yang, and H. Tian, "Method for estimating quantum efficiency for CMOS image sensors," *Proceedings SPIE*, vol. 3301, pp. 178–185, 1998.

[210] K. M. Kitchens, R. B. Kolhatkar, P. W. Swaan, N. D. Eddington, and H. Ghandehari, "Transport of poly(amidoamine) dendrimers across Caco-2 cell monolayers: Influence of size, charge and fluorescent labeling," *Pharmaceutical Research*, vol. 23, pp. 2818–2826, 2006.

[211] R. Jevprasesphant, J. Penny, R. Jalal, D. Attwood, N. B. McKeown, and A. D'Emanuele, "The influence of surface modificaton on the cytotoxicity of PAMAM dendrimers," *International J. Pharmaceutics*, vol. 252, pp. 263–266, 2003.

[212] D. W. Zabriskie and A. E. Humphrey, "Estimation of fermentation biomass concentration by measuring culture fluorescence," *Applied and Environmental Microbiology*, vol. 35, pp. 337–343, 1978.

[213] C. Ratledge, "Yeast physiology – a micro-synopsis," *Bioprocess and Biosystems Engineering*, vol. 6, pp. 195–203, 1991.

[214] N. Nelson, S. Prakash, D. Sander, M. Dandin, A. Sarje, H. Ji, and P. Abshire, "A handheld fluorometer for UV excitable fluorescence assays," in *Proc. of the IEEE Biomedical Circuits and Systems Conference 2007*, Montréal, Canada, 2007, pp. 111–114.

[215] J. H. Lee, R. K. Prud'homme, and I. A. Aksay, "Cure depth in photopolymerization: Experiments and theory," *J. Mater. Res.*, vol. 16, no. 12, pp. 3536–3544, 2001.

[216] M. Gaudet, J. Camart, L. Buchaillot, and S. Arscott, "Variation of absorption coefficient and determination of critical dose of SU-8 at 365 nm," *Appl. Phys. Lett.*, vol. 88, no. 2, 2006.

[217] A. Vert, S. Soloviev, and P. Sandvik, "SiC avalanche photodiodes and photomultipliers for ultraviolet and solar-blind light detection," *Phys. Status Solidi A-Appl. Mat.*, vol. 206, pp. 2468–2477, 2009.

[218] T. Velten, H. H. Ruf, D. Barrow, N. Aspragathos, P. Lazarou, E. Jung, C. Malek, M. Richter, J. Kruckow, and M. Wackerle, "Packaging of bio-MEMS: Strategies, technologies, and applications," *IEEE Trans. Adv. Packag.*, vol. 28, pp. 533–546, 2005.

[219] R. Delille, M. Urdaneta, S. J. Moseley, and E. Smela, "Benchtop polymer MEMS," *J. Microelectromech. Syst.*, vol. 15, pp. 1108–1120, 2006.

[220] Y. Liu, E. Smela, N. M. Nelson, and P. Abshire, "Cell-lab on a chip: a CMOS-based microsystem for culturing and monitoring cells," in *Proceedings of the 26th Annual International Conference of the IEEE EMBS*, San Francisco, CA, USA, 2004, pp. 2534–2537.

[221] S. B. Prakash and P. Abshire, "Tracking cancer cell proliferation on a CMOS capacitance sensor chip," *Biosens. Bioelectron.*, vol. 23, pp. 1449–1457, 2008.

[222] S. B. Prakash, M. G. Urdaneta, M. Christophersen, E. Smela, and P. Abshire, "*In situ* electrochemcial control of electroactive polymer films on a CMOS chip," *Sens. Actuator B-Chem.*, vol. 129, pp. 699–704, 2008.

[223] M. Urdaneta, Y. Liu, M. Christophersen, S. B. Prakash, P. Abshire, and E. Smela, "Integrating conjugated polymer microactuators with CMOS sensing circuitry for studying living cells," in *SPIE's 12th Annual Int'l. Symp. Smart Structures and Materials*, San Diego, California, Mar. 2005.

[224] S. M. Martin, T. D. Strong, and R. B. Brown, "Design, implementation, and verification of a CMOS integrated chemical sensor system," in *International Conference on MEMS, Nano and Smart Systems*, Los Alamos, CA, USA, 2004, pp. 379–385.

[225] W. B. Davenport and W. L. Root, *An Introduction to the Theory of Random Signals and Noise*. IEEE Press, 1987.